Triannual Report 1999 — 2001

Research Group "Scanning Probe Methods"

University of Hamburg
Microstructure Advanced
Research Center Hamburg
and Institute of Applied Physics

Jungiusstraße 11
D-20355 Hamburg, Germany

Contact:
Prof. Dr. Roland Wiesendanger
Tel. (++49) 40-42838-5244 (direct)
(++49) 40-42838-3203/-7045 (secretary)
FAX (++49) 40-42838-6188
e-mail `wiesendanger@physnet.uni-hamburg.de`
WWW www.nanoscience.de

Contents

Chapter 1

Preface

This is the third triannual report of the research group "Scanning Probe Methods" at the Institute of Applied Physics and "Microstructure Advanced Research Center Hamburg (MARCH)" of the University of Hamburg.

MARCH was established in 1996 at the University of Hamburg as a joint effort of the Bund and the State of Hamburg. Six research groups, headed by professors, and three independent junior research groups are involved in MARCH covering the following research topics: Semiconductor physics, nanostructure physics, scanning probe methods, surface and interface physics, low temperature physics and magnetism, growth of semiconductor heterostructures and nanostructures. In total 135 scientists are working at MARCH including 55 Ph.D. students and 42 diploma students. In 1996 the DFG-Graduiertenkolleg "Physics of nanostructured solids" was initiated which primarily involves scientists at MARCH (chairperson: Prof. Dr. W. Hansen, MARCH). The focus of this Graduiertenkolleg is on the growth and characterization of nanostructured solids with a strong emphasis on collective physical (such as magnetic and superconducting) properties of nanostructures. In contrast, the DFG-Graduiertenkolleg "Spectroscopy on localized atomic systems" established in 1999 at the "Fachbereich" of Physics (chairperson: Prof. Dr. G. Huber, Institute of Laser Physics) focusses on physical properties of localized atoms in traps, at surfaces, and in host lattices. This Graduiertenkolleg also involves two research groups of MARCH leading to a stimulating scientific exchange between the two priority areas of micro-/nanostructure physics and laser physics of the "Fachbereich" of Physics. In 1997 a DFG-Sonderforschungsbereich (SFB 508) on "Quantum materials" was initiated (chairperson: Prof. Dr. D. Heitmann, MARCH) which involves research groups at MARCH, at the I. Institute of Theoretical Physics, at HASYLAB/DESY, and at the Institute of Physical Chemistry. The SFB 508 deals with quantum phenomena in nanostructured matter which are manifested in energy-quantization, tunnel-effects as well as Coulomb, exchange, and correlation effects. It includes a wide range of spectroscopic investigations, transport measurements, structural characterization, and theory. The preparation techniques for nanostructures range from molecular-beam-epitaxy combined with optical and electron-beam-lithography to wet chemical synthesis. This wide variety of physical problems and experimental techniques is balanced by an almost exclusive focus on one class of materials, namely III-V semiconductors. The three primary research topics include "lateral nanostructures", "hybrid structures" (e.g. semiconductor-superconductor and semiconductor-ferromagnet hybrids), and "clusters". The latter research activity has led to a very fruitful exchange of ideas and personnel between the Institute of Physical Chemistry (research groups of Prof. Dr. H. Weller and Prof. Dr. S. Förster) and MARCH which was an essential starting point for transdisciplinary initiatives.

Another joint activity between the "Fachbereiche" of Chemistry and Physics has started in early 2001: the DFG-Graduiertenkolleg "Design and characterization of functional materials" (chairperson: Prof. Dr. D. Rehder, Institute of Inorganic and Applied Chemistry) which includes research groups of several institutes of the "Fachbereiche" of Chemistry, Earth Sciences, MARCH, and HASYLAB. The highly interdisciplinary research area "functional materials" spans the range from molecular and nano-particle dimensions to macroscopic materials. It includes the design, synthesis, and characterization of mesoporous systems, heterogeneous catalysts, biocompatible materials, conductors and semiconductors, materials with specific optical surface properties, and colloids, often starting on the molecular level or modifying a given macroscopic material, and requiring a broad arsenal of modern analytical methods. Stimulation of interdisciplinary research will be enhanced by bringing together motivated students from different "Fachbereiche" by joint lectures and seminars, as well as workshops.

Since 1998 MARCH is hosting a coordination site of the German "Center of Competence in Nano-scale Analysis" (CCN) funded by the Federal Ministry for Education and Research (BMBF). This Center of Competence (current chairperson: Prof. Dr. R. Wiesendanger, MARCH) is organized as a transregional network of in total 60 groups at universities, at research centers and in industry and promotes technology transfer, activities leading to new start-up companies, and public information services in the area of nanoscience and nanotechnology. The CCN provides a valuable support of the infrastructure at MARCH, e.g. for secretary services, public relation services, and technology transfer. In 1999 a successful start-up company (C & W Ingenieursgesellschaft mbH) was initiated by two coworkers of the Hamburg coordination site of the CCN focussing on the development of customized antivibration systems for applications in micro-electronics and biotechnology.

Major events in the past three years time period include the organization of the Third International Conference on Non-Contact Atomic Force Microscopy (NC-AFM 2000, July 16-19, 2000) and the Second International Conference on Scanning Probe Spectroscopy (SPS-2000, July 19-22, 2000). Both conferences were held in the Congress Center Hamburg (CCH) with great success. We have also organized two symposia on Interdisciplinary Nanoscience in Hamburg as starting events for the establishment of a new Interdisciplinary Nanoscience Center Hamburg. The proposal for this new Center was put forward by the strategic initiative INA (Interdisciplinary

Nanoscience Alliance) which was formed in the summer of 1999. The declared long-term goal of this initiative is to gain fundamental new insight into nanoscience-related problems through more intensive research in areas bordering the traditional disciplines and in this way to create a sound basis for future technological developments in Northern Germany.

The outstanding scientific achievements of the research group "Scanning Probe Methods" were recognized by several prizes and awards given to members of our group in the past three years time period. In 1999 Roland Wiesendanger received the Karl Heinz Beckurts-Prize from the Karl Heinz Beckurts Foundation while Udo Schwarz was winner of the Gaede Award from the German Vacuum Society. In the same year Udo Schwarz received a Heisenberg stipend from the Deutsche Forschungsgemeinschaft (DFG). In 2000 Mathias Getzlaff received the Max Auwärter-Award from the Max Auwärter Foundation while Roland Wiesendanger became member of the Academy of Sciences Leopoldina (Halle) and member of the Jungiusgesellschaft (Hamburg). In 2001 Stefan Heinze received an Emmy-Noether stipend from the DFG which allows him to set up a junior research group. Finally, Robert Ravlic received the 1st Prize Poster Award at the International Conference on Metallic Multilayers (MML 2001).

This research report provides a good opportunity to thank all funding agencies including the BMBF, the DFG, the EU, the Stifterverband, the German-Israeli Foundation (GIF), as well as industrial companies for their support of our activities in nano-science research and organization. In particular we would like to thank the Ministry of Science and Research of the Free and Hanseatic City of Hamburg for its strong devotion to establish MARCH as an internationally recognized Center of Excellence in nano-science and technology. I would also like to take the opportunity to thank all members of the research group "Scanning Probe Methods" for their outstanding efforts and achievements during the past three years leading, e. g. to two greatly recognized publications in "Science", ten publications in the "Physical Review Letters" and 332 presentations at conferences, seminars, and colloquia including 69 invited talks at international meetings. Finally, we gratefully acknowledge the excellent support by our central mechanical and electronical workshops, as well as by our secretaries and administration staff.

Hamburg, December 2001

Prof. Dr. Roland Wiesendanger

Chapter 2

Staff Members

Head

Prof. Dr. Roland Wiesendanger

Secretary

Ute Brenger
Renate Schulze

Public Relations Office

Dipl.-Jour. Dipl. Phys. Klaus Schoepe

Technical Support

Dipl.-Ing. Sönke Carstens (until September 1999)
Dipl.-Ing. Michael Langer
Dipl.-Ing. Christian Wobbe (until November 1999)
PTA Norbert Dix

Senior Scientists

Dr. Wolf Allers (until April 2001)
Dr. Makoto Ashino
Dr. Matthias Bode
PD Dr. Mathias Getzlaff
Dr. Daniel Haude
Dr. Stefan Heinze (until September 2001)
Dr. Hendrik Hölscher (until March 2001)
Dr. Markus Morgenstern
Dr. Oswald Pietzsch

Dr. Alexander Schwarz
PD Dr. Udo Schwarz

Ph. D. Students

Kirsten von Bergmann
Axel Born (until October 2000)
Michael Dreyer (until June 1999)
Karsten Gerlof (until February 1999)
Torben Hänke
Volker Hagen
Johannes Isenbart
Alexander Kelch (until September 2000)
Michael Kleiber (until December 2000)
Jan Klijn
André Kubetzka
Shenja Langkat
Marcus Liebmann
Theophilos Maltezopoulos
Christian Meyer
Jens Müller (until December 2000)
René Pascal (until July 1999)
Robert Ravlic
Tobias Richter
André Wachowiak
Jens Wiebe
Christoph Zarnitz (until December 1999)

Diploma Students

Carsten Bartsch (until May 2000)
Luis Berbil-Bautista
Leif Busse (until April 2000)
Uwe Kaiser
Oliver Krause (until April 2000)
Focko Meier
Jan Peter Podsiadly (until November 1999)
Lilli Sacharow
Martin von Sprekelsen
Lutz Tröger (until April 2001)
Anja Wehner (until January 2001)
Richard Werner (until July 2000)

Guest Researchers

Dr. Ryszard Czajka, Poznan University of Technology, Poland (August - September 1999)
Dr. Tao Liu, Chinese Academy of Sciences, Beijing (February - April 1999)
Prof. Dr. Sergej Nepijko, Ukrainian Academy of Sciences, Kiev (until March 1999)
Dr. Denis Ovchinnikov, Russian Academy of Sciences, Kazan (October 1999)
Ung Hwan Pi, Seoul National University, South Korea (June - November 2000 and December 2001)
Prof. Dr. Bronislaw Susla, Poznan University of Technology, Poland (until February 1999)
Dr. Nobuki Tezuka, Tohoku University, Sendai, Japan (June 1999 - September 2000)

Chapter 3

Research Activities 1999-2001

3.1 Overview

R. Wiesendanger

Our research activities are concentrated on nanometer-scale probe methods. In particular, emphasis is put on the investigation of the fundamental relationship between nanostructure and nanophysical properties. Scanning probe methods are ideally suited for such investigations because they provide high spatial resolution combined with spectroscopical capabilities. By choosing an appropriate type of interaction between probe tip and sample, almost any kind of nanophysical property can be studied by scanning probe methods. We apply scanning probe methods (SPM) to various classes of materials, including metals, semiconductors, insulators, superconductors, magnetic materials, as well as organic thin films and materials.

To be able to make significant contributions to this rapidly developing field, a major part of our activities is devoted to new developments or further improvements on SPM instrumentation, including the development of new positioning devices with nanometer-scale accuracy, the development of new types of sensors, or the development of dedicated SPM instruments which can operate under extreme conditions (e.g. UHV, low temperatures and high magnetic fields). Special emphasis is also put on the development of new experimental methods based on the local probe geometry, which usually requires adjustments of the hardware and software for SPM data acquisition. These developments are often made in close collaboration with European companies specialized in SPM instrumentation.

In the following, a brief summary of the highlights of our research activities in the time period of 1999 - 2001 is provided which will be decribed in more detail in the subsequent chapters. This may help to guide you directly to the chapters of your specific interest. To keep the extent of this report at a reasonable level we will, of course, only provide short summaries of the results of our research projects. For further information, please do not hesitate to contact us. We will be glad to provide reprints of publications on specific topics.

3.1.1 Nanomagnetic studies

Our research activities in this field concentrate on the correlation between nanostructural, local electronic and local magnetic properties of magnetic thin films, multilayer systems, as well as laterally structured thin films and multilayers ('magnetic dot and nanowire arrays'). The experimental methods for these investigations include variable-temperature spin-resolved scanning tunneling spectroscopy and magnetic force microscopy under UHV conditions in combination with spin-resolved photoelectron spectroscopy, Hall-probe magnetometry (in cooperation with the semiconductor research group of Prof. D. Heitmann) and SQUID magnetometry (in cooperation with the low-temperature physics group of Prof. J. Kötzler).

In the previous triannual report the first demonstration of spin-polarized vacuum tunneling into exchange-split surface states was reported which allowed the imaging of the nanomagnetic domain structure of Gd thin films as well as the clear separation between structural, electronic and magnetic information. The quantitative values of the measured local spin polarization were found to be in excellent agreement with results from spin-resolved photoemission and inverse photoemission spectroscopy. Non-destructive magnetic imaging by SP-STS could be achieved by using magnetically coated STM tips with a thickness of the magnetic coating well below 100 nm in order to reduce the tip's magnetic stray field. The technology of in-situ tip preparation for magnetic studies has been introduced earlier when we have realized the first UHV-compatible magnetic force microscope (MFM) with single magnetic layer sensitivity. Within the time period 1999-2001 we have applied the spectroscopic mode of the spin-polarized STM to study antiferromagnetically coupled iron nanowires being one and two atomic layers high and a few nanometers wide. Domain walls with widths down to the atomic scale could directly be observed for the first time. In addition first observations of magnetic hysteresis on the nanometer scale were made and have been correlated with real-space observations of microscopic processes of magnetic domain nucleation and domain wall motion.

A second study focussed on the investigation of nano-scale iron islands. Their magnetic anisotropy was found to depend critically on the island height and on the particular substrate chosen. To study the magnetic switching behavior of such nano-scale iron islands, specially prepared tips with an antiferromagnetic coating were used in order to exclude any disturbing influence from a magnetic stray field which would be present in case of a ferromagnetically coated probe tip.

The topological antiferromagnetic order of the Cr(001) surface has been reinvestigated by the spectroscopic mode of the spin-polarized STM as well. The highly spin-polarized surface state of Cr(001) close to the Fermi level results in a strong spin-resolved spectroscopic contrast. It also leads to a periodic alternation of measured monoatomic step heights in the constant-current mode of STM operation as first reported eleven years ago. While the spectroscopic mode of the SP-STM provides superior magnetic contrast on a nanometer scale compared to the constant-current mode, the latter seems to be more powerful for resolving atomic-scale spin structures. While first experiments on magnetic imaging on the atomic scale have been reported on ferrimagnetic magnetite nine years ago, we recently succeeded in imaging the antiferromagnetic spin structure of a single atomic layer of manganese on a tungsten substrate. While a non-magnetic tip is clearly sensitive to the chemical unit cell, magnetically coated probe tips were found to image the magnetic unit cell in excellent agreement with theory.

Within the time period 1996-1998 we had reported on first results obtained by a UHV- MFM instrument applied to study the reorientation transition of magnetic anisotropy in ultra-thin Co/Au(111) films. Within the past three years, we have used this instrument to study ultra-thin iron films on Cr(001) surfaces. A direct combination of UHV-MFM and SP-STM was realized within a single instrument thereby allowing the investigation of spin dependent electronic structure and magnetic stray field distribution at the same sample spot with nano-scale spatial resolution. In parallel, we have developed a new UHV-compatible low-temperature MFM which can operate in external magnetic fields up to 5 Tesla. This instrument has been applied to study microscopic processes of reversal of magnetization in manganese-oxide based thin films.

3.1.2 Nanoelectronic studies

In this field our research activities are focussed on local tunneling spectroscopic studies of electronic states in III-V semiconductors at low temperatures and in high magnetic fields. Previously, we had studied Landau quantization of electronic states in InAs in magnetic fields up to 7 T. The high quality of our spectroscopic data allowed to determine the energy-dependence of the effective electron mass in InAs. Spatially resolved spectroscopic studies of the Landau quantization led to the observation of spatial potential fluctuations on the order of a few mV induced by inhomogeneities in the dopant density distribution.

More recently, we have extended the studies on InAs(110) probing electron systems in all four spatial dimensionalities. The three-dimensional electron system of the bulk conduction band has been studied in the so-called extreme quantum limit, in which only the last spin-polarized Landau level is occupied by electrons. Surprisingly, we obtained experimental evidence for so-called drift states, which are usually expected in two-dimensional electron systems in the Quantum Hall regime. We also studied the two-dimensional electron system itself, which has been induced close to the InAs surface by adsorbates such as Fe, Nb and Co. In zero field indications of weak localization have been found, while in magnetic field the expected drift states finally leading to the Quantum Hall effect have been observed. A one-dimensional electron system has been discovered below a charged step edge of the surface. Its local density of states has been measured and related to the underlying disorder potential. Finally, the tip induced quantum dot has been investigated in detail. Tracing the spin levels of this quantum dot as a function of position led to a nice visualization of the non-locality of the exchange interaction.

The spectroscopic STS studies of electronic states in InAs are complemented by transport measurements in the research group of Prof. Heitmann (MARCH), by photoelectron spectroscopy experiments performed in collaboration with Prof. R.L. Johnson (HASYLAB), and by theoretical studies in the group of Prof. V. Gudmundsson (Reijkjavik).

A second activity of our research group in the field of nanoelectronic studies is devoted to Si-based devices being probed by scanning capacitance microscopy (SCM) and spectroscopy. We have demonstrated dopant profiling by SCM on the nanometer scale with great potential for quality control and failure analysis in the semiconductor industry. The experimental investigations are complemented by theoretical device simulations which are expected to lead to a quantitative analysis of dopant concentration profiles by SCM-based methods. Scanning capacitance spectroscopy will be developed further for the investigation of electronic states in semiconductor quantum structures at low temperatures. This work is done in close collaboration with the research group of Prof. W. Hansen at MARCH.

3.1.3 Nanomechanical studies

Our research activities in this field concentrate on quantitative investigations of interaction potentials based on low-temperature scanning force microscopy (SFM) data. We have developed a UHV-compatible SFM system which can operate in the dynamic non-contact mode. This instrument allowed to achieve 'true atomic resolution' on InAs(110) semiconductor surfaces, on van der Waals surfaces (e.g. graphite(0001)), or on insulators (e.g. xenon(111) films and NiO (100) surfaces). Due to the extremely high mechanical stability of this microscope it was possible to obtain high quality force spectroscopy data which allowed to extract information about tip-sample interaction potentials. Furthermore, we developed a theory for explaining the atomic resolution capability of the dynamic SFM operation mode.

In summary, the low-temperature SPM achivities have greatly progressed in many different areas of modern solid state research, including nanomagnetism, semiconductor quantum physics, dielectric solids, ultrathin films, and surface physics. There is also a great potential of SPM studies in the field of nanobiology which remains to be further explored.

3.2 Nanomagnetism

3.2.1 Application of Spin-Polarized Scanning Tunneling Microscopy and Spectroscopy

M. Bode, M. Getzlaff, S. Heinze, M. Hennefarth, M. Kleiber, A. Kubetzka,
O. Pietzsch, R. Ravlič, and R. Wiesendanger

Introduction

In recent years great progress has been achieved in the preparation of self-organized and lithographically manufactured magnetic nanostructures [1]. The structural properties of these nanostructures could routinely be investigated by high-resolution real-space imaging techniques like scanning electron microscopy (SEM) and scanning tunneling microscopy (STM) down to the atomic scale. In contrast, a detailed understanding of nanomagnetic properties has been hindered by the fact that magnetic data have been obtained by experimental methods which average over a fraction of the sample surface being much larger than the atomic length scale. So far, the limit of spatial resolution of the most advanced magnetic imaging techniques like magnetic force microscopy (MFM) and SEM with polarization analysis (SEMPA) has been on the order of several tens of nanometers (nm). Therefore, it has been proposed very early by Pierce [2] to make the tip of the STM sensitive to the spin of the tunneling electrons by illuminating GaAs tips with circularly polarized light or by using ferromagnetic tips. Although spin-polarized electron tunneling in planar junctions is an established experimental technique [3] it turned out that the realization of this idea is difficult. Spin-polarized tunneling using an STM has first been observed by Wiesendanger and co-workers in the early 1990s [4, 5]. In this experiment, CrO_2 thin film tips with a high degree of spin polarization were successfully used to detect periodic alternations of the measured monatomic step heights in constant-current images. The deviations of the measured step height values from the topographic monatomic step height could directly be related with the effective spin polarization of the tunnel junction. A significant drawback of this experimental approach was the superposition of topographic and magnetic structure information.

As we have shown in the previous triannual report of our research group we could overcome this problem by combining SP-STM with spectroscopic techniques. In these early experiments the extraordinary electronic structure of the ferromagnetic rare-earth metal Gd(0001) which is characterized by an exchange-split surface state was used to proof spin-polarized vacuum tunneling. As we will show in the following section (see p. 14*ff*) this know-how allowed the successful separation of topographic, electronic and magnetic information thereby achieving magnetic domain and domain wall images of even micromagnetically complicated magnetic surfaces with subnanometer spatial resolution. We will show that, nevertheless, spin-polarized scanning tunneling microscopy (SP-STM) performed in the constant-current mode is the method of choice to resolve complex surface spin-structures, as, e.g., collinear or non-collinear antiferromagnetic structures on atomically flat areas (pages 39*ff*).

Experimental

The experiments have been performed in an ultra–high vacuum (UHV) system with separate chambers for substrate preparation, sample transfer, metal vapor deposition (MVD), surface analysis, and cryogenic STM equipped with a 2.5 T magnet [6]. A brief description of this system can be found in Sect. 3.6 of this report. The base pressure in each chamber is in the low 10^{-11} torr range. The W(110) single crystal used as a substrate is miscut by 1.6° with respect to the (110)-plane leading to an average terrace width of about 9 nm. It is cleaned by numerous cycles of long-term heating at 1500 K in an oxygen atmosphere of 10^{-7}–10^{-6} torr and subsequent flashing up to 2300 K [7]. Fe and Gd films were deposited at a rate below 1 monolayer per minute (ML/min) by electron beam evaporation from a rod or from a W crucible, respectively. During metal evaporation the pressure did not exceed $p = 5 \times 10^{-10}$ mbar. We used etched W–tips which were electrochemically ac-etched ($U \approx 5$ V) in a saturated solution of NaOH in destilled water. After introduction into the UHV-chamber the tips were flashed *in-vacuo* by electron bombardment at $T > 2200$ K to remove oxide layers. As illustrated in Fig. 3.1, this thermal treatment causes the tips, which were relatively sharp after the etching procedure (tip diameter $D \approx 20 - 50$ nm), to become quite blunt with D on the order of 1 μm probably due to melting of the tip apex. In the

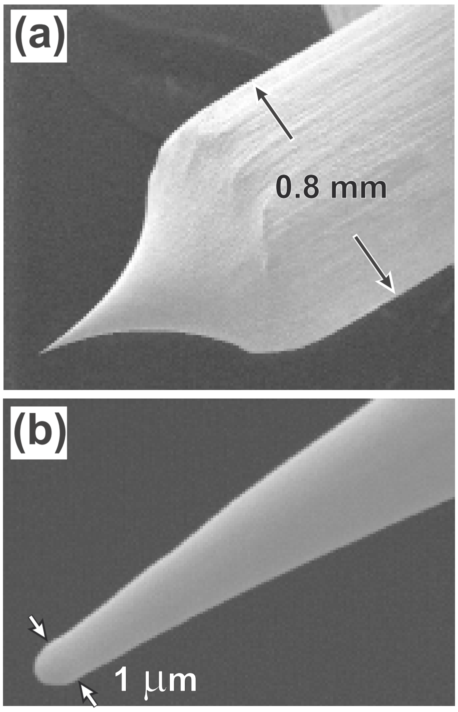

Figure 3.1: SEM-micrographs of an electrochemically etched, polycrystalline W-tip after a high temperature flash at $T > 2200$ K. **(a)** The overview shows the shaft of the tip which exhibits a diameter of 0.8 mm. **(b)** High-resolution SEM image of the very end of the tip. The tip apex has an angle of about 15° and the tip diameter amounts to approximately 1μm.

MVD–chamber the tips were magnetically coated with 7 ± 1 ML Gd, 10 ± 2 ML Fe, 11 ± 5 ML $Gd_{14}Fe$, or 35 ± 10 ML Cr while held at 300 K, subsequently annealed at $T \approx 550$ K for 4 min, and then transferred into the cryogenic STM. The alloy films were prepared by coevaporation. During the measurements, tip and sample were at a temperature $T = 16$ K. All topographic STM data were recorded in the constant current mode. It turned out that in spite of the huge tip diameter as apparent in the SEM-image of Fig. 3.1(b) sample step edges could be routineously imaged as long as their height do not exceed several atomic layers. Probably, this is caused by the presence of a small cluster with a size below the resolution limit of the SEM which forms the tip apex. A magnetic contrast was almost always obtained. As we will show below Fe thin film probe tips are preferentially sensitive to the in-plane component of the spin-polarization while all other tips described above exhibit a perpendicular orientation. The tunneling spectra presented below were acquired by *scanning* the sample and measuring one $\mathrm{d}I/\mathrm{d}U$-spectrum at *every* pixel by adding an ac–component ($U_{\mathrm{mod}} \leq 30$ mV, $\nu \approx 2$kHz) to the gap voltage U and measuring the $\mathrm{d}I/\mathrm{d}U$–signal by lock-in technique.

3.2.2 Imaging Magnetic Nanostructures by Spin-polarized Scanning Tunneling Spectroscopy (SP-STS)

Fe Nanowires on stepped W(110)

A basic requirement for the development of any new technique is the availability of an appropriate test sample. In the case of high-resolution magnetic imaging the test sample must exhibit a lateral domain size which is well below the scan range. Furthermore, in order to show the improvement obtained by spin-polarized scanning tunneling spectroscopy (SP-STS) the magnetic length scale should be well below the resolution limit of other magnetic imaging techniques like SEMPA, i.e. about 20 nm. Motivated by previous experiments of Elmers *et al.* [8, 9] we chose perpendicularly magnetized Fe doublelayer (DL) nanowires epitaxially grown on a stepped W(110) single crystal with an average terrace width of about 9 nm (Fig. 3.2(a)). The sample is prepared by deposition of 1.6 ML Fe on the W(110) substrate held at elevated temperature $T \approx 450$ K. This preparation procedure leads to step-flow growth of the second Fe monolayer on top of the closed first Fe layer thereby creating a system of nanowires with alternating Fe ML and DL coverage elongated along the step edges of the substrate [schematic drawing below the section-line shown in Fig. 3.2(b)]. According to combined longitudinal and polar Kerr-effect measurements [8, 9], an onset of perpendicular magnetization for Fe coverages $\Theta \geq 1.1$ ML was found. In particular, the coverage range between 1.4 ML and 1.8 ML Fe/W(110) is characterized by magnetic saturation at relatively low external perpendicular fields combined with the absence of a hysteresis, i.e. zero remanence. As schematically represented in Fig. 3.2(c) this antiparallel order is a consequence of the dipolar coupling which reduces the stray magnetic field of the perpendicularly magnetized Fe double layer. At domain walls

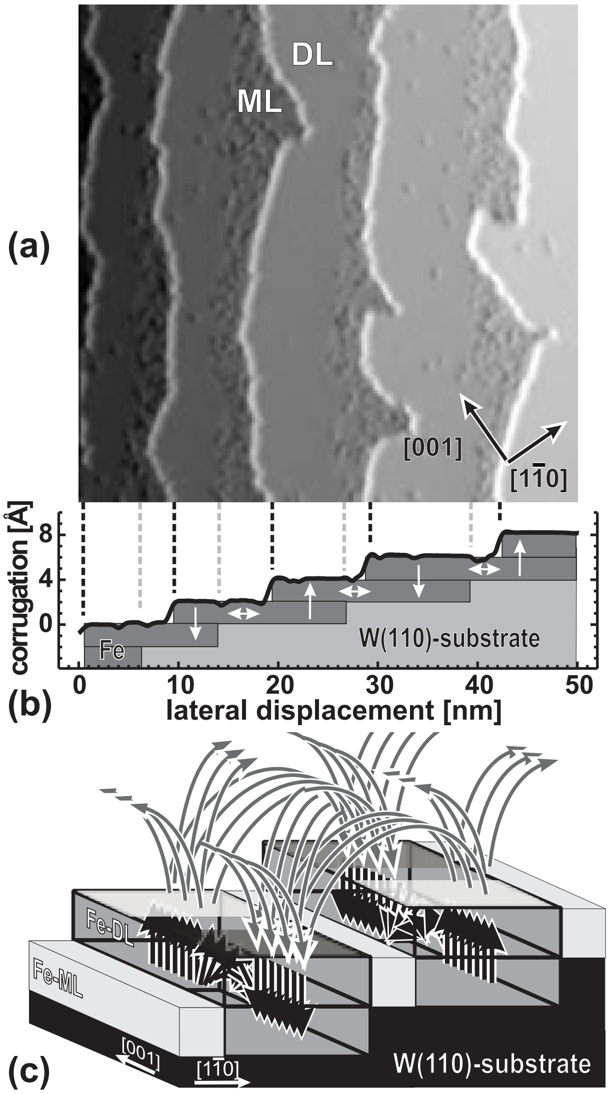

Figure 3.2: **(a)** Topographic STM image (scan range: 50 nm × 50 nm) of 1.6 ML Fe/W(110) after annealing to 450 K. **(b)** Line section measured at the bottom edge of the STM image. The local coverage alternates between one and two atomic layers. White arrows symbolize the easy magnetization directions of the mono- and the double layer, i.e. in-plane and perpendicular to the surface, respectively. **(c)** According to Elmers *et al.* [9] adjacent perpendicularly magnetized double layer stripes exhibit an antiparallel dipolar coupling. Within domain walls the Fe double layer on W(110) locally exhibits an in plane magnetization.

the double layer may locally be magnetized along the hard magnetic axis, i.e. in-plane. Details of the magnetic structure, however, remained unclear. Since, e.g., the typical domain wall width of 180° walls amounts to about 100 nm [10], it was controversially discussed whether in an ultra-thin magnetic film a spin-rotation can occur on a lateral scale of a few nanometers.

We have performed STS measurements on this sample system using many different pure and Gd-coated W-tips. The results of three measurements are shown in Fig. 3.3(a)-(c). The spectra of Fig. 3.3(a) have been obtained with a clean (flashed) W-tip. Two different spectra with major peaks at $U = +0.4$ V and $U = +0.68$ V can be recognized which are characteristic for the Fe ML and DL on W(110), respectively. We would like to emphasize that between different nanowires no variations of the $\mathrm{d}I/\mathrm{d}U$ signal could be observed over the bias voltage range under study. In contrast, as shown in Fig. 3.3(b) and (c), respectively, two DL spectra were found when using

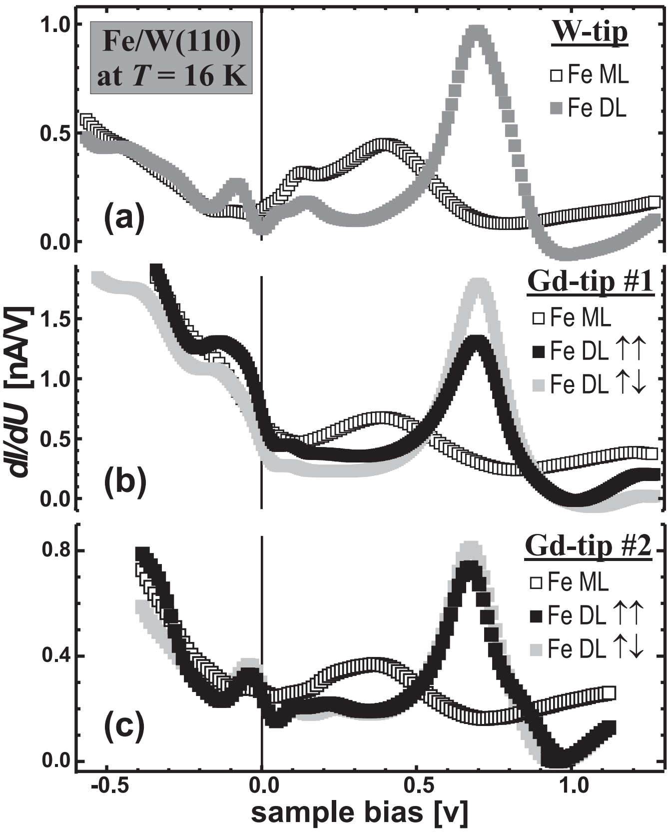

Figure 3.3: Tunneling dI/dU spectra which have been measured above Fe ML and DL sites using different **(a)** uncoated and **(b)**,**(c)** Gd-coated W-tips. All spectra show the characteristic features of the Fe ML and DL on W(110), i.e. peaks at $U = +0.40$ V and $U = +0.68$ V, respectively. No magnetic contrast can be obtained with the W-tip. Spin-polarized tunneling can be observed with Gd-coated tips at the out-of-plane magnetized Fe DL nanowires. The particular bias voltage at which the magnetic contrast P becomes maximal varies between different tips. While for Gd-tip # 1, $P(U = 0.68\ \text{V}) \approx 40\%$ it amounts to only 5% for Gd-tip # 2. Instead, for the latter tip $P(U = -0.5\ \text{V}) \approx 40\%$.

Gd-coated tips that differ in intensity. This difference is caused by spin-polarized tunneling between the magnetic tip and sample, i.e. the differential conductivity dI/dU depends on whether tip and sample are *magnetized* parallel (↑↑) or antiparallel (↑↓). In more detail, the size of the dI/dU signal depends on the *spin-polarization* of both electrodes: an equal sign of the spin-polarization in both electrodes leads to a high dI/dU signal and *vice versa.* This may lead to the apparently counter-intuitive situation that in spite of the fact that both electrodes are magnetized parallel the differential conductivity is lower than in the antiparallel configuration due to a negative spin-polarization in one electrode. This so-called *inverse tunnel magnetoresistance* is also known from planar junctions [11]. Consequently, a negative spin-polarization in *both* electrodes will again lead to a normal tunnel magnetoresistance. Obviously, the magnetic contrast P which is defined by the difference of the dI/dU signal between the parallel (↑↑) and the antiparallel (↑↓) case divided by the smaller value at the DL peak position varies for different tips [cf. Fig. 3.3(b) and (c)]. While it amounts to $P(U = 0.68\ \text{V}) \approx 40\%$ for Gd-tip #1 it is reduced to 5% for Gd-tip #2. This result is caused by different spin-dependent electronic properties which are due to the fact that the detailed atomic configuration of the cluster at the very end of the tip cannot be controlled experimentally so far. As a consequence, the bias voltage at which the magnetic contrast becomes maximal will differ for different tips. For example, Gd-tip

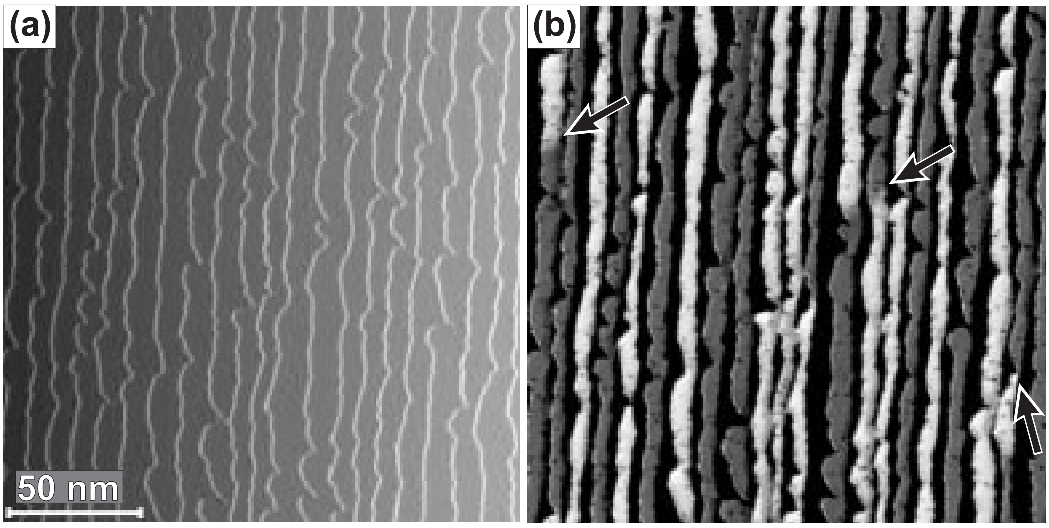

Figure 3.4: **(a)** STM topograph and **(b)** magnetic dI/dU image of Fe nanowires on W(110). Both images have been measured simultaneously. The imaging parameters are $I = 0.3$ nA and $U = +0.7$ V. The sample exhibits a demagnetized antiferromagnetic ground state which is energetically favorable due to flux closure between adjacent perpendicularly magnetized Fe nanowires [8].

#1 and #2 are best used at $U = 0.68$ V and $U = -0.5$ V, respectively.

In the following we have used tunneling spectroscopy to image the magnetic domain structure of Fe DL nanowires. Since we know from the data shown in Fig. 3.3 how the DL contrast has to be interpreted it is no longer necessary to measure full spectra at every pixel of the image which is very time consuming (about 10-20 h per image). Instead, we only have to measure the dI/dU signal at a fixed sample bias which gives a good contrast. Figure 3.4 shows the simultaneously recorded (a) topography and the (b) dI/dU signal at $U = 0.7$ V of 1.5 ML Fe/W(110). The measurement time for this image was about 30 min. Due to its different electronic properties the Fe ML appears dark. We would like to emphasize that this is not related to the magnetic properties. Instead, the ML is known to exhibit an in-plane magnetization which cannot be detected by Gd-tips being sensitive only to out-of-plane magnetization. Obviously, the magnetic domain structure is dominated by DL nanowires which are alternately magnetized up and down thereby confirming the model proposed by Elmers *et al.* [8,9]. However, exceptions from this model can easily be recognized. Several domain walls within single Fe nanowires are visible. Some of them are marked by arrows in Fig. 3.4(b). Furthermore, there are numerous adjacent nanowires which couple ferromagnetically instead of antiferromagnetically. Probably, these DL nanowires approach very close or even touch each other so the exchange coupling dominates.

Figure 3.5 shows two different types of domain walls which have been observed within the DL stripes. Relatively broad domain walls with a width $w_0 = 6 \pm 1$ nm were found in homogeneous DL stripes. This finding is in strong disagreement with a recent

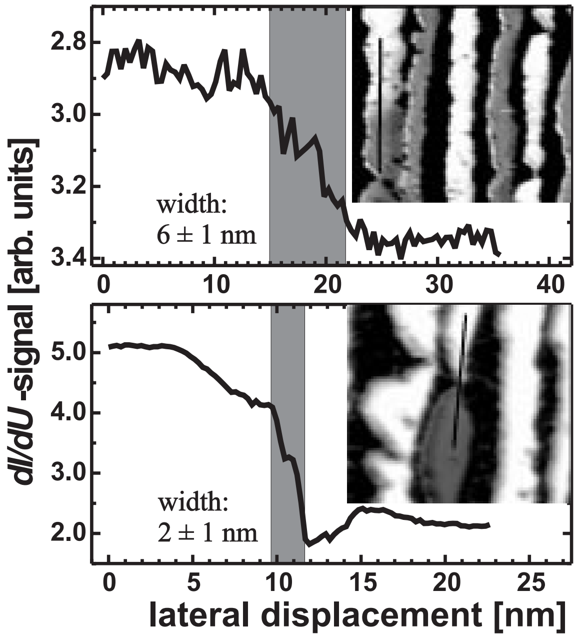

Figure 3.5: Line-sections showing the change of the dI/dU signal when crossing a domain wall being located in a smooth (upper panel) or constricted (lower panel) Fe DL stripe. Maps of the dI/dU signal are shown in the inset. The positions at which the line sections were drawn are marked by black solid lines.

publication, in which the DL exchange length was estimated to $L_{\mathrm{DL}} = 0.5$ nm based on Kerr-effect measurements [9]. Instead, using the definition $w_0 = 2L = 2\sqrt{A/k}$ [12] our results suggest that $L_{\mathrm{DL}} = 3$ nm. With $k_{\mathrm{DL}} = 1 \times 10^{-6}$ J/m^3 [9] this leads to $A_{\mathrm{DL}} = 9 \times 10^{-12}$ J/m which almost perfectly agrees with the bulk value $A = 1 \times 10^{-11}$ J/m. At structural constrictions which often serve as pinning centers for domain walls we found, however, narrower domain walls as can be seen in the line-section shown in the lower panel of Fig. 3.5. Typically, the width of domain walls being pinned at structural constrictions amounts to $w^{\star} = 2 \pm 1$ nm. This behavior has recently been proposed theoretically by Bruno [12]. We have applied Bruno's approach by modelling the width of the DL stripe $S(x)$ by the quadratic approximation $S(x) = S_0(1 + \frac{x^2}{d^2})$ (model II in Ref. [12]). Here, S_0 is the minimum width of the constriction positioned at $x = 0$, x is the distance from minimum, and d is a fit parameter. Indeed, in our case the constriction could well be fitted by using $S_0 \approx 0.8$ nm and $d = 1$ nm which results in a reduced domain width $w^{\star} = \frac{8d}{\pi} \approx 2.5$ nm being in fair agreement with the experimental observation.

Nanometer-scale magnetic imaging is particularly challenging if a strong external magnetic field is to be applied to the system under study, a condition being, in general, prohibitive for microscopy techniques relying on a yield of secondary electrons. Acquisition of hysteresis curves of thin films remained mainly the realm of techniques using polarized photons as a probe such as magneto-optical Kerr effect (MOKE) measurements, which, even if applied as a microscopy method, suffer from an appropriate spatial resolution owing to the limit of optical wavelengths. It is clear that the signal obtained is spatially averaged over a considerable fraction of the surface. Since STM is a near-field technique the above mentioned restrictions of electron-based imaging

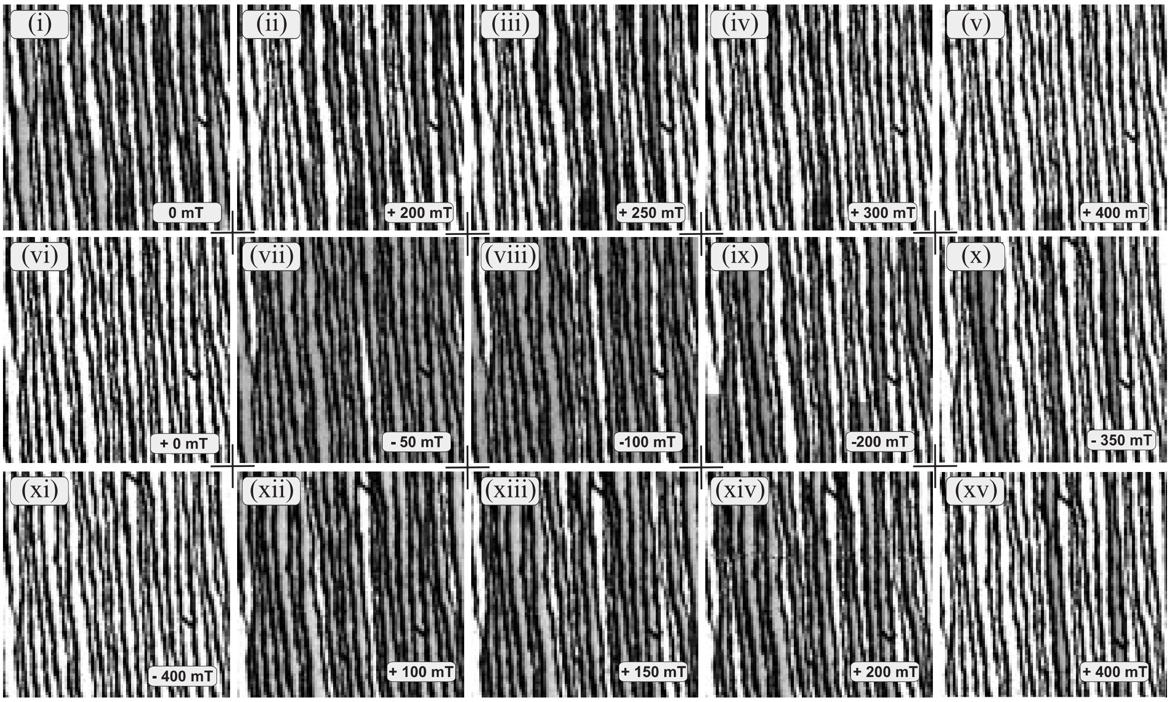

Figure 3.6: 15 images selected from a series of 24 taken at field values as indicated. The scan range is 200 nm × 200 nm. With increasing positive field dark domains progressively vanish, and at saturation only bright domains remain. High remanence is observed. A small negative field of -50 mT is sufficient to switch the tip magnetization while the sample stays almost unaffected. A contrast reversal results. At negative saturation, again all stripes are bright. The tunneling parameters are $I = 0.5$ nA, $U = +700$ mV.

techniques do not apply. Indeed, we could observe the evolution of the DL magnetic domain structure as a function of a variable magnetic field applied perpendicular to the sample plane. The result is shown in Fig. 3.6 which displays 15 frames selected from a series of 24 images. The scan range is 200 nm × 200 nm.

In the magnetic virgin state of the sample [Fig. 3.6(i)] the antiparallel order of the DL areas shows up as alternating white and grey stripes (in the following, the DL contrasts will be referred to as bright and dark). Within the frame, fifteen domain boundaries can be seen, and a certain tendency to form spatial correlations of domain walls among neighboring stripes in a checkerboard manner is found. The widths of the walls confirm the previously reported result of 6 ± 1 nm (cf. Fig. 3.5). As the overall distribution of bright and dark DL areas is balanced, i.e. the sample is macroscopically demagnetized. Panels (ii) to (xv) show the development of the domains as a function of the external magnetic field. With increasing positive field bright areas grow at the expense of dark areas until, at +400 mT, almost all dark DL areas have vanished indicating saturation [Fig. 3.6(v)]. So far, we can identify bright areas as being magnetized parallel to the external field, i.e. up (↑), while the dark domains are magnetized down (↓). High remanence is observed [Fig. 3.6(vi)]. Taking the step from remanence to -50 mT [Fig. 3.6(vi)–(vii)] a change takes place in the distribution of bright and dark. The contrast of all DL stripes is reversed. This is explained by a switching of the tip's magnetization by the external field from (↑) to (↓) while the sample remains almost unaffected. As a consequence, at (↑) domains the tip-sample configuration is changed from (↑↑) to (↓↑), and the opposite happens for (↓) domains where (↑↓) is changed to (↓↓). A further field increase in $-z$ direction leads again to a growth of bright DL domains until, at -400 mT, saturation in the negative direction is reached, again with no dark domains left [Fig. 3.6(xi)]. At $+50$ mT the tip has switched again [Fig. 3.6(xii)], symmetrical to the previous switching event, and the effect on the images is analogous. This observation allows an estimation of the coercive field for the Gd tip, $\mu_0 H_\mathrm{C}^\mathrm{tip} \leq 50$ mT.

By evaluating the bright DL stripe length percentage we obtain the butterfly hysteresis curve displayed in Fig. 3.7(a). The shape of this curve results from the fact that two ferromagnetic electrodes are involved, namely tip and sample. Taking the effect of tip switching into account pure sample properties can easily be separated. They are represented by the second hysteresis curve [Fig. 3.7(a)] which displays the percentage of (↑) domains as a function of the applied field. A remanence-to-saturation ratio $M_\mathrm{R}/M_\mathrm{S} \approx 0.98$ is observed. The sample coercivity is $\mu_0 H_\mathrm{C}^\mathrm{sample} \approx 200 \pm 50$ mT. The corresponding domain structure is shown in Fig. 3.6(xiv). Comparing this frame to the initial demagnetized state [Fig. 3.6(i)] we observe that the detailed magnetic

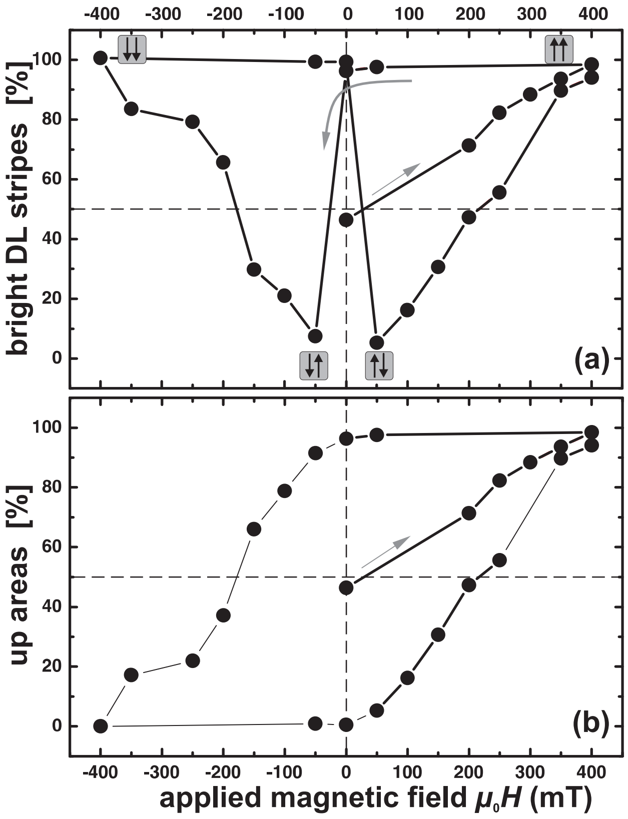

Figure 3.7: Hysteresis curves obtained from the distribution of bright domains **(a)** and stripes with $+z$ magnetization (↑) **(b)**. The butterfly curve in **(a)** shows properties of the complete tunneling junction consisting of two ferromagnetic electrodes, while the curve in **(b)** displays only sample properties. Arrow panels in **(a)** indicate the relative alignment of tip and sample magnetization.

order of the stripes has changed significantly. No domain wall can be found at its initial location. This is not surprising, as the existence of a hysteresis is already a consequence of the irreversibility of the remagnetization process. The initial contrast pattern alternating from one stripe to the next is replaced by an occurrence of bunches of two, three or even four stripes of the same magnetization next to bundles of stripes of opposite magnetization. The dipolar order has coarsened significantly, attributed to the different history of these demagnetized states. The initial order was formed when the sample was cooled down from its growth temperature to 14.5 K. At the DL Curie temperature $T_{\mathrm{C}}^{\mathrm{DL}} = 300$ K the thermal energy is of a magnitude comparable to that of the magnetization-related energy contributions. This supports the formation of a fine-sized equilibrium order such that the stray field energy is minimized. This effect of thermal energy is greatly reduced at low temperatures. The virgin state emerged from a transition from the paramagnetic phase with no magnetic order while coercivity was preceded by saturation with all domains perfectly aligned, i.e. maximum magnetic order. The general shape of the hysteresis loop of Fig. 3.7(b) is not a simple square loop but shows a slope. It is clear that the magnetic reorientation does not take place in a single jump from one saturated state to the opposite one but progresses successively. Except for the weak spatial correlations of domain walls mentioned earlier and caused by dipolar interaction, the DL stripes are found to be effectively decoupled even by ML stripes as narrow as ≈ 1.5 nm. Every single stripe is remagnetized individually.

Two mechanisms of remagnetization are observed, domain creation and domain wall motion. Wall motion is restricted to the direction along the stripe. Both mechanisms are illustrated in Fig. 3.8. Two new domains (a) and (b) are created. Since the spins have to rotate continuously at both domain ends, the sense of rotation within the two Bloch walls bounding a new domain must be opposite, namely +180° and −180° [Fig. 3.8(b]. With increasing field, the lower wall of domain (a) moves towards

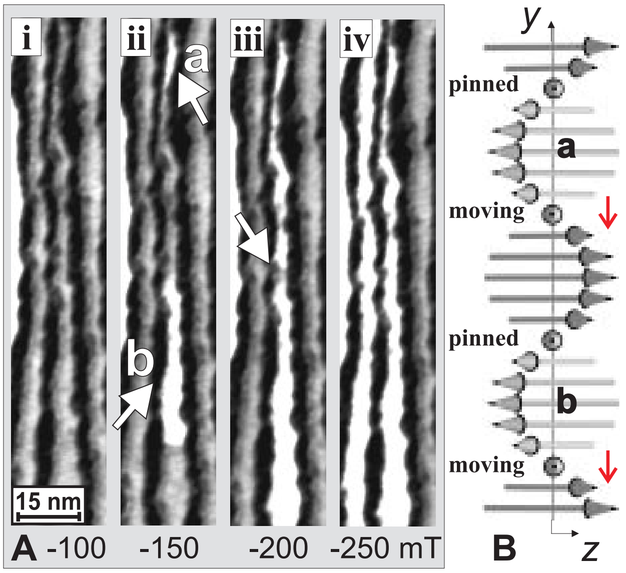

Figure 3.8: **A** Creation and annihilation of domains. Two new bright domains (a) and (b) are being created, bounded by Bloch walls. The lower wall of (a) moves towards (b), the trapped dark area shrinks. The last dark portion is marked in (iii), immediately before it gets annihilated. **B** Sketch of the magnetization reorientation process roughly at the stage of panel (ii) (side view, not to scale). Arrows indicate the magnetization direction. Note the vector orientation at the wall centers, all pointing into the same direction. The new domains will again be annihilated on field reversal.

domain (b). Finally, (a) and (b) merge, which is equivalent to an annihilation of the dark domain trapped between them. In panel (iii) the last dark portion, marked by an arrow, is visible just before it vanishes. From the viewpoint of the dark domain, its bounding walls get unwound. On field reversal, the new bright domain will also be annihilated because the same arguments apply.

In the following we describe experiments which have been performed on substrates with different miscuts. In order to allow a more intuitive understanding of the measured data we have superposed rendered perspective topographic images on the magnetic $\mathrm{d}I/\mathrm{d}U$ signal in a greyscale representation. The substrate of Fig. 3.9(a) (scan range: 200 nm × 200 nm) is miscut by 1.35° with respect to the (110)-plane leading to an average terrace width of about 9 nm. The Fe DL nanowires were prepared by room-temperature deposition of 1.75 ML Fe and subsequent annealing at $T \approx 550$ K. Although numerous magnetic defects like, e.g., domain walls, can be recognized, the magnetic structure of Fig. 3.9(a) is governed by Fe DL stripes which periodically change their magnetization direction (*up* or *down*) between adjacent DL stripes. Although the Fe coverage of 1.69 ML is almost identical to the previous example the lower

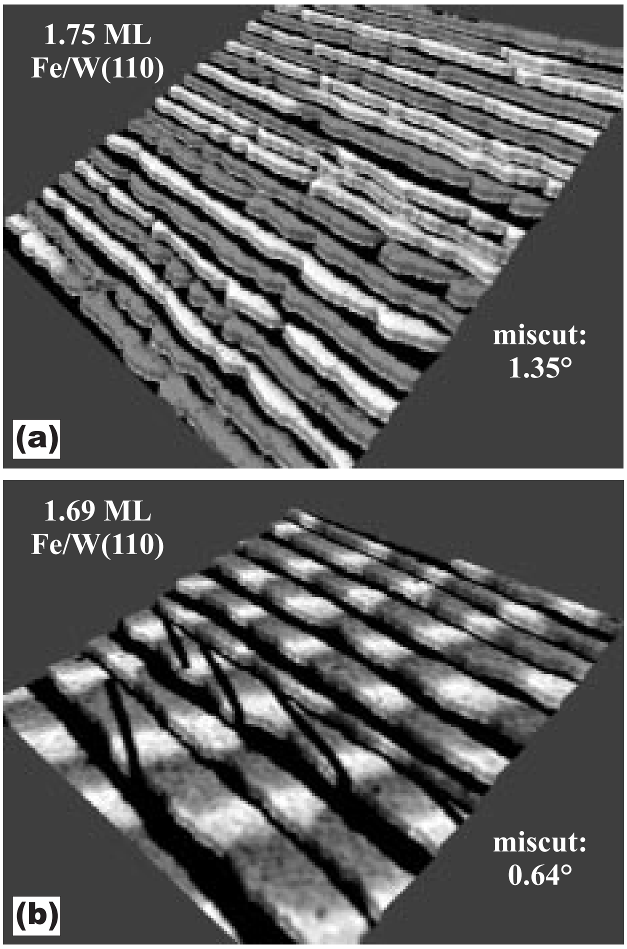

Figure 3.9: Rendered perspective topographic images (200 nm × 200 nm each) of Fe nanostripes prepared on different W(110) substrates combined with greyscale representations of the magnetic $\mathrm{d}I/\mathrm{d}U$ signal. **(a)** At a coverage of 1.75 ML Fe deposited on a substrate that is miscut by 1.35° with respect to the (110)-plane an antiferromagnetic coupling between adjacent Fe nanowires can be observed. **(b)** In contrast, stripe domains running along the [001] direction were found at an almost identical Fe coverage but deposited on a substrate which exhibits a smaller miscut of about 0.64°.

step density in Fig. 3.9(b) (scan range: 200 nm × 200 nm) leads to a domain structure which is completely different. The miscut of this substrate amounts to 0.64° which results in an average terrace width of about 20 nm. Instead of periodically changing the magnetization direction *between adjacent* DL stripes in this case the magnetization periodically changes between up and down *within a single* Fe DL stripe by introducing numerous domain walls along the $[1\bar{1}0]$ direction. The magnetic period along the Fe DL stripes is about 50 nm and a certain correlation between adjacent stripes can be recognized. We would like to emphasize that the four black lines running along the [001] direction are caused by a local change of the electronic structure of Fe/W(110) due to the creation of dislocation lines [13, 14]. We believe that this domain structure is a precursor of a striped domain phase with stripes along the $[1\bar{1}0]$ direction which is expected for the closed Fe double layer.

For domain walls in ultra-thin out-of-plane magnetized films it is energetically favorable to rotate the magnetization vector parallel to the wall plane (Bloch-type) thereby avoiding magnetic charges. In this particular case a Bloch-type wall is also supported by the anisotropy of the adjacent Fe monolayer which is magnetized in-plane along the $[1\bar{1}0]$ direction, too. Since, however, the magnetization may rotate either clockwise or counter-clockwise the local magnetization in the center of the wall can

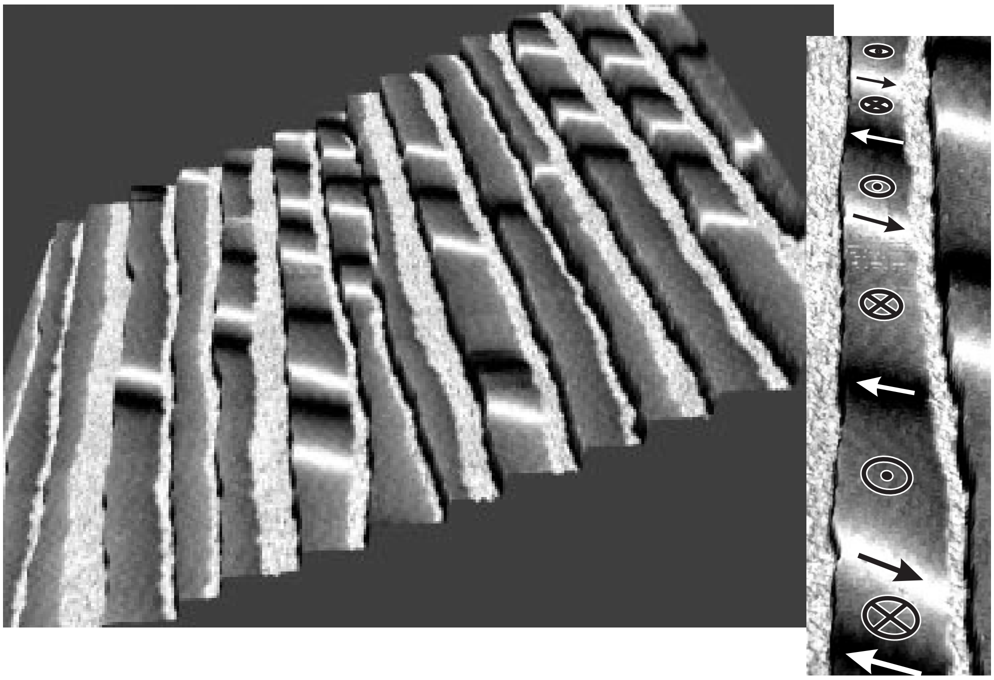

Figure 3.10: Rendered perspective topographic image (200 nm × 200 nm) of the magnetic domain-wall structure of Fe nanostripes imaged with an Fe coated tip. The Fe coverage amounts to 1.6 ML Fe. Domain walls appear alternatively black and white indicating that the orientation of domains as well as domain walls alternates thereby generating a spin-spiral along a particular DL nanostripe (inset).

point either into the $[1\bar{1}0]$- or into the opposite, i.e. the $[\bar{1}10]$ direction. So far we have shown that Gd coated probe tips are sensitive to the out-of-plane component of the magnetization thereby providing an image of the *domain* structure. In contrast, the data of Fig. 3.10 which have been measured with a Fe coated tip reveal a sensitivity to the in-plane component of the magnetization. This is indicated by a vanishing domain contrast due to the orthogonal magnetization between tip (in-plane) and sample (out-of-plane). Within the domain walls, however, the magnetization locally possesses an in-plane orientation. As stated above, in the center of the domain wall the magnetization vector may point either along the $[1\bar{1}0]$- or the $[\bar{1}10]$ direction. Although we cannot control the azimuthal orientation of the tip magnetization it is clear that as long as the projection of the tip magnetization vector onto the $[1\bar{1}0]$ direction is non-vanishing we will be able to distinguish both cases due to the spin-valve effect leading to two different $\mathrm{d}I/\mathrm{d}U$ signals. Indeed, numerous domain walls showing up as black or white lines along the $[1\bar{1}0]$ direction can be recognized in the $\mathrm{d}I/\mathrm{d}U$-map of Fig. 3.10. Black and white domain walls were found to alternate within each particular nanowire.

On the first view, the strong dependence of the tip magnetization on the coating material might be surprising since the elongated shape of the tip should always lead to some shape anisotropy such that the magnetization vector—independent of the particular coating material—should always point along the tip-axis, i.e. out-of-plane. However, we would like to emphasize that compared to the thickness of the magnetic coating layer which typically amounts to a few atomic layers only, the tips are extremely blunt ($D \approx 1\ \mu$m). This leads to an almost vanishing curvature at the very end of the tip which makes the contribution from the tip shape anisotropy very small. Instead, the results suggest that the anisotropy of thin film tips is dominated by surface and interface terms as can be illustrated by comparing the properties of thin film tips with equivalent magnetic films deposited on a flat W(110) surface. This dense-packed W surface is most likely created at the tip apex after melting the tip during the flash. While it has been proposed that thin Gd films ($\Theta \leq 9$ ML) on W(110) exhibit a low-temperature phase with a perpendicular easy axis [15] it is well known that 5 ML Fe/W(110) are magnetized in-plane [16] being consistent with the different sensitivities as found for thin film tips.

With in-plane sensitive tips in hand we can investigate the domain structure of the first Fe monolayer on W(110) as well, which—acording to the proposal of Elmers *et al.* [9]—exhibits an in-plane easy axis. Figure 3.11 shows the topography (a) and the magnetic $\mathrm{d}I/\mathrm{d}U$ signal (b) of 1.25 ML Fe/W(110) grown at $T \approx 500$ K. Several domain walls separating dark and bright domains of the Fe ML can clearly be recognized in the overview of Fig. 3.11(b). Since the total Fe coverage exceeds 1 ML, DL stripes have formed along the step edges of the substrate [17]. Due to their different electronic properties the DL stripes appear dark at this particular sample bias, i.e. $U = +130$ mV (cf. Ref. [17]). Approximately in the center of the white box in Fig. 3.11(b), a bright spot shows up which is caused by a domain wall in this particlar DL. The inset of Fig. 3.11(b) shows this location at higher magnification. Averaged line sections drawn along the white lines across domain walls in the ML and the DL are plotted in Fig. 3.11(c) bottom and top, respectively. Obviously, the ML domain wall is much narrower than the DL wall. The inset of Fig. 3.11(c) shows the data in the vicinity of the ML domain wall in more detail revealing a domain wall width $w < 1$ nm. In order to allow a more quantitative discussion we have fitted the measured data with a theoretical tanh function of a 180° wall profile [18]. It can be extended to an arbitrary

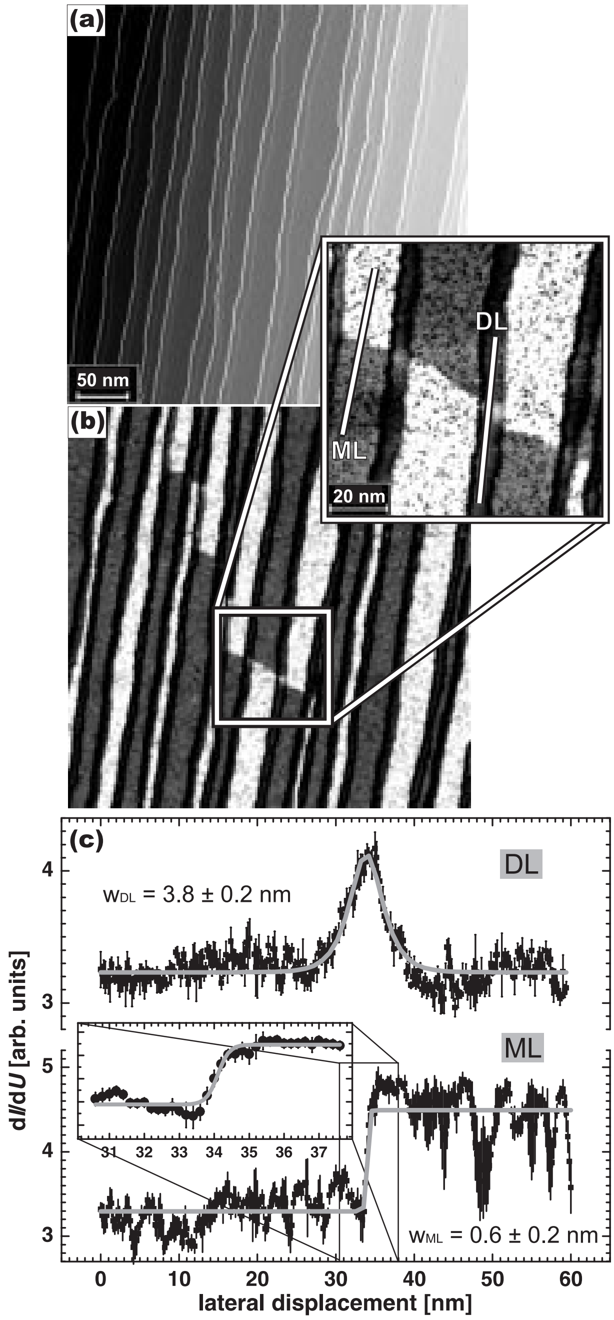

Figure 3.11: **(a)** Topographic and **(b)** spin-resolved dI/dU image showing the in-plane magnetic domain structure of 1.25 ML Fe/W(110) (tunneling parameters: $I = 0.8$ nA, $U = +130$ mV). Several ML and DL domain walls can be recognized in the higher magnified inset. **(c)** Line-sections showing domain wall profiles of the ML (bottom) and the DL (top). The inset reveals that the ML domain wall width is on the atomic scale, i.e. $w_{\mathrm{ML}} = 6 \pm 2$ Å. In spite of this fact the data can nicely be fitted by micromagnetically calculated wall profiles (details see text).

angle between the magnetization axis of tip and sample ϕ by

$$y(x) = y_0 + y_{\mathrm{sp}} \cos \left(\arccos \left(\tanh \left(\frac{x - x_0}{w/2} \right) \right) + \phi \right), \tag{3.1}$$

where $y(x)$ is the $\mathrm{d}I/\mathrm{d}U$ signal measured at position x, x_0 is the position of the domain wall, w is the wall width, and y_0 and y_{sp} are the spin-averaged and spin-polarized $\mathrm{d}I/\mathrm{d}U$ signal, respectively. In this case we work with an Fe coated tip which exhibits in-plane sensitivity. Therefore, we have to use $\phi_{\mathrm{DL}} = \pi/2$ and $\phi_{\mathrm{ML}} = 0$. The best fit to the wall profile of the DL is achieved with $w_{\mathrm{DL}} = 3.8 \pm 0.2$ nm [17]. It turns out that the profile of the ML domain wall is much narrower. If the fit procedure is performed over the full length of the line section we find $w_{\mathrm{ML}} = 0.50 \pm 0.26$ nm while $w_{\mathrm{ML}} = 0.66 \pm 0.18$ nm is found if the fit is applied to the data in the inset of Fig. 3.11(c), thereby confirming the result of the analysis of the magnetization curves, i.e. an almost atomically sharp domain wall. However, we emphasize that the excellent agreement between the measured data (black points) and the fit (gray curve) has to be interpreted with some care. First, at this length scale the spatial resolution of the instrument certainly plays a role. The lateral resolution of STM has been estimated to $[(2\text{Å})(R + d))]^{1/2}$, where R is the tip radius and d is the width of the vacuum gap between tip and sample [19]. Even under the assumption of an atomically sharp tip and a gap width d = 7-10 Å the lateral resolution is approximately 4-5 Å, i.e. the measured wall width $w_{\mathrm{ML}} = 0.6 \pm 0.2$ nm represents an upper limit only. Second, the fact that the magnetization direction changes by 180° over a lateral distance of only one or two atomic sites implies that a basic assumption of micromagnetic theory, i.e. a small angle between adjacent Heisenberg spins, is no longer valid. It remains to be investigated in how far the itinerant nature of the Fe $3d$ electrons allows treating the spin-rotation in terms of continuum micromagnetism. In this context it would be interesting to measure domain wall profiles in localized moment magnets as, e.g., rare-earth metals.

The so far achieved detailed understanding of the contrast mechanism allows the detection even of complex physical properties, as, e.g., intra-atomic non-collinear magnetism (NCM). Usually, the total magnetization of the sample is regarded as the sum of atomic spins as introduced within the Heisenberg model. Instead, this concept treats the spin-density as a vector-field which, if integrated over the whole magnetic volume, gives the global magnetization, but which also allows that its orientation "varies on the length scale of an atom" either by "different quantization axes for different orbitals on the same atom ... or by nontrivial spin mixture produced by the spin-orbit coupling" [20]. While the existence of inter-atomic NCM is well-established we are not aware of any direct experimental evidence of intra-atomic NCM. Fig. 3.12 shows the (a) topography and the $\mathrm{d}I/\mathrm{d}U$ signal at (b) $U = -0.1$ V and (c) $U = +0.1$ V which have been *simultaneously measured* line-by-line in the forward and backward scan direction, respectively, using an Fe coated probe tip. Again, Figure 3.12(b) exhibits a pure domain wall contrast as expected from the in-plane sensitive Fe coated

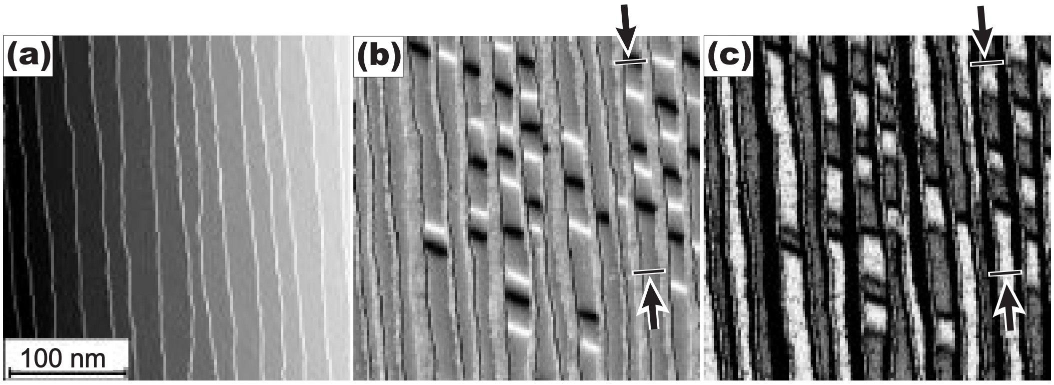

Figure 3.12: **(a)** Topography and dI/dU signal of Fe nanowires as simultaneously measured at **(b)** $U = -0.1$ V and **(c)** $U = +0.1$ V with an Fe coated probe tip. While the dI/dU image at negative sample bias shows a pure domain wall contrast the dI/dU image measured at positive bias exhibits a significant out-of-plane contribution to the signal which results in a clear domain contrast. Averaged line sections drawn between the arrows indicated in (b) and (c) are shown in Figure 3.13.

tip (cp. Fig. 3.10). In contrast, the dI/dU-map of Fig. 3.12(c) is clearly dominated by a domain contrast, i.e. an out-of-plane spin contrast. In order to allow a more detailed analysis we have drawn line sections between the arrows along one particular nanowire in Fig. 3.12(b) and (c). On the basis of more dI/dU images (not shown here) which were imaged at the *same* location of the sample using the *same* tip and the *same* tunneling current $I = 0.3$ nA we have also analyzed equivalent line sections for many different bias voltages. The results are plotted in Fig. 3.13. Along the line section four domain walls can be found which, at in-plane spin-contrast, show up as peaks or dips in the dI/dU signal corresponding to a parallel or antiparallel orientation of the sample spins with respect to the tip. This *normal* situation is observed at $U \leq 0$ mV and at $U \geq +200$ mV. Under these conditions no offset from the average dI/dU signal could be found above different domains indicating that we have no sensitivity to the out-of-plane component of the sample magnetization. At small positive sample bias, however, a significant offset is found. Although some contrast from the domain walls remains always visible an appropriate choice of the bias voltage ($U \approx +200$ mV) leads to a strongly dominating domain contrast. In the following we want to discuss these observations which cannot be understood on the basis of simple collinear magnetism. We consider four different effects to explain the experimental facts at least qualitatively, namely electric dipole forces, current-induced magnetic torque [21], coherent spin-rotation at the interface [22], and intra-atomic non-collinear magnetism [20].

Probably, the apex of the tip is formed by a small cluster of magnetic material which protrudes from the spherical end of the tip. To our experience it is sufficiently sharp in order to routinely image step edges on the sample surface as long as their heights do not exceed several atomic layers. First, let us assume that the cluster is collinearly magnetized in equilibrium, i.e. with no electric field present within the vacuum gap. Since the magnetic anisotropy is only a small correction to the total energy of the system it is very sensitive even to minor structural changes. Hence, we can speculate that the application of an electric field may lead to a slight change of the interlayer distance between the apex atom and the first subsurface layer at the tip. This may result in a field dependence of the anisotropy of the last atom of the tip. We believe, however, that this explanation is very unlikely mainly because of the small bias voltage value at which the effect is observed and because it vanishes again at higher voltages.

If a current-induced magnetic torque $\vec{L}$ would be responsible for the observations, the effect should increase linearly with the current density j [21]. Our results indicate, however, that the SDO of the tip is independent of the tunneling current. Coherent spin-rotation is caused by the precession of the electron spin around the magnetic field [22]. In our case it might occur in the vacuum gap between the sample and the tip. Since, however, the angle of precession $\epsilon \propto E^{-1/2}$ it should be largest for a small bias voltage which is in contrast to our observations. In particular, for Gd coated tips the effect was largest at a relatively large bias voltage $U = -700$ mV. Therefore, we

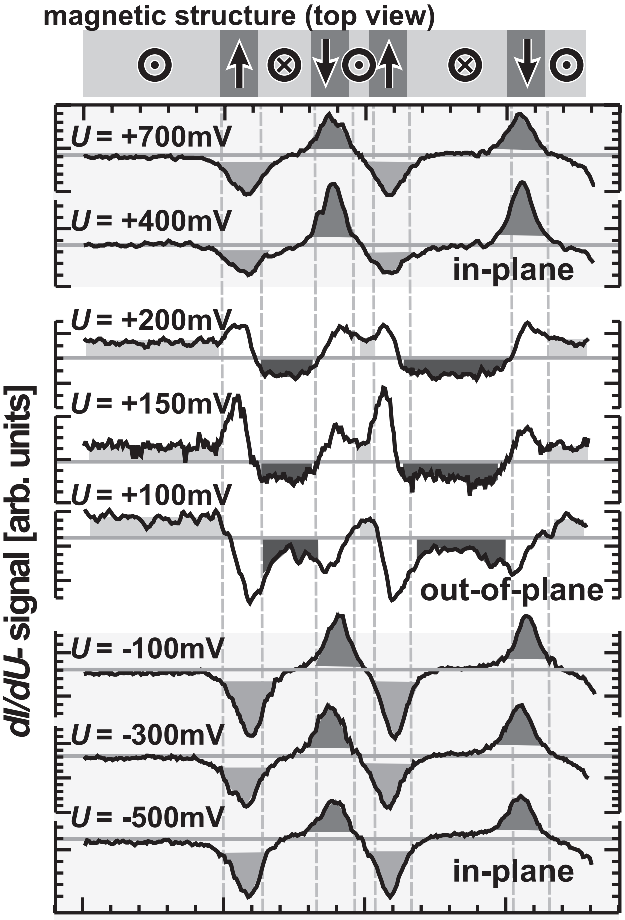

Figure 3.13: Averaged line sections of the dI/dU signal as drawn between the arrows indicated in Fig. 3.12(b) and (c). A pure in-plane contrast in the magnetic dI/dU signal is found for $U < 0$ V and $U > +0.2$ V. In contrast, some out-of-plane contribution appears at 0 V $< U < +0.2$ V. All data were measured with the same tunneling current $I = 0.3$ nA.

can exclude that either a current-induced magnetic torque or coherent spin-rotation play an important role.

The most likely explanation for our observation is found in the concept of intra-atomic non-collinear magnetism. We probably observe tunneling from different tip orbitals, e.g. e_g- and t_{2g}-like d-orbitals as it has already been suggested in Ref. [23]. Under *normal* conditions, i.e. for negative and high positive sample bias, the tunneling current flows through orbitals which have a SDO being collinear with the magnetization direction, i.e. in-plane for an Fe coated tip. At small positive sample bias, however, another occupied orbital of the tip with a SDO being almost orthogonal to the global tip magnetization probes the sample's density of states leading to an out-of-plane contrast. Besides the possibility that different orbitals of the probing atom at the tip apex may exhibit different SDOs [23] another mechanism which also produces intra-atomic NCM has recently been described by Nordström and Singh [20]. Since the physical origin of this mechanism is, however, spin-orbit coupling which is very small for transition metals like Fe it is very improbable that our observations are caused by this effect. In fact, it has been calculated for fcc-Pu, a material with "substantial" spin-orbit coupling, that the maximal deviation of the local SDO from the global magnetization direction amounts to 5° [20]. Although symmetry breaking—a situation which is certainly fulfilled at the tip apex—may lead "to a further tipping" of the spin-orientation [20] we do not believe that the resulting effect in an Fe tip can account for the observations.

Fe Nanoislands on W(110)

So far we have concentrated on our model system, i.e. Fe nanowires which have been prepared by step-flow growth on stepped W(110) substrates held at elevated temperature. An even more complicated sample morphology can be obtained by room temperature (RT) growth of Fe on W(110) which leads to doublelayer (DL) islands surrounded by a single ML Fe, with island sizes of a few nanometers. For this system Weber *et al.* [24] suggested a model of spatially switching anisotropy where the easy axis of magnetization changes discontinuously from in-plane in the ML to out-of-plane in the DL islands. From the competition of anisotropy and exchange energy a complex magnetic ordering is to be expected, the details of which could, so far, not be investigated directly. Fig. 3.14 shows a sequence of constant current images (left) and simultaneously acquired $\mathrm{d}I/\mathrm{d}U$ maps (right) with an Fe coverage from 1.2 up to 2.1 ML. At 1.2 ML all DL islands are in a single domain state. They display a two-stage contrast corresponding to an out-of-plane antiferromagnetic (AFM) ordering. Small islands, however, show an intermediate $\mathrm{d}I/\mathrm{d}U$ signal, a finding we will discuss in detail later. Also at 1.3 ML we observe an out-of-plane AFM ordering with the islands as single domain particles. There is, however, one exception to this rule for an island with a constriction (see arrow). Here a domain wall is found right at the constriction where the domain wall energy is minimal. Furthermore, the magnetic structure of the island ensemble is not completely random. Chains of parallelly magnetized islands are found along the step edges, reminiscent of the AFM coupled DL wires investigated in Ref. [17]. This ordering is obviously a result of ferromagnetic (FM) coupling between the islands which is mediated by exchange coupling to the DL stripes that have grown at the W step edges. This kind of magnetic structure becomes even more pronounced at 1.6 ML. At this coverage island coalescence has started and extended islands display misfit dislocation lines oriented along [001]. We marked two such islands by ovals in the topography image. The dislocation lines are also visible as white lines in the dI/dU map due to their local influence on the electronic structure.

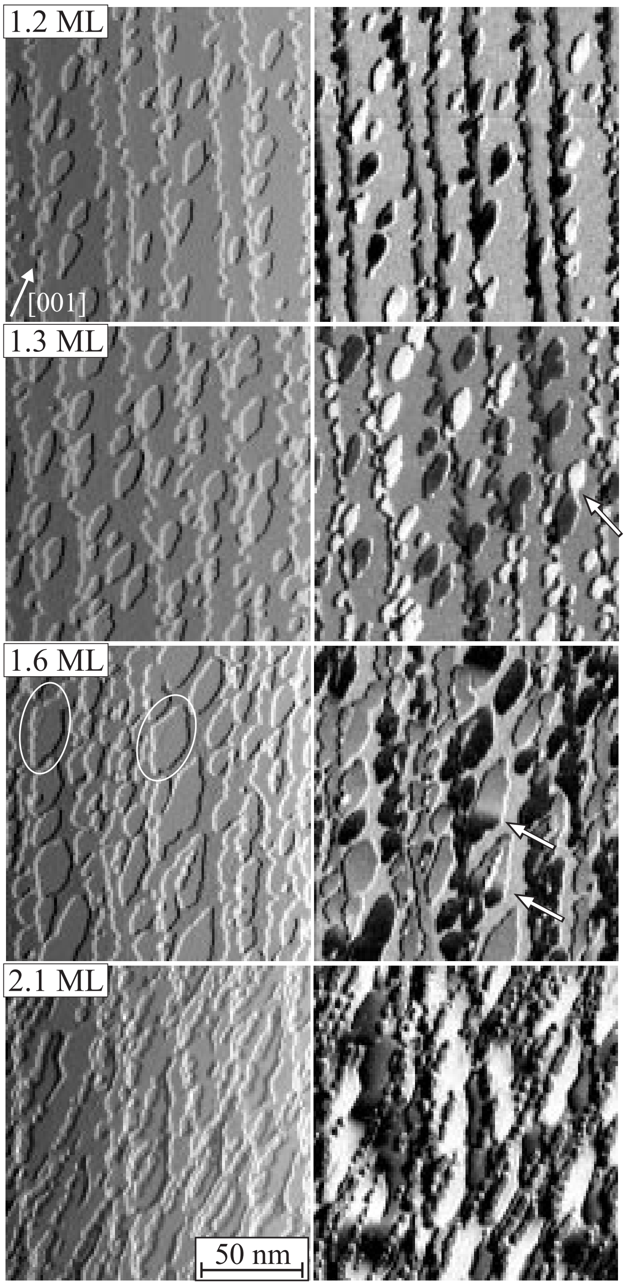

Figure 3.14: Constant current images (left) and simultaneously recorded dI/dU maps (right). **1.2 ML** (U=-0.4 V) and **1.3 ML** (U=-0.8 V): All DL islands are in a single domain state with the magnetization pointing up or down. An exception is marked by an arrow. Small islands exhibit intermediate gray levels due to a reorientation to in-plane. **1.6 ML** (U=+0.7 V): Dislocation lines are visible (see ovals) as well as small patches of the third layer. Two domain walls oriented along [1$\bar{1}$0] are marked by arrows. **2.1 ML** (U=-1.0 V): The DL is nearly closed and the third layer contribution is substantial. Nevertheless, an out-of-plane AFM ordering is present in the DL.

In contrast to lower coverages domain walls are present in islands beyond a length of $\approx$ 30 nm even in the absence of constrictions. They are always oriented along $[1\bar{1}0]$ with a wall width of 7 ± 1 nm. Two domain walls are marked by arrows. The lower one crosses a dislocation line on which third layer patches have nucleated. Surprisingly, the appearance of dislocation lines and the accompanied partial release of misfit strain has no detectable influence on the magnetic domain structure. We neither observe a loss of out-of-plane contrast nor any local interaction of dislocation lines and domain walls. At 2.1 ML the second layer is nearly closed except for trenches running roughly along [001]. Lines of third layer patches have nucleated along the same direction. Nevertheless, the $\mathrm{d}I/\mathrm{d}U$ map reveals that out-of-plane AFM ordering is still present in the DL, with domain sizes governed by the substrates terrace width, i.e. 25 nm.

Utilizing the high spatial resolution of SP-STS we have performed a detailed analysis of the size dependence of the magnetization of the DL islands. The inset of Fig. 3.15(a) shows two small islands displaying an intermediate $\mathrm{d}I/\mathrm{d}U$ signal (left) and the corresponding topography (right). From the model of spatially switching anisotropy [24] a reorientation of island magnetization to in-plane is expected below a critical island size, driven by exchange coupling to the in-plane magnetized ML. In order to verify this prediction quantitatively we plotted the average $\mathrm{d}I/\mathrm{d}U$ signal of $\approx$ 140 free standing DL islands vs. their width along $[1\bar{1}0]$ for the sample of 1.3 ML coverage presented in Fig. 3.14. The result is shown in Fig. 3.15(a) with each gray square corresponding to a particular island. The error bar represents the standard deviation over the island area. Beyond 4 nm width a strong two-stage contrast is displayed corresponding to $P_{\mathrm{eff}} \approx 0.45$. This contrast vanishes between 2 and 3 nm

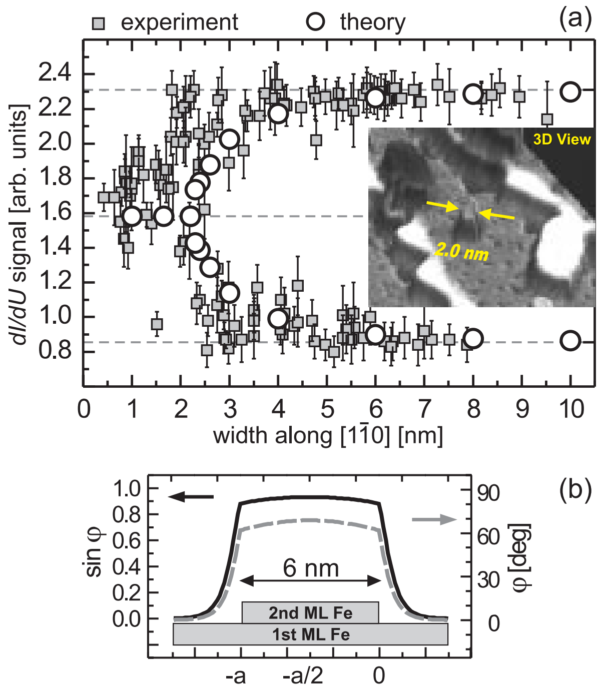

Figure 3.15: **(a)** Average $\mathrm{d}I/\mathrm{d}U$ signal of DL islands (gray squares) vs. island widths along $[1\bar{1}0]$. A vanishing of magnetic out-of-plane contrast is observed with decreasing width at 2-3 nm. Calculations (circles) suggest a transition to in-plane magnetization at 2.4 nm. The inset shows a rendered three-dimensional image of islands with three distinct magnetization directions. **(b)** Calculated magnetization direction $\varphi(x)$ (gray curve) and its sine (black curve) as a function of lateral distance across a DL.

width and the dI/dU signal then stays constant within our measurement accuracy at an intermediate level. To understand this result we performed micromagnetic calculations in the spirit of Ref. [25]. Taking into account exchange and anisotropy energy only and neglecting the finite island length along [001], we searched for one dimensional functions of the magnetization angle $\varphi(x)$ that minimize the energy integral across a single DL area of width a. With the DL between $x = -a$ and 0 and $\varphi = 0$ corresponding to in-plane magnetization, the relevant integration extends from -a/2 to ∞:

$$\Gamma_{\mathrm{DL}} = 2\int_{-\frac{a}{2}}^{0} \left\{ A_{\mathrm{DL}} 2t \left(\frac{d\varphi}{dx}\right)^2 + K_{\mathrm{DL}} 2t \cos^2\varphi \right\} dx \tag{3.2}$$

$$\Gamma_{\mathrm{ML}} = 2\int_{0}^{\infty} \left\{ A_{\mathrm{ML}} t \left(\frac{d\varphi}{dx}\right)^2 + K_{\mathrm{ML}} t \sin^2\varphi \right\} dx. \tag{3.3}$$

Here A is the exchange stiffness, K the anisotropy constant, and $t = 2$ Å is the layer thickness. We parametrized test functions in a way that they automatically satisfied the boundary conditions and numerically calculated the set of parameters minimizing $\Gamma_{\mathrm{DL}} + \Gamma_{\mathrm{ML}}$ for a number of widths a. We used the boundary conditions $\varphi'(-\frac{a}{2}) = 0$, $\varphi(\infty) = 0$, $\varphi(0^-) = \varphi(0^+)$, and $\varphi'(0^+) = 2\,A_{\mathrm{DL}}/A_{\mathrm{ML}} \cdot \varphi'(0^-)$. The last condition ensures a continuous torque at the boundary between ML and DL, with a factor of 2 arising from the different layer heights. The anisotropy constants have been determined experimentally to $K_{\mathrm{ML}} = 5\times10^6$ Jm^{-3} and $K_{\mathrm{DL}} = 1\times10^6$ Jm^{-3} [9]. For an estimate of A_{DL} we utilize the domain wall width $w_{\mathrm{DL}} = 7\pm1$ nm as observed by SP-STS. With the equation $w_{\mathrm{DL}} = 2\sqrt{A_{\mathrm{DL}}/K_{\mathrm{DL}}}$ we get $A_{\mathrm{DL}} = 1.25\times10^{-11}$ Jm^{-1}. The exchange stiffness of the ML is chosen to $A_{\mathrm{ML}} = 1.25\times10^{-12}$ Jm^{-1} to achieve a good agreement with the experimental data. In Fig. 3.15(a) we have plotted the sine of the magnetization angle in the middle of the DL area, $\sin\varphi(-a/2)$, vs. the width a (white circles), with the dashed grid lines corresponding to 0 and ±1, respectively. The calculated values display a transition to perfect in-plane magnetization in the DL at $a_c = 2.4$ nm, in good agreement with the experimental data. The scattering of experimental values between 2 and 3 nm is not surprising, since the energy difference between in-plane and a slightly tilted magnetization becomes very small in the vicinity of the critical width, and the actual angle therefore depends on the exact local configuration, like, e.g., island shape and local stray field. Furthermore, we only considered a symmetric boundary condition with the ML magnetized parallel on both sides of the DL. In an antiparallel configuration, however, the magnetization must rotate via 90° in the DL which might explain some deviations observed for small islands. Fig. 3.15(b) shows the calculated magnetization direction $\varphi(x)$ (gray curve) and its sine (black curve) for a width of $a = 6$ nm. Since for an out-of-plane magnetized tip the dI/dU signal is proportional to the sine of the magnetization angle the black curve is the one as measured by SP-STS. It agrees with the experimental data in the way that the dI/dU signal appears rather flat on the DL and we do not observe any magnetic contrast in the ML in the vicinity of the DL islands. We therefore assume that the rotation takes place in a very narrow region at the interface of ML and DL.

The Topological Antiferromagnet Cr(001)

The magnetic structure of the Cr(001) surface has been of great interest already for a long time because of the existence of surface ferromagnetic order despite the antiferromagnetic bulk structure [26, 27] and because of the important role of the magnetic properties of Cr(001) in exchange-coupled Fe/Cr bilayers and superlattices [28–30]. In 1989 Blügel *et al.* [27] recognized the influence of surface defects, such as monatomic steps, on the overall magnetic properties of the Cr(001) surface. The presence of such monatomic steps leads to a topological antiferromagnetic order with neighbored terraces exhibiting a magnetization in opposite directions. Though this model of so-called "topological antiferromagnetism" is simple and convincing, it turned out to be a hard task to prove it experimentally. Imaging the magnetic structure of the Cr(001) surface requires both, extremely high spatial resolution to be able to resolve single terraces whose width is usually below 100 nm as well as highest surface sensitivity to only measure the magnetization of the topmost layer.

Both conditions are fulfilled by spin-polarized scanning tunneling microscopy (SP-STM). Figure 3.16(a) shows an average $\mathrm{d}I/\mathrm{d}U$ spectrum (30×30 single input spectra)

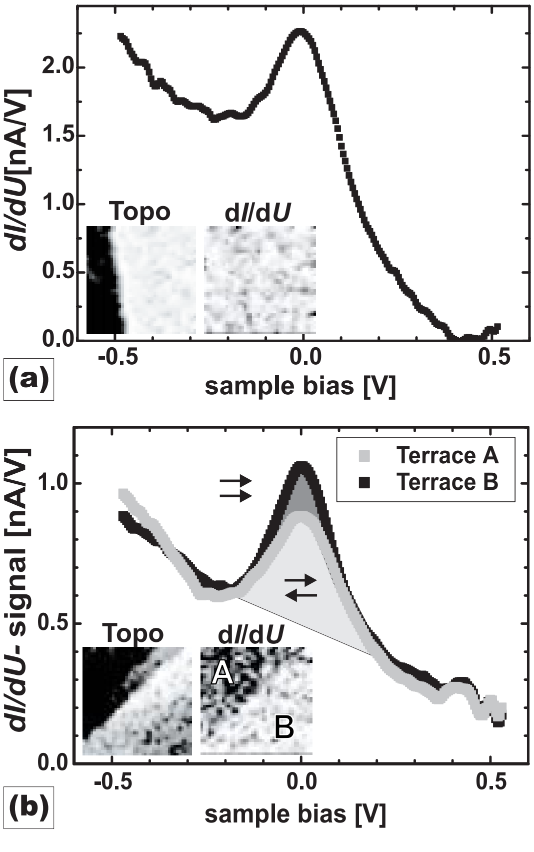

Figure 3.16: Typical tunneling spectrum of Cr(001) as measured **(a)** with a non-coated W-tip and **(b)** with a Fe-coated tip. All spectra are dominated by a strong peak at $U = -20$ meV which represents the d_{z^2}-like surface state [31]. The insets show the topography (left) and maps of the $\mathrm{d}I/\mathrm{d}U$ signal at the surface state peak position (right). In both cases the topography shows two atomically flat terraces which are separated by a monoatomic step edge. While the spectra measured with the W tip are identical on both terraces the spatially resolved $\mathrm{d}I/\mathrm{d}U$ signal as measured with the Fe-coated tip reveal significant differences between the two terraces due to the vacuum-tunneling magnetoresistance effect.

as measured with a non-coated W tip. The spectrum is dominated by a surface state which shows up as a peak close to the Fermi level ($U = -20$ meV) and which has previously been described by Stroscio and co-workers [31]. This surface state is known to exhibit d_{z^2}-like symmetry and is highly spin-polarized which makes it favorable for spin-polarized STS measurements. The two insets included in the Fig. 3.16(a) show the simultaneously acquired constant-current image on the left and the spatially resolved $\mathrm{d}I/\mathrm{d}U$ signal at the surface state peak position. While two terraces separated by a monoatomic step edge are clearly visible in the constant-current topograph no difference between the terraces can be recognized in the $\mathrm{d}I/\mathrm{d}U$ map. This result is expected since the two terraces are electronically equivalent. Fig. 3.16(b) shows spectra that were taken with an Fe coated probe tip. Now the peak height differs between the two terraces: the average of all spectra taken over the left terrace shows a significantly smaller peak than the one taken over the right terrace. This behaviour is due to spin-polarized tunneling.

Again, the information of the full spectra is only needed once to understand the contrast mechanism and to know at which bias voltage maximum contrast is to be expected. Therefore, in the following the imaging of the magnetic structure has been performed by measuring $\mathrm{d}I/\mathrm{d}U$ maps at a single bias value with increased pixel resolution. The data presented in Fig. 3.16(b) might suggest that a high magnetic contrast can be achieved at the Cr(001) surface state peak position, i.e. very close to the Fermi level. We have, however, to take into account that the tip–sample distance is not constant but—as a result of the constant-current mode of operation—depends on the local differential conductivity which is not only an intrinsic property of the sample surface but which in spin-polarized experiments is also influenced by the relative magnetization direction of tip and sample. In the following we will show that if the Cr(001)—which is chemically homogeneous—is scanned in the constant-current mode with a magnetic tip at a bias voltage corresponding to the energetical position close to the surface state the tip–sample distance is increased (decreased) above Cr terraces magnetized (anti)parallely with respect to the tip. As already shown in 1990 [4] and confirmed recently [32] this variation of the tip–sample distance shows up as deviations of the measured step height values from the topographic step height. This, however, leads to a strong reduction of the variation of the differential conductivity $\mathrm{d}I/\mathrm{d}U$ above oppositely magnetized Cr(001) terraces. A high (magnetic) $\mathrm{d}I/\mathrm{d}U$ contrast can only be achieved if non–spin-polarized electronic states contribute to the tunneling current, a situation which is fulfilled at enhanced sample bias. To our experience on Cr(001) the highest $\mathrm{d}I/\mathrm{d}U$ contrast is obtained at $U \approx \pm(250 \pm 50)$ mV.

Fig. 3.17(a) shows a constant-current mode STM-image which has been measured at this bias voltage range, i.e. $U = -290$ mV. Nine terraces descending from the lower left to the upper right corner are visible. The line section drawn along the rectangle is plotted in the lower panel of Fig. 3.17(a). It reveals that all terraces are separated by monoatomic steps. Due to the high value of the sample bias used in this measurement ($U = -290$ mV) the contribution from non–spin-polarized electronic states to the

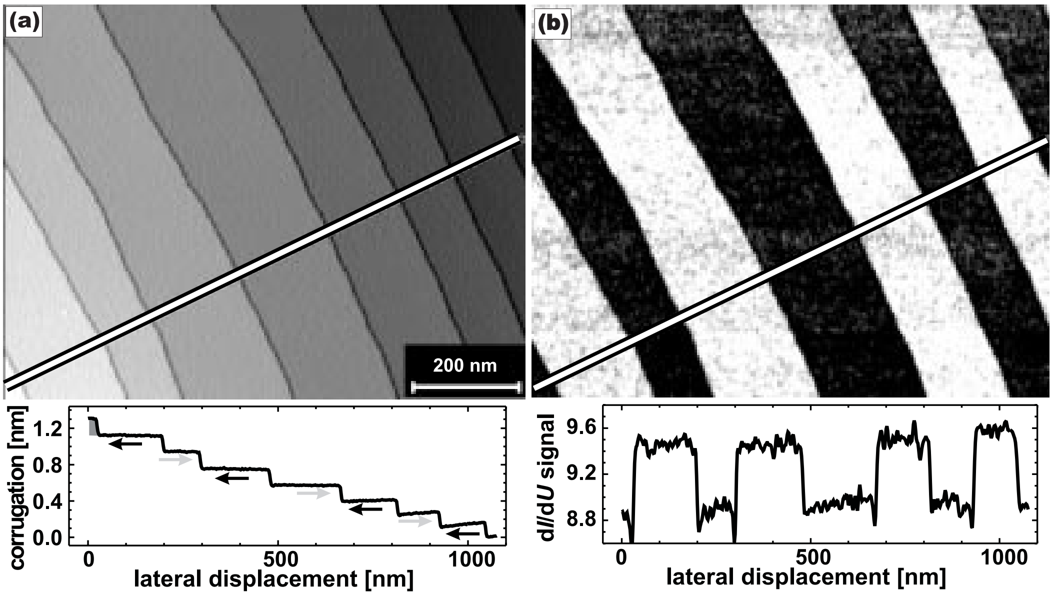

Figure 3.17: **(a)** Constant-current mode STM image of the Cr(001) surface. Nine terraces separated by monoatomic steps are visible. **(b)** Simultaneously acquired spin-resolved $\mathrm{d}I/\mathrm{d}U$ map at $U = -290$ mV sample bias. The signal changes at every step between low and high due to antiparallel magnetization of adjacent terraces thereby confirming the model of "topological antiferromagnetism" proposed by Blügel *et al.* [27].

tunneling current is rather high. In accordance with the explanation given above we could not find any magnetically induced variation of the topological step height within our measurement accuracy. However, the simultaneously acquired $\mathrm{d}I/\mathrm{d}U$ signal exhibits a strong magnetic contrast. The $\mathrm{d}I/\mathrm{d}U$ map of Fig. 3.17(b) reveals that the $\mathrm{d}I/\mathrm{d}U$ signal changes between low and high at every step edge thereby confirming Blügel‘s model [27] of topological antiferromagnetism. The line-section taken at the same position as for (a) shows two levels in the $\mathrm{d}I/\mathrm{d}U$ signal separated by steep edges which demonstrates the extremely high lataral resolution of spin-polarized STS. As pointed out above Fe coated tips are preferentially magnetized parallel to the sample‘s surface plane. Therefore, our results on Cr(001) terraces are also expected to show the in-plane component of the surface magnetization.

In a second experiment we have looked at similar surface region but choosing another bias voltage ($U = -60$ mV) close to the Cr(001) surface state peak position (Fig. 3.18). Three screw dislocations appear (marked by arrows) which are frequently observed at Cr(001) surfaces by STM. Obviously, the screw dislocations result in spin frustration in their surroundings which will be discussed lateron. Fig. 3.18(b) shows the simultaneously measured spin-resolved spectroscopic image which in dislocation-free areas again exhibits $\mathrm{d}I/\mathrm{d}U$-signal intensity variations over the different (001) terraces. However, in contrast to the previous measurement where no magnetically induced variation of the topological step height was found [Fig. 3.17(a)] the topologi-

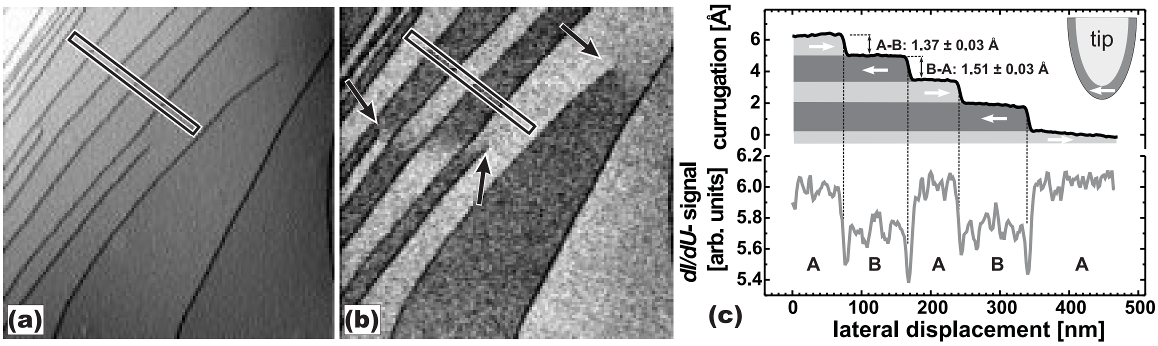

Figure 3.18: **(a)** Constant-current STM image ($1\ \mu$m $\times 1\ \mu$m) and **(b)** spin-polarized $\mathrm{d}I/\mathrm{d}U$ map of the Cr (001) surface. Three screw dislocations are visible (arrows). The data were measured at a sample bias $U = -60$ mV. **(c)** Averaged topographic (top) and spectroscopic (bottom) line-section drawn along the box indicated in (a). The step heights periodically alternate as found earlier by using CrO_2-tips [4]. The lower part shows the periodic alteration of the spectroscopic $\mathrm{d}I/\mathrm{d}U$-signal.

cal antiferromagnetic order is now reflected by alternating measured monatomic step heights as demonstrated by the line profile of Fig. 3.18(c)(top part). The correlation of the simultaneously measured topographic and spectroscopic signal as plotted in Fig. 3.18(c) nicely confirms our considerations regarding the differences between measurements performed in the constant-current and constant-separation mode mentioned above. More quantitatively, the measured step-height values differ periodically by about 0.14 Å. This variation is smaller by a factor of three than reported previously [4, 5] which, however, is expected since the degree of spin-polarization of the Fe-tip is smaller than the one of CrO_2-tips as used in the earlier study [4, 5]. By assuming a spin-polarization P_{Fe} of about 40 % for the Fe-coated probe tip as deduced from earlier experiments [33] the measured step height difference of $2\Delta s = 0.14$ Å can be translated into a value for the spin-polarization P_{Cr} of the Cr(001) surface. Making use of the relationship (4) from Ref. [4] we find $P_{\mathrm{Cr}} = 17\%$. This is consistent with the earlier result obtained by using CrO_2 thin film tips [4] if one assumes a polarization of the CrO_2 tip close to 100 % which was indeed found by spin-resolved photoemission [34] and planar tunneling junction experiments.

We have seen that for a simple step structure like in Fig. 3.17(a) the topographic structure of the Cr(001) surface determines its magnetic structure. This situation becomes more complicated if defects like screw dislocations are present on the surface, as, e.g., visible in Fig. 3.19. The presence of screw dislocations leads to a change of the magnetization direction within a given (001) plane in the vicinity of their cores thereby introducing the formation of domains and domain walls. This is most clearly seen for the two screw dislocations indicated by arrows in Fig. 3.19(a). The induced domain wall follows a straight line between the two screw dislocations. The width of the domain wall can be determined from line sections drawn across the walls along lines (i) and (ii) in Fig. 3.19(b) which are plotted in Fig. 3.19(c). As already described on

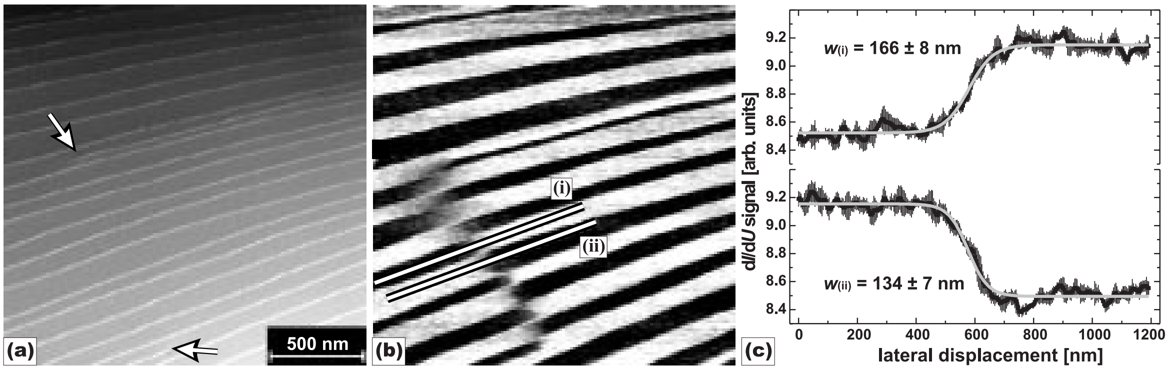

Figure 3.19: **(a)** Constant-current STM image of the Cr(001) surface. Two screw dislocations (arrows) are visible within the field of view. **(b)** The dI/dU map shows a domain wall between the screw dislocations. Two domain wall profiles [(i) and (ii)] are plotted in **(c)**. The wall profiles can nicely be fitted by micromagnetic theory resulting in domain wall widths of $w_{(\mathrm{i})} = 134 \pm 7$ nm and $w_{(\mathrm{ii})} = 166 \pm 8$ nm.

page 26 we have fitted the measured data by Equ. 3.1 [18]. The best fits to the domain wall profiles were achieved with wall width of $w_{(\mathrm{i})} = 134 \pm 7$ nm and $w_{(\mathrm{ii})} = 166 \pm 8$ nm. Summarizing over many domain walls we found widths between 120 nm and 170 nm.

The bulk magnetic structure of Cr is not commensurate, i.e. the magnetization direction of the ferromagnetically coupled (001) planes does not simply alternate between adjacent layers. Instead, an additional sinusoidal modulation exists which forms an incommensurate spin-density wave. The period of the spin-density wave L in bulk Cr is about 54 ML at room temperature [30]. At our measurement temperature, i.e. $T = 300$ K, only the transverse spin density wave (T-SDW) exists. The magnetic surface structure that we measure may be explained by a T-SDW having its wave vector perpendicular to the (001) surface plane and the magnetization parallel to the surface. If the spin-density wave is not altered by the symmetry break at the surface a modu-

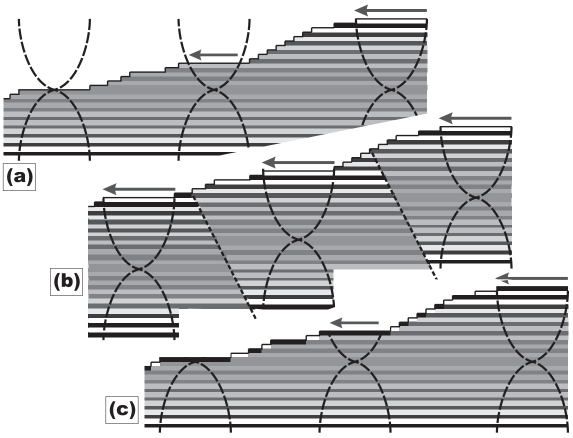

Figure 3.20: Three different models of the Cr spin-density wave (SDW) at the surface: **(a)** The bulk SDW is not affected by the presence of the surface. In this case a long-range modulation of the magnetic moment should be visible. **(b)** The SDW exhibits a maximal magnetic moment for every individual (001) plane. **(c)** The bulk SDW remains unchanged, but the coupling of the Cr(001) surface layer to the first subsurface layer varies such that the surface magnetic moment is maximized for any terrace.

lation of the magnetic signal should be visible in larger scale SP-STS images. In other words, as a consequence of the sinusoidal modulation of the incommensurate SDW the signal should exhibit a node every 27 terraces. This situation is schematically represented in Fig. 3.20(a). Another possible spin-configuration is drawn in Fig. 3.20(b). It is characterized by a SDW which exhibits a maximal magnetic moment for every individual (001) plane of the surface. This situation may be favorable due to an enhanced magnetic moment in the Cr surface layer. It would, however, imply that domain walls with the plane of the wall directed perpendicular to the miscut surface must exist. At the position of the domain wall the phase of the SDW in a particular (001) plane shifts by $2\pi/L$. A third possibility is shown in Fig. 3.20(c). Here the bulk SDW remains unchanged at all, but the coupling of the Cr(001) surface layer to the first subsurface layer varies such that the surface magnetic moment is maximized for any terrace. Consequently, a parallel coupling of the surface and the first subsurface layer would occur on every Lth terrace. Obviously, the situations described in Fig. 3.20(b) and Fig. 3.20(c) result in the same surface magnetic structure.

Whether the model of Fig. 3.20(a) or Figs. 3.20(b) and (c) describe the reality at the Cr(001) surface can be decided by a large scale image which simultaneously shows the

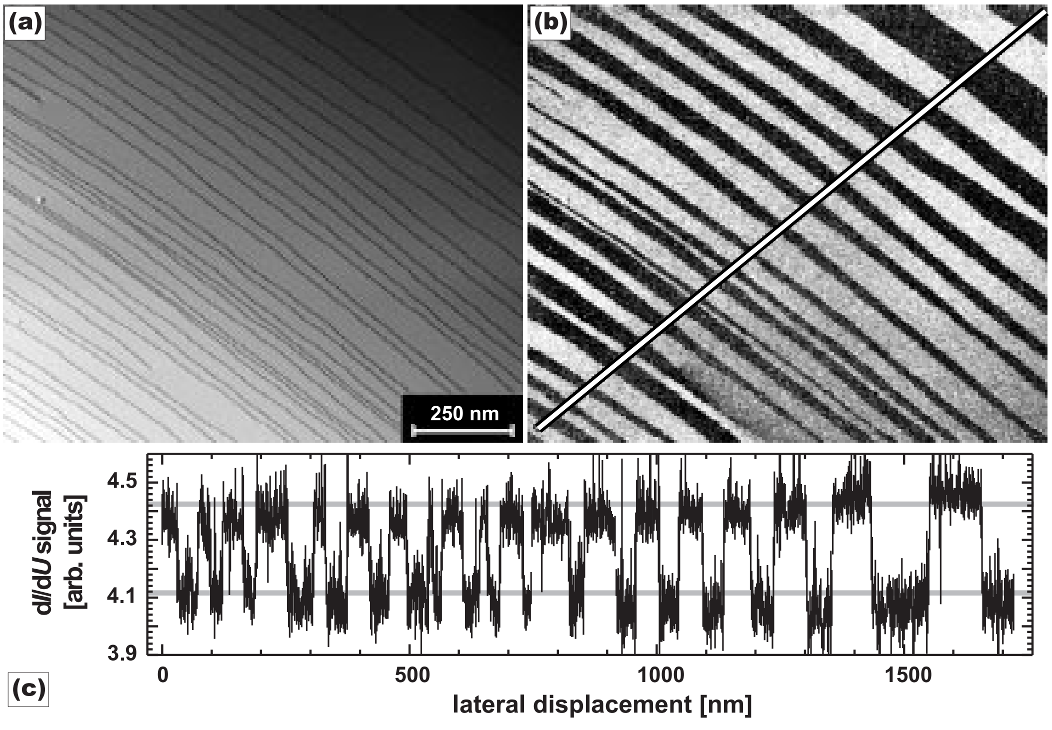

Figure 3.21: **(a)** Large area constant current mode STM-image of the Cr(001) surface. Forty terraces separated by monoatomic steps are visible. **(b)** Simultaneosly acquired spin-resolved dI/dU map at $U = +190$ mV sample bias. The signal changes at every step between low and high due to antiparallel magnetization of adjacent terraces. No additional long-range modulation is visible; instead the contrast remains almost constant over 40 terraces.

approximate number of terraces forming a single period of the SDW. Fig. 3.21(a) shows the topography and (b) the spin-resolved dI/dU map of our Cr(001) single crystal. The field of view contains 40 terraces separated by monoatomic steps. Fig. 3.21(c) shows an averaged line section taken along the box in (b). Obviously, the amplitude of the magnetic contrast remains almost constant over 40 terraces. No node of the signal is visible. This result proves that the SDW exhibits a maximal magnetic moment at the surface indicating that the bulk spin-density wave (SDW) is modified at the surface due to symmetry breaking. At present, however, we cannot decide whether domain walls extend within the bulk or are located between the surface and the first subsurface layer.

3.2.3 Atomic-Resolution Imaging of Surface Spin-Structures by Spin-polarized Scanning Tunneling Microscopy

The Two-Dimensional Antiferromagnetic Monolayer of Mn on W(110)

In the past only few experimental techniques were available for the investigation of ultrathin antiferromagnetic films. The resulting lack of experimental work is even more annoying as the rapid development in computational physics allows to calculate the magnetic properties of specific and realistic overlayer–substrate systems with high accuracy. In particular, already more than 10 years ago Blügel *et al.* gave detailed predictions on the existence of 2D antiferromagnetic monolayer films of V, Cr, and Mn on (100) oriented Pd substrates [35] and later also on noble-metal substrates [36]. In such a film the magnetic moments of nearest-neighbor atoms couple antiferromagnetically to each other giving rise to a checkerboard arrangement of magnetic moments with opposite orientation. From these *ab initio* calculations based upon the full-potential linearized augmented plane wave (FLAPW) method it has been concluded that the hybridization between the monolayer and the noble-metal substrate is negligible and the monolayer film behaves as a perfect 2D system.

There have been several attempts to verify the existence of these 2D antiferromagnets and some evidence has been given [37–40]. However, a definite experimental proof was hindered by three problems: (i) First, the preparation of flat $3d$-metal overlayers on noble-metal substrates with an atomically sharp interface is very demanding. Interdiffusion between the substrate and the overlayer has been predicted theoretically [41] as well as observed experimentally even at room temperature [42]. (ii) Second, the Néel temperature below which magnetic order exists is unknown and probably very low. (iii) The main problem, however, is related to the AFM structure itself: due to the fact that in this ultimate limit adjacent atoms at nearest-neighbor sites have magnetic moments with opposite directions the total (average) magnetization cancels on length scales beyond the atomic scale. Therefore, spatially averaging techniques like those mentioned above are not suitable to decide whether or not a thin film is in a 2D antiferromagnetic ground state.

The problem of interdiffusion can be avoided by choosing a more stable substrate like W(110). Indeed, an antiferromagnetic c(2×2) structure has been predicted for the pseudomorphic Mn monolayer on W(110) as well [45]. The drawback of W(110) compared to noble-metal substrates is a strong hybridization of the $3d$-monolayer with such a $5d$-substrate influencing the magnetic properties. As a consequence, the $3d$ bands of the transition-metal broaden which reduces the possible exchange-splitting and thereby also the magnetic moment. Nevertheless, the two-dimensional antiferromagnetism within the monolayer film should not be destroyed since it does not depend on a high density of states at the Fermi energy as in the case of ferromagnetism but rather on a low density of states in the center of the d-band which becomes sometimes even lower due to the hybridization with the substrate. The second problem, i.e. the unknown and probably very low Néel temperature, can be solved by cooling the sample with liquid helium (LHe). Problem (iii), however, requires a measurement technique which combines magnetic sensitivity with high spatial resolution on an atomic scale. Obviously, these requirements are fulfilled for spin-polarized scanning tunneling microscopy (SP-STM).

Mn exhibits a great variety of different structural phases. The equilibrium room temperature structure is cubic α–Mn which exhibits an untypically large bulk unit cell containing 58 atoms. In bulk Mn simple cubic phases, namely face-center cubic (fcc) γ-Mn and body-center cubic (bcc) δ-Mn, are stable only at high temperatures close to the melting point. Another possibility to stabilize Mn—and any other element—in a non-equilibrium crystalline symmetry is by heteroepitaxial growth on an appropriate substrate. The dense-packed (110) surface of W is a very popular substrate. W exhibits a bcc crystal structure and an equilibrium lattice constant $a_{\mathrm{W}} = 3.16$ Å, i.e. the misfit f to δ-Mn ($a_{\mathrm{Mn}} = 2.95 \pm 0.03$ Å) [43,44] amounts to $f = (a_{\mathrm{W}} - a_{\mathrm{Mn}})/a_{\mathrm{Mn}} = 7.3 \pm 1.1\%$.

The room-temperature growth of the Mn monolayer on a W(110) substrate is illustrated by the series of six STM images shown in Fig. 3.22. Figure 3.22(a) shows the bare W(110) substrate. Ten atomically flat terraces being separated by steps of monatomic height can be recognized. Due to a certain fluctuation of the step-density a variety of different terrace widths was found: while an approximately 100 nm wide terrace can be seen in the middle of the image the width of terraces is strongly reduced in the upper right and lower left of the image down to about 20 nm. This surface was incrementely exposed for 30 s to the flux of the Mn evaporator. As can be seen in Fig. 3.22(b) the first evaporation cycle leads to the nucleation of small islands with a typical length of a few tens of a nanometer and which are elongated along the [001] direction of the substrate. In order to allow a quantitative analysis of the apparent height of the Mn monolayer on W(110) in STM images we have drawn a line section across one particular island in Fig. 3.22(b) indicated by a hatched line. The result is plotted in Fig. 3.23. Based on a comparison with the monatomic step height of the W(110) surface which amounts to 2.24 Å the apparent height of the Mn monolayer can be determined to 2.36 ± 0.02 Å. The step edges are decorated by smaller Mn fingers.

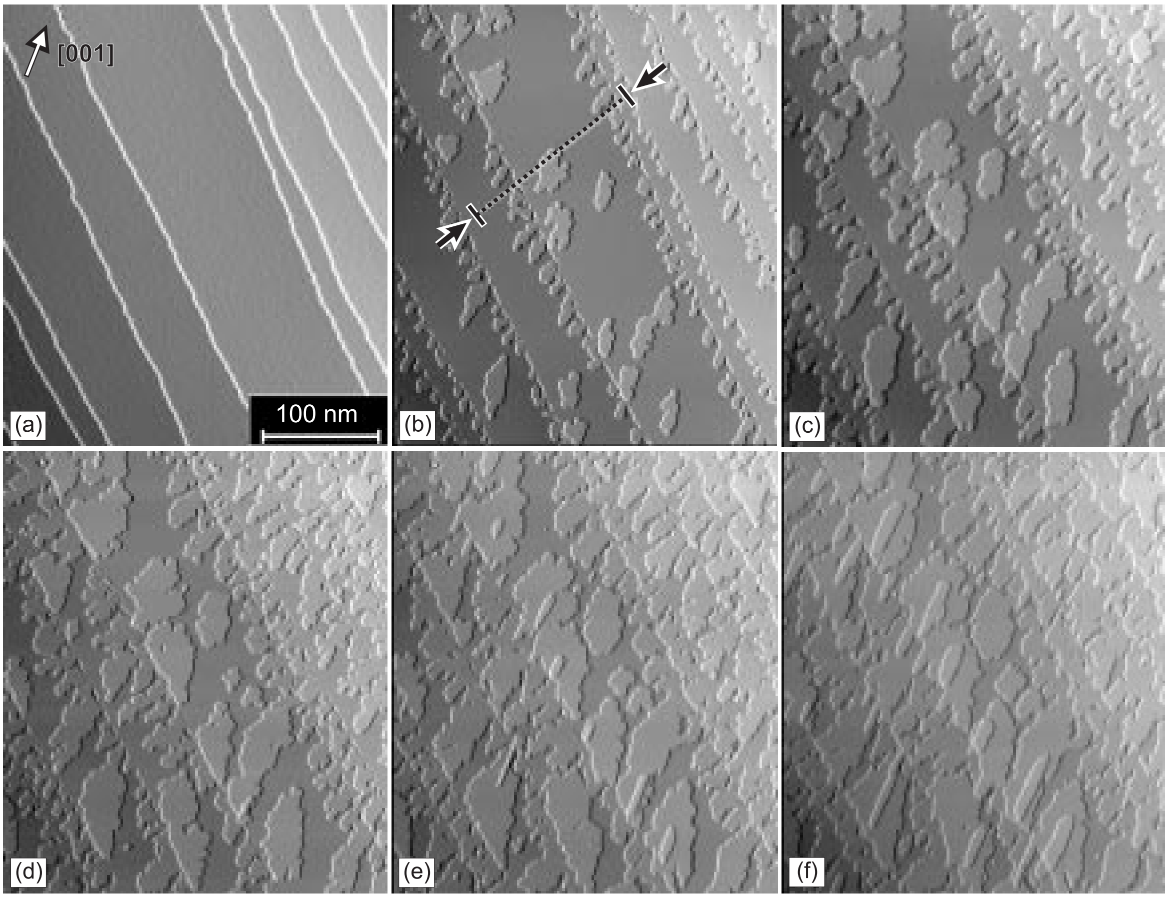

Figure 3.22: Topography of the same spot of the sample surface showing **(a)** the clean W(110) substrate and after the deposition of **(b)** 0.17 ML, **(c)** 0.34 ML, **(d)** 0.51 ML, **(e)** 0.68 ML, and **(f)** 0.85 ML. The measurement parameters were $U = +0.2$ V and $I = 0.2$ nA.

The apparent coverage amounts to 0.17 ± 0.01 ML. Since the nucleation density is very low (≈ 1 island per 4000 nm^2) almost no island can be found on terraces which are narrower than about 25 nm [cf. Fig. 3.22(b)]. Significant nucleation of second monolayer islands on top of islands of the first monolayer can be observed at a coverage

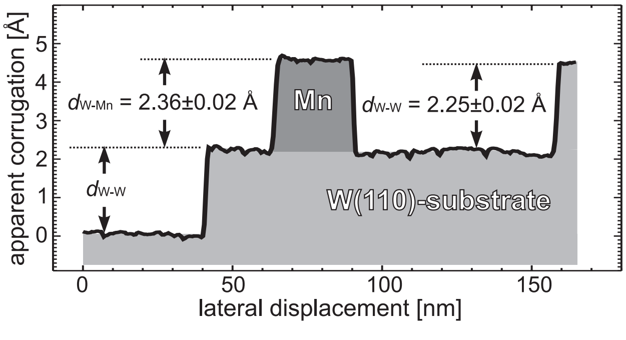

Figure 3.23: Single line–section (black line) drawn along the hatched line in Fig. 3.22(b). The tungsten substrate and the Mn monolayer have been differently grey shaded. At this particular tunneling parameters ($U = +0.2$ V and $I = 0.2$ nA) the apparent height of the Mn monolayer amounts to 2.36 ± 0.02 Å.

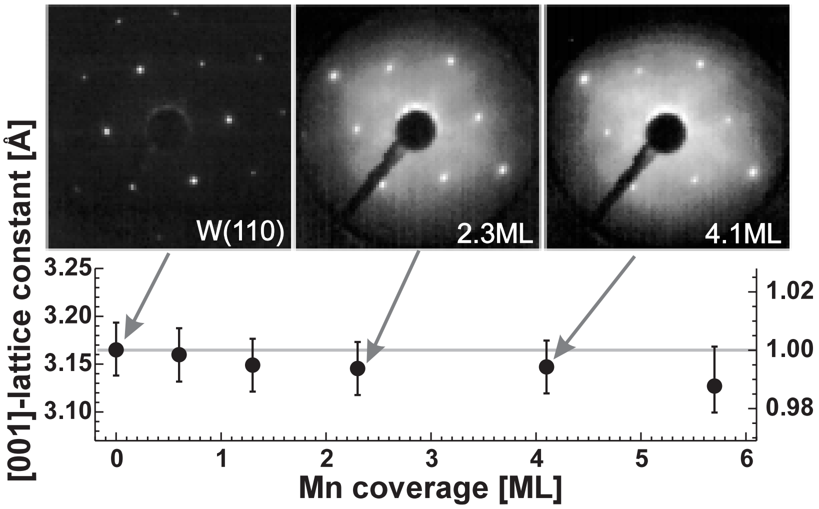

Figure 3.24: Plot of the lattice constant a_{cub} along the [001] direction versus the amount of Mn deposited on a W(110) substrate as determined from the LEED–pattern at $E_{\mathrm{p}} = 160$ eV. a_{cub} remains constant within the error bar. The inset shows LEED–patterns at three selected coverages. No satellite spots were found at any coverage. Instead, with increasing Mn coverage the diffuse background becomes more and more intensive indicating pseudomorphic growth at low coverage and poor medium range order at higher coverage.

of 0.68 ML in Fig. 3.22(e). Obviously, the tendency to grow anisotropically along the [001] direction is much stronger for the second layer than for the first monolayer.

It is well known that any relaxation between the adlayer and the substrate as a consequence of different crystallographic properties, i.e. the symmetry or the periodicity of the crystal lattice, leads to the appearance of dislocation lines or networks, as, e.g., found for Fe films on W(110) either by LEED or in STM studies. Instead, in the case of the Mn monolayer on W(110) we found no hint for dislocations neither in the STM topographs [Fig. 3.22(b)–(f)] nor in the LEED pattern which is free of superstructures and satellite spots. This can be recognized in Fig. 3.24 showing three LEED patterns which were observed at different Mn coverages. We have also analyzed the spot-spacing of the LEED pattern for Mn coverages of up to 5.7 ML quantitatively (Fig. 3.24). All data were calibrated to the bare W substrate which is known to exhibit a cubic lattice constant $a_{\mathrm{cub}} = 3.165$ Å. Although the data points suggest a certain tendency towards relaxation the determined values for a_{cub} are constant within the error bar. Beside a slight broadening of the LEED spots along the $[1\bar{1}0]$–direction which is caused by the reduced width of the Mn islands along this direction, the LEED pattern is the same as for the bare substrate even at a coverage of 4.1 ML. Based on our LEED and STM data we conclude that Mn grows pseudomorphically at this coverage on W(110), i.e. Mn mimics the bcc symmetry as well as the lattice constant of the underlying substrate in spite of the enormous tensile strain.

It has been shown theoretically by Blügel and co-workers [45,46] that the constant-

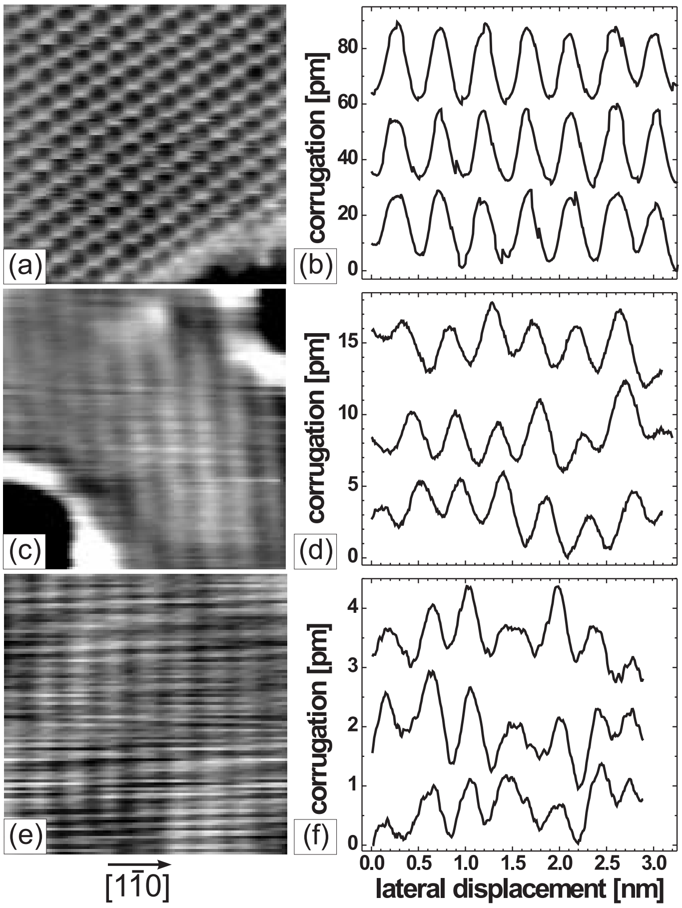

Figure 3.25: Atomic scale STM images (raw data) of a Mn monolayer on W(110) and single line sections drawn along the [1$\bar{1}$0] direction as measured with a bare W- [**(a)**, **(b)**], a Fe- [**(c)**, **(d)**], and a Gd-coated probe tip[**(e)**, **(f)**], respectively. The measurement parameters are $U = -3$ mV and $I = 40$ nA [(a)-(d)] or $U = -10$ mV and $I = 10$ nA [(e)-(f)].

current mode of a SP-STM is suitable to image surface magnetic spin-structures at the atomic scale. The principle of SP-STM on the atomic scale is based on the exponential decay of star coefficients with increasing length of the reciprocal lattice vector [45,46]. This measurement mode is based on the fact that any magnetic superstructure as, e.g. the predicted antiferromagnetism of a Mn monolayer on W(110) [45], lowers the translational symmetry of the underlying structural (chemical) lattice. Then, smaller reciprocal lattice vectors may contribute to the image. Since these lattice vectors possess exponentially larger coefficients, i.e. decay slower, they dominate the STM-image even in the case of small effective spin-polarization. It is of general validity and it may lead to the understanding of many more magnetic structures on this shortest possible length scale in the future [46].

As we zoom onto an atomically flat Mn island using a pure flashed W tip the atomic structure of the Mn monolayer on W(110) becomes visible [Fig. 3.25(a)]. With a pure (non–spin-polarized) W tip we are not sensitive to the spin of the tunneling electrons. Consequently, we cannot detect the modulation of the spin-polarization of the Mn atoms within the antiferromagnetic unit cell. Instead, we measure the total density of states which is equal above both atoms and the resulting image [Fig. 3.25(a)] shows the chemical unit cell. Three single line-sections drawn along the [1$\bar{1}$0] direction are plotted in Figure 3.25(b). The measured corrugation amounts to 20–30 pm. If, however, a magnetic probe tip is used the (larger) magnetic superstructure dominates the image as can be seen in Fig. 3.25(c). Since it was predicted that the easy axis of 1 ML Mn/W(110) is in-plane these data have been measured with an Fe coated tip. The strong dependence of the observed magnetic corrugation on the magnetization direction of the tip can be exploited to gain further information on the magnetization direction of the sample. In particular, the use of a tip which exhibits an easy magnetization axis which is *almost perpendicular* to the sample surface should lead to a much smaller corrugation amplitude than the previous example. Indeed, if a Gd coated probe tip is used the stripes along the [001] directions which are typical for the SP-STM image of the antiferromagnetic Mn monolayer on W(110) are only weakly visible [Fig. 3.25(e)] and the corrugation never exceeded 1 pm [Fig. 3.25(f)].

Acknowledgement

We would like to acknowledge the theoretical support of X. Nie and S. Blügel (Forschungszentrum Jülich).

References

[1] F.J. Himpsel, J.E. Ortega, G.J. Mankey, and R.F. Willis, Adv. Phys. **47**, 511 (1998).

[2] D.T. Pierce, Phys. Scr. **38**, 291 (1988).

[3] R. Meservey and P.M. Tedrow, Physics Reports **238**, 173 (1994).

[4] R. Wiesendanger, H.-J. Güntherodt, G. Güntherodt, R.J. Gambino, and R. Ruf, Phys. Rev. Lett. **65**, 247 (1990).

[5] R. Wiesendanger, I.V. Shvets, D. Bürgler, G. Tarrach, H.J. Güntherodt, J.M.D. Coey, and S. Gräser, Science **255**, 583 (1992).

[6] O. Pietzsch, A. Kubetzka, D. Haude, M. Bode, and R. Wiesendanger, Rev. Sci. Instr. **71**, 424 (2000).

[7] M. Bode, R. Pascal, and R. Wiesendanger, Surf. Sci. **344**, 185 (1995).

[8] J. Hauschild, U. Gradmann, and H.J. Elmers, Appl. Phys. Lett. **72**, 3211 (1998).

[9] H.J. Elmers, J. Hauschild, and U. Gradmann, Phys. Rev. B **59**, 3688 (1999).

[10] H. P. Oepen and J. Kirschner, Phys. Rev. Lett. **62**, 819 (1989).

[11] J.M. De Teresa, A. Barthélémy, A. Fert, J.P. Contour, R. Lyonnet, F. Montaigne, P. Seneor, and A. Vaurés, Phys. Rev. Lett. **82**, 4288 (1999).

[12] P. Bruno, Phys. Rev. Lett. **83**, 2425 (1999).

[13] H. Bethge, D. Heuer, Ch. Jensen, K. Reshöft, and U. Köhler, Surf. Sci. **331–333**, 878 (1995).

[14] M. Bode, R. Pascal, M. Dreyer, and R. Wiesendanger, Phys. Rev. B **54**, 8385 (1996).

[15] G. André, A. Aspelmeier, B. Schulz, M. Farle, and K. Baberschke, Surf. Sci. **326**, 275 (1995).

[16] H.J. Elmers and U. Gradmann, Appl. Phys. A **51**, 255 (1990).

[17] O. Pietzsch, A. Kubetzka, M. Bode, R. Wiesendanger, Phys. Rev. Lett. **84**, 5212 (2000).

[18] A. Hubert, R. Schäfer, Magnetic Domains, Springer, 1998.

[19] J. Tersoff and D. R. Hamann, Phys. Rev. B **31**, 805 (1985).

[20] L. Nordström and D.J. Singh, Phys. Rev. Lett. **76**, 4420 (1996).

[21] J.C. Slonczewski, J. Magn. Magn. Mater. **195**, L261 (1999).

[22] W. Weber *et al.*, New Journ. Phys. **1**, 9.1 (1999).

[23] T. Oda, A. Pasquarello, and R. Car, Phys. Rev. Lett. **80**, 3622 (1998).

[24] N. Weber, K. Wagner, H. J. Elmers, J. Hauschild, U. Gradmann, Phys. Rev. B **55**, 14121 (1997).

[25] H. J. Elmers; J. Magn. Magn. Mater. **185**, 274 (1998).

[26] C.L. Fu and A.J. Freeman, Phys. Rev. B **33**, 1755 (1986).

[27] S. Blügel, D. Pescia, and P.H. Dederichs, Phys. Rev. B **39**, 1392 (1989).

[28] P. Bödecker *et al.*, Phys. Rev. Lett. **81**, 914 (1998).

[29] E.J. Escorcia-Aparicio *et al.*, Phys. Rev. Lett. **81**, 2144 (1998).

[30] H. Zabel, J. Phys.: Cond. Matter **11**, 9303 (1999).

[31] J.A. Stroscio, D. T. Pierce, A. Davies, R. J. Celotta, and M. Weinert, Phys. Rev. Lett. **75**, 2960 (1995).

[32] M. Kleiber, M. Bode, R. Ravlić, and R. Wiesendanger, Phys. Rev. Lett. **85**, 4606 (2000).

[33] M. Bode, M. Getzlaff, and R. Wiesendanger, J. Vac. Sci. Techn. A **17**, 2228 (1999).

[34] K.P. Kämper *et al.*, Phys. Rev. Lett. **59**, 2788 (1987).

[35] S. Blügel, M. Weinert, and P. H. Dederichs, Phys. Rev. Lett. **60**, 1077 (1988).

[36] S. Blügel and P. H. Dederichs, Europhys. Lett. **9**, 597 (1989).

[37] C. Krembel, M. C. Hanf, J. C. Peruchetti, D. Bolmont, and G. Gewinner, J. Magn. Magn. Mat. **93**, 529 (1991).

[38] J. E. Ortega and F. J. Himpsel, Phys. Rev. B **47**, 16441 (1993).

[39] P. Schieffer, C. Krembel, M.-C. Hanf, M.-H. Tuilier, P. Wetzel, G. Gewinner, and K. Hricovini, Eur. Phys. J. B **8**, 165 (1999).

[40] P. Schieffer, C. Krembel, M.-C. Hanf, G. Gewinner, and Y. Gauthier, Phys. Rev. B **62**, 2944 (2000).

[41] M. Eder, J. Hafner, and E. G. Moroni, Phys. Rev. B **61**, 11492 (2000).

[42] A. Rabe, N. Memmel, A. Steltenpohl, and Th. Fauster, Phys. Rev. Lett. **73**, 2728 (1994).

[43] R. Pfandzelter, T. Igel, and H. Winter, Surf. Sci. **389**, 317 (1997); further references therein.

[44] D. Tian, S.C. Wu, F. Jona, and P. M. Marcus, Sol. State Commun. **70**, 199 (1989).

[45] S. Heinze, M. Bode, A. Kubetzka, O. Pietzsch, X. Nie, S. Blügel, and R. Wiesendanger, Science **288**, 1805 (2000).

[46] D. Wortmann, S. Heinze, Ph. Kurz, G. Bihlmayer, and S. Blügel, Phys. Rev. Lett. **86** , 4132 (2001).

3.2.4 Magnetic Alloy Formation

M. Getzlaff, R. Pascal, H. Tödter, M. Bode

Introduction

Alloys of 3d transition metals with 4f rare earth metals, as e.g. FeGd and FeTb, are of intense technological interest because they exhibit outstanding magnetic properties. The Curie–temperature of alloys of Gd or Tb with Fe as well as their coercitivity can be tuned over a wide range by changing the mixing ratio [1]. This behavior, in combination with a strong magneto–optical effect, makes them of particular interest for magneto–optical storage. Furthermore crystalline alloys, especially $TbFe_2$, exhibit a strong magnetocrystalline anisotropy resulting in an easy magnetization direction being perpendicular to the film plane in thin film systems [2]. A perpendicular anisotropy is also present in the amorphous alloys [3]. Films with perpendicular magnetization direction allow on the one hand enhanced writing densities as well as on the other hand an increased signal–to–noise ratio. Another aspect of technological interest are magnetostrictive properties of 3d/4f–alloys. For such applications, the preparation of single crystalline thin films is of importance because a well defined orientation of the crystallographic directions is needed to make use of the magnetostrictive effect in small devices.

While the magnetic and magnetostrictive properties of the bulk material in dependence of the fabrication process are well understood, very little is known about thin film properties. Until now, only some attempts have been made to grow very thin crystalline films of 3d/4f–alloys. $TbFe_2$ [4] and YCo_2 [5] have been grown on sapphire with Mo(110) and W(110) buffer layers, respectively. In both cases twin formation occured. Oderno et al. recently succeeded in preparing $DyFe_2$, $TbFe_2$ and $Dy_{0.7}Tb_{0.3}Fe_2$ epitaxial thin films on sapphire with a Nb(110) buffer layer [6]. M. Huth et al. presented results on the preparation of well–ordered epitaxial films of $TbFe_2$ on sapphire substrates with a Mo(110) buffer layer [7]. On the other hand, most of the experiments on the magnetic thin film properties of the pure elements Fe, Gd and Tb have been carried out for films grown on W(110). The growth of these films from the submonolayer coverage range to thick films is well understood and forms the basis for understanding the magnetic properties. The experiments presented in the following turn the attention to the following questions:

- What does the initial state of 3d/4f–alloy formation on W(110) look like?
- Is it possible to grow epitaxial films of $GdFe_2$ on W(110) without additional buffer layers?
- What is the influence of the substrate on the growth behavior and what consequences on the crystallographic structure will result from this?

- Which crystallographic orientation will the film grow in?

Here we present a study on the epitaxial growth of very thin films of $GdFe_2$ on a W(110) single crystal carried out by LEED and STM / STS. We will show that the epitaxial growth of up to two monolayer (ML) thick films of $GdFe_2$ is possible on W(110). The crystallographic structure of the films with a thickness of up to two monolayers was found to be different from the $GdFe_2$ bulk structure (Laves phase C15). Based on our atomically resolved STM images and LEED data we propose a structure model for the ultra–thin $GdFe_2$ / W(110) films.

Experimental

The experiments were carried out in a two–chamber UHV–system with a base pressure below 1×10^{-10} torr. The rare earth metal Gd was evaporated from a W crucible heated by electron bombardment. Fe was evaporated from a commercial e-beam evaporation source. The evaporators were repeatedly calibrated with submonolayer accuracy via STM by growing pure films of Gd or Fe. Consequently, we could ascertain the amount of evaporated metal by about ± 0.2 ML for the very thin films of $GdFe_2$. The exact amount was determined afterwards via STM. The W(110) single crystal substrate was prepared as described earlier [8]. During thin film evaporation the pressure did not exceed 5×10^{-10} torr. After preparation the samples were transferred into a separate analysis chamber with a base pressure below 1×10^{-11} torr. All topographic STM images were measured in the constant–current mode. The scanner was calibrated on the well known Gd/W(110) superstructures [9–11]. The ionic radii of Gd and Fe differ significantly from each other. The first ML of Fe on W(110) that grows pseudomorphically holds 1.56 times the number of adsorbate atoms compared with the first ML Gd/W(110). For this reason, the amount of evaporated material is given in substrate units to preserve the mixing ratio to be directly comparable. The first closed monolayer of Gd on W(110) holds 0.64 monolayers as measured in substrate units; the first closed monolayer of Fe on W(110) that grows pseudomorphically consequently holds 1 monolayer in substrate units.

Growth in the submonolayer regime

Both elements, Fe and Gd, exhibit Frank–van der Merwe or Stranski–Krastanov growth depending on the film thickness and annealing temperature in the coverage range above one monolayer [12–14]. The thin film growth behavior of the two metals in the coverage regime below one monolayer differs drastically from each other. This is demonstrated in Figure 3.26 where two samples of both metals in pure form, prepared under similar conditions, are presented. While Fe (Fig. 3.26a) exhibits the formation of one monolayer film patches as well as stripes of material growing along the substrate steps (step flow growth) [12, 13], the Gd atoms (Fig. 3.26b) tend to cover the W(110)–surface as quasi–one–dimensional superstructures [9, 10].

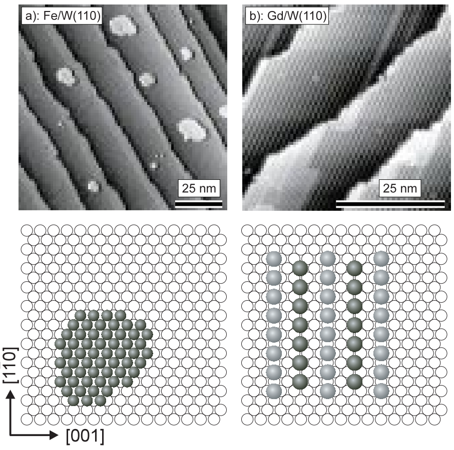

Figure 3.26: Comparison of the growth of Fe (a) and Gd (b) on W(110) in the submonolayer coverage regime. For both metals the coverage is about 0.25 ML. The scan–range for both images is 70 nm × 70 nm. Below the STM–images structure models are shown to highlight the difference in the growth mode.

The reason for this behavior of the Gd–atoms is a strong difference in electron affinity between the W(110)–substrate and the electropositive Gd–atoms triggering a charge–transfer from the Gd–atoms to the substrate. The resulting dipole–moment of the individual atoms induces a repulsive dipole–dipole interaction within the layer giving rise to the formation of evenly spaced chainlike superstructures. The distance between the chains decreases in discrete steps with increasing coverage. These chain–like superstructures coincide with the appearance of $(n \times 2)$ LEED–patterns $(n = 10, 8, 7, 6, 5)$. The sample presented in Fig. 3.26b mainly shows the (8×2) superstructure. If the periodicity exceeds 15 Å, a stable imaging of the Gd chains is not possible. This is in agreement with previous results obtained via low energy electron diffraction showing that no stable superstructures with periodicities larger than for the (10×2) could be observed [10]. At a coverage corresponding to $\Theta \approx 0.35$ monolayers a closed, pseudohexagonal c(5×3) structure is formed. Additional coverage results in the first closed monolayer of Gd on W(110). It represents a coverage of $\Theta \approx 0.64$ monolayers; its nearly hexagonal symmetry reflects the symmetry of the Gd(0001) lattice.

Given these two elements, Gd and Fe, differing drastically from each other in their thin film growth behavior on W(110), the question arises which growth mode an alloy of the two components will show and which stoichiometry is the most stable one on top of the W(110) surface. Figure 3.27 shows a topographic STM image of an alloy of 0.3 ML Gd and 0.4 ML Fe. The sample was prepared by evaporating 0.3 ML Gd onto the substrate held at 400 K and subsequently by an additional evaporation of 0.4 ML Fe. Post–annealing was performed at 700 K for 5 minutes. The substrate is covered by a film consisting of two different kind of domains, a striped one with the stripes running along the [1$\bar{1}$0] direction of the substrate being typical for Gd, as well as a smooth one. This sample exhibited a LEED-pattern labeled as $\binom{2\,1}{1\,2}$ not known from pure Gd or Fe films. In view of the mixing ratio and the assumption that the striped areas consist mainly of Gd, the smooth areas are expected to consist of an alloy with a mixing ratio of Gd to Fe to be 1:2. To strengthen this hypothesis, a sample was prepared that holds 0.3 ML of Gd and 0.6 ML of Fe. The preparation steps as well as

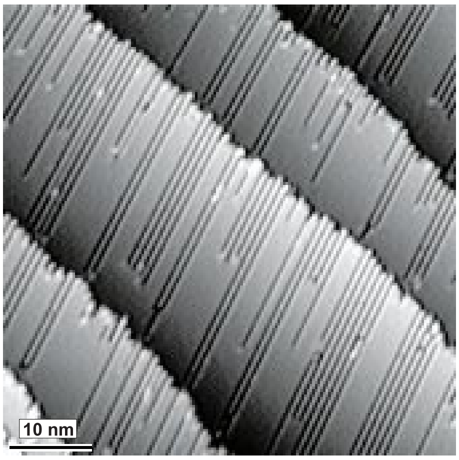

Figure 3.27: Constant current STM–image of an alloy of approximately 0.3 ML Gd and 0.4 ML Fe. The striped areas represent the well-known Gd superstructures with the stripes being aligned along the [001]–direction of the substrate. The smooth areas correspond to an alloy of $GdFe_2$. The scan–range is 70 nm × 70 nm. Sample bias: $U = 0.2$ V, tunneling current $I = 0.3$ nA.

the annealing procedure was the same as for the sample displayed in Figure 3.27.

Figure 3.28 a) shows the resulting sample topography. The substrate is completely covered by a smooth film with the underlying W(110) substrate steps visible. The LEED-pattern of this sample corresponds to a sharp $\binom{2\,1}{1\,2}$ superstructure. A photograph of the LEED–pattern as well as its interpretation is presented in the Figures 3.28 c) and d) respectively. The atomic distances as determined from the diffraction pattern is 9.48 Å in the [001] direction and 4.47 Å in the $[1\bar{1}0]$ direction of the substrate. The same periodicity as in the LEED pattern can be found in atomically resolved STM images of the first ML $GdFe_2$. Figure 3.28 b) shows a part of the sample presented in Figure 3.28 a) atomically resolved at 180 mV sample bias and 3 nA tunneling current.

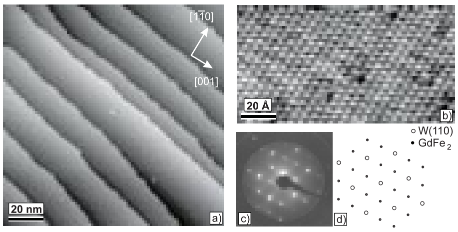

Figure 3.28: a): Completely closed and smooth first ML of $GdFe_2$ on W(110). b): Atomic resolution obtained on this sample at a sample bias of $U = 0.18$ V and a tunneling current of $I = 3$ nA. c): Photograph and d): sketch of the $\binom{2\,1}{1\,2}$ LEED-pattern of this sample. The crystallographic directions are the same for all figures.

Based on the LEED– and STM–data as well as on the stoichiometry of the prepared films we present a structure model for the alloy, as shown in Fig. 3.29. All atoms are drawn to scale of their metallic radii. In our model we have placed the Gd as well as the Fe atoms on bridge sites with respect to the underlying W(110). We assume this to be the energetically favorable adsorption site for both atomic species, since recent work could show this to be true for Fe on W(110) [15]. Comparing the structure model with the atomic scale STM images, it becomes clear that we do only see one atomic species of the alloy, the Gd atoms. The fact, that the Gd atoms are much larger than the Fe atoms may play a major role, but a definite statement concerning this point can only be given if LDOS calculations for this structure will become available.

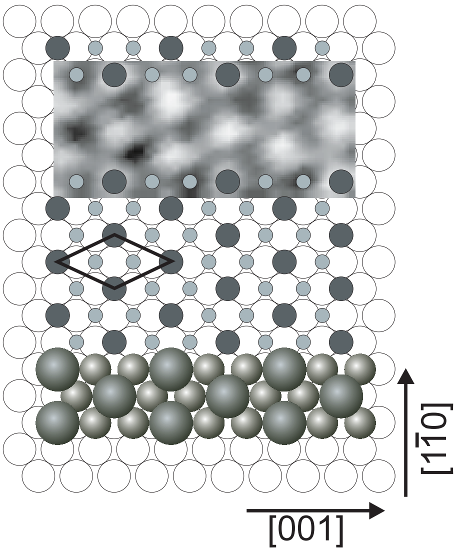

Figure 3.29: Structure model for the first ML $GdFe_2$ on W(110). Gd is represented as large, Fe as small balls. The atoms are scaled down by a factor of two for better clarity of the registry between substrate and adsorbate. In the lower part of the model the atoms are drawn to scale. A part of an atomically resolved STM image is inserted in the structure model at the same scale.

The preparation of samples consisting of less than one ML $GdFe_2$ results in a W(110) substrate partially covered by the first ML $GdFe_2$, as can be seen in Fig. 3.30. The substrate was held at room temperature during evaporation of 0.25 ML Gd.

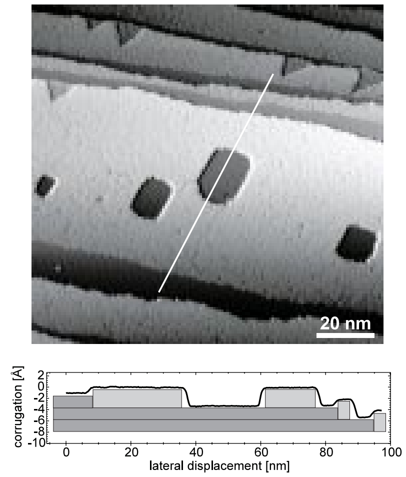

Figure 3.30: Approximately 0.75 ML $GdFe_2$ growing in step flow along the W(110) step edges. Rectangular holes in the film are oriented along the [001] and [1$\bar{1}$0]–directions of the substrate. From the line section indicated in the image the monoatomic step height is determined to be 3 Å from the top of the bare tungsten substrate to the top of the first ML $GdFe_2$. The scan–range is 135 nm × 135 nm, the tunneling parameters are $U = -0.24$ V, $I = 0.2$ nA.

After the additional evaporation of 0.5 ML Fe, the sample was post–annealed at 700K for 5 minutes. The one ML thick $GdFe_2$ film grows along the substrate steps (step flow growth). However, some rectangular holes in the film being oriented along the main crystallographic directions of the substrate remain. The line section indicates the monoatomic step height from the substrate to the top of the first ML of the alloy to be 3.0 Å as seen by STM in the constant current mode of operation.

Properties with increasing film thickness

The growth of the $GdFe_2$ structure could be continued to the second ML by evaporating approximately 0.5 ML of Gd and 1 ML Fe and subsequent annealing to 500K. The resulting sample topography is shown in Fig. 3.31. Again, the substrate is completely covered by a smooth alloy of Gd and Fe but additionally patches of the second ML $GdFe_2$ are present. A line section taken from this image is shown together with a sketch of the cross section of the sample.

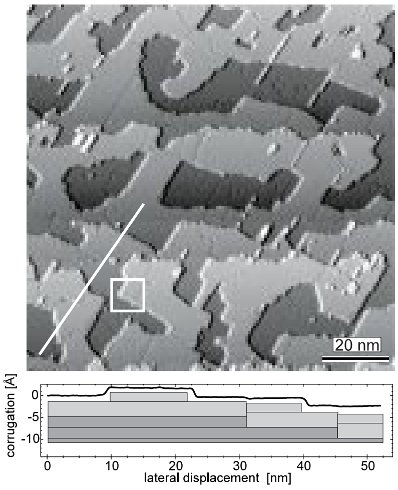

Figure 3.31: First and second ML $GdFe_2$ on W(110). In the area marked with a box we obtained atomic resolution. From the line section the monoatomic step height between the first and second layer of $GdFe_2$ can be determined to be only 1.9 Å.

Fig. 3.32 displays the tunneling spectroscopy measurements that were carried out on this sample. The given differential conductivity dI/dU is a direct measure of the local density of states (LDOS). Within the error of the measurement there is no difference between the first and the second ML $GdFe_2$. This observation reflects the identical geometric arrangement of the alloy in both layers (see below).

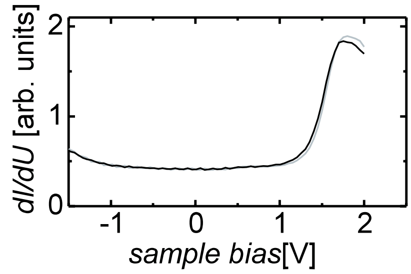

Figure 3.32: Differential conductivity dI/dU obtained on the first (grey) and second (black) ML $GdFe_2$ on W(110). The stabilization parameters are $U = 2$ V, $I = 0.5$ nA.

In the area marked by a frame in Fig. 3.31 we could achieve atomic resolution on top of the first as well as on the second monolayer simultaneously. These data are presented in Fig. 3.33a. The atomic structure of the first and the second ML looks similar. This is consistent with the observation of similar tunneling spectra. Using the atomically resolved images we are able to investigate the positions of the atoms of the second ML with respect to the atoms of the first ML by using a registration grid. Again we assume the maxima visible in the atomically resolved STM images to represent the Gd atoms. The resulting structure model (Fig. 3.33b) shows the Gd atoms of the second ML residing on top of the first ML Fe atoms. This atomic arrangement is also assumed to be the reason for the extraordinary small monoatomic step height of 1.9 Å between the first to the second ML $GdFe_2$ (see Fig. 3.31), being lower than the monoatomic step height of the W(110) substrate (2.24 Å).

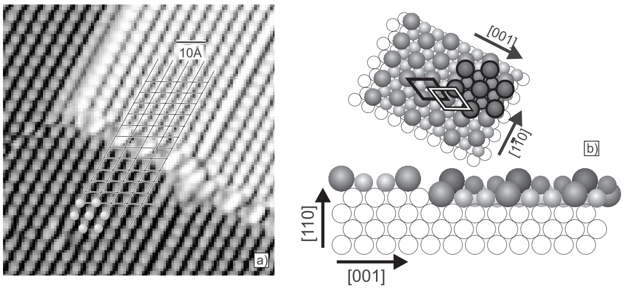

Figure 3.33: a) Atomic resolution on the first and second ML $GdFe_2$ on W(110) obtained at $U = 55$ mV and $I = 3$ nA. The grating and the balls are the result of a procedure to determine the registry between the atoms of the first and the second ML. b) Structure model in top– and in side view of the first and second ML $GdFe_2$ on W(110) deduced from the atomically resolved STM images.

In the next step our structure model for ultra–thin $GdFe_2$ films is compared with the known crystallographic structure of bulk $GdFe_2$, the so-called C15 Laves phase being a complicated arrangement of the two atomic species (for further details see, e.g., [16]). We could find no crystallographic direction with low indices of the Laves phase corresponding to the model we deduced as a result of our STM and LEED data. This is not surprising, because the first as well as the second ML grows pseudomorphically, i.e. the atomic arrangement in the alloy is mainly determined by the substrate, resulting in a relatively large deviation of the atomic positions when comparing the deposited film and the bulk Laves phase. The geometric arrangement of the Gd–atoms in the $GdFe_2$ films of up to two ML thickness appears to resemble the (111) plane of the C15 Laves phase, compressed by 14 % in the [1$\bar{1}$0]–direction of the W(110) substrate and strained by 5.3 % in the [001] direction. However, the arrangement of the Fe–atoms with respect of the Gd–atoms is completely different from the bulk structure. Assuming a release of this deviation with growing film thickness it can be expected that the C15 Laves phase develops at larger film thickness of $GdFe_2$ on W(110) as deduced for $TbFe_2$ on Mo(110) [7]. This would imply the existence of a structural phase transition in the $GdFe_2$ system being the subject of current investigations.

In summary, we have presented an atomic scale study of the very early stages of $GdFe_2$ alloy formation on W(110). The first ML $GdFe_2$ grows in a step flow growth mode on top of the W(110) substrate. We were able to prepare and atomically resolve the second ML as well. A structure model based on LEED and atomically resolved STM data was developed for the first and second ML of $GdFe_2$. Tunneling spectroscopy measurements showed no difference between the first and the second ML of $GdFe_2$.

The atomic structure of the ultra–thin films was found to be different from the bulk structure of the $GdFe_2$ (C15 Laves phase).

References

[1] J. C. Suits, R. D. Rugar, and C. J. Lin; J. Appl. Phys. **64**, 252 (1988).

[2] T. Morishita, Y. Togami, and K. Tsushima; J. Phys. Soc. Jpn. **54**, 37 (1985).

[3] F. Hellman, A. L. Shapiro, E. N. Abarra, R. A. Robinson, R. P. Hjelm, P. A. Seeger, J. J. Rhyne, and J. I. Suzuki; Phys. Rev. B **59**, 11408 (1999).

[4] C.T. Wang, R.M. Osgood, R.L.White, and B.M. Clemens, MRS Spring Meeting Proc., San Francisco, CA, 1995

[5] F. Robaut, P. Milkulik, N. Cherief, O.F.K. McGrath, D. Givord, T. Baumbach, and J.Y. Veuillen *J. Appl. Phys.* **78**, 997 (1995)

[6] V. Oderno, C. Dufour, K. Dumesnil, Ph. Mangin, and G. Marchal, *J. Cryst. Growth* **165**, 175 (1996)

[7] M. Huth and C. P. Flynn; Phys. Rev. B **58**, 11526 (1998).

[8] M. Bode, R. Pascal, and R. Wiesendanger; Surf. Sci. **344**, 185 (1995).

[9] R. Pascal, Ch. Zarnitz, M. Bode, and R. Wiesendanger; Phys. Rev. B **56**, 3636 (1997).

[10] J. Kolaczkiewicz, and E. Bauer; *Surf. Sci.* **175**, 487 (1986)

[11] R. Pascal, Ch. Zarnitz, M. Bode, and R. Wiesendanger; Surf. Sci. **385**, L990 (1997).

[12] H. Bethge, D. Heuer, Ch. Jensen, K. Reshöft, and U. Köhler; Surf. Sci. **331–333**, 878 (1995).

[13] M. Bode, R. Pascal, M. Dreyer, and R. Wiesendanger; Phys. Rev. B **54**, R8385 (1996).

[14] D. Weller and S. F. Alverado; J. Appl. Phys. **59**, 2908 (1986).

[15] E.D. Tober, R.X. Ynzunza, C. Westphal, and C.S. Fadley; *Phys. Rev. B* **53**, 5444 (1996)

[16] *Handbook of the Physics and Chemistry of Rare Earths*, Vol. 2, eds. K.A. Gschneidner Jr. and L. Eyring (North Holland, Amsterdam)

3.3 Nanochemistry

M. Getzlaff, R. Pascal, M. Bode

The *bare* surfaces of rare earth metal systems were described above with respect to their structural and electronic behavior. As already mentioned occasionally in the previous Chapter, adsorbates from the residual gas alter the electronic properties of the clean surfaces due to the hybridization of adatom and substrate states (for example, the Gd surface state can only exist if the surface is atomically clean). The strong influence of adatoms on the surface due to this chemisorption process does not only induce variations in the electronic properties – this will be discussed for hydrogen and oxygen being adsorbed on Gd(0001), respectively – but may also lead to distinct structural changes (e.g., surface reconstructions) which will be exemplarily shown for hydrogen being dissolved in gadolinium films. Using the distinct surface sensitivity of scanning tunneling microscopy and photoelectron spectroscopy it will be shown by describing the coadsorption of hydrogen and CO on gadolinium surfaces that the combination of both techniques allows a detailed analysis of processes in surface chemistry at the nanometer scale.

3.3.1 Unusual adsorption characteristics for hydrogen on Gd surfaces

In this part the electronic properties of chemisorbed hydrogen on Gd(0001) will be discussed. For the photoemission investigation, smooth Gd(0001) films were prepared and subsequently exposed to hydrogen. It was already shown that the Gd surface state exists both on smooth films and multilayer Gd islands. Therefore, multilayer island films were chosen for the STM investigations to provide topographical contrast in order to distinguish between sample states and tip induced artifacts as well as to determine the influence of different island heights.

"Direct" observation of the hydrogen induced state

The determination of the differential cross section plays an important role describing the photoemission process. For a fixed spatial arrangement the angular distribution of photoelectrons can be deduced if the dipole matrix elements and the phase shifts of the outgoing photoelectron wave are known. One example for the determination of these values is the Circular Dichroism in the Angular Distribution of photoelectrons (CDAD) [1]. Using this experimental technique the photoelectron intensity as a function of detection angle is compared for excitation with left and right circularly polarized light, respectively. The important parameters describing the intensity difference are the dipole matrix elements and the relative phase shifts.

This type of investigation is usually carried out with a *fixed polarization* of the incoming light and a variation of the emission angle. A disadvantage of this experimental arrangement is given by the limited range of the detection angle being further reduced due to the refraction of the escaping photoelectrons at the electrostatic surface barrier being explained on p. 61. Measurements at a *fixed detection angle* with a rotating electrical field vector enables to avoid this restriction due to the possibility of using the whole angle range of 180° giving a significantly more accurate set of data.

Additionally, information on quantum mechanical quantities are usually obtained with a large experimental or theoretical effort. In contrast, the theoretical description of the latter type of angle resolving photoemission experiments as well as the experimental procedure are relatively simple because this method is suitable to be carried out in a laboratory; it does *not* need a sophisticated experimental setup as synchrotron radiation sources. It may therefore play an important role for a proceeding understanding of the photoemission process.

In the following we will report on an "elegant" method to provide information about the dipole matrix elements and phase shifts being essential for the theoretical description of the photoemission process in a relatively simple way and with a pronounced accuracy [2]. This can be achieved by means of photoelectron spectroscopy with linearly polarized light using the ability of a *continuous rotation of the electric field vector*. The method is exemplarily demonstrated at the system hydrogen on Gd(0001)/W(110) which possesses a pronounced d_{z^2}-like adsorbate induced state.

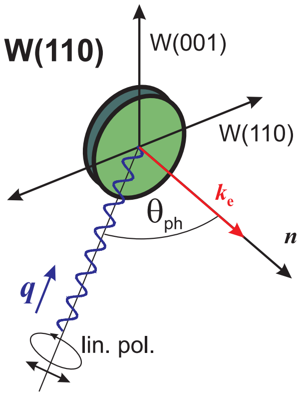

Figure 3.34: Schematic view of the experimental setup. The $\vec{E}$ vector of the incoming linearly polarized radiation can be rotated as indicated by the circle.

Photoelectrons were gained by linearly polarized VUV radiation from a discharge lamp (Ne I resonance line: $h\nu$=16.85eV) with a triple reflection polarizer. The angle of the incoming photon beam was $\theta_{ph} = 45°$ with respect to the surface normal. The experimental setup is shown schematically in Fig. 3.34.

Photoelectron spectra from the clean Gd(0001) surface and after hydrogen exposures are presented in Fig. 3.35. The spectra were taken in normal emission and at room temperature. The sharp feature near the Fermi edge is due to the Gd surface state and is only observed on contamination-free high-quality hcp(0001) surfaces. After hydrogen exposure a pronounced feature at a binding energy of about 4eV appears. The energy width (FWHM) = 0.4eV of this hydrogen induced state is similar

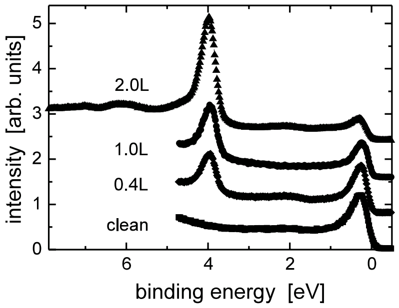

Figure 3.35: Photoemission spectra at normal emission for different hydrogen exposures on Gd(0001)/W(110). The photon energy is 16.85eV.

to that of the surface state. The weak feature at about 2eV is caused by Gd Δ_2 bulk bands [3]. Dosing additional hydrogen suppresses the Gd surface state as previously demonstrated by Li et al. [4].

In Fig. 3.36 photoelectron spectra of the H induced state are presented for different angles α of the $\vec{E}$ field vector of the incoming linearly polarized photon beam with respect to the plane of incidence. $\alpha = 90°$ denotes the case for s-polarized light, and it is this angle where the intensity of the H induced state nearly vanishes whereas the intensity is significantly enhanced for more p-polarized light.

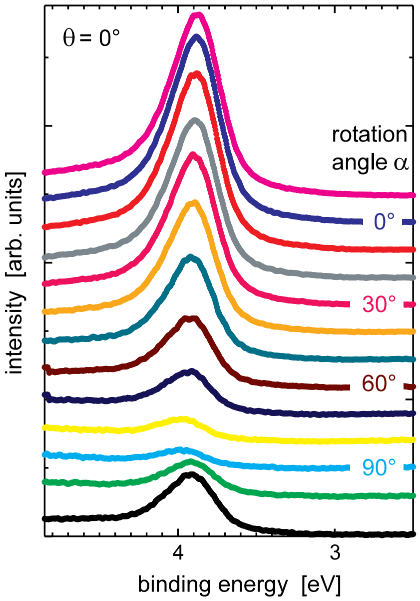

Figure 3.36: Photoelectron spectra at $\theta = 0°$ (normal emission) for the hydrogen induced structure as a function of the rotation angle α of the linear polarizer

The photoelectron intensity I (with the detector being at infinity) for atomic orbitals which are excited by a linearly polarized radiation source can be calculated via the differential cross section $d\sigma/d\Omega$ [5]:

$$I = \frac{d\sigma}{d\Omega} = \frac{4\pi}{3}\alpha a_0^2 h\nu \left| \left\langle \phi_{E_{kin},\vec{k}} \mid \vec{\epsilon}\cdot\vec{r} \mid \phi_{n\ell x} \right\rangle \right|^2 \tag{3.4}$$

where α is the fine structure constant, a_0 the Bohr radius, $\vec{k}$ the direction of the outgoing electron, $\vec{\epsilon}$ the polarization vector, and $\vec{r}$ the position vector at angles θ, ϕ. The initial real atomic orbital is given by

$$\phi_{n\ell x} = R_{n\ell}(r) \sum_m n(m) Y_{\ell m}(\theta, \phi) \tag{3.5}$$

where $Y_{\ell m}(\theta, \phi)$ is a spherical harmonic and $n(m)$ are the coefficients needed to form real orbitals such that ℓx is s, p_z, etc. The final state is written [6] as a partial wave expansion

$$\phi_{E_{kin},\vec{k}} = 4\pi \sum_{\ell' m'} i^{\ell'} e^{-i\delta_{\ell'}} Y^*_{\ell',m'}(\theta_k, \phi_k) Y_{\ell',m'}(\theta, \phi) R_{E_{kin},\ell'} \tag{3.6}$$

Using these Eqs. 3.4 - 3.6 and dipole selection rules $\Delta\ell = \pm 1$ and $\Delta m = \pm 1, 0$ the dipole matrix element can be written as

$$\begin{aligned} \left\langle \phi_{E_{kin},\vec{k}} \mid \vec{\epsilon} \cdot \vec{r} \mid \phi_{n\ell x} \right\rangle &= \sqrt{8}\pi \sum_{\ell' m} n(m) (-i)^{\ell'} e^{i\delta_{\ell'}} \\ &\times R_{\ell'}(E_{kin}) (\epsilon_x [-Y_{\ell',m+1}(\theta_k, \phi_k) C^1(\ell', m+1, \ell, m) \\ &+ Y_{\ell',m-1}(\theta_k, \phi_k) C^1(\ell', m-1, \ell, m)] \\ &+ i\epsilon_y [Y_{\ell',m+1}(\theta_k, \phi_k) C^1(\ell', m+1, \ell, m) \\ &+ Y_{\ell',m-1}(\theta_k, \phi_k) C^1(\ell', m-1, \ell, m)] \\ &+ \sqrt{2}\epsilon_z Y_{\ell',m}(\theta_k, \phi_k) C^1(\ell', m, \ell, m)) \end{aligned} \tag{3.7}$$

where $C^1(\ell', m', \ell, m)$ are Gaunt coefficients [7].

The photoelectron intensity of the hydrogen induced state was determined (cf. Fig. 3.36) as a function of the vector potential of the incoming radiation and is shown in Fig. 3.37 (open circles). The electric field vector of the light was rotated

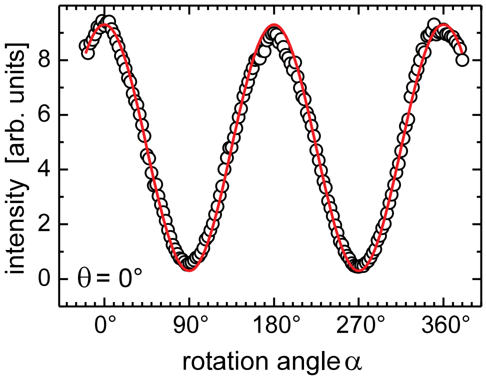

Figure 3.37: Photoemission intensities of the maximum for the hydrogen induced feature at about 4eV binding energy in dependence of the rotation angle α of the incoming linearly polarized radiation; the solid line represents a fit with $\cos^2$ function. The spectra were taken in normal emission.

by the angle α in the plane perpendicular to the direction of propagation. For $\alpha = 0°$, the light is highly p-polarized, whereas for $\alpha = 90°$ it is s-polarized (cf. Fig. 3.34). The intensity exhibits maxima at 0° and 180°, respectively. A d_{z^2}-like orbital symmetry of this state was previously deduced by Li et al. [4] from the observation that the constant initial state spectra were the same for both the hydrogen induced state and the Gd surface state. The dipole matrix element for such a d_{z^2} initial state can be calculated to be

$$\begin{aligned}\left\langle \phi_{E_{kin},\vec{k}} \mid \vec{\epsilon}\cdot\vec{r} \mid d_{z^2} \right\rangle &= \sqrt{8\pi}[e^{i\delta_p}R_p\left(\sqrt{1/10}\sin\theta(\epsilon_x\cos\phi+\epsilon_y\sin\phi)-\epsilon_z\sqrt{2/5}\cos\theta\right)\\ &\quad + e^{i\delta_f}R_f\sqrt{9/40}(\sin\theta(5\cos^2\theta-1)(\epsilon_x\cos\phi+\epsilon_y\sin\phi)\\ &\quad + \epsilon_z(5cos^3\theta-3\cos\theta))] \qquad (3.8)\end{aligned}$$

In normal emission ($\theta = 0$) this expression is determined by ϵ_z being proportional to $\cos\alpha$. The intensity using a rotating electric field vector is therefore $\propto \cos^2\alpha$ (s. Eq. 3.4). This behavior is demonstrated by the solid line in Fig. 4 presenting a fit with a $\cos^2$ function.

Dispersion effects of the parallel momentum component $k_{||}$ from the outgoing electron was investigated by rotating the sample with the radiation source and analyzer kept fixed in space. The photoelectron spectra for angles between $\theta = 0°$ and $60°$ are shown in Fig. 3.38. Whereas in normal emission the spectrum is dominated by the hydrogen induced structure at about 4eV binding energy, this feature looses intensity with increasing detection angle and shifts in energy pointing directly to a non-vanishing dispersion. For higher angles additional structures at 1eV and 5.5eV binding energy appear. Figure 3.39 shows the experimentally determined band dispersion along the $\bar{\Gamma}$ - $\bar{M}$ - direction in the Gd surface Brillouin zone. The highly localized Gd surface state near E_F exhibits nearly no dispersion. In contrast, the H induced states possess different binding energies when varying the photoelectron detection angle θ. The $k_{||}$ dispersion suggests an overlap of the hydrogen wave functions within the overlayer or

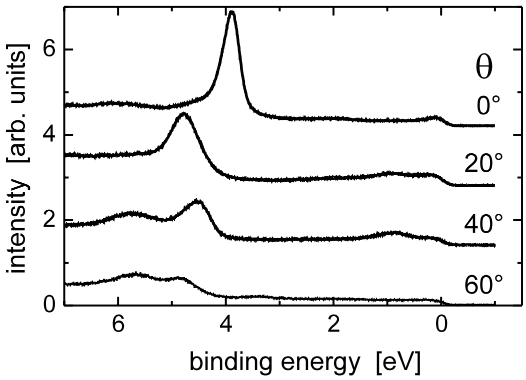

Figure 3.38: Photoelectron spectra for different detection angles θ. Variations in binding energy, pointing to a dispersion, as well as in intensity are present.

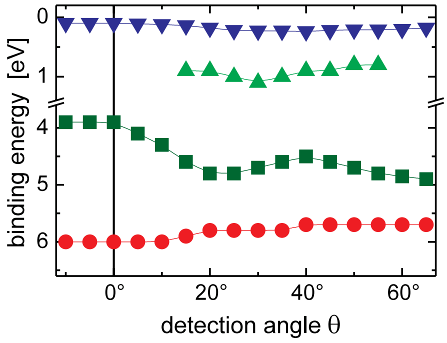

Figure 3.39: Two-dimensional band dispersion along the $\bar{\Gamma} - \bar{M}$ direction of the Gd surface Brillouin zone

hybridization with the Gd bulk bands. Since the electronic properties of this hydrogen induced state are different from those of the Gd surface state it is clearly not a surface state.

The dipole matrix element contains the radial parts R_p and R_f as well as phase shifts δ_p and δ_f (s. Eq. 3.8). In order to obtain information about these properties

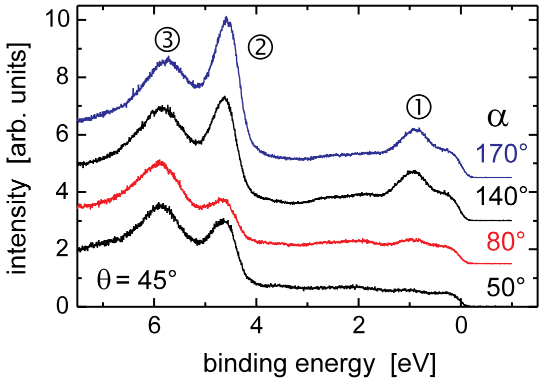

Figure 3.40: Photoemission intensities at a fixed detection angle $\theta = 45°$ for special values of the rotation angle α (see text)

the photoelectron intensities were determined at a fixed detection angle $\theta = 45°$ as a function of the rotation of the $\vec{E}$-field vector. The spectra in Fig. 3.40 are shown for special values of α at which the maximum and minimum intensities are reached for the peak 2 at 4.7eV (4.0eV in normal emission) with $\alpha = 170°$ and 80° as well as for the feature 1 at 1eV and structure 3 at 6eV with $\alpha = 140°$ and 50°, respectively. The intensity values are summarized in Fig. 3.41 (♦: Peak 1, ○: Peak 2, ■: Peak 3). The curves for peak 1 and 3 show the same shape which may be caused by emission from orbitals with the same symmetry but being different with respect to the d_{z^2}-like state (peak 2). Equation 3.7 can be expressed in terms of quantities $X_{\ell\pm1,x}$ [5] as follows:

$$\left\langle \phi_{E_{kin},\vec{k}} \mid \vec{\epsilon} \cdot \vec{r} \mid \phi_{n\ell x} \right\rangle = (-i)^{\ell-1} \left(e^{i\delta_{\ell-1}} X_{\ell-1,x} + e^{i\delta_{\ell+1}} X_{\ell+1,x} \right) \tag{3.9}$$

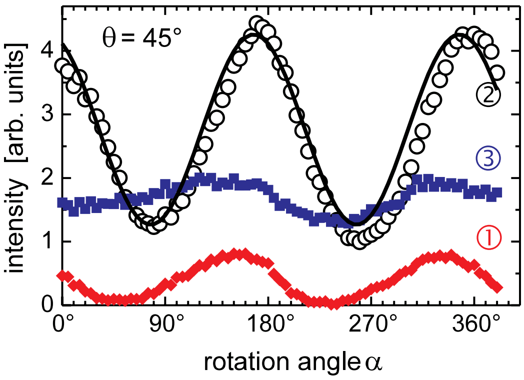

Figure 3.41: Photoemission intensities of the maximum for the three peaks labeled in Fig. 3.40. The shape of curves 1 and 3 is the same one but different to the one for curve 2. The solid line represents a fit as discussed in the text.

For this experimental geometry these X-functions are given by

$$\begin{aligned} X_{\ell-1,x} &= R\left(\sin\theta\,(\sin\alpha+\sqrt{1/2}\cos\alpha)-2\cos\theta\,(\sin\alpha-\sqrt{1/2}\cos\alpha)\right) && (3.10)\\ X_{\ell+1,x} &= 1.5\,\Big(\sin\theta\,(5\cos^2\theta-1)(\sin\alpha+\sqrt{1/2}\cos\alpha)\\ &\quad +\cos\theta\,(5\cos^2\theta-3)(\sin\alpha-\sqrt{1/2}\cos\alpha)\Big) && (3.11)\end{aligned}$$

using the simplification $R_f = 1$ and $R = R_p/R_f$. The photoelectron intensity can then be written as

$$I \propto X^2_{\ell+1,x} + X^2_{\ell-1,x} + 2X_{\ell+1,x}X_{\ell-1,x}\cos(\delta_{\ell+1}-\delta_{\ell-1}) \qquad (3.12)$$

However, the angle θ in these equations is not the detected one as can be seen by the following consideration.

In off-normal measurements ($\theta \neq 0$) the detection angle θ with the detector at infinity corresponds to a smaller one in or near the crystal. This effect is due to the refraction of an outgoing electron wave at the electrostatic surface barrier. When surmounting this barrier, the momentum parallel to the surface remains constant, the one perpendicular becomes reduced. This phenomenon results in an increased emission angle (with respect to the surface normal) outside the surface region. The inner, i.e. true, emission angle θ^{in} can be deduced from the outer, i.e. observed, angle $\theta^{out} = \theta$ using the relation [8, 9]

$$\sqrt{E_{kin}+V_0}\cdot\sin\theta^{in} = \sqrt{E_{kin}}\cdot\sin\theta^{out} \qquad (3.13)$$

where E_{kin} is the kinetic energy of the photoelectron and V_0 the inner potential being the difference in kinetic energy inside and outside the surface barrier. The binding energy of the hydrogen induced structure corresponds to a kinetic energy of about

10eV. Assuming a typical value for the inner potential of $V_0 = -10$eV the maximum value for the detection angle $\theta^{out} = 90°$ corresponds to an inner angle $\theta^{in} = 45°$; i.e. the "observable" angle range is limited to this value of 45°. The detection angle $\theta = 45°$ (cf. Fig. 3.40) therefore corresponds to an inner angle $\theta^{in} = 30°$ which must be used in Eqs. 3.10 and 3.11. A least–squares fit for the d_{z^2}-like hydrogen induced structure (curve 2 in Fig. 3.41) results in $R = 2.4 \pm 0.3$ and $\delta_f - \delta_p = 310° \pm 10°$. In order to verify these values the intensity of the same feature was determined as a function of the detection angle (cf. Fig. 3.38). These values are presented in Fig. 3.42. Calculating the X-function for this experimental geometry and inserting $R = 2.4$ and $\delta_f - \delta_p = 310°$ into the equation results in the function which is shown as a solid line in Fig. 3.42. There is good agreement within the experimental error corroborating the findings for the ratio of the radial matrix elements and the relative phase shift. It should be mentioned that these considerations are carried out within a pure atomic model being an approximate description although this d_{z^2}–like hydrogen state is largely atomic–like.

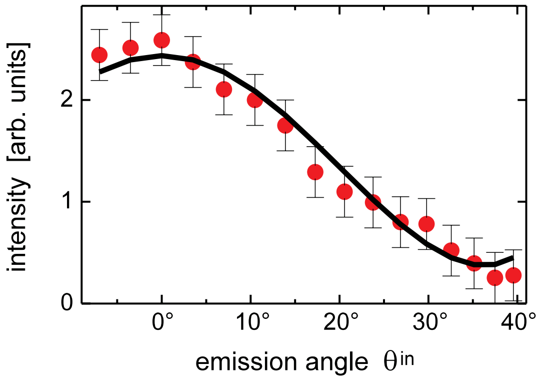

Figure 3.42: Photoemission intensities as a function of the detection angle θ. The angle scale is given by the emission angle θ^{in} inside the surface barrier which can be deduced from the detection angle taking into account the inner potential (s. Eq. 3.13).

Spatially resolved structural and electronic properties

As shown in the photoelectron spectra (s. Fig. 3.35), the hydrogen induced state has a binding energy of about 4eV and is therefore nearly unaccessible to STM investigations. It is nevertheless possible to resolve the spatial distribution of hydrogen since the suppression of the Gd surface state leads to a drastic reduction of the differential conductivity at low bias voltages.

This behavior is illustrated in Fig. 3.43 which shows the tunneling dI/dU spectra measured on Gd(0001) island surfaces (solid curve), on the first Gd monolayer between the islands (dash-dotted line), and on areas which have been modified by hydrogen adsorption (dashed line). The suppression of the gadolinium surface state is obvious. The strong decrease in the differential conductivity which is basically proportional to

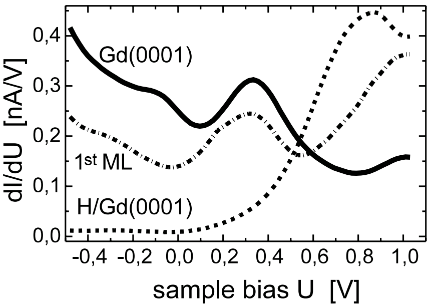

Figure 3.43: Tunneling dI/dU spectra (stabilization parameters: $U = 1.0\text{V}$, $I = 0.3\text{nA}$) measured on Gd island surfaces (solid), on the first Gd monolayer between the islands (dash-dotted), and on areas which have been affected by hydrogen adsorption (dashed).

the local density of states (LDOS) at the surface demonstrates the strong geometric localization of the surface state; bulk states do not show such pronounced differences. The tunneling spectra reveal that for the Gd monolayer only one peak at about 0.3V is present (s. Fig. 3.43) which cannot be attributed to the surface state. This can be deduced from the observation that no changes in the tunneling spectra occur after hydrogen adsorption; a surface state, in contrast, is very sensitive to adsorbates (cf. Fig. 3.35). Additionally, the determination of the energies of both spin counterparts from the surface state as a function of temperature shows a shift towards the Fermi level; the feature of the monolayer, however, remains fixed in energy [10]. Hydrogen adsorption does not significantly modify the electronic structure of the monolayer.

In Fig. 3.44(a) and (b), constant-current topographs of Gd islands on W(110) after different hydrogen exposures are shown. Between the high Gd islands which exhibit a (0001) surface, a Gd monolayer covers the tungsten substrate. In addition, two and three monolayer high islands are visible. The steps of the tungsten substrate even remain visible on the high Gd islands. The lines arise from lattice dislocations through the whole island due to different lattice constants in perpendicular direction.

Fig. 3.44(a) shows this system after an exposure of 0.2L hydrogen. The gadolinium monolayer and the low islands remain nearly unaffected. The monolayer of Gd on W(110) possesses a strained hcp structure with a dilatation of about 8% [11]. Two different kinds of behavior can be observed on top of the high islands. Some of them show a smooth surface which is undisturbed by hydrogen. Others present a lagoon–like appearance of alterations. In the regions with a "collapsed" appearance the Gadolinium surface state is suppressed whereas in the unaltered regions it still exists. Due to the reduction in the differential conductivity of the hydrogen covered areas the tip has to move towards the surface in order to maintain a constant current. Therefore, the change in appearance is not a topographical effect but mainly caused by the modification in the electronic structure, the suppression of the Gd surface state.

The special behavior of the adsorption process may be understood by examining the areas which are labeled A, B, and C. In region A there are lattice dislocations even for the clean Gd surface which are marked by arrows (more easily to be seen

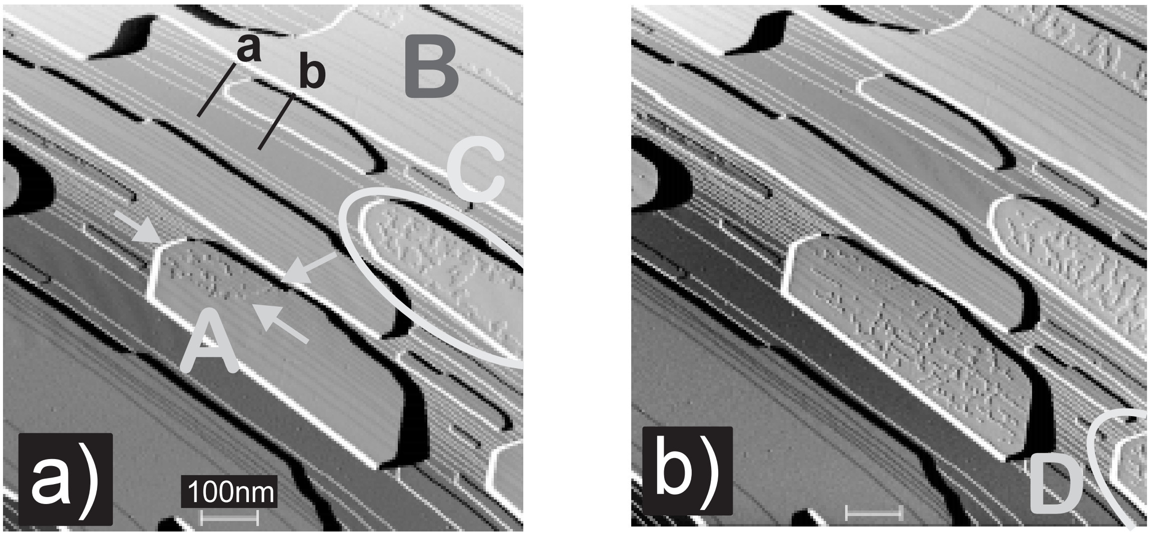

Figure 3.44: Constant-current topograph ($U = -0.3$V, $I = 0.03$nA) of Gd islands on W(110). Between high Gd islands with a (0001) surface, a Gd monolayer covers the tungsten substrate. Additionally, two and three monolayer high islands are visible. **(a)** To this system, 0.2L hydrogen was dosed. **(b)** The same area as in (a) but with an additional dosage of 0.8L resulting in a total amount of 1.0L hydrogen.

in Fig. 3.46 marked by the ellipse). These are the starting points for the adsorption process. In region B it can be observed that the spreading of the adsorption is strongly suppressed at step edges due to surface steps on the tungsten substrate. The further evolution of this process is demonstrated in region C. Once the adsorption of hydrogen has started the suppression of the surface state then extends over the whole area. This behavior is also shown in Fig. 3.44(b). It is the same area as in Fig. 3.44(a) but with an additional exposure of 0.8L resulting in a total amount of 1.0L hydrogen. The areas which were already affected after 0.2L have spread out. Additionally, the adsorption occured on another island (region D).

For comparison with results obtained by photoelectron spectroscopy one should keep in mind that the photoemission experiment averages over these regions; so both the peak of the Gd surface state and the hydrogen induced feature are coexistent as observed in the spectra in Fig. 3.35.

The adsorption of hydrogen seems to occur in two steps. Hydrogen is first adsorbed at surface imperfections and secondly, starting from these points, the adsorption spreads out to the step edges which form boundaries for the further process [12–14].

The steps of the tungsten substrate are even visible on-top of the Gd islands. This observation is caused by the different separations of the W(110) and Gd(0001) layers being 2.23Å and 2.89Å, respectively. Between the islands, the whole substrate is covered with a Gd monolayer; therefore, the step height of the monolayer is the same one as for W(110) as shown by the dotted line section in Fig. 3.45 which corresponds to line "a" in Fig. 3.44(a). The solid line section (cf. line "b" in Fig. 3.44(a)) demonstrates

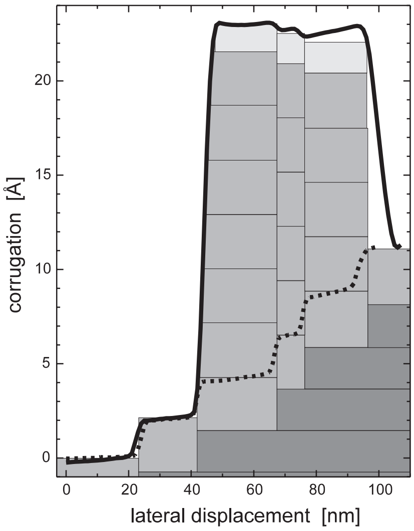

Figure 3.45: Line section (see lines "a" and "b" in Fig. 3.44(a)) of a Gd island (solid line) and the Gd monolayer on-top of the tungsten substrate (dotted line). Tungsten is marked by dark gray, Gadolinium by gray, and the "electronic height" due to the surface state by light gray shaded areas. In order to minimize the surface energy the Gd island tries to create a flat surface resulting in an inverted step height behavior on-top of the island.

the inverted step height behavior on-top of the Gd island, i.e. the tungsten terrace being one atomic layer *higher* appears *lower* on the island surface. An analogous observation was made for Gd/W(100) [15]. The surface of the island tries to be atomically flat in order to reduce its surface energy. Therefore, the height decreases from the left to the right from 7 to 5 layers. To the "topographic" height (see gray shaded area) the "electronic" height of the surface state (see light gray shaded areas) must be added. This is due to the large fade-out length into the vacuum of the d_{z^2}-like surface state accompanied by a relatively high local density of states above the surface. In the STM experiment operating in the constant-current mode the tip has therefore to be moved upwards. The tungsten substrate is marked by dark gray shaded areas.

The same area as in Fig. 3.44 is shown in Fig. 3.46. At the beginning of the scan

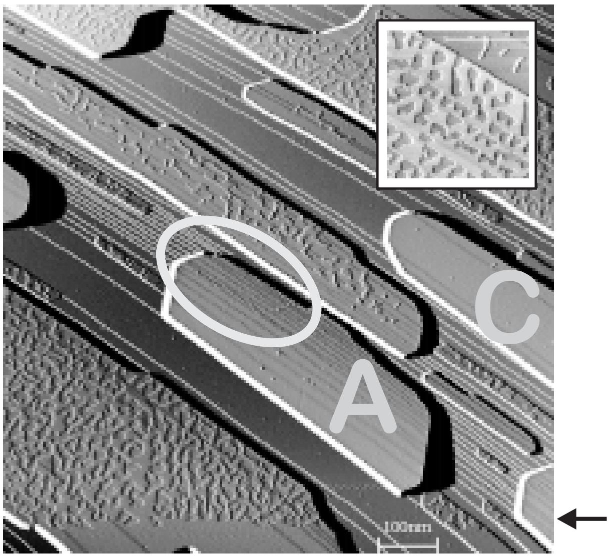

Figure 3.46: The same area as in Fig. 3.44. At the beginning of the scan (bottom), the dosage was 1.6L. During the scan, 1L of hydrogen was additionally offered (marked by the black arrow). Now, unconnected areas are present (see inset).

(bottom), the total exposure so far was 1.6L dosed during the past one hour. During the scan, the sample was exposed within a few seconds to an additional amount of 1L (marked by the black arrow). Now, the islands containing regions A and C present a suppressed surface state on top of the whole island. The lattice dislocation already present in the clean Gd island is marked by an ellipse. The large island in the lower left corner shows a domain–like modification due to the additional hydrogen exposure. After the additional exposure the whole island exhibits a suppression of the surface state. The exposure time for the additional 1L of hydrogen was substantially shorter than the previous time for 1.6L. This observation indicates that the adsorption process changes with the dosage.

In order to determine the collision rate, one can estimate the flux, i.e. the total number of collisions per unit surface area, by $p/\sqrt{2\pi m k_B T}$ [16] where p is the pressure, m the mass of a molecule, and T the temperature. Considering the ion gauge correction factor the collision rate at room temperature for 1L is about 30 hydrogen molecules per nm^2. On the clean surface the presence of two or more hydrogen molecules *simultaneously* seems to be necessary to cause adsorption. This conclusion is corroborated by the observation that prior to the supplementary exposure of 1L the hydrogen covered areas are connected but afterwards the additionally created regions are mainly isolated from each other (see inset). This means that on areas of the surface being clean and of high crystallographic order the adsorption of hydrogen cannot be carried out via a spreading process but only by a simultaneous presence of at least two hydrogen atoms at one time. On the Gadolinium monolayer no alterations can be observed. Significant modifications take place on the lower islands as will be shown below.

Figure 3.47(a) shows the topography of approximately 5 ML Gd evaporated on the W(110) substrate held at 530 K. Since the Gd islands are atomically flat and the substrate exhibits several one–atomic high steps below the island surface, the local coverage Θ_{loc} decreases for every island from the left towards the right edge. Simultaneously with the topography, the dI/dU spectrum was measured at every pixel of the scan. Figures 3.47(b) and 3.47(c) show maps of the differential conductivity dI/dU for different sample bias: (b) $U = +0.7\mathrm{V}$ and (c) $U = -0.3\mathrm{V}$. The differential conductivity is gray-coded, i.e. the higher the local dI/dU signal the brighter a location appears. At a sample bias $U = +0.7\mathrm{V}$ the tunneling current is dominated by electrons which tunnel from the tip into unoccupied sample states with a binding energy of +0.7eV. A comparison with the topographic data of Fig. 3.47(a) reveals that at this particular binding energy the differential conductivity above the Gd monolayer is higher than above those parts of the islands which have not been affected by hydrogen. Beside few small bright pixels, the dI/dU signal measured above the Gd island is uniform and therefore independent of the local coverage. No contrast was found in the dI/dU maps on the Gd island at any sample bias (cf. Figs. 3.47(b) and (c)) in the voltage range under study ($-0.6\mathrm{V} \leq U \leq +0.9\mathrm{V}$). A high contrast occurs for the island B in the lower part of the image. The bias voltage of 0.7V was chosen due to the large

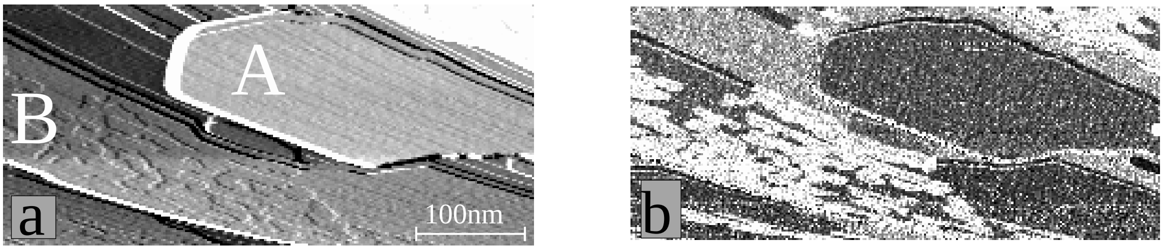

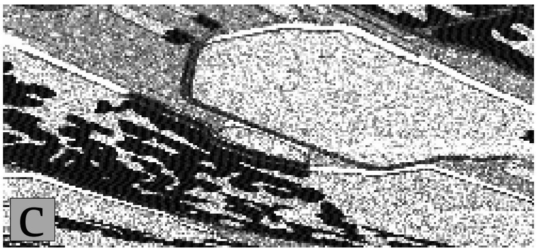

Figure 3.47: **(a)** Topography of a Gd island system being exposed to hydrogen. The clean Gd surface is marked by A, the hydrogen affected island by B. **(b,c)** Maps of the differential conductivity dI/dU for a bias voltage of $U = 0.7$V in (b) and $U = -0.3$V in (c) being gray coded. The bright areas in the lower part are caused by hydrogen covered areas (b) whereas they look dark for negative voltages (c). This behavior is obvious in connection with the dI/dU spectra in Fig. 3.43.

differential conductivity for hydrogen covered areas (cf. Fig. 3.43). The bright parts in Fig. 3.47(b) are therefore areas which have been affected by hydrogen. The dark appearance of the island A in the upper right part points to a clean surface. The tunneling spectra reveal (s. Fig. 3.43) that at a bias voltage of -0.3V the differential conductivity for hydrogen affected areas is significantly reduced. This inversion of the contrast is shown in Fig. 3.47(c) with black areas indicating adsorbed hydrogen.

The left part of Fig. 3.48 shows an enlarged image of a three monolayer high Gd island corresponding to the system presented in Fig. 3.46. Only those areas with hydrogen already adsorbed on exhibit small clusters. This observation is due to the onset of Gadolinium hydride being formed which will be discussed in Ch. 3.3.2. The line section (line "a") shows a uniform height of these clusters being about 4Å (middle). The suppression of the Gd surface state caused by hydrogen adsorption occuring as a collapsed region (labeled by B, the clean Gd surface is marked by A) is demonstrated by the line section in the right part of Fig. 3.48 (s. line "b"). The depth of this purely *electronically* induced suppression already discussed above amounts to 1.4Å. This value is smaller than for the suppression on high Gd islands. The Gd surface state is fully developed even for at least four monolayer high areas [17]. The island with a height of three atomic layers possesses a surface state with a reduced fade-out length into vacuum. The suppression due to hydrogen adsorption therefore seems to be smaller than for high Gd islands.

The question arises whether or not the former findings are specific for Gd islands, i.e. depend on the sample morphology, or are also characteristic for the element gadolinium. Therefore, hydrogen adsorption was additionally investigated for thick

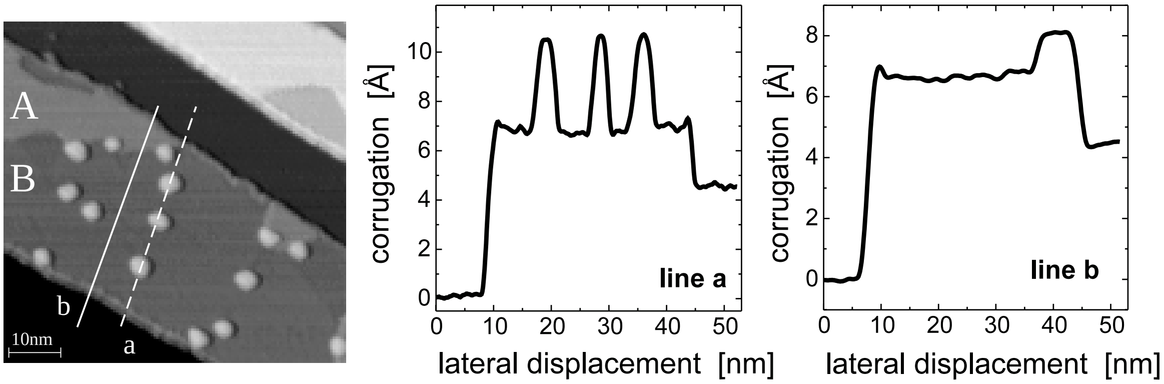

Figure 3.48: Left: Constant-current topograph ($U = -0.3$V, $I = 0.03$nA) for an enlarged image of a three monolayer high Gd island on W(110) after an hydrogen exposure of 1.6L and subsequently of 1L (cf. Fig. 3.46). Clean Gd is marked by A, the hydrogen affected areas by B. Middle: Line section of the clusters (line "a"). The width and the height are nearly uniform and amount to 35Å and 4Å. respectively. Right: The suppression of the surface state due to hydrogen adsorption results in a "collapsed" looking area. The depth of this purely electronically induced depression amounts to about 1.4Å as being obvious from the line scan (line "b").

smooth Gd films. In Fig. 3.49(a) the corresponding topography is shown after hydrogen exposure of 0.3L. Again, the adsorption starts at the step edges and surface imperfections. As for Gd islands the affected areas are coherent (cf. Fig. 3.44(a)). The hydrogen "island–like" formation was also deduced from photoemission experiments for H/Gd(0001) [4] and H/Be(0001) [18] by determination of peak heights from hydrogen induced states as a function of dosage. Further exposure (3.6L in Fig. 3.49(b)) demonstrates the same behavior in the adsorption process, a lagoon–like appearance. After a dosage of 9L (s. Fig. 3.49(c)) nearly the whole Gd film is covered with hydrogen. These observations point to no significant differences in the adsorption process of hydrogen on islands or on smooth films.

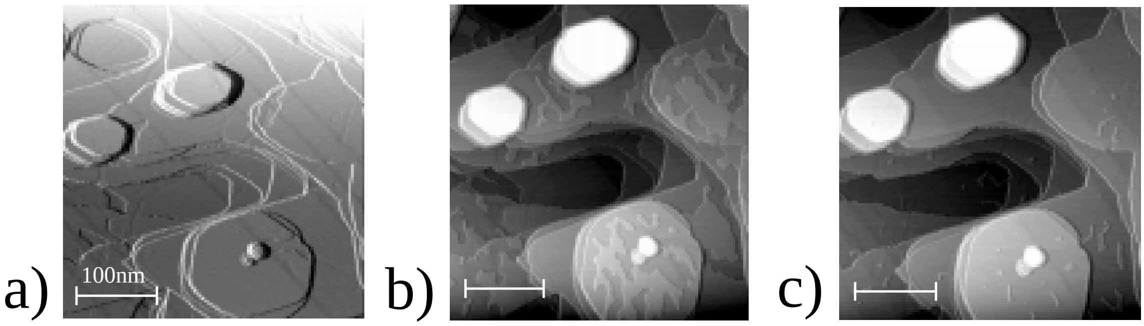

Figure 3.49: Topography of a thick (about 40 monolayer) smooth Gd film being exposed to 0.3L **(a)**, 3.6L **(b)**, and 9L **(c)** hydrogen. The adsorption starts at surface imperfections.

The influence of the bias voltage on the topography is demonstrated in Fig. 3.50.

At negative voltages ($U = -0.3$V in Fig. 3.50(a)) the hydrogen affected areas exhibit a reduced apparent height due to the drastically reduced LDOS (cf. Fig. 3.43). Using moderate positive bias voltages ($U = 0.8$V in Fig. 3.50(b)) it is possible to obtain equal apparent heights for the clean Gd(0001) surface and hydrogen affected areas. This observation is caused by the drastic increase of the LDOS for hydrogen on Gd(0001) towards higher voltages as already demonstrated in Fig. 3.43. For high positive voltages ($U = 3.2$V in Fig. 3.50(c)) an inversion of the corrugation, i.e. the hydrogen affected areas now appearing higher than for negative voltages, is present as can be additionally deduced from the shape of the LDOS curves. Therefore, the depth

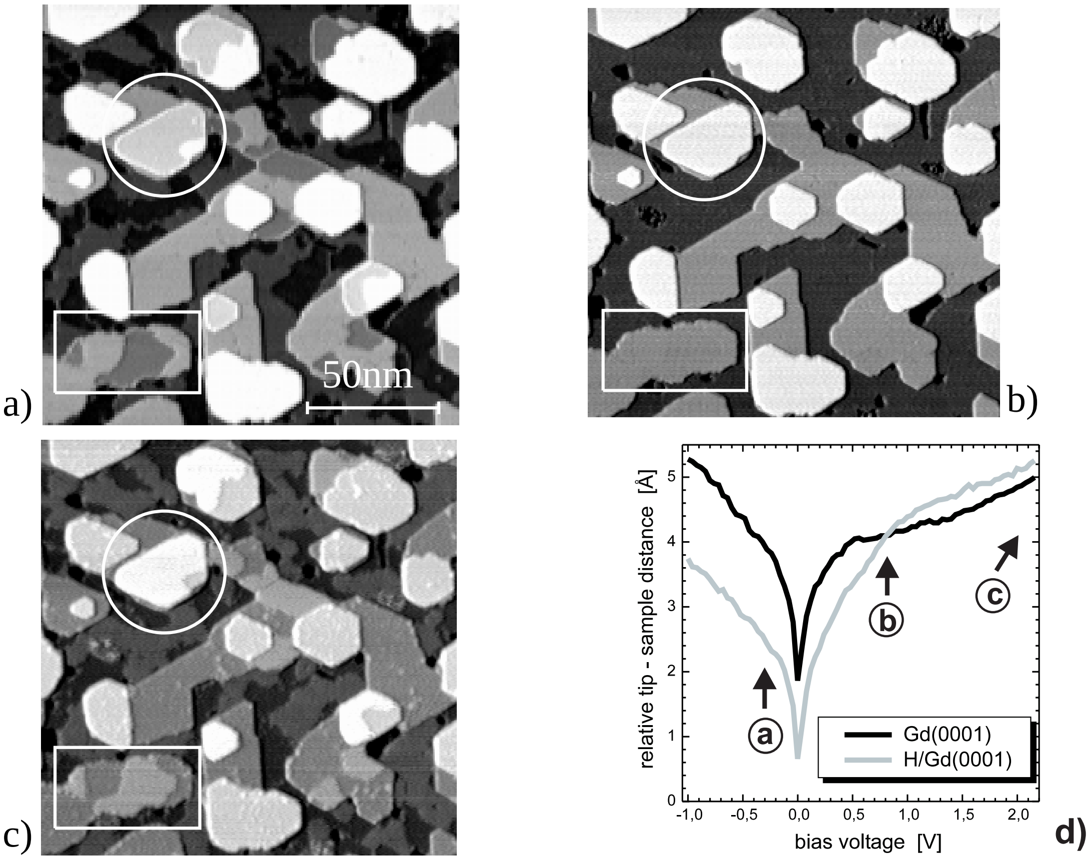

Figure 3.50: Topography of a thick Gd film being exposed to about 1L of hydrogen as a function of the bias voltage. For negative values ($U = -0.3$V in **(a)**) the hydrogen affected areas appear deeper due to their very small differential conductivity whereas an inversion can be observed ($U = 3.2$V in **(c)**) for high positive voltages. The contrast vanishes at low positive voltages ($U = 0.8$V in **(b)**). This behavior is obvious for the island being nearly completely covered with hydrogen (marked by the circle) and the region with a partial coverage (marked by the rectangle). The bar corresponds to 50nm. **(d)** Dependence of the relative tip – sample distance on the bias voltage for uncovered Gd(0001) and hydrogen affected areas ($I = 0.2$nA). The voltages which the images are taken at are marked by a - c. It is obvious that at 0.8V no difference between these two areas are present.

of the so-called "collapse" (cf. Fig. 3.48) is not uniform and depends significantly on the bias voltage. For a direct determination of this dependence $z(U)$ measurements were carried out by scanning the sample bias at a constant tunneling current with the feedback left on and measuring the z-feedback signal versus sample voltage. With the z-calibration, obtained at monoatomic Gd(0001) steps, one gets the relative tip displacement as function of sample bias. The determination of the displacement was obtained in a current imaging mode at a region of the sample that consists of both clean Gd(0001) as well as hydrogen covered areas. For each curve, about fifty measurements were averaged. Fig. 3.50(d) shows the relative tip – sample distance as a function of the bias voltage for uncovered Gd(0001) and hydrogen affected areas. Those voltages which the images are taken at are marked and correspond to the ones in Figs. 3.50(a) - (c). It is obvious that at negative and low positive bias voltages up to 0.8V the hydrogen affected areas exhibit a significantly reduced apparent height whereas at increasing positive voltages they appear a little bit higher than the clean Gd(0001) regions. At 0.9V no differences between the two types of areas are present. The dependence on the bias voltage is clearly visible in the areas which are marked by a circle representing an island which is nearly completely covered with hydrogen and a rectangle showing a partially affected island, respectively.

3.3.2 Hydrogen incorporation in gadolinium

In the following we will continue the discussion of the behavior of thin Gd films being exposed to hydrogen but for significantly higher doses [19].

Hydrogen incorporation in thin films can produce an extremely high out-of-plane expansion due to the clamping of the thin film to the substrate [20]. Within the solid solution phase the expansion can be predicted by linear elastic theory [21]. However, deviations from linear elastic theory were reported for high H concentrations due to the onset of plastic deformation in the film [22].

Two different processes have been proposed for plastic deformation and stress relaxation in thin films [22]: The emission of extrinsic dislocation loops during hydride precipitation as observed experimentally in bulk material [23] and the glide of dislocation segments that originate from misfit dislocations in the vicinity of the interface between the film and the substrate [24]. The strain energy of the film increases during hydrogen incorporation since the misfit between the adhering film and the substrate increases with H concentration. Thus, above a certain H concentration the formation of a misfit dislocation is energetically favored.

As already discussed above the electronic structure of clean and well-ordered Gd(0001) exhibits a pronounced surface. After hydrogen adsorption the surface state disappears, and a significant decrease in the differential conductivity occurs at negative bias voltages. This means that the hydrogen covered areas of the sample appear lower in the STM images obtained in the constant-current mode. Figure 3.51 shows a Gd(0001) surface after hydrogen exposures of 5 L (a), 10 L (b), 20 L (c,d). The topography reflects the symmetry of the (0001) oriented epitaxial Gd film with a thickness

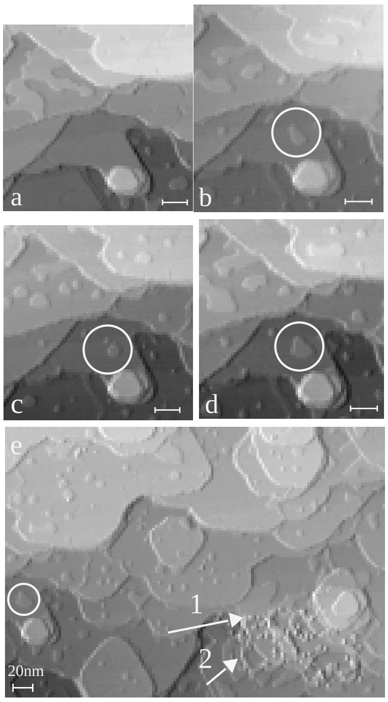

Figure 3.51: STM images of a Gd(0001) film after total hydrogen exposures of 5 L **(a)**, 10 L **(b)**, and 20 L **(c,d)**; all bars represent 20 nm. The Gd surface state is detectable as areas appearing higher on the *same* terrace in (a) whereas in (c) it has almost disappeared. It reappears after 40 min, as can be seen in (d) indicating the removal of hydrogen from the surface. After 20 L, two different types of surface pattern appear **(e)** small islands with disc-like shape (1.) and ramps (2.).

of about 10 nm: the steps of the terraces lie in $< 11\bar{2}0 >$ directions and subtend 60° angles. After 20 L exposure (c) only a small area remains free of hydrogen and since this area still has the Gd surface state it appears slightly higher. In the following STM image (s. Fig. 3.51(d)), taken 40 min later, the elevated area has increased. This suppression of the Gd surface state is revealed by the adsorption of hydrogen. The suppression and reappearance of the Gd surface state on the *same* terrace is indicated by white circles in Fig. 3.51(b)-(d). Its existence can be deduced from the shrinkage followed by a growth of the apparently higher areas. The reappearance of the Gd surface state in turn shows that hydrogen has disappeared from the surface. Hydrogen has a large negative heat of solution in rare earth metals, and therefore it dissolves in interstitial sites even at very low gas pressures [25]. Thus it is concluded that the hydrogen being initially adsorbed *on* the surface has diffused *into* the interior of the film.

After an exposure of 20 L the surface topography changes in certain areas. Figure 3.51(e) shows such a location of the sample; the circle marks the same area as the circle in Fig. 3.51(d). Two different features were observed: 1) a large number of disc-like islands and 2) occasionally ramp-shaped features. The disc-like islands have a diameter of 35 Å and a height of about 3 Å (s. Fig. 3.52(a)). The patterned area appears to be rough compared to the smooth Gd or H/Gd surface on each terrace and is induced by the surface modification to be discussed below. The height profiles show that the edges of the island have steep steps. A height profile taken along the sloped region of a ramp is shown in Fig. 3.52(b). The line scan is taken from the left. The steep step occurs at the left side. The inclination extending from the step to the right,

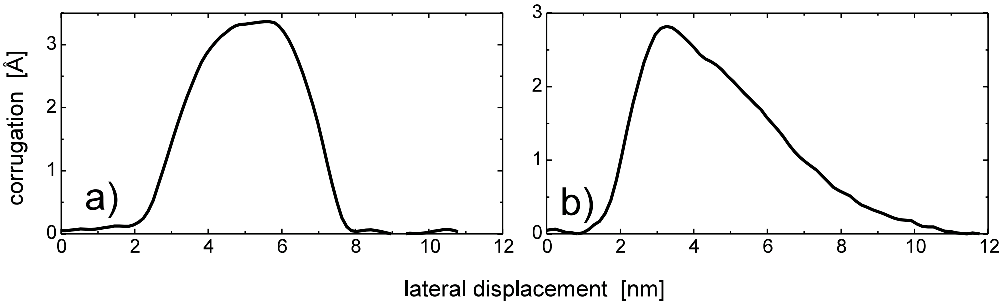

Figure 3.52: Height profiles of small disc-like islands **(a)** showing steps at their sides, and a ramp **(b)**, taken perpendicularly to the straight line. Here a steep step is followed by an inclination over several nanometers to the base level. Note the different scales for lateral displacement and corrugation.

covers several nanometers until it reaches the base level. Both, islands and ramps are elevated (by about the distance of the (0001) planes) compared to the level of the Gd terrace and, therefore, are generated by *local material transport to the surface.*

The ramps only appear in regions where disc-like island formation has already taken place and seem not to originate from chains of close packed disc-like islands since such an elevation should result in a step at all border lines, as shown in Fig. 3.52(a). In contrast a level inclination was found on one side and a step on the other side. Thus the two surface patterns have a different origin.

In the case of bulk Nb [23], the volume increase during hydride precipitation is released by transporting surplus atoms into less stressed regions by emission of extrinsic dislocation loops. The local volume increase per Gd atom is about 12%. Misfit stress in $< 0001 >$ directions is twice as large as in $< 11\bar{2}0 >$ directions because of the anisotropy of the system. In a quantitative treatment this anisotropy has to be taken into account. During hydride precipitation misfit stress appear both in-plane and out-of-plane. In the case of clamped thin films the emission of dislocation loops results in an in-plane and out-of-plane stress release, as shown schematically in Fig. 3.54(a). As soon as an emitted dislocation loop reaches the film surface it can be locally detected by an additional layer of atoms and corresponds to the observed disc-like islands. It should be noted that a surface hydride cannot explain the disc-like islands because it appears deeper compared to the base level in the STM image. The disc-like islands are attributed to localized hydride formation in the underlying Gd film.

To verify this interpretation the average hydrogen concentration can be estimated by measuring the relative amounts of disc-like islands containing patterned area and unchanged surface area which gives the hydride volume (with about 1.8 H/Gd) and the α-phase volume (with about 0.03 H/Gd), respectively. In the case of the STM image taken after a total exposure of 20 L (s. Fig. 3.51(c,d)) this estimate leads to an average value of 0.08 H/Gd. An upper estimate for the hydrogen concentration in the Gd film at this stage (s. Fig. 3.51(c,d)) can be given by assuming that all exposed gaseous hydrogen (20 L) is absorbed by the 35 monolayers of Gd. This yields a maximum estimated hydrogen concentration of 1.14 H/Gd which is well inside of the two phase field. Because the sticking coefficient is less than unity the true concentration is lower consistent with the average value obtained above. Thus, the inhomogeneous pattern arises from an inhomogeneous hydrogen distribution inside the film, as expected within the two phase region.

Further hydrogen exposure results in a spreading-out of the patterned areas that contain islands and ramps, as presented in Figs. 3.53(a) and (b). The disc and ramp covered areas are correlated with the presence of the GdH_2-phase in the film. It should be noted that the disc-like islands are identified with the emission of dislocation loops that are generated at Gd - H solid solution surrounded GdH_2-precipitates. The ramps, however, occur in areas which only consist of GdH_2.

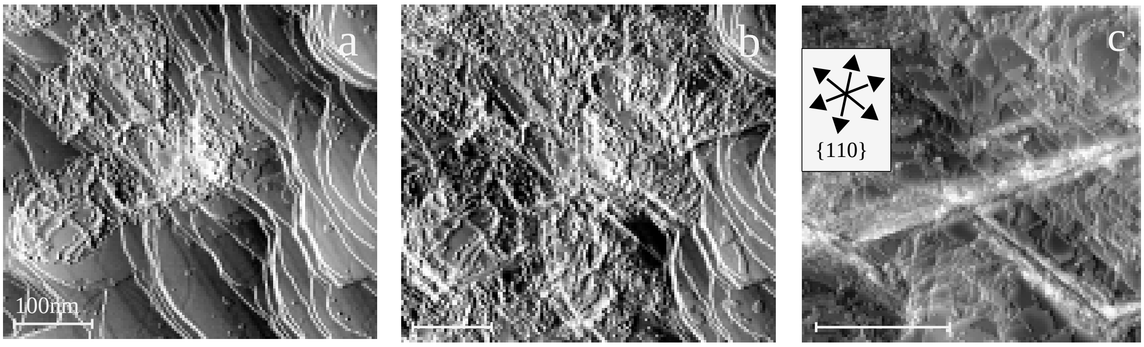

Figure 3.53: STM images of the Gd surface after an hydrogen exposure of 80 L (a) and 200 L (b). Further hydrogen exposure results in a spread out of the localized surface pattern. After more than 3000 L (c) the whole surface is covered with straight lines that predominantly occur oriented to $< 110 >$ fcc GdH_2 lattice directions, respectively former $< 11\bar{2}0 >$ hcp Gd-H lattice directions. The right part of the area shown in (c) coincides with the upper left corner in (a) and (b).

According to the lever rule the volume fraction of the GdH_2-phase increases with increasing total hydrogen content in the two phase region. After high H exposure the spreading-out of the elevated areas covers the whole analyzed region representing the high hydrogen concentration within the whole Gd film. The spreading-out contains two different features: first, new disc-like islands and ramps appear. Second, the existing ramps elongate predominately in the direction of the rim (cf. Fig. 3.54).

Heavy hydrogen exposure leads to a surface pattern consisting almost exclusively of straight lines. They lie in $< 11\bar{2}0 >$-directions of the as-prepared film, as shown in Fig. 3.53(c).

Since new ramps occur inside the regions where the underlaying film is GdH_2, they cannot be attributed to the misfit stress that appear at the GdH_2 - Gd interface. However, they can be related to high local in-plane stress between the GdH_2 film and the substrate. With regard to the bulk phase diagram, GdH_2 possesses fcc structure. In the following it is assumed that the former hcp lattice of Gd transforms into the

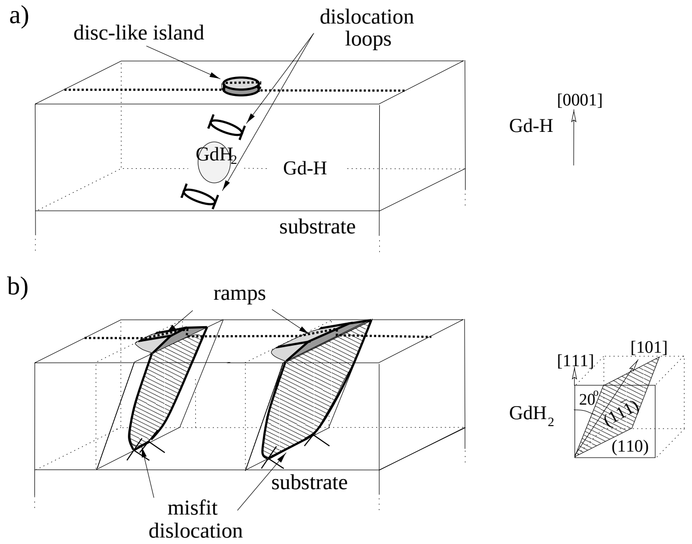

Figure 3.54: (a) Schematic drawing of the model proposed for the disc-like island formation. During internal hydride precipitation the surplus atoms are emitted in extrinsic dislocation loops and form islands. (b) Schematic drawing of the process proposed for ramp formation for the orientation of the analyzed Gd films. The in-plane stress releasing 60°-misfit dislocations near the interface to the substrate is connected to the surface via a mixed type dislocation line. At the surface such a dislocation line results in an elevated area above the edge dislocation. An atomic step appears where the $(11\bar{1})$-glide plane crosses the film surface. Height profiles along the broken lines can be compared with results of Fig. 3.52.

fcc lattice of GdH_2 by changing the stacking sequence of densest packed planes and, therefore, $< 11\bar{2}0 >$ (hcp) are parallel to $< 110 >$ (fcc).

The ramps can be interpreted by the formation of stress releasing dislocations. A detailed discussion on the origin and the behavior for increasing hydrogen exposure is given in [19]. Two appropriate dislocations are shown schematically in Fig. 3.54(b) for the specific orientation of the GdH_2 film. The dislocation (drawn as a bold line) reduces in-plane misfit stress as soon as its glide plane is inclined to the normal vector of the interface. In the fcc lattice the $\{111\}$ planes are glide planes with $< 110 >$ glide directions. The marked dislocation with a Burger vector of $1/2 < 110 >$ that corresponds to a 60°-misfit dislocation, possesses an angle of 19°68' to the interface normal. Therefore, it can release in-plane stress. The area where glide occured is hatched in Fig. 3.54(b). It is surrounded by three different parts: First, one part that is close to the interface and corresponds to an edge-type misfit dislocation. Second, two parts that extend from the interface to the surface which are predominantly screw type dislocations. The third part is the rim of the ramp. It corresponds to the glide step on the surface. For thin films this type of dislocation has been proposed before [24], however, it cannot be decided from the measurements whether the dislocation is formed on the surface and glides towards the interface, or vice versa.

The dislocation line is expected to have a high mobility in its glide plane. Gliding of the predominantly screw type sections in $< 110 >$-directions on $\{111\}$-planes leads to an elongation of the misfit dislocation near the interface. This is accompanied by an extension of the rim belonging to the ramp. While the moving dislocation line passes, the local bonds between Gd-atoms and the neighboring atoms reform and the atom rows move towards the surface. Following the $(11\bar{1})$-glide plane to the surface results in an atomic step on one side and a slope towards the other side, the ramp enlarges. This is shown in Fig. 3.54(b).

The sloped region of the ramp is assumed to meet the original level at a position where the underlying $(11\bar{1})$-glide plane intersects with the interface, i.e. at the position of the misfit dislocation. Since the angle between the $(11\bar{1})$-plane and the surface is constant, the raised area depends on the distance between the surface and the dislocation line. Assuming a maximum distance of 10 nm for the $d = 10$ nm thick Gd film, a slope field expansion of $\Delta = 3.4$ nm is obtained, using $d \cdot \sin(19°68') = \Delta$. This is in good agreement with the experimental findings shown in Fig. 3.52(b) where the raised area extends over about 5 nm (this is additional evidence for the dislocation mechanism being proposed).

At higher hydrogen concentrations the elongation of ramps along the rims leads to further stress release. As dislocation glide occurs in $\{111\}$-glide planes, glide steps on the surface form along $< 110 >$-directions. In the STM images this elongation results in the straight lines that cover the whole film after heavy hydrogen exposure. The angles between these lines are 60°, as can be seen in Fig. 3.53(c), as expected for $\{111\}$-planes of an fcc lattice intersecting a (111) surface. To conclude, ramps and island formation verify that plastic deformation of the film occurs during hydrogen incorporation.

The STM measurements have shown that during hydrogen loading of thin epitaxial Gd films surface patterns develop above a critical concentration. Two different types were found: disc-like islands and ramps. These surface patterns can be well described with two plastic deformation processes in the films that lead to glide steps on the film surface. Firstly the emission of dislocation loops during hydride precipitation occurs, and secondly misfit dislocations form near the film-substrate interface. Since plastic deformation leads to stress release we suggest that a lot of thin metal films that are clamped to a substrate relax plastically after reaching a certain hydrogen-induced stress which corresponds to a critical hydrogen concentration. Overall, combining the ability of preparing high-quality epitaxial thin films with the detailed analysis of the mechanical properties during hydrogen absorption may lead to a deeper fundamental understanding of hydrogen switchable thin films. It may also improve their industrial applications.

3.3.3 Coadsorption characteristics

In order to get a deeper insight into the coadsorption of hydrogen and carbon monoxide (CO) on gadolinium it is necessary to understand what happens when exposing the Gd surface to each single type of molecules. The behavior of hydrogen was already discussed above; the adsorption of CO will first be described subsequently the adsorption of oxygen.

Gadolinium exposed to carbon monoxide

The adsorption process of CO on gadolinium is strongly depending on the substrate temperature. Exposing Gd to CO results in a behavior which is illustrated in Fig. 3.55. The left image is related to the adsorption of 0.8L CO at low temperature (90K), the right one corresponds to 0.6L CO at room temperature. The surfaces of the Gd islands are differently structured. The inset in Fig. 3.55(b) shows, on the *same* scale, the Gd surface after an oxygen dosage of 0.08L. Whereas at low temperature the adsorption seems to occur molecularly in good agreement, e.g., with investigations on CO adsorption on Fe(110) [26] and on Co(0001) [27], dissociation on this Gd surface takes place at 300K as already shown by Searle et al. [28] and additionally, e.g., for CO on Fe(100) surfaces [29, 30]. The similarity between CO and O_2 adsorption is a strong hint to the dissociation of the carbon monoxide molecule at room temperature. Direct evidence will be given by means of photoelectron spectroscopy (see below).

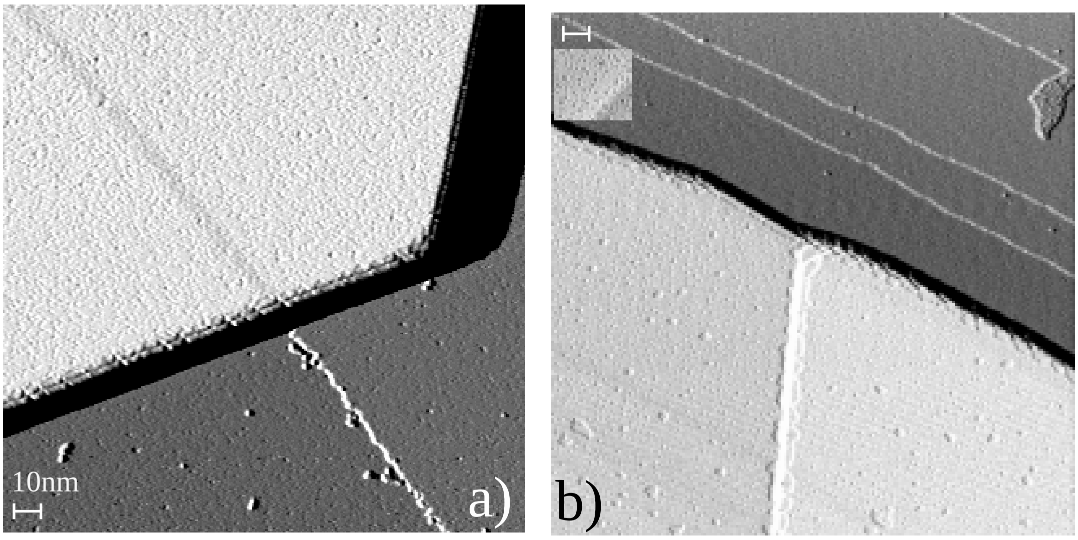

Figure 3.55: Topography of Gd islands being exposed to CO at 90K **(a)** and 293K **(b)**. The surfaces of the Gd islands are differently structured due to a molecular adsorption at low temperature and to a dissociation of the CO molecules at room temperature. Both scale bars correspond to 10nm.

An exposure sequence obtained at room temperature is presented in Fig. 3.56. For small dosages (1L in Fig. 3.56(a)) the surface is relatively smooth with single localized areas being depressed. For higher exposures (20L in Fig. 3.56(b)) the appearance has been changed. As will be discussed in more detail below the rough surface points to the creation of carbonate species.

Oxygen on rare earth metal surfaces

The very first step of the adsorption process of oxygen on Gd(0001) will be discussed in the following. Oxygen on Gd islands with the remaining monolayer in-between is

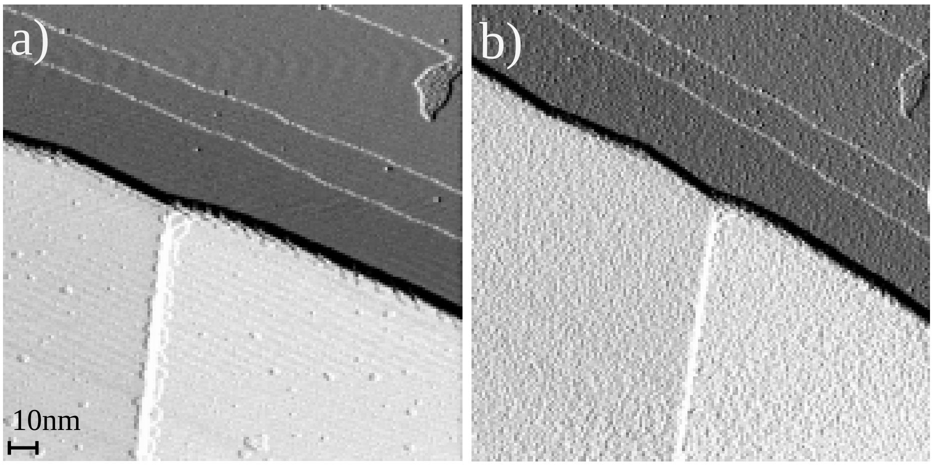

Figure 3.56: For small exposures at room temperature (1L in **(a)**) the surface looks relatively smooth whereas for higher dosages (20L in **(b)**) it becomes rough

shown in Fig. 3.57. In the left image the exposure amounts to 0.08L, in the right one,

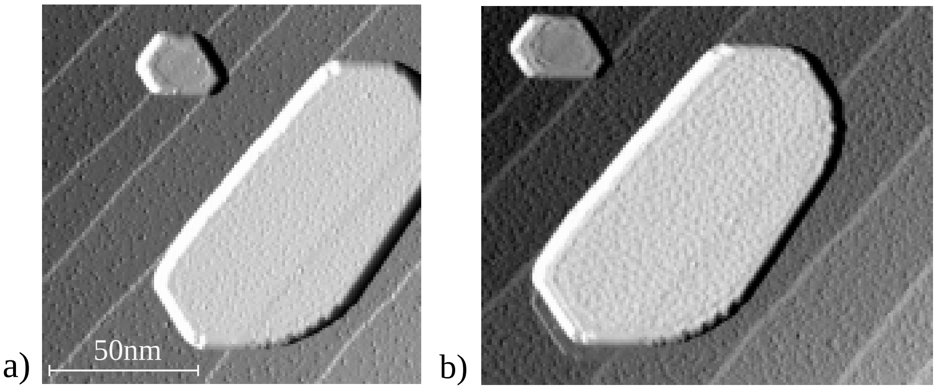

Figure 3.57: Topography of a Gd island with the monolayer covering the tungsten substrate between the islands being exposed to 0.08L **(a)** and 0.2L **(b)** oxygen.

showing the same area of the sample, it was increased to 0.2L. It is obvious that in contrast to hydrogen the adsorption can be seen as process leaving oxygen regularly distributed over the surface.

For demonstrating the differences between oxygen and hydrogen adsorbed on gadolinium the surface was covered with small amounts of hydrogen and subsequently exposed to 0.1L oxygen. The topography is shown in Fig. 3.58(a). The large depressed area C on-top of the island is caused by hydrogen, the small areas by oxygen. A map of the differential conductivity dI/dU at -0.2V is presented in Fig. 3.58(b) showing the reduced local density of states for adsorbed hydrogen at negative bias voltages (cf. Fig. 3.47(c)). Tunneling spectra (see Fig. 3.58(c)) were recorded on-top of the island for the unaffected Gd surface (A), the oxygen induced small areas (B) as well as

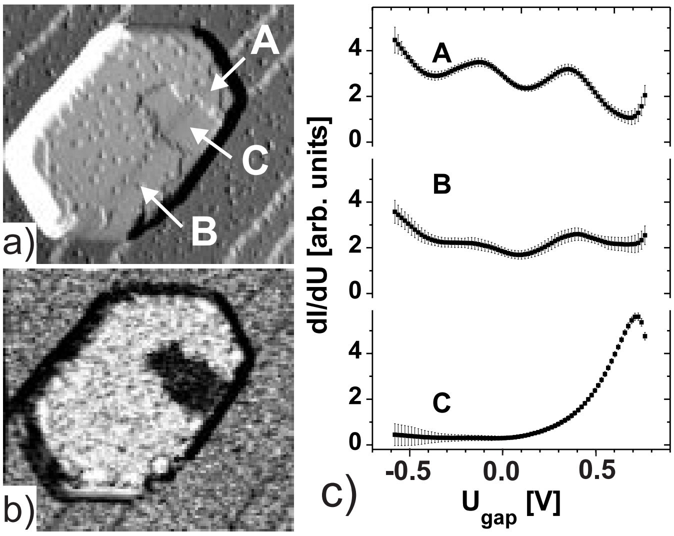

Figure 3.58: Gd being exposed to small amount of hydrogen and subsequently to 0.1L oxygen. **(a)** Topography (70 × 60nm, $U = -0.7$V, $I = 1$nA). **(b)** Map of the differential conductivity at -0.2V. **(c)** Tunneling spectra of the Gd island for uncovered gadolinium (A), oxygen induced small areas (B), hydrogen affected area (C). These regions are marked in (a).

the hydrogen affected areas (C). Spectrum A demonstrates that on the non-covered areas the exchange split Gd surface state is present. The differential conductivity within the hydrogen covered area is comparable to the one in Fig. 3.43. Curve B shows that at the oxygen induced regions the Gd surface state is still present. The further steps in the adsorption process will be discussed below in connection with coadsorption of CO and H_2.

In the following we will turn the attention to oxygen adsorption on the Gd monolayer located between the Gd islands. Fig. 3.59(a) shows a detailed image of the monolayer after an exposure of 0.08L (cf. Fig. 3.55(b)). Due to their strong electronegativity the dissociatively adsorbed oxygen molecules are visible as black holes, i.e. adsorbed oxygen is imaged as a depression; this behavior was already found, for example, for O/W(110) [31] and was also theoretically predicted [32]. The oxygen overlayer forms an ordered structure. This is not present (s. Fig. 3.59(b)) after the additional amount of 0.12L of oxygen on the surface (cf. Fig. 3.57(b)).

In order to determine the geometrical arrangement a more detailed image is shown in the left part of Fig. 3.60. The adsorption sites of the oxygen atoms form a hexagonal structure which is schematically outlined in the left part of Fig. 3.60. The nearest neighbour distance amounts to (13 ± 1)Å.

The monolayer of Gd which possesses a rectangular (7×14) unit cell [33] is drawn in the right part of Fig. 3.60 as light gray balls. The interatomic distances were taken from [33]. The proposed model of the adsorbate overlayer is included in this Figure which can be attributed to a $(2\sqrt{3} \times 2\sqrt{3})R30^\circ$ structure with a nearest neighbour

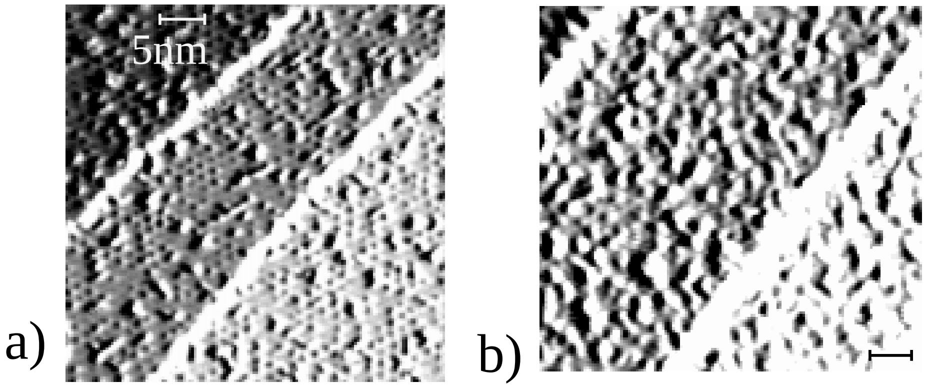

Figure 3.59: Topography of the Gd monolayer covering the tungsten substrate between the islands being exposed to 0.08L oxygen **(a)** and 0.2L **(b)**. The oxygen overlayer forms an ordered structure which is not visible for higher exposures.

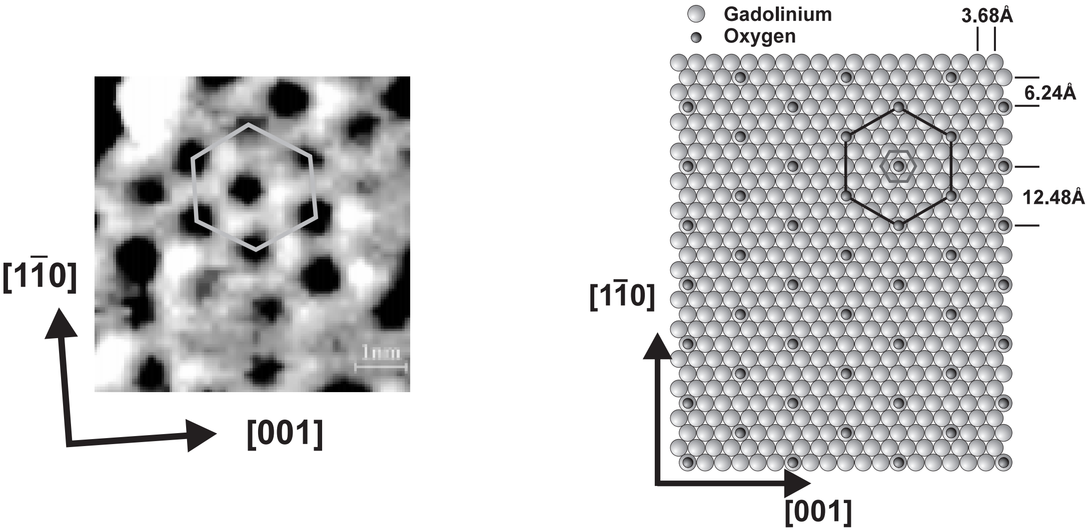

Figure 3.60: Left: The same sample as in Fig. 3.57 with an expanded scale. Adsorbed oxygen is imaged as a depression. The adsorption sites of the oyxgen atoms form a hexagonal structure which is schematically included with nearest neighbour distances of (13 ± 1)Å. The crystallographic axes are in reference to the tungsten substrate. Right: The Gd monolayer possessing a (7×14) unit cell is drawn as light gray balls. The proposed model of the oxygen overlayer is included by dark gray balls. This structure can be attributed to $(2\sqrt{3}\times 2\sqrt{3})R30^\circ$ with a nearest neighbour distance of 12.48Å.

distance of 12.48Å being in excellent agreement with the experimental results. The basic unit cells are shown in dark gray colour for the Gd monolayer and in black for the adsorbate system, respectively. It should be noted that the presentation with on-top sites is arbitrary and that it is not possible to distinguish between on-top, three-fold hollow, and bridge sites based on the STM observations.

Coadsorption of hydrogen and carbon monoxide

For a better understanding of catalytic processes the coadsorption of hydrogen and carbon monoxide was investigated. For this purpose the Gd surface was exposed to small amounts of hydrogen with a subsequent dosage of CO [13, 34]. The basic steps of this process were determined with a sample exposed to 1L hydrogen being adsorbed on a Gd(0001) surface. This system was subsequently exposed to CO with dosages up to 0.81L. The photoemission spectra are presented in Fig. 3.61. With increasing CO exposure it can be observed that the Gd surface state near the Fermi level remains nearly unaffected apart from a small decrease in intensity when initiating the CO exposure and a slight shift to higher binding energies. Additionally, the hydrogen induced feature at 4.0eV binding energy looses intensity and is absent after 0.81L CO. In the energy region around 2eV an additional structure appears with increasing CO exposure; it is not apparent at low coverages.

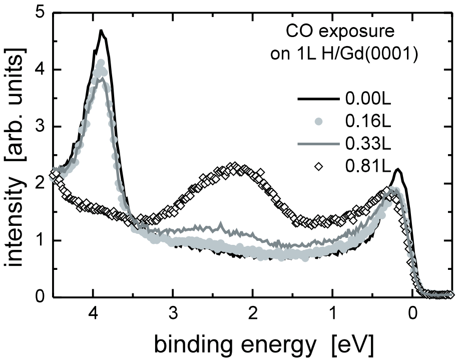

Figure 3.61: Photoemission spectra taken in normal emission with $h\nu = 16.85$eV for a smooth Gd film being pre-exposed to 1L hydrogen as a function of CO dosage. With increasing offer the hydrogen induced peak at 4eV binding energy disappears completely whereas around 2eV a broad structure shows increasing intensity.

It was shown [35] for uranium (U), possessing a related electronic structure ([Rn] $5f^3\,6d^1\,7s^2$) to gadolinium ([Xe] $4f^7\,5d^1\,6s^2$), that after CO adsorption two features appear; one structure at 2.4eV binding energy is due to C 2p emission from uranium carbide (UC) and the other one at 2.2eV from U caused by the existence of oxygen.

Due to the similar electronic structure to uranium, the peak intensities for Gd as substrate were analogously determined at 2eV, 2.4eV, and 4eV as a function of CO exposure (s. Fig. 3.62). The procedure consists of the subtraction of a linear background and a fit with Gaussian functions. It is obvious that the diagram can be classified by four regions, i.e. the adsorption process up to 0.81L consists of four steps.

At the beginning the hydrogen induced intensity decreases very fast whereas the dissociatively adsorbing CO causes no features in the spectra neither for the C 2p state at 2.4eV nor for the oxygen caused Gd state at 2.0eV. In the next step the loss of intensity of the hydrogen state is diminished, the emission of the carbon state starts, and no feature caused by oxygen is present. Step 3 consists of the decrease in hydrogen induced intensity with the same slope as in step 1, increasing carbon induced intensity with the same slope as in step 2, and the onset of oxygen induced intensity from a Gd state. In step 4 no hydrogen induced intensity is present and the carbon induced and

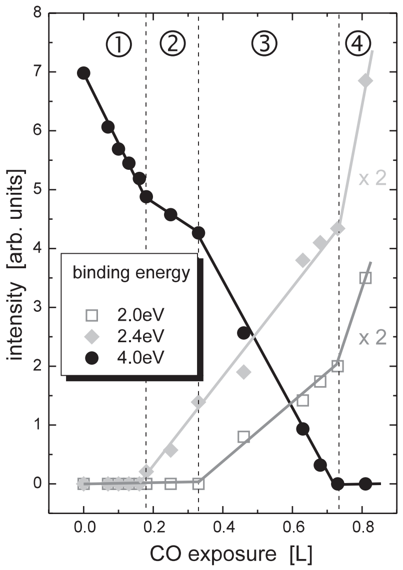

Figure 3.62: Peak intensities as a function of CO dosage. The shapes of the curves point to four regions with different behavior in the adsorption process (the details are discussed in the text).

oxygen caused states show a strengthened increase in intensity.

In the following we will describe the chemical reactions being induced by increasing CO exposure; the superscript *gas* means gaseous, *ads* means adsorbed in any way. In order to get a better standard of comparison all formulae were referenced to a total of four CO molecules.

During the first step only hydrogen is removed, no additional species are adsorbed; all products therefore are gaseous pointing to the creation of formaldehyde which can directly be created via a gas phase reaction:

$$\textbf{Step 1}: \qquad 8\,\mathrm{H}^{ads} + 4\,\mathrm{CO}^{gas} \longrightarrow 4\,\mathrm{H_2CO}^{gas}$$

The ratio of eight H atoms to four CO molecules for the complete removal of hydrogen can *independently* be estimated by the following consideration.

It was shown by Li et al. [4] that 2L H_2 are necessary in order to get a full coverage of Gd(0001) with an (1×1) overlayer. Due to the dissociative adsorption of H_2 one can estimate, using the Gd lattice constants, that the surface is covered with about eight H atoms per nm^2. In this investigation Gd was exposed to 1L H_2, i.e. the density amounts to four H atoms per nm^2. The extrapolation in region 1 (see Fig. 3.62) results in 0.6L CO being necessary to remove all hydrogen. 1L CO is equivalent to a collision rate of 3.5 molecules/nm^2 (cf. the estimation for hydrogen in Ch. 3.3.1), therefore 0.6L CO give a rate of about two CO molecules/nm^2. This means that two CO molecules in relation to four H atoms cause a complete removal of hydrogen as stated above (see reaction scheme of step 1).

In the next step the reaction changes; only half a rate of hydrogen is removed as can be seen by the change in slope for the H induced feature in Fig. 3.62. Thus, another reaction seems to occur. The additional amount of CO causes the creation of carbon on or near the surface but no oxygen atom is adsorbed. The reaction can therefore be written as

$$\textbf{Step 2}: \qquad \mathrm{Gd} + 4\,\mathrm{H}^{ads} + 4\,\mathrm{CO}^{gas} \longrightarrow 2\,\mathrm{CO_2}^{gas} + \mathrm{CH_4}^{gas} + \mathrm{GdC}^{ads}$$

The formation of carbide was also observed for U exposed to CO [35].

During further exposure hydrogen is removed with the same rate compared to the initial step 1. The rate of carbon creation remains constant, but now oxygen is adsorbed creating a subsurface oxide and causing emission from Gd^{2+} states as already discussed for oxygen adsorbed on Gd [36]. This reaction can be described by

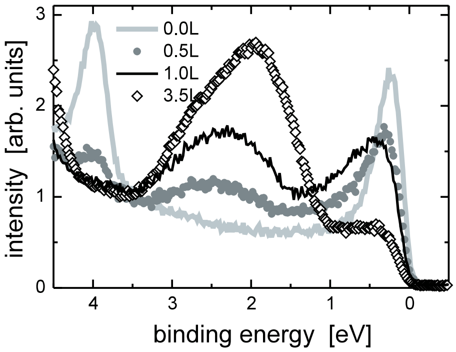

Figure 3.63: Photoemission spectra for 0.4L H/Gd(0001)/W(110) with increasing CO dosage (cf. Fig. 3.61)

$$\textbf{Step 3}: \qquad 3\,\mathrm{Gd} + 8\,\mathrm{H}^{ads} + 4\,\mathrm{CO}^{gas} \longrightarrow \mathrm{CO_2}^{gas} + 2\,\mathrm{CH_4}^{gas} + \mathrm{GdC}^{ads} + 2\,\mathrm{GdO}^{ads}$$

At the end of step 3 the *whole* amount of hydrogen has been removed from the surface.

The next step is characterized by the creation of carbon and Gd suboxide through direct CO dissociation:

$$\textbf{Step 4}: \qquad 4\,\mathrm{Gd} + 4\,\mathrm{CO}^{gas} \longrightarrow 4\,\mathrm{GdC}^{ads} + 4\,\mathrm{GdO}^{ads}$$

As every CO molecule is transformed now the increase in the peak intensities around 2eV binding energy becomes even more pronounced.

In order to determine the influence of higher CO dosages a Gd film covered with the equivalent of 0.4L hydrogen was subsequently exposed to CO by up to 3.5L. These spectra are presented in Fig. 3.63. In the low coverage regime the results are comparable with the system discussed above. In contrast, the spectrum for 3.5L CO appears significantly different. No feature at the Fermi level is present anymore and the one around 2eV binding energy shows a twin-peak structure. The peak intensities as a function of CO exposure are given in Fig. 3.64. It is obvious that the same mechanism takes place. The corresponding STM images taken for 0L and 0.6L CO, shown with an expanded scale in Fig. 3.67, demonstrate the removal of hydrogen (see discussion below).

Above 1L an additional regime 5 occurs. This is illustrated by an expanded scale in Fig. 3.65; the corresponding STM image is given for a CO dosage of 3.5L. The

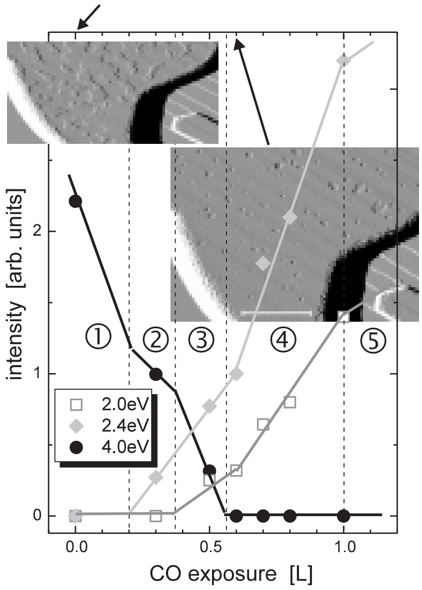

Figure 3.64: Intensities of the hydrogen induced structure at 4eV, the oxygen caused Gd state at 2.0eV, and the C 2p state at 2.4eV as a function of CO dosage. The adsorption process can be divided into five steps. The corresponding topography is shown for 0L CO and 0.6L CO as insets. The removal of hydrogen can be observed due to the reappearance of the Gd surface state.

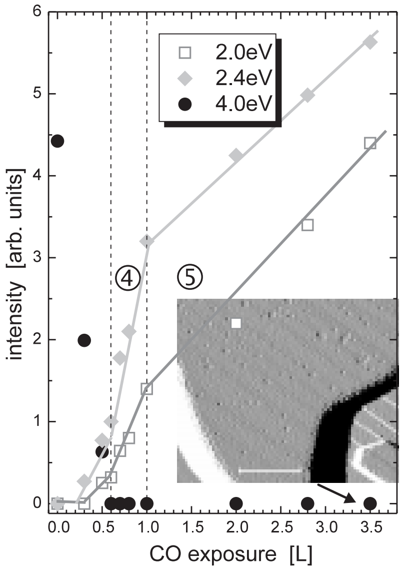

Figure 3.65: Same as in Fig. 3.64 but for higher coverages. The corresponding STM image is taken for a dosage of 3.5L CO.

increasing intensity becomes less pronounced compared to region 4. The change in the electronic properties is additionally visible in the energy range of O 2p states around 6eV binding energy. Fig. 3.66 shows the spectra taken after CO exposures of 0.8L and 2.8L, respectively. Whereas for the low dosage a single broad peak can be observed pointing to oxygen in Gd subsurface oxide [37], at higher exposures a double-peak structure appears which is characteristic for Gd_2O_3 [36].

It is known [38] that sesquioxides of rare earth metals RE_2O_3 are able to induce the transformation of CO to CO_2 which then form a stable carbonate-like species at the surface. In Gd_2O_3 Gd is present in the oxidation stage Gd^{3+} thus having lost all valence electrons; the intensity near the Fermi level is drastically decreased (see Fig. 3.66). The significantly different structure around 2eV binding energy is attributed to emission from the carbonate-like species as already supposed by Searle et al. [28]. Taking these considerations into account the further step in the process can be described by

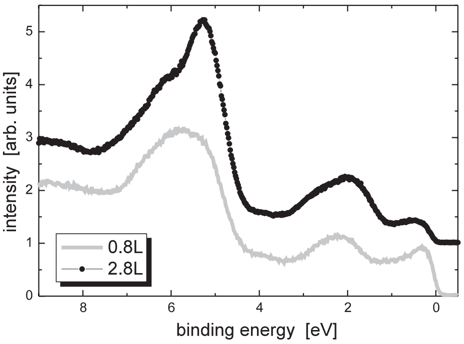

Figure 3.66: Gd films being pre-exposed to hydrogen for different CO dosage. The broad peak around 6eV binding energy is due to oxygen. The double-peaked structure for higher dosages points to the formation of Gd_2O_3. This is in agreement with the drastically decreased intensity near the Fermi level.

$$\textbf{Step 5}: \qquad 6\,\mathrm{GdO} + 4\,\mathrm{CO}^{gas} \longrightarrow 2\,\mathrm{GdC}^{ads} + 2\,(\mathrm{Gd_2O_3} \bullet \mathrm{CO_2})^{ads}$$

It should be noted that a part of the carbonate-like species may desorb as ${CO_2}^{gas}$.

The "visualization" of this process was carried out via scanning tunneling microscopy. For this purpose Gd islands with hcp(0001) surfaces were exposed to 0.4L hydrogen. The affected areas can be seen in Fig. 3.67(a) (cf. additionally Fig. 3.64).

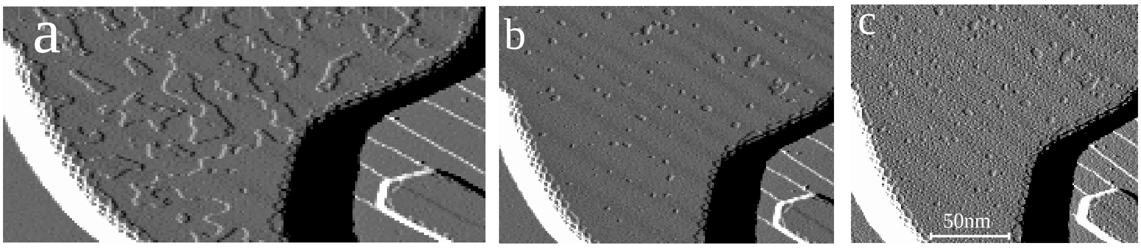

Figure 3.67: Enlarged images of the STM pictures in Figs. 3.64 and 3.65 taken at CO dosages of 0L **(a)**, 0.6L **(b)**, and 3.5L **(c)**

CO was subsequently dosed to this system. After 0.6L CO exposure no collapsed areas are observable (see Fig. 3.65) pointing to no hydrogen remaining on the surface. At this point region 4 is reached, and the complete hydrogen adsorbate is removed by CO. The single areas with a reduced apparent height are caused by contamination during Gd film preparation. They are also observable in Fig. 3.67(a). Fig. 3.67(c) shows the sample which was exposed to 3.5L CO. In step 5 carbonate species are created which cause the surface roughness.

This direct comparison, i.e. the *visualization* of the changes in the electronic properties caused by chemical reactions at the surface, expresses the advantage of the combination of photoelectron spectroscopy with scanning tunneling microscopy and spectroscopy.

We would like to acknowledge fruitful discussions with A. Pundt (University of Göttingen) concerning "Hydrogen incorporation in metals".

References

[1] C. Westphal, J. Bansmann, M. Getzlaff, and G. Schönhense. *Phys. Rev. Lett.* **63**, 151 (1989).

[2] M. Getzlaff, M. Bode, and R. Wiesendanger. *Phys. Rev. B* **58**, 9681 (1998).

[3] B. Kim, A.B. Andrews, J.L. Erskine, K.J. Kim, and B.N. Harmon. *Phys. Rev. Lett.* **68**, 1931 (1992).

[4] D. Li, J. Zhang, P.A. Dowben, and M. Onellion. *Phys. Rev. B* **48**, 5612 (1993).

[5] S.M. Goldberg, C.S. Fadley, and S. Kono. *J. Electr. Spectr. Relat. Phen.* **21**, 285 (1981).

[6] J.W. Gadzuk. *Phys. Rev. B* **12**, 5608 (1975).

[7] E.U. Condon and G.H. Shortley. *The theory of atomic spectra.* University Press cambridge, Cambridge, (1967).

[8] K. Horn, A.M. Bradshaw, and K. Jacobi. *Surf. Sci.* **72**, 719 (1978).

[9] M. Scheffler, K. Kambe, and F. Forstmann. *Sol. State Comm.* **25**, 93 (1978).

[10] M. Getzlaff, M. Bode, S. Heinze, R. Pascal, and R. Wiesendanger. *J. Magn. Magn. Mater.* **184**, 155 (1998).

[11] D. Weller and S.F. Alvarado. *J. Appl. Phys.* **59**, 2908 (1986).

[12] M. Getzlaff, M. Bode, and R. Wiesendanger. *Surf. Sci.* **410**, 189 (1998).

[13] M. Getzlaff, M.Bode, R. Pascal, and R. Wiesendanger. *Phys. Rev. B* **59**, 8195 (1999).

[14] M. Getzlaff, M.Bode, R. Pascal, and R. Wiesendanger. *Appl. Surf. Sci.* **142**, 63 (1999).

[15] R.G. White, M.H. Lee, N.P. Tucker, S.D. Barrett, and P.W. Murray. *Phys. Rev. B* **56**, 10071 (1997).

[16] D. Menzel and J.C. Fuggle. *Surf. Sci.* **74**, 321 (1978).

[17] M. Bode, M. Getzlaff, S. Heinze, R. Pascal, and R. Wiesendanger. *Appl. Phys. A* **66**, S121 (1998).

[18] K.B. Ray, X. Pan, and E.W. Plummer. *Surf. Sci.* **285**, 66 (1939).

[19] A. Pundt, M. Getzlaff, M. Bode, R. Kirchheim, and R. Wiesendanger. *Phys. Rev. B* **61**, 9964 (2000).

[20] G. Song, A. Remhof, K. Theis-Bröhl, and H. Zabel. *Phys. Rev. Lett.* **79**, 5062 (1997).

[21] Q.M. Yang, G. Schmitz, S. Fähler, H.U. Krebs, and R. Kirchheim. *Phys. Rev. B* **54**, 9131 (1996).

[22] U. Laudahn, A. Pundt, M. Bicker, U. v. Hülsen, U. Geyer, T.Wagner, and R. Kirchheim. *J. Alloys Comp.* **293-295**, 490 (1999).

[23] T. Schober. *Scripta Met.* **7**, 1119 (1973).

[24] W.D. Nix. *Metall. Trans. A* **20**, 2217 (1989).

[25] Y. Fukai. *The metal-hydrogen system.* Springer Verlag, Berlin, (1993).

[26] M. Getzlaff, J. Bansmann, C. Westphal, and G. Schönhense. *J. Magn. Magn. Mater.* **104-107**, 1781 (1992).

[27] M. Getzlaff, J. Bansmann, and G. Schönhense. *J. Chem. Phys.* **103**, 6691 (1995).

[28] C. Searle, R.I.R. Blyth, R.G. White, N.P. Tucker, M.H. Lee, and S.D. Barrett. *J. Synchrotron Radiat.* **2**, 312 (1995).

[29] T.N. Rhodin and C.F. Brucker. *Sol. State Comm.* **23**, 275 (1977).

[30] M. Getzlaff, J. Bansmann, and G. Schönhense. *Fresenius J. Anal. Chem.* **353**, 748 (1995).

[31] K.E. Johnson, R.J. Wilson, and S. Chiang. *Phys. Rev. Lett.* **71**, 1055 (1993).

[32] N.D. Lang. *Comments Condens. Matter Phys.* **14**, 253 (1989).

[33] E.D. Tober, R.X. Ynzunza, C. Westphal, and C.S. Fadley. *Phys. Rev. B* **53**, 5444 (1996).

[34] M. Getzlaff, M.Bode, and R. Wiesendanger. *Appl. Surf. Sci.* **142**, 428 (1999).

[35] T. Gouder, C.A. Colmenares, J.R. Naegele, J.C. Spirlet, and J. Verbist. *Surf. Sci.* **264**, 354 (1995).

[36] K. Wandelt and C.R. Brundle. *Surf. Sci.* **157**, 162 (1985).

[37] J. Zhang, P.A. Dowben, D. Li, and M. Onellion. *Surf. Sci.* **329**, 177 (1995).

[38] F.P. Netzer and E. Bertel. In: K.A. Gschneidner and L. Eyring, (Ed.), *Handbook on the physics and chemistry of rare earths*, Vol. 5, page 217. North Holland, Amsterdam, (1982).

3.4 Nanoelectronics

3.4.1 Probing the Local Density of States of Dilute Electron Systems in Different Dimensions

M. Morgenstern, D. Haude, J. Klijn, Chr. Meyer, M. Getzlaff, A. Wachowiak, and J. Wiebe

Introduction

The development of scanning tunneling spectroscopy (STS) in recent years provides the opportunity to measure the local density of states with high spatial and energy resolution. The basic requirement is to measure at low temperature which increases the instrumental stability as well as the energy resolution. While first experiments focused on the visualization of single particle properties as the wave nature of electrons [1,2], more recent experiments tackle properties of the electron system guided by interaction effects as, most simply, lifetime properties [3], or, more complex, superconductivity [4], magnetism [5] or the Kondo effect [6].

A nice playground to study the consequences of interaction effects systematically are degenerately doped semiconductors. While a description of electrons as Bloch waves within the band structure picture is restricted to a periodic confinement potential and weak interactions, both conditions are not fullfilled for degenerate semiconductor samples. The ionized dopants surrounded by a screened Coulomb potential strongly disturb the periodicity of the potential and the low electron density increases the importance of electron-electron interactions. Moreover, a magnetic field can be used to quench the kinetic energy leading to systems which are largely determined by the interaction of the electrons with potential perturbations and/or electron-electron interactions. Depending on the dimensionality of the system, different electron phases result leading to a variety of physical effects as metal-insulator transitions, quantum Hall transitions, composite fermion phases, Wigner crystals, Luttinger liquids, etc..

While these electron phases have been largely studied by macroscopic means as transport, magnetization or optical spectroscopy, the important microscopic properties of the phases have barely been probed, although detailed predictions are given from theory. The most basic microscopic parameter is the local density of states ($LDOS$). As long as a single particle description is adequate, it is simply defined as:

$$LDOS(E,r) = \sum_{\delta E} |\Psi_i(E,r)|^2 \tag{3.14}$$

with Ψ_i being the single particle wave functions as a function of energy E and position r and δE being an energy window usually identified with the energy resolution of the experiment. Obviously the LDOS is straightforwardly linked to the Schrödinger equation and thus a basic property of the system. STS probes exactly this property, which is proportional to the measured differential conductivity $dI/dV(V,r)$, where I is the tunneling current and V the applied voltage.

Here, we present a systematic STS study of electron systems belonging to the conduction band of InAs. The conduction band is isotropic, largely parabolic and exhibits a low effective mass of only $m_{eff} = 0.023\ m_e$. Thus it is ideally suited for basic studies of electron systems. To put it differently, the distribution of kinetic energies is as simple as in a free electron gas, while the effect of a magnetic field is largely enhanced due to the low m_{eff}. Moreover, the InAs conduction band exhibits a high g-factor of $g = 14.3$ stressing the importance of the spin in magnetic field, which itself is a relevant parameter in the electron-electron interaction processes. Finally, cleaving the sample in situ at a base pressure of 10^{-10} mbar results in a clean InAs(110) surface with a very low surface point defect and adsorbate density of 10^{-9} cm^{-2} [7]. This density does not increase within weaks after cleavage due to the extreme UHV conditions within the cryostat. Thus, features in the LDOS can be ascribed unambigously to the properties of a well defined electron system housed in n-type InAs of a given dopant concentration.

Most exciting, this single sample allowed us to investigate electron systems in all four different dimensionalities. We probed the three-dimensional electron system (3DES) of the bulk InAs, which reached up to the surface [2,8]. We induced a two-dimensional electron system (2DES) in the region close to the surface by putting low amounts of adsorbates on the surface [9–11]. We found a one-dimensional electron system (1DES) confined below a charged [112] step edge and we induced a zero-dimensional electron system (0DES) taking advantage of the fact that the tip acts as a local gate with respect to the surface, if the work functions of tip and sample are different [7,12–15].

This report is organized as follows. After a short description of the experimental procedures, we first present measurements of the LDOS of the 3DES in the extreme quantum limit (EQL), which surprisingly shows so called drift states, usually expected in the 2DES. The results will be linked to a pecularity in the Hall resistivity, already found in 1958, but up to now not convincingly explained. Second, we describe mesurements of the 2DES. The preparation of the 2DES and its characterization by photoelectron spectroscopy (UPS) will be explained, the LDOS of this 2DES will be shown and its pattern largely determined by interaction of the electrons with the inhomogeneous potential will be reproduced by solving the corresponding Schrödinger equation numerically. Landau quantization of this 2DES and first results of the corresponding LDOS will be given. Third, the LDOS of the 1DES in direct comparison with the inhomogeneous one-dimensional potential will be shown. Finally, the tip-induced quantum dot will be used to probe the sensitivity of spin splitting on residual disorder, giving a nice real-space visualization of the non-locality of the exchange interaction.

Experimental procedures

The UHV low-temperature scanning tunneling microscope (STM) is described elsewhere [16]. It works down to 6 K and in magnetic fields up to 6 T perpendicular to the sample surface. The spectral resolution in STS is about 0.5 mV as determined from the sharpest peaks observed in dI/dV curves. This is in accordance with the expected thermal broadening of the Fermi level of the tip. Degenerate n-InAs ($N_{\mathrm{D}} = 1.1(1.8) \times 10^{16}/\mathrm{cm}^3$) is used. The dopant density and the degeneracy of the electron gas are checked by van-der-Pauw measurements at $T = 4 \ - 300$ K. The compensation ratio of the two samples has been directly deduced from STM images and is found to be 30 % and 10 %, respectively (see Fig. 3.72a). After in-situ cleavage at a base pressure below 1×10^{-8} Pa, the InAs-sample is transferred into the STM and moved down into the cryostat. The procedure results in a clean InAs(110)-surface with an STM-detectable adsorbate density of about $10^{-7}/\mathrm{\AA}^2$, an even lower surface vacancy density and a step density well below $1/\mu$m. Some of these steps are [112] steps. The samples have been directly used for the 3DES, 1DES and 0DES measurements. To induce the 2DES, Fe, Nb or Co is deposited on the surface from an e-beam evaporator. The coverage is either determined by counting the atoms (Fe, Nb) or by determining the coverage independently on a Au substrate (Co) [17]. The coverage is given with respect to the unit cell of InAs(110), i.e. one monolayer corresponds to one adsorbate atom per InAs unit cell. The purity of the adsorbates is checked by Auger electron spectroscopy.

The ex-situ etched W-tip is prepared in-situ by field emission and by applying voltage pulses up to 30 V and 10 ms between the tip and a W(110)-sample. All topographic images are recorded in constant-current mode with the voltage V applied to the sample. Most dI/dV curves are measured at fixed tip position with respect to the surface. The distance is fixed at a current I_{stab} and a voltage V_{stab} before the feedback is turned off. The $dI/dV(V)$ signal is then recorded by lock-in technique ($f = 1.5$ kHz, $V_{\mathrm{mod}} = 0.4 - 3$ mV$_{\mathrm{rms}}$) while sweeping the voltage. Maps of the LDOS presented here result mainly from arrays of dI/dV curves, where the spatial dependence of the dI/dV signal at a particular voltage is shown. Some of the dI/dV images are measured directly in constant-current mode. They are marked by I instead of V_{stab} and I_{stab}. It has been checked that the latter images do not show any important difference from the former. Finally, the influence of the spatially changing tip-surface distance has been checked to be of minor importance in these measurements and therefore has not been taken into account [2]. Several tests have been performed to check that the tip has not changed during a set of measurements, in particular dI/dV curves of the tip-induced quantum dot [7, 12] and the atomic resolution images are compared prior and after a set of measurements. The STS-measurements are performed at $T = 6 - 9\ K$. All images presented are raw data.

Magnetotransport-measurements were done in cooperation with I. Meinel (MARCH). They are performed in the Hall geometry in a standard He-bath cryostat at $T = 4.2$ K and at a current density of 0.5 mA/cm^2. The use of lower current densities did not change the observed transversal and Hall resistances but only lead to a worse signal-to-noise ratio, excluding spreading resistance effects. Both polarities of the magnetic field are used to properly separate Hall and transversal voltages.

Most angle-resolved ultraviolet photoelectron spectroscopy (ARUPS)-experiments are performed in cooperation with L. Plucinski and R. L. Johnson (Hamburg University). They are used to determine the adsorbate induced E_F shift and the resulting 2DES subband energies. ARUPS-spectra were taken with the VG ADES 400 spectrometer using s-polarized light from the Seya-Namioka monochromator at HASYLAB with photon energies $h\nu = 10 - 30$ eV . The 2DES samples are prepared identically as in the STS experiments. Partly, we used different doping levels, if explicitely mentioned in the text. The Fermi level E_F as well as the energy resolution of the instrument were determined for each photon energy using a clean Ta-foil as a reference. The data around E_F were fitted by the usual Fermi distribution curve. For $h\nu = 13$ eV, a pass energy of the analyzer $E_{pass} = 4$ eV and a temperature $T = 300$ K, we obtained an instrumental energy broadening of $\Delta E = 40$ meV. The angular resolution is known from fits of the angular resolved 2DEG peak to be $\pm 0.8°$. [9,10]

A set of four photoemission-spectra in normal emission was taken at each coverage to determine the E_F shift. Most of the ARUPS-spectra were recorded within $10 - 60$ min after cleavage or adsorbate deposition. Only ARUPS-spectra of the angular dependence of the 2DEG peak took longer (about 4 hours). At each coverage, we checked that no additional E_F shift occurred during the measurement by recording the same spectrum at the beginning and at the end of the measurement. The influence of the residual gas on the valence band spectra has been checked for the clean and the adsorbate covered surfaces and was found to be negligible.

High resolution ARUPS experiments are performed with s-polarized light from the Honormi monochromator at HASYLAB with photon energy $h\nu = 10$ eV in cooperation with R. Adelung, K. Rossnagel, L. Kipp, and M. Skibowski (Christian-Albrecht University Kiel). The energy resolution in this experiment was 20 meV and the angular resolution 0.25° in one and 0.45° in the other direction [18]. The Fermi level is determined on a clean Ta-foil with an accuracy of 5 meV.

3.4.2 Three-dimensional electron systems in the extreme quantum limit

The behaviour of electronic systems in the extreme quantum limit (EQL), where only the last spin-polarized Landau level is occupied by electrons, is of fundamental interest. It represents the interesting case, where the scales of kinetic energy, electron-impurity interaction and electron-electron interaction are all of the same magnitude. Moreover, their relative magnitude can be tuned by the magnetic field (B). While the kinetic energy E_{kin} decreases with increasing B-field due to the increasing degeneracy of the Landau level ($E_{kin} \propto 1/B^2$), the electron-donor interaction $E_{don,e}$ increases with increasing B-field due to the shrinking magnetic length ($E_{don,e} \propto \sqrt{B}$). The electron-

electron interaction depending in a complex way on the spin degeneracy, the degree of localization, and the extension of the individual states has usually the weakest dependence on magnetic field.
For the lowest available dopant concentration of InAs ($N_D = 1.1 \times 10^{16}$ cm^{-3}), we estimate for $B = 0$ T: $E_{kin} = 3/5\ E_F \simeq 7$ meV, $E_{exch} = 0.9$ meV$/r_s \simeq 2$ meV [20] and $E_{don,e} = 1$ Ryd$\times m_{eff}/\epsilon^2 \simeq 1.5$ meV with ϵ being the dielectric constant and r_s being the usual parameter to describe the ratio between Coulomb and kinetic energy [21]. Obviously, at low magnetic fields E_{kin} dominates, while at very high magnetic fields $E_{don,e}$ dominates, eventually leading to magnetic freeze out (MI-transition) [19]. In between, we expect a B-field region where the electron-electron interaction dominates by considering the fact that the exchange interaction E_{exch} increases in the EQL due to the spin polarization of the system, thus being larger than 2 meV and that $E_{don,e}$ is reduced effectively in real systems due to the overlap of adjacent donor potentials.
Indeed the transport properties of low gap materials (materials where the EQL is reached well below the onset of magnetic freeze-out) are peculiar [22–24]. They exhibit oscillations of the Hall constant that could not be explained by the oscillations of the density of states (DOS) at E_F [25]. In particular, above the EQL a strong reduction of the Hall constant up to 50 % has been observed [24], i. e. the shape of the Hall curve exhibits a step-like feature in the region between the EQL and the MI-transition (see Fig. 3.68). Another peculiarity is the resistivity parallel to the magnetic field. It decreases with increasing temperature. In contrast, the resistivity perpendicular to the magnetic field increases with increasing temperature in the region between the EQL and the MI-transition [23].
A convincing explanation of these pecularities has not been given, but several contradicting models have been proposed:

1. Mani assumed that the DOS at the lower energy edge of each Landau level is localized [26]. Although his model produces oscillations of the Hall constant, it fails to explain the experimentally observed reduction of the Hall constant.

2. Based on the observation of a double peak in cyclotron resonance experiments, Shayegan et al. proposed that donors sitting occasionally far apart from adjacent donors can bind electrons well below the MI-transition. Assuming that these regions do not contribute to the transport, they developed a model which more or less quantitatively reproduces the reduction of the Hall constant [24].

3. The preceding increase of the Hall constant (see Fig. 3.68c and d) has been explained qualitatively by Viehweger et al.. They assumed that both spin-polarized parts of the lowest Landau level exhibit a lower energy tail of localized states. Thus a reduced number of free electrons exists at the Fermi level E_F, if E_F is located in the lower energy tail of the upper spin-polarized lowest Landau level. This leads to an increased Hall constant at the transition to the EQL. The central argument is that states of opposite spin do not mix (absence of spin-orbit

coupling), thus maintaining the localized character of the states in the upper spin level [27].

4. A completely different explanation has been given by Aronzon et al., who assumed localized metallic droplets confined in larger scale potential fluctuations. Then the longitudinal transport is determined by hopping conduction between droplets, while the Hall constant is largely influenced by movement of electrons inside the droplets. A complex analysis of this model reproduces general trends of several experiments, but is not meant to be quantitative [30].

5. The most exciting proposal has been given by Murzin et al., who claimed that a so-called Hall insulator phase might exist between the metallic and the insulating phase at appropriate charge densities [23]. They analyzed the relation of the time scales for backscattering along the magnetic field, electron drift perpendicular to the magnetic field, and inelastic scattering. The corresponding model reproduces the temperature dependence of the resistivities. The authors claim that the system in the EQL becomes partly localized parallel to B and thus exhibits a quasi-2D character. This leads to the surprising conclusion that the oscillation of the Hall constant in the extreme quantum limit is a precursor of a quantized Hall step. For a so-called "three dimensional layer", which is a confined GaAs-layer with an elastic mean free path smaller but a coherence length larger than the thickness of the layer, they indeed observe several step-like features [31].
   Theoretical results by Chalker et al. point in the same direction [32]. They generalize a 2D network model to consider a 3D system and find that a quantized Hall conductor consisting of an insulating bulk and extended states at the edges can exist if E_F is located between individual Landau levels. However, since their model neglects the interaction between different Landau levels and the electron-electron interaction, they suppose that the Landau level interaction might destroy the quantized Hall conductor. Moreover, their analysis is restricted to a regular network, which differs from the typical random potential present in doped semiconductors.
   Azbel et al. study the case of a random potential using a semiclassical description of the electron orbits in 3D systems. They find wave functions reproducing 2D-like equipotential lines. Since such states are usually assumed to exist in 2D systems exhibiting the integer quantum Hall effect (QHE) [33], they suggest that an effect similar to the QHE also might exist in 3D [34].

Obviously, each of the five models predicts a different LDOS, respectively a different energy dependence of the LDOS. Mani's model results in localized states looking similar at the lower energy edge of each Landau level, Shayegan's model exhibits spatially isolated localized states at some dopants, Viehweger's model shows localized states exclusively in the lower band tails of the two spin-polarized lowest Landau levels, Aronzon's model gives rise to metallic droplets increasing in size with increasing energy up to the percolation level and Murzin's model results in states looking similar to equipotential lines of a 2D system as expected in real 2D systems. Since scanning tunneling spectroscopy (STS) images the energy dependent LDOS, it is the adequate technique to distinguish between these models. We used in-situ cleaved InAs to perform STS measurements at 6-9 K in magnetic fields up to 6 T and found that only the last model is compatible with our experimental results. Based on the data, we give a tentative explanation for the oscillation of the Hall constant in the EQL. A partial localization of the electrons explains the increase of the Hall constant. The increasing density of localized electrons with increasing B-field causes an overlap of adjacent localized states, which finally results in a one-dimensional (1D) network of states resembling equipotential lines of a 2D potential landscape. Assuming that these states act as 1D conductors and that the network of 1D conductors has a lower resistance than the residual 3D electron gas, we straightforwardly explain the reduced slope of the Hall constant as a precursor of a quantized Hall step.

The next five sections describing the 3DES LDOS are organized as follows. After showing transport measurements and describing in detail the influence of the probe on the LDOS, we interpret the results concerning the 3D system. In particular the energy, temperature and B-field dependence of the LDOS are discussed. Then we describe possible origins of the quasi 2D character of the 3DES and give a tentative explanation of the behaviour of the Hall resistance. Finally, we show that a pseudogap evolves at the Fermi level compatible with the quadratic gap predicted by Efros and Shlovskii [42] in the case of localization.

Magnetotransport

Figure 3.68 shows the magnetotransport data of the two investigated samples. The low doped sample exhibits lower mobility leading mostly to $\rho_{xy}/\rho_{xx} = \omega_c \cdot \tau \leq 1$ (ω_c: cyclotron resonance, τ: momentum relaxation time). For the higher doped sample, we find $\omega_c \cdot \tau \geq 1$ in a large B-field range, where we consequently observe Shubnikov-de-Haas oscillations. The transition to the EQL, as calculated from the development of the DOS in magnetic field, is marked [30]. At this field, we observe the knee-like structure in ρ_{xy} in agreement with earlier results [23]. The plot of the Hall constant $R_H = \rho_{xy}/eB$ is given in Fig. 3.68 c and d and exhibits the well-known oscillations [22]. The understanding of the last oscillation within the EQL is the aim of this section. But, first, we make sure that STS indeed measures the LDOS of the 3DES.

The influence of the probe

Since it is well known that the probe in scanning tunneling spectroscopy can change the DOS of a semiconductor sample [12, 35, 36], it is important to study the influence of the probe in detail. This section is exclusively devoted to the influence of the probe. The physical content of the results is described in the next sections. Fig. 3.69

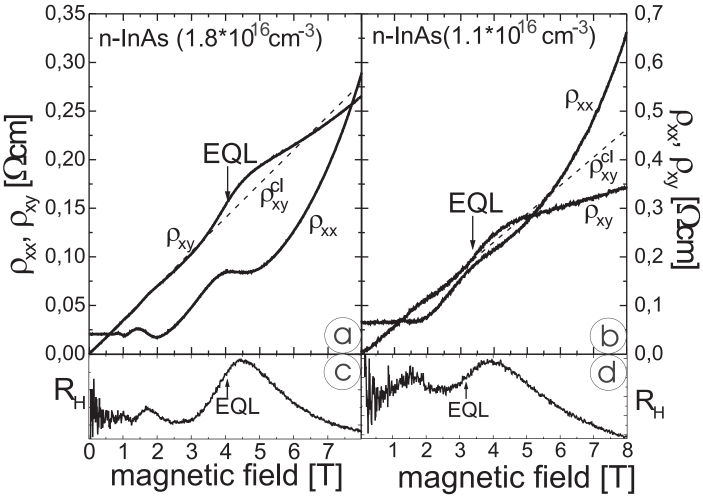

Figure 3.68: Magnetotransport measurements of n-doped InAs at $T = 4.2\,\mathrm{K}$: a.) $N_\mathrm{D} = 1.8 \times 10^{16}\,\mathrm{cm}^{-3}$; b.) $N_\mathrm{D} = 1.1 \times 10^{16}\,\mathrm{cm}^{-3}$; c.), d.) Hall constant $R_\mathrm{H} = \rho_{xy}/eB$ deduced from a.) and b.), respectively; measurements are performed with both orientations of B and the average is taken to avoid influences of improper contacts. The transition to the extreme quantum limit (EQL) as well as the classically expected Hall resistance $\rho_{xy}^{cl} = B/ne$ is marked.

shows the reproducibility of the observed patterns in dI/dV images. The two images are obtained on the same surface area, but two weeks passed in between the two measurements. Obviously the patterns are reproducible in all details. Only a lateral shift caused by the thermal drift of the STM (1 Å/ hour) can be seen. An influence of adsorption from the residual gas can be excluded on the base of these images. From previous measurements, we expect the adsorption of no more than 2 adsorbates on the depicted surface area during the two weeks. Indeed some minor changes of the LDOS patterns are sometimes observed on that time scale.
In addition, the two images in Fig. 3.69 are measured with reversed magnetic field

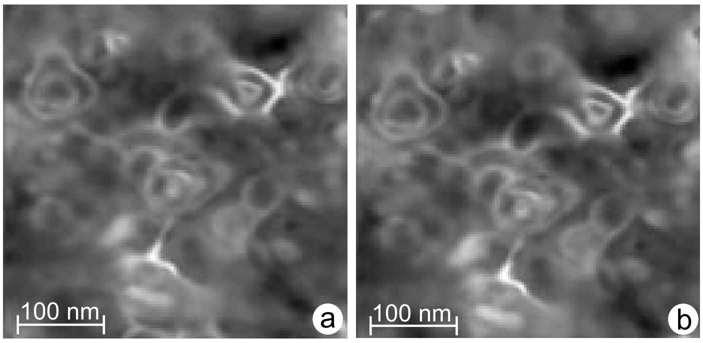

Figure 3.69: Two dI/dV images recorded on the same surface area; $V = 55$ mV, $I = 500$ pA, $T = 6$ K; a.) $B = 6$ T; b.) $B = -6$ T, b.) is recorded two weeks later than a.)

direction. This demonstrates that the broken time reversal symmetry does not act on the observed patterns, which is not surprising since STS measures the LDOS, which is time independent.

Fig. 3.70 shows dI/dV images of a particular area measured at $V = 0$ mV with $V_{stab} = 100$ mV and different I_{stab} and V_{mod}. Histograms of the contributing dI/dV values are added and related to the images by arrows.

The change of I_{stab} (top to bottom) tests the influence of the charge provided by the tunneling current. It might lead to so-called spreading resistance effects [36]. However, the patterns are not changed by increasing I_{stab} from 50 pA to 300 pA. Also the histograms of obtained dI/dV values are rather similar for both images, if scaled by the factor of six in I_{stab}. In contrast, slight changes of the patterns can be observed in the upper left corner at $I_{stab} = 500$ pA. These results exclude an important influence of the spreading resistance up to $I_{stab} = 300$ pA.

The change of V_{mod} (left to right) influences the energy resolution of the experiment, i.e. the energy interval contributing to the observed LDOS ($\delta E \simeq 2.5 \times V_{mod}$). At lower V_{mod} less states contribute to an image. Therefore the sharpness of the LDOS pattern increases with decreasing V_{mod}. This is indeed found down to about $V_{mod} = 1 - 2$ mV. Nevertheless, the images remain nearly unchanged for a further decrease down to $V_{mod} = 0.4$ mV (see also histograms). This result is reasonable, since the energy resolution is additionally restricted by the finite width of the Fermi distribution at the tip. A total energy resolution of $\delta E \simeq \sqrt{(3.3kT)^2 + (2.5V_{mod})^2}$ with $kT = 0.5$ meV

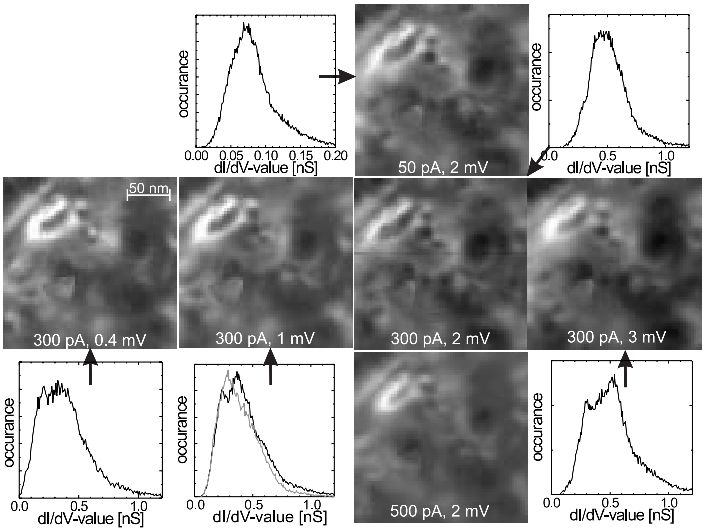

Figure 3.70: a.) dI/dV images, $B = 6$ T, $V = 0$ mV, $V_{stab} = 100$ mV, $T = 8$ K, I_{stab} in pA and V_{mod} in mV is marked in the lower parts of the images; histograms of the dI/dV values of some of the images are shown and related to the corresponding images by arrows. The light grey curve in one of the histograms results from an additional measurement of the same surface area with the same parameters showing the reproducibility of the histograms. The small differences are due to different noise levels.

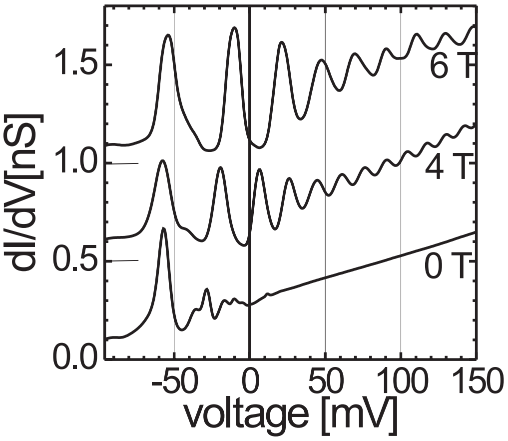

Figure 3.71: Spatially averaged dI/dV curves, $V_{stab} = 200$ mV, $I_{stab} = 300$ pA, $V_{mod} = 2$ mV, $T = 8$ K, B as indicated. Notice that the movement of the Landau levels with B-field points to an origin close to -50 mV, which is the ground state of the tip-induced quantum dot and not to an origin at -10 mV, which would be the conduction band minimum of the 3DES.

($T = 6$ K) results.

In turn the observed changes down to $V_{mod} = 1$ mV give additional evidence that the energy resolution of our experiment is indeed restricted by temperature and not by additional high-frequency noise [37]. The histograms obtained for different V_{mod} are nearly identical but the onset of the histograms at low dI/dV increases with increasing V_{mod}. This is expected from the overlap of additional states contributing to the dI/dV signal at higher V_{mod}.

With the experimentally confirmed energy resolution down to $\delta E = 3$ meV, we can estimate the average number of states depicted in an image (eq. 3.14). We take the coherence length $\lambda_{coh} = 100$ nm estimated from the visible length scale of scattering states around individual dopants [2,15] as the depth up to which states contribute to the tunneling current. With a calculated finite lifetime broadened DOS $D(E)$ as the state density at $B = 6$ T [13], we obtain $N \simeq D(E) \cdot \delta E \cdot \lambda_{coh} \cdot A = 25$ states on an area $A = 200 \times 200$ nm^2, respectively an average area per contributing state of about $A_n \simeq 40 \times 40$ nm^2.

Next, the influence of the electric field of the tip has to be discussed [35]. Since our measurements are restricted to low applied voltages, the field mainly results from the difference in work function between the tip and the sample leading to the so-called tip-induced quantum dot (QD) [12]. The QD has a vertical extension of about 40 nm and a lateral diameter of about 100 nm. Its potential depth varies from tip to tip between 100 and 400 meV. The QD contains quantized states extended down to about 10 nm below the surface [38]. In magnetic field, these states are classified by three quantum numbers: the Landau level number n, the orbital momentum m and the spin s. In previous measurements, we found that only the $m = 0$ states, which have a lateral diameter (FWHM) of the magnetic length ($l_b = 10$ nm at 6 T), can significantly couple to the tunneling current [13]. Consequently, the averaged dI/dV

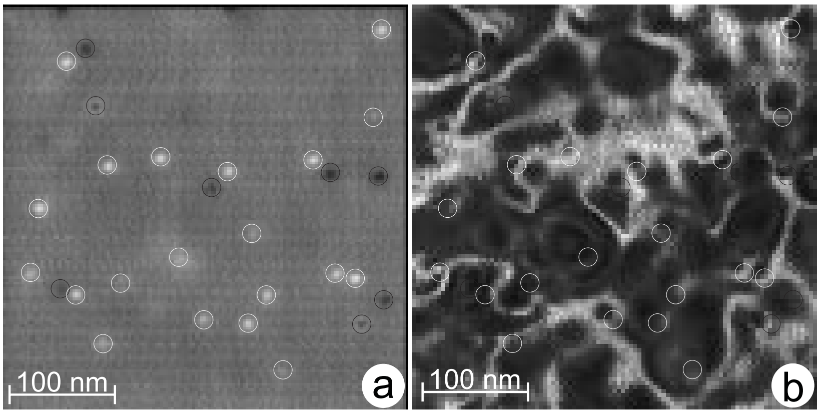

Figure 3.72: a.) Constant-current image, $V = 100$ mV, $I = 500$ pA, bright and dark spots resulting from charged donors and acceptors located down to about 8 nm below the surface [38] are encircled white and black, respectively. The diameter of the circles is the screening length of the sample, thus marking the effective potential length of individual dopants; b.) dI/dV image of the same surface area, $V = 0$ mV, $V_{stab} = 100$ mV, $I_{stab} = 300$ pA, $V_{mod} = 1$ mV, $T = 7$ K, $B = 6$ T; the same circles as in a.) are drawn.

curves are dominated by ($m = 0$) states exhibiting Landau and spin levels of the QD. Often, the spin levels are not visible due to inherent broadening effects [13]. Fig. 3.71 shows dI/dV curves at different magnetic fields illustrating that the observed Landau levels indeed belong to the QD. They point to an origin at $V = -50$ mV and not to an origin at $V = -6$ mV, which would be the onset of the bulk conduction band.
Naturally the question arises if the observed LDOS patterns in dI/dV images also belong to a spatial dependence of the QD states. Several experimental observations contradict this assumption:

1. The observed contrast visible in Fig. 3.69 and 3.70 always appears at the transition to the EQL of the bulk 3DES, although the ground state of the quantum dot varies between -50 meV and -100 meV leading to completely different filling factors of the QD at this B-field.

2. The dopants influencing the QD states are located down to about 10 nm below the surface. They are directly visible in constant current images. Fig. 3.72 shows a constant-current image and a dI/dV image ($B = 6$ T, $V = 0$ mV) of the same surface area. It proves that there is no obvious correlation between the dopants and the observed contrast. To illustrate that, circles with the diameter of the screening length surround the dopants and thus mark the length scale of the dopant potential. Obviously, strong contrasts exist far away from these areas.

3. The influence of the fluctuating surface potential on the Landau levels of the QD has already been analyzed. It leads to a weaker contrast with a lateral fluctuation length of about 50 nm [15]. Depending on the actual QD the markedly

different serpentine contrast shown in Fig. 3.69 and 3.70 changes its intensity with respect to the long range QD contrast. Sometimes the QD contrast dominates [15], sometimes the serpentine 3D contrast dominates [39], and sometimes both contrasts coexist as in Fig. 3.73. Notice, that the long range QD contrast oscillates with the energy distance of the Landau levels (marked circle), while the more elaborate serpentine contrast exhibits a different, monotonous energy dependence.

4. Analyzing the relative strength of the corrugation $C(V)$ as a function of voltage, one finds that the 3D contrast is most intense in energy regions away from the QD energy levels. This is shown in Fig. 3.74. The upper part is a spatially averaged dI/dV curve. Its maxima mark the Landau levels of the QD. The corrugation strength $C(V)$ is determined by

   $$C(V) = \frac{\sum_{x,y}[dI/dV(x,y,V|dI/dV > t) - t]}{\sum_{x,y} dI/dV(x,y,V)} \tag{3.15}$$

   The threshold t is chosen arbitrarily such that only 10 % of the dI/dV values are smaller than t. Obviously, C(V) is not strongest at the maxima of the dI/dV curve (see arrows).

These arguments exclude the possibility that the LDOS of the QD dominates the observed serpentine contrast. However, it does not exclude the possibility that charging

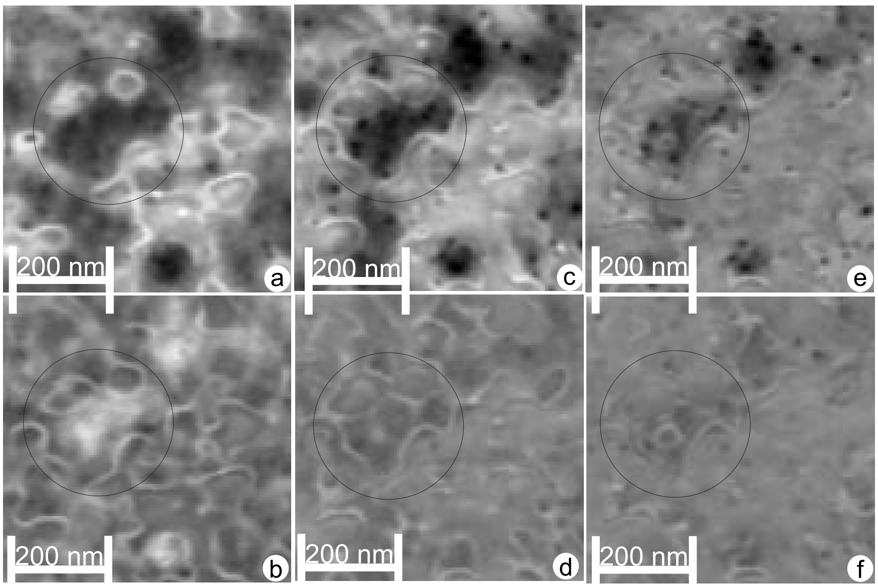

Figure 3.73: dI/dV images measured with a tip exhibiting both, the 3D caused serpentine contrast and the long range QD contrast (see text). An area showing the latter contrast most pronounced is encircled. Notice that the long range contrast (QD) oscillates with energy, while the serpentine 3D contrast shows a monotonous energy dependence; $I = 500$ pA, $T = 6$ K, $B = 6$ T, $V_{mod} = 1$ mV; a.) $V = 50$ mV; b.) $V = 60$ mV; c.) $V = 70$ mV; d.) $V = 80$ mV; e.) $V = 90$ mV; f.) $V = 100$ mV;

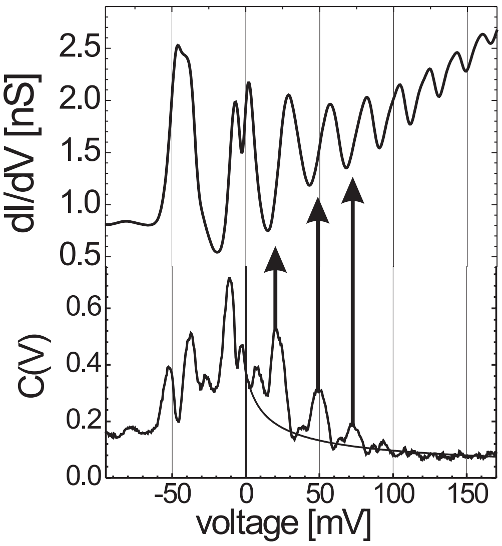

Figure 3.74: Upper part: spatially averaged dI/dV curve obtained with a specific tip-induced quantum dot, $I_{stab} = 500$ pA, $V_{stab} = 200$ mV, $B = 6$ T, $T = 7$ K, lower part: corrugation strength $C(V)$ determined from a (150 nm)^2-area as described in the text. The curves correspond to the images shown in Fig. 3.76. Arrows compare the energies of largest contrast with the dI/dV curve. The small line in the lower part indicates the expected $1/\sqrt{E}$-dependence of the DOS of the lowest Landau level.

phenomena of the QD exist and lead to the observed contrast. A possible scenario would be that the QD probes the complex potential landscape necessary for the QD to be charged by an additional electron. Such an effect has been observed in the capacitance experiments by Ashoori et al. on a 2D system [40]. However, a quantitative estimate rules out this possibility. Assuming single electron charging effects detected with $U_{mod} = 1$ mV and $f = 1.5$ kHz, a conductivity change of $3 \times 10^{-13} S$ is expected. In contrast, the detected change in conductivity leading to the observed contrast is about $10^{-9} S$, i.e. significantly larger. We conclude that the origin of the serpentine contrast is not the QD but the 3D electron system (3DES) of the semiconductor.

To explain the experimental observation of the 3D DOS in the presence of the QD, we like to give a plausible argument. Obviously all electrons within the coherence length λ_{coh} contribute to the local DOS probed by the tip. The extension of the QD is smaller than λ_{coh}. Especially the extension of the confined charge in the QD is about an order of magnitude smaller that λ_{coh}. Consequently, the QD is only a perturbation to the probed local DOS. It is strongest close to the surface but disappears deeper into the bulk. Naturally, it should also be strongest at energies where confined states of the QD exist. Depending on the actual QD the observation of a patterned LDOS of the 3DES might be inhibited due to strong mixing of QD states with the 3DES, but there is no reason that this mixing must inhibit the observation. To put it differently, one can imagine that the confined QD states act as part of the scanning probe. Thus they

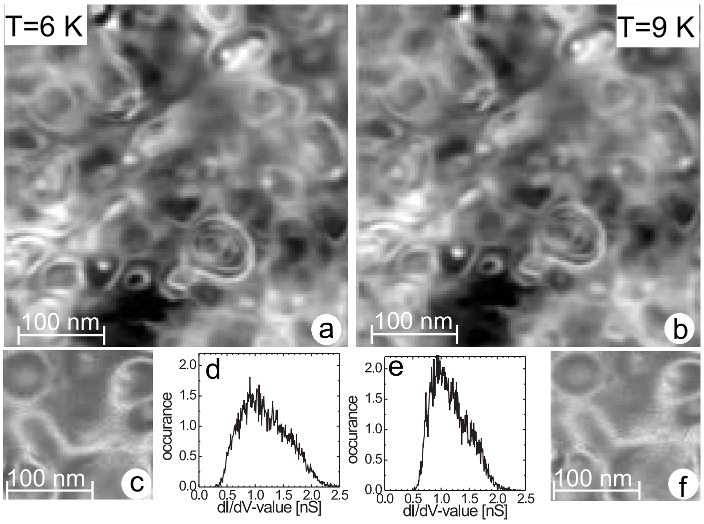

Figure 3.75: dI/dV images measured at different temperature T, $V_{mod} = 1$ mV, $I_{stab} = 500$ pA, $B = 6$ T; a.) $V = 55$ mV, $T = 6$ K; b.) $V = 55$ mV, $T = 9$ K; c.) $V = 0$ mV, $T = 6$ K; d.) histogram corresponding to c.); e.) histogram corresponding to f.); f.) $V = 0$ mV, $T = 9$ K.

mainly restrict the possible lateral resolution.
However, this scenario requires a consideration of the disturbing influence of the probe states on the 3D DOS. It is reasonable to assume that a similar intensity of the 3D DOS couples similarly to the QD DOS. Moreover, it is likely that the coupling does not invert the dI/dV contrast with respect to the 3D LDOS patterns. So we assume that the measured patterns indeed reflect the 3D DOS, although we can not exclude slight changes due to the QD DOS.

Temperature and energy dependence of the local DOS in the EQL

After having established that the 3D DOS is imaged in our experiment, we will discuss its temperature and energy dependence. Fig. 3.75 shows dI/dV images obtained at $B = 6$ T and slightly different temperature T. The small T-change induces no obvious change in the LDOS patterns, but the contrast becomes markedly weaker as proven by the two histograms plotted for the ($dI/dV(V = 0$ mV))-images. They contain less dI/dV values (x axis) with increasing T. There are two possible reasons for this decreasing contrast. On the one hand, the slightly decreased energy resolution due to the Fermi level broadening at the tip could be responsible. However, according to the formula given above, δE does only change from 3 meV to 3.5 meV. As shown in Fig. 3.70 the much stronger change in V_{mod} from 1 mV to 3 mV changes the intensity distribution much less. On the other hand, the 3D DOS of the sample also depends on temperature as can be deduced from the smaller decrease of the Hall constant in the EQL at increased temperature [23]. We believe that the observed decreasing

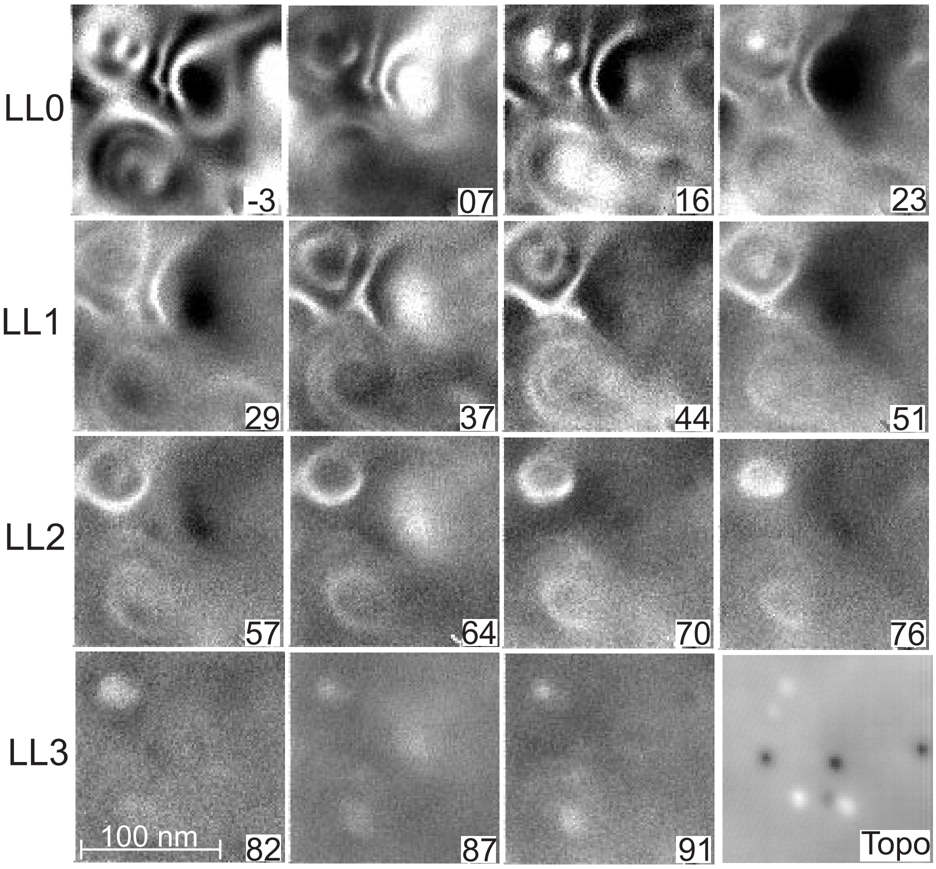

Figure 3.76: dI/dV images (all of the same surface area), I_{stab} = 500 pA, V_{stab} = 200 mV, V_{mod} = 1 mV, B = 6 T, T = 7 K; V in mV is indicated in the lower right corner of the images. The images are ordered, so that each line corresponds to one Landau level (LLn) of the 3DES. The image contrast is aligned, so that the same gray values represent the same differential conductivity dI/dV in all dI/dV images. The last image (Topo) is a constant-current image of the same area, V = 70 mV, I = 500 pA; the corresponding spatially averaged dI/dV curve and the observed contrast $C(V)$ are shown in Fig. 3.74.

contrast coincides with the observed raising Hall constant. Thus, we conclude that the corrugated part of the 3DES LDOS decreases with increasing T.

Next, we discuss the energy dependence of the LDOS in the EQL. Fig. 3.76 and Fig. 3.77 show three sets of energy dependence of dI/dV images. The last two sets are measured on the same sample area at different magnetic fields. The contrast in each set is aligned, i.e. the same gray value represents the same differential local conductivity dI/dV. Topographic images are added showing again that there is no obvious correlation between dopant positions and contrast. In Fig. 3.77b and c the spatially averaged dI/dV curve is compared with the contrast $C(V)$. The same is shown in Fig. 3.74 for the dI/dV images in Fig. 3.76. Again the contrast is strongest away from the QD states. Moreover, the contrast becomes weaker with increasing energy. The functional dependence of the decrease of the contrast is ambiguous, but, as indicated by the drawn $1/\sqrt{E}$-lines, it is compatible with the decrease of the DOS in the lowest Landau level. Surprisingly, the contrast persists up to an energy of about 90 meV, where already four Landau levels contribute to the measured dI/dV signal (Fig. 3.76).

Most interestingly, the serpentine structures exhibit an energy dependence resembling equipotential lines of a 2D system [40,41]. Each image corresponds to a different set of equipotential lines, respectively a different potential value. According to theory states along equipotential lines are indeed expected for 2D systems [33]. The surprising fact that we find such states also in 3D is discussed below. Considering the energy dependence of individual lines, and assuming that the change of curvature indicates a saddle point of the corresponding potential, we conclude that the relevant potential spatially fluctuates on the order of 50 meV and exhibits one extremum on an area of about $(50\text{ nm})^2$. These values are reasonable considering the doping level of the sample. The contrast patterns are similar for $B = 4$ T and $B = 6$ T (Fig. 3.77), but obviously the contrast at 4 T is weaker, which correspondingly leads to slightly lower $C(V)$-values.

Notice that a minimum in the averaged dI/dV curves is always observed at $V = 0$ mV, respectively E_F (Fig. 3.74, 3.77b and c). At $B = 4$ T the minimum is less obvious, since it falls in an energy region of low dI/dV intensity, but still exists. Interestingly, we found this minimum always, when the 3D contrast is observed, but not if only the QD contrast is visible. In [39] we show that the depth of this gap largely determines the observed 3D contrast at E_F. There we interpret the minimum as a result of a Coulomb gap caused by partial localization of 3D electronic states.

Magnetic field dependence of the local DOS at E_F

Next, we discuss the magnetic field dependence of the LDOS. We focus on the behaviour at E_F to directly compare our data to the transport measurements of Fig. 3.68. Fig. 3.78a–g show dI/dV images obtained at different B-fields and at $V = 0$ mV (E_F). The Hall curve and the corresponding Hall constant are shown for comparison in Fig. 3.78i. The onset of the EQL determined by calculating the position of E_F in the DOS, consisting of Landau and spin bands, is marked by a dashed line. Again all images have the same contrast meaning that the local conductivity at constant tip-surface distance is shown. $C(V)$ obtained according to eq. 3.15 is also given in Fig. 3.78h. For the purpose of comparison the $C(V)$-values from another data set (different tip, different area) are included. It is obvious that the contrast increases with increasing magnetic field. Moreover, the contrast is markedly below 100 % at the highest available B-field.

The pattern itself appears rather uncorrugated at low magnetic fields. At $B = 2$ T only the long range contrast attributed to the properties of the QD states is visible [15]. Close to the EQL ($B = 3$ T), a contrast of smaller length scale appears which becomes stronger with increasing field. Up to about $B = 4$ T isolated patterns of this

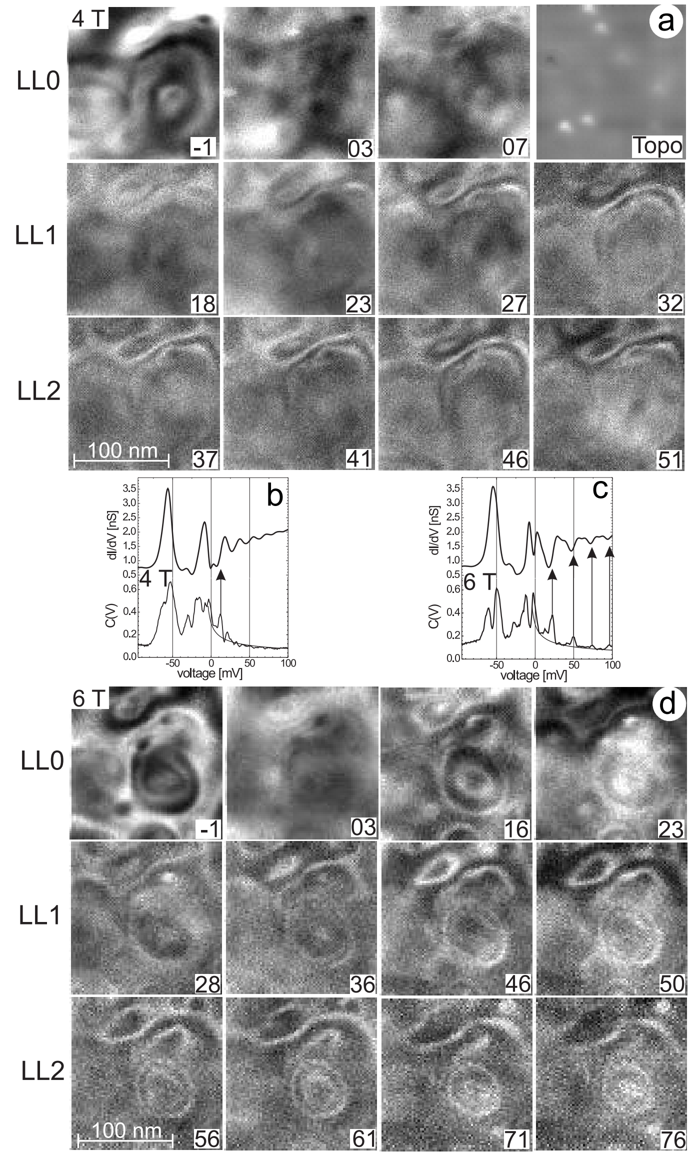

Figure 3.77: a.) dI/dV images at different V indicated in the lower right corner in mV, I_{stab} = 500 pA, V_{stab} = 100 mV, V_{mod} = 1 mV, B = 4 T, T = 7 K, the fourth image (Topo) is a constant-current image of the respective surface area, V = 55 mV, I = 500 pA. The image contrast is aligned, so that the same gray values represent the same differential conductivity dI/dV in all dI/dV images; b.) spatially averaged dI/dV curve and $C(V)$-curve corresponding to a.). The small line marks the $1/\sqrt{E}$ dependence of the DOS in the lowest Landau level. Arrows mark the energies of maximum contrast; c.) same as b.) but for the images in d.); d.) dI/dV images of the same surface area as depicted in a.) but for B = 6 T. All other parameters are identical.

contrast do not overlap. At higher fields above $B = 5$ T the isolated patterns start to overlap forming a network of stripes penetrating the whole area. The width of the

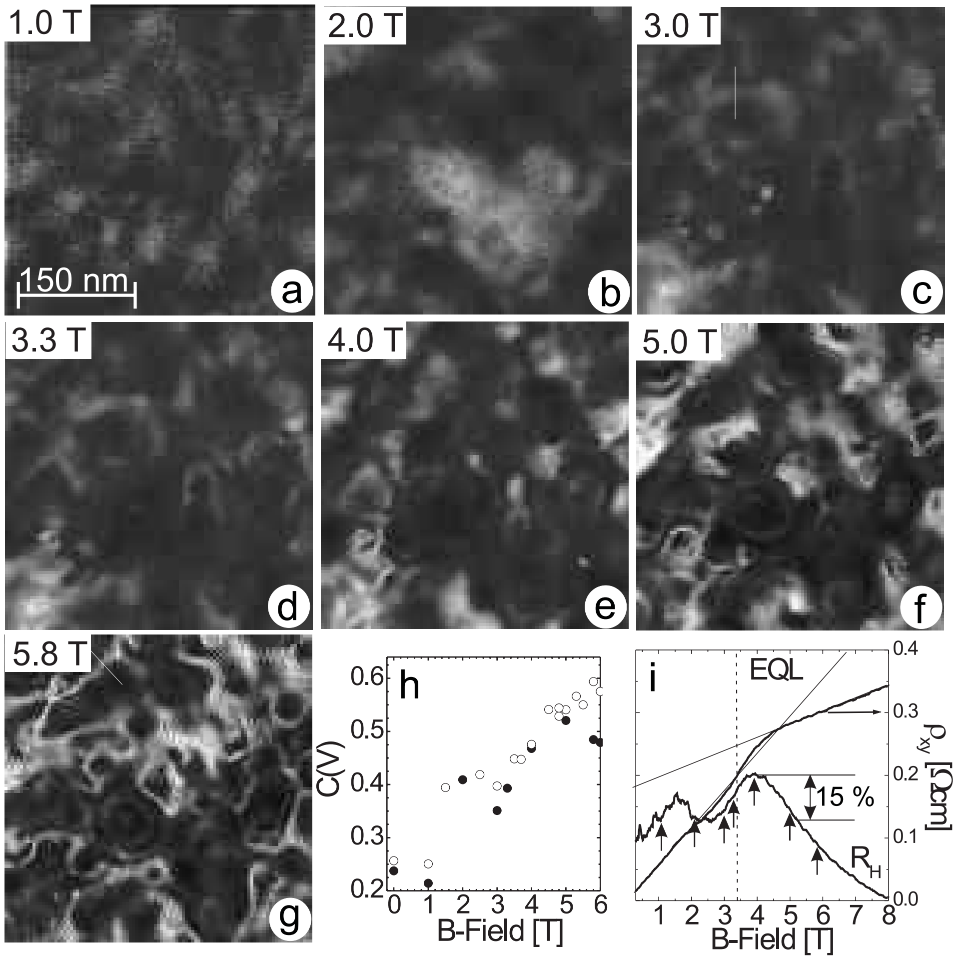

Figure 3.78: a.)-g.) dI/dV images of the same surface area obtained at $V = 0$ mV and different magnetic fields B as indicated, $I_{stab} = 500$ pA, $V_{stab} = 100$ mV, $V_{mod} = 1$ mV, $T = 6.5$ K; a constant-current image of the same surface area is given in Fig. 3.72a.); the small white lines in c.) and g.) mark the direction of line sections shown in Fig. 3.79; the image contrast is aligned, so that the same gray values represent the same differential conductivity dI/dV in all dI/dV images; h.) C(V=0 mV) values at different B; white circles correspond to the shown data set, black circles to another data set obtained at a different surface area with a different tip; i.) Hall resistance ρ_{xy} and Hall constant $R_H = \rho_{xy}/eB$ of the sample investigated in a.)-g.). The onset of the EQL is marked by a dashed line; the different slopes of the Hall resistance are marked by two thin straight lines; the B-fields corresponding to the images are marked by arrows at the R_H-curve; the 15 % increase of R_H at $B = 4$ T is also marked.

serpentine structures is about the magnetic length (l_b) as demonstrated by the line scans indicated in Fig. 3.78c and g and shown in Fig. 3.79 in comparison with l_B.

How can we correlate these observations to the behaviour of the Hall constant? At $B = 4$ T, the Hall constant has a maximum being about 15 % larger than the classically expected Hall constant $1/ne$ (n: charge density). In this region the serpentine patterns at E_F are still isolated. It is tempting to assume that the isolated patterns represent localized states, although we can not prove their localized character directly. Taking the number of imaged states in Fig. 3.78, $N \simeq 100$, we expect about 15 localized states at $B = 4$ T from the measured increase of the Hall constant. This loosely corresponds to the number of patterns observed. Moreover using a different, more adequate procedure to determine the corrugated part of Fig. 3.78e depicted in Fig. 3.80, we find indeed that about 15 % of the LDOS is corrugated. So we interpret the increase of the Hall constant straightforwardly as a decrease of the free charge carrier density n caused by partial localization. The existence of the pseudo gap discussed below is another indication of partial localization.

At higher B-fields the Hall constant drops up to 30 % below the classical value $1/ne$. At the same magnetic fields the isolated patterns of the LDOS start to overlap and form a network of channel structures penetrating the whole sample. Notice that some of the structures are not included in the network, which probably remain as localized states. As mentioned above the width of the channels is about the magnetic length. The average distance of the channels is about 150 nm and the distance between nodes in the network is also about 150 nm. It is natural to assume that the channels act as one-dimensional conductors analogous to the edge channels in 2D systems [33]. While individual channels must exhibit dispersionless transport properties and a universal Hall resistance of h/e^2, the nodes in the network allow backscattering resulting in a finite resistance of the network. A good estimate of the mean free path in the network is about twice the distance between nodes assuming a backscattering probability of 0.5 at each node. This is considerably larger than the mean free path of the 3DES

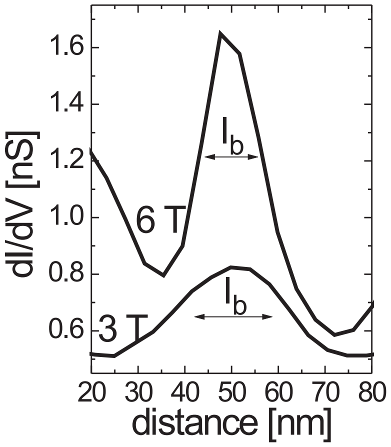

Figure 3.79: Line sections across typical serpentine structures (along the white lines in Fig. 3.78); the magnetic length l_b at the two different B-fields is marked.

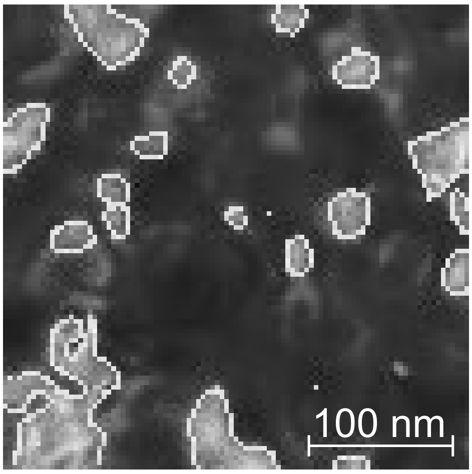

Figure 3.80: Same dI/dV image as shown in Fig. 3.78e. The enclosed areas mark the intuitively assigned strong corrugations attributed to localized states. They correspond to 15 % of the total LDOS.

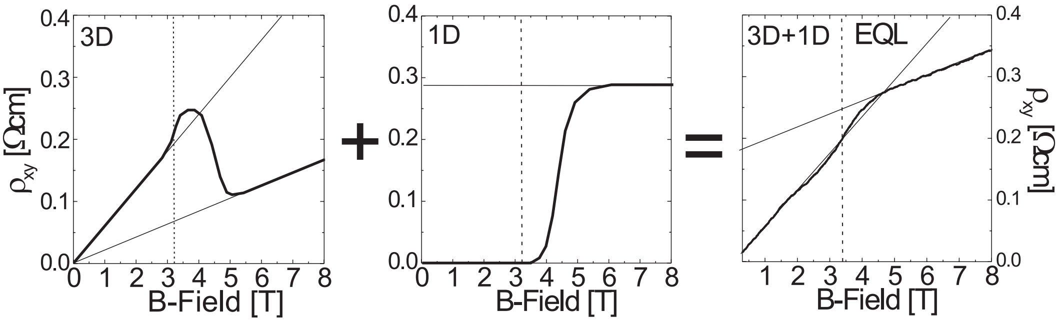

Figure 3.81: Tentative model to explain the Hall resistance in the extreme quantum limit (EQL). The 3D part increases first similar to B/ne. At $B = 3$ T localization sets in reducing the effective charge density n and thereby increasing the Hall resistance. Finally, around $B = 5$ T, parallel conduction through a 1D network sets in reducing the carried current by the 3D charge density and thereby the corresponding Hall voltage (left image). The 1D part gives rise to a Hall plateau caused by the conduction via the 1D network (middle image). Adding the two curves results in a curve very similar to the measured one (right image).

($\leq$ 60 nm). Thus the network resistivity is lower than the 3D resistivity.

From the T-dependence of the contrast (Fig. 3.75) and the $C(V)$-values obtained at $B = 6$ T, we conclude that the corrugation leading to the serpentine structures does not contain 100 % of the 3D DOS. So a part of the DOS remains uncorrugated at the temperatures and B-fields investigated. This part of the DOS should maintain its 3D transport character leading to the usual Hall effect. Assuming that the uncorrugated and the corrugated DOS act as parallel resistors, we can give a tentative explanation of the reduced Hall slope. Since the mean free path of the 3DES is lower than the mean free path in the network, it is clear that the average drift velocity $\overline{v}_{network}$ in the network is larger than $\overline{v}_{3DES}$ of the 3DES, exactly by the ratio of the mean free paths. Since the total current in the experiment is constant, $\overline{v}_{3DES}$ determining the Lorentz force on the 3DES electrons is reduced with resepct to the average drift velocity of the whole system. Consequently the Hall slope caused by the 3DES is reduced by about the ratio of the mean free paths. On the other hand, the Hall voltage resulting from the network ($U_{H,network}$) should lead to a Hall plateau if the number of channels remains constant over the corresponding B-field range. It can be estimated to

$$U_{H,network} = I \cdot \frac{\overline{v}_{network} \cdot d_{network} \cdot h}{(\overline{v}_{network} + \overline{v}_{3DES} \cdot n_{3DES}/n_{network}) \cdot d_{sample} \cdot e^2} \tag{3.16}$$

with $d_{network} \simeq 150$ nm being the distance of channels perpendicular to the current, $d_{sample} = 3$ mm being the width of the sample and $n_{network}$, n_{3DES} being the corresponding charge densities (h is Planck's constant). Using $\overline{v} \propto \sqrt{\lambda}$ and a relation $n_{3DES}/n_{network} \simeq 0.5$ estimated by the same method as shown in Fig. 3.80, we get $U_{H,network}/I = 1\Omega$. Addition of the two Hall voltages reproduces the shape of the Hall curve as shown in Fig. 3.81. This leads us to the surprising assumption that two independent conducting phases coexist in the 3D system. Moreover the step-like structure in the Hall resistivity is indeed explained as a precursor of a quantized Hall step.

We like to stress that the above model is tentative for several reasons. First, we can not rule out a small remaining influence of the QD on the 3DES DOS. Second, the estimates used above have errors, adding up to an error of the Hall voltages of about 50 %. Third, we do not have an experimental proof that the channels are indeed 1D, since we do not image the DOS parallel to B. Fourth, we can not prove that the network indeed penetrates the entire sample. Finally the coexistence of two independent DOS phases overlapping in space and energy is at least surprising and needs some verification from theory.

Tentative model

It is tempting to test the models described in the introduction in the light of the new results. The Mani model [26] is obviously wrong, since the corrugations are not restricted to small energy intervals at the tails of the Landau levels. Moreover the patterns do not show any periodicity with the Landau levels (distance 30 meV at $B = 6$ T) as expected for this simple model. Shayegan's model predicts localized states at some dopants [24]. Since he gives an explicit formula for the number of localized states, we can calculate that in a (400 nm)^2 area only 0.4 dopants, which are 70 nm apart from each other dopant, should exhibit a localized state at $B = 6$ T, again assuming that only states within the coherence length of 100 nm are visible. This is in obvious contradiction to the STS results which show corrugations homogeneously distributed over the whole images. Viehweger argues that localized states exist in the tail of the upper spin level of the lowest Landau level. Indeed, we find corrugations in that region, but the corrugations are not restricted to this energy region, but smoothly distributed over a much larger energy range making this model also doubtful. Aronzon argued that metallic droplets exist in large scale potential fluctuations. This implies that channels of reduced DOS should separate the droplets. Moreover, the potential fluctuations should be increasingly filled with states with increasing energy up to the percolation level. Neither is found in our measurements ruling out this model as well. The predictions for the LDOS of the last model proposed by different authors independently [23, 32, 34] are given explicitly by Azbel for similar conditions as in our experiment [34]. Indeed the patterns obtained by the semiclassical calculation are rather similar to the patterns we observe, and indeed an effect similar to the quantum Hall effect in 3D is predicted in accordance with our analysis. The same prediction is given by Chalker [32] using a modified network model to calculate 3D states. However, he finds extended states only at the edge of the sample. Probably the regular network used in the calculation is the reason for this result which is not in accordance with our findings. Murzin [23] gives a more qualitative argument to explain the behaviour of the 3DES in the EQL: He argues that the increased probability for backscattering parallel to an increasing magnetic field, which is caused by a reduced kinetic energy in that direction and the reduced drift velocity perpendicular to the field, leads to a z-localization of states in potential fluctuations. He does not give explicit predictions for the resulting LDOS. However, since the backscattering length must be of the order of the mean free path of 60 nm, potential fluctuations on that length scale should lead to localization. Since this length scale is larger than the magnetic length ($l_B \simeq 10$ nm), an effective 2D character of the electron system in these fluctuations results and states resembling equipotential lines of the resulting 2D potential appear [33].

With increasing magnetic field or decreasing temperature a larger part of the sample exhibits effective backscattering within the time the electron drifts inside the corresponding potential fluctuation without loosing its phase coherence due to inelastic scattering.

We believe that the complex connection of these different local 2D areas finally leads to the effective 2D-like behaviour of the LDOS observed experimentally. The fact that we observe extended states (networks) at several energies of the same Landau level (see e.g. Fig. 3.76), in contrast to predictions in 2D [33], is probably related to the 3D coupling of the 2D-like droplets.

Notice that even at 6 T and 6 K, only a part of the LDOS is corrugated, since there exists a remaining part that is not effectively backscattered before it drifts out of the corresponding potential fluctuation or gets scattered inelastically. This directly explains the remaining uncorrugated DOS and the increased corrugation with decreasing T. Since such a model nicely corresponds to our results, we believe that a 2D like patterning of the 3D DOS indeed happens.

A rather surprising observation is the fact that the corrugations appear to influence the DOS of the lowest Landau level up to very high energies, where it overlaps energetically with as many as three other Landau levels. A reason might be that the different symmetry of the states of different Landau levels parallel to the B-field reduces the mixing of states of different Landau levels.

Consequences of localization in the EQL: pseudogap at E_F and broadening of $f(\alpha)$ spectra

The analysis above assumes that the corrugation patterns observed in dI/dV-images in the EQL are related to localized states. This implies that the DOS must exhibit a pseudogap at E_F [42]. From quasiclassical considerations of interacting localized particles, Efros and Shlovskii deduce a shape of this gap corresponding to $DOS(E) \propto |E - E_F|^2$ [42]. Indeed such a gap has been found in spatially averaged dI/dV-curves. It is already visible in Fig. 3.74 and Fig. 3.77b close to E_F. Since the localization does only affect a part of the states, the minimum of the pseudogap does not correspond to $dI/dV(V = 0 \text{ mV}) = 0$. However, after subtracting a linear background, which also removes the influence of the QD states on the dI/dV-signal, the parabolic shape of the gap becomes evident. Fig. 3.82a shows the resulting dI/dV curve close to E_F for different measurements and magnetic fields in comparison with a parabola. The presentation of the same data on a logrithmic scale in Fig. 3.82b reveals that the exponent is 1.9 ± 0.1 in excellent agreement with the prediction.

A usual way to analyze the behaviour of the LDOS at localization-delocalization transitions is the multifractal analysis [28,29]. Due to the lack of experimental data, it is usually applied to numerically calculated wave functions, but, of course, it can also be applied to experiments. Images are divided into exclusive boxes of size δ and the different momenta q of the normalized content of the ith box $\mu_i(q, \delta)$ is calculated. A

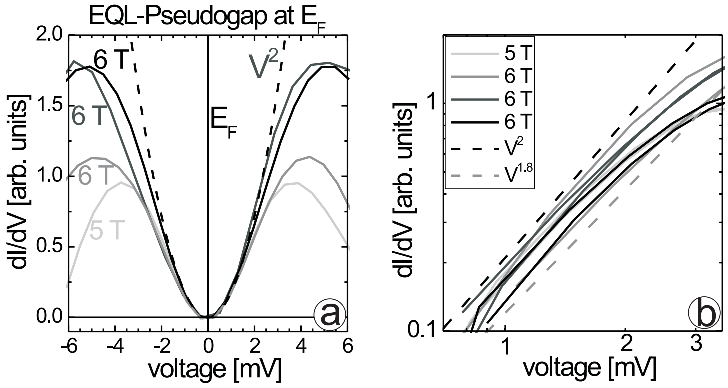

Figure 3.82: a.) Spatially averaged dI/dV curves measured at different magnetic field B as indicated (solid lines); $I_{stab} = 500$ pA, $V_{stab} = 100$ mV, $V_{mod} = 1$ mV, $T = 7$ K; a linear background has been subtracted. For comparison a curve corresponding to $dI/dV(V) \propto V^2$ is shown (dashed line). b.) Same data as in a.) but on a logarithmic scale to determine the exponent x of the $dI/dV(V) \propto V^x$ dependence. Curves corresponding to $x = 2$ and $x = 1.8$ are added for comparison.

measure of the fractal dimension of the corresponding momentum is the slope of the curve $\sum_i \mu_i(q,\delta) ln(\mu_i(1,\delta))$ versus $ln(\delta)$. For the magnetic field at the EQL transition ($B = 3.3$ T), the resulting curves are shown in Fig. 3.83a. The slopes deduced from linear regression are called $\alpha(q)$. Another measure for the fractality is $f(\alpha(q))$, the slope of $\sum_i \mu_i(q,\delta) ln(\mu_i(q,\delta))$ versus $ln(\delta)$. From scaling arguments, it follows that a random potential equivalent to a log-normal distribution of $|\Psi(r)|^2$ leads to a negative, parabolic $f(\alpha)$-curve with an origin at $f(\alpha(0)) = D$, where D is the dimension of the analyzed area (here $D = 2$) and $\alpha(0)$ is related to the dimension of the LDOS. The most simple consequence of localization is a broadening of the $f(\alpha)$ spectrum. Fig. 3.83b shows the resulting $f(\alpha)$ for different magnetic fields. Indeed, one sees the parabolic shape of the curves as well as their broadening in the EQL. Interestingly, the curve is not widest at the highest field, but shrinks again at B-fields where the localized structures start to overlap and thus form a network. If this is related to the formation of the assumed extended 1D states is still unclear and needs further analysis. However, the results show already that the multifractal analysis, up to now exclusively applied to computer generated data, can also be applied to experimental results. We acknowledge the help of V. Uski and R. Römer from the TU Chemnitz concerning the multifractal analysis.

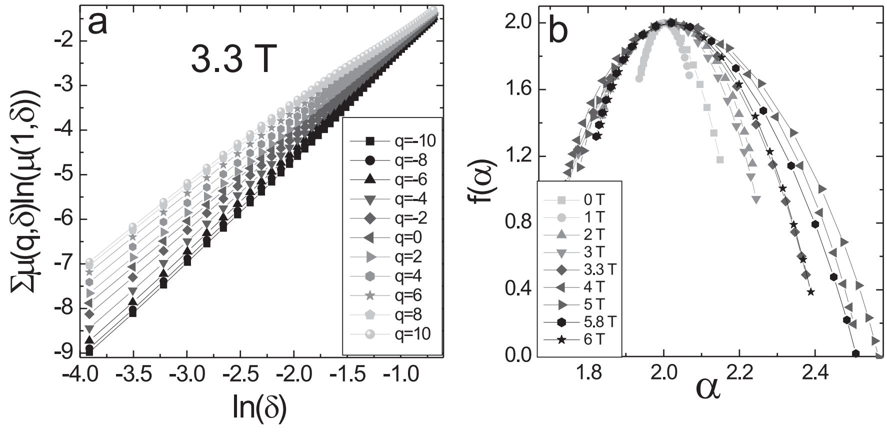

Figure 3.83: a.) $\Sigma\mu_i(q,\delta) ln(\mu_i(1,\delta))$ curves as a function of $ln(\delta)$, $B = 3.3$ T corresponding to Fig. 3.78d; $\mu_i(q,\delta)$ is the normalized q. moment of the content of a box of normalized width δ; i counts the boxes. The linearity of the curves allows to define a fractal dimension of the q. moment of the LDOS. b.) $f(\alpha)$ spectra of the LDOS images shown in Fig. 3.78. The method to determine $f(\alpha)$ is described in [28,29]

3.4.3 Two-dimensional electron systems

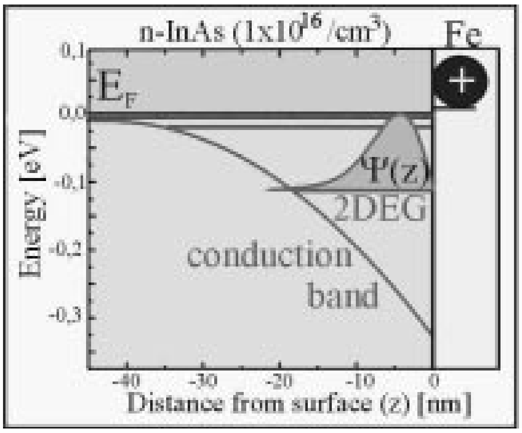

Figure 3.84: Schematic picture of the adsorbate induced 2DES. Adsorbates (Fe) act as surface donors donating electrons to the sample. The remaining positive charge at the dopants bends the bands of the semiconductor and thus leads to a confinement potential at the surface housing the 2DES. The depicted band shape is calculated assuming a surface band shift of 320 meV.

The observation of a 3DES LDOS in the EQL which is similar to the expected 2DES LDOS in the Quantum Hall region makes it natural to ask, if also a 2DES LDOS can be mapped. The 2DES has been evolved to be the paradigmatic case of dilute electron systems, very intensively investigated since the discovery of the Quantum Hall effect [43]. A number of phases of the 2DES have been found including insulating phases due to weak localization, a density dependent metal-insulator transition, Wigner crystals, the Quantum Hall phases (mainly insulating but conducting exactly at half filling), Composite Fermion phases at filling factors below 3/2 and the so-called stripe phase at half filling between 11/2 and 7/2. All these phases are accompanied by clear predictions concerning their LDOS, which have never been probed directly. Of course, STS is the adequate technique to measure the LDOS, but one faces the problem that the high mobility 2DES's, usually investigated in transport experiments, are buried about 100 nm below the surface. Thus they are difficult to probe by surface sensitive techniques as scanning probe measurements and even, if one can detect the 2DES LDOS, the resolution is only of the order of that depth [41]. Unfortunately, this is larger than the typical length scales determining the 2DES as Fermi wave length λ_F or magnetic length l_B. To circumvent this problem, we prepare a near surface 2DES on a conducting bulk sample by putting low amounts of adsorbates on the surface [44]. These adsorbates basically act as surface donors, donating electrons to the substrate. The remaining positive charge of the adsorbate layer keeps the electrons close to the surface, which thus form a 2DES in the near surface region. Fig. 3.84 shows the resulting band bending and the confined 2DES schematically.

Prior to local STS measurements, we characterized the 2DES samples by ARUPS to

deduce the surface band shift and the subband energies of the 2DES.
In this section we first describe the ARUPS measurements using different adsorbates and substrates. Then, we discuss STS measurements at $B = 0$ T, which visualize the strong interaction of the 2DES with potential inhomogenities. Finally, we show first measurements in magnetic field revealing characteristics of the expected drift states.

ARUPS measurements

Figure 3.85 shows two sets of photoemission spectra obtained after depositing different amounts of Fe on p-InAs(110) ($N_{\mathrm{A}} = 3 \times 10^{18}/\mathrm{cm}^3$) (a) and Nb on n-InAs(110) ($N_{\mathrm{D}} = 1.1 \times 10^{16}/\mathrm{cm}^3$) (b). Bulk related valence band peaks are marked as P_{III} and P_{IV}. In contrast to surface related peaks, the bulk related peaks do not change their shape, but exhibit an energy shift . They can thus be used to monitor the adsorbate induced E_F-shift. We measured four different spectra in normal emission at each coverage including peaks related to three surface bands and four bulk bands [45]. Only sharp P_n-peaks spectra related to bulk bands are used to determine E_F. Two systematic errors have to be considered to deduce the correct E_F-shift at the surface:

1. The different values of the escape depth of the photoelectrons λ combined with the z-extension of the band bending (see Fig. 3.84) imply that the measured peak energy is averaged over a λ-dependent part of the band bending. For the used p-InAs the parabolic band bending extends up to 13 nm into the bulk [46]. It is straightforward to calculate that the resulting peak shifts are 10 % and 60 % lower than the E_F-shifts at the surface for $\lambda = 0.8$ nm and 15 nm, respectively [47]. These are the extreme values of λ corresponding to the considered peaks. For the used n-InAs the shape of the band bending is more complicated. Numerical integration of the Poisson equation shows that it extends up to 40 nm into the bulk. The resulting difference between measured peak shifts

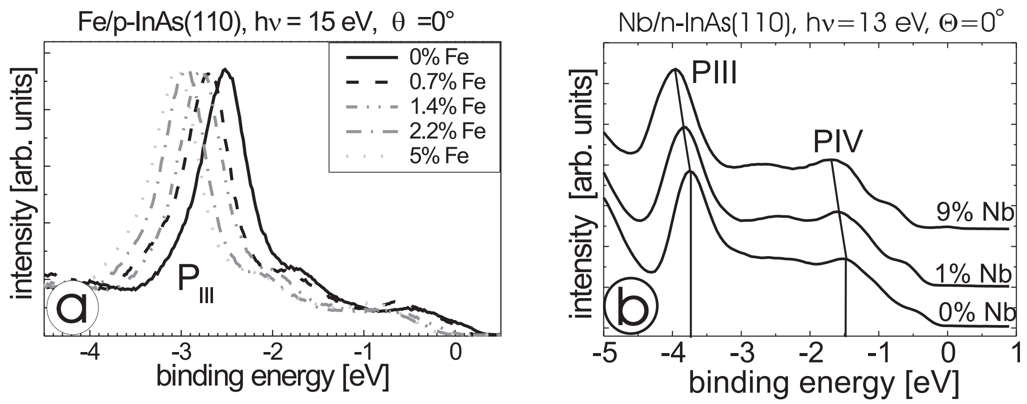

Figure 3.85: a.) ARUPS-spectra of Fe/p-InAs(110) ($N_{\mathrm{A}} = 3 \times 10^{18}/\mathrm{cm}^3$) at different coverages as indicated, $h\nu = 15\ eV$, $\theta = 0°$, $E_{pass} = 2.5$ eV; b.) ARUPS-spectra of Nb/n-InAs(110) ($N_{\mathrm{D}} = 1.1 \times 10^{16}/\mathrm{cm}^3$), $h\nu = 13\ eV$, $\theta = 0°$, $E_{pass} = 2.5$ eV; Peaks labeled according to Andersson [45].

and E_F-shift at the surface is 3 % (20 %) at $\lambda = 0.8$ nm (15 nm).

2. An adsorbate-induced shift of the final state energies with respect to the initial state energies would shift the k_z-value of an observed transition at selected hν. This changes the initial state probed and leads to an apparent energy shift of the peak not due to an E_F-shift. The resulting error for the E_F-determination depends on the dispersion of the initial and final states. In any case, this error is minimized by using peaks originating from flat areas of the valence band.

Taking these considerations into account, it turns out that the P_{IV}-peak measured at photon energy $h\nu = 21$ eV gives the most accurate measure of the surface E_F-shift. It belongs to the valence band maximum of the P_{IV}-band, i.e. from a flat part of the dispersion, and the photoelectrons have an estimated escape depth of only $\lambda \simeq 0.5$ nm.

Figure 3.86 shows the determined peak shifts for different peaks (different symbols) as a function of coverage. Results for Fe on differently doped samples (a,b), for Nb (c) and Co (d) are shown. Although the valence band peaks shift to lower energy,

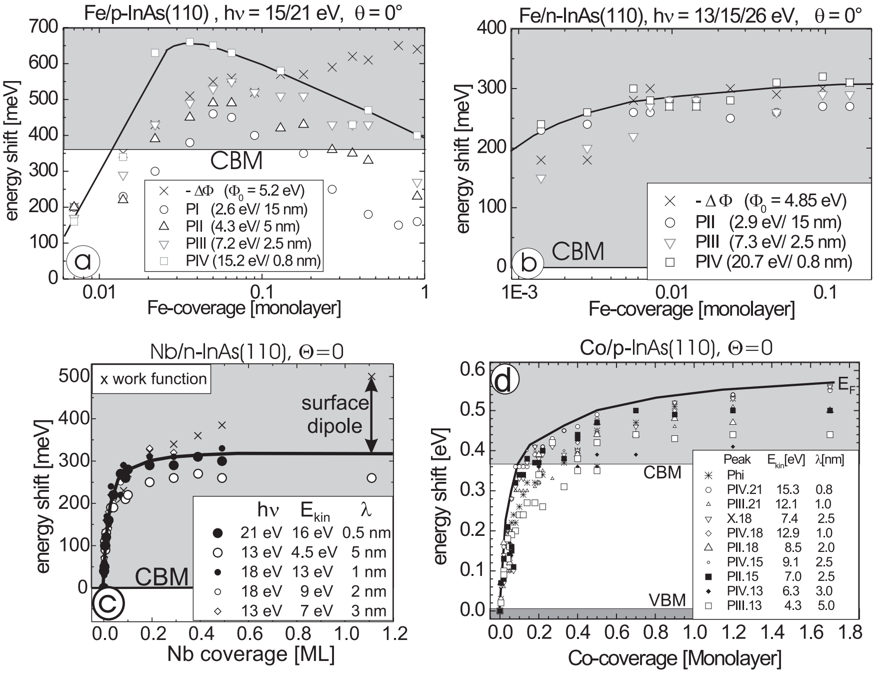

Figure 3.86: Peak shifts (symbols) and negative work function shifts (crosses,stars) obtained from ARUPS-spectra recorded at different adsorbate coverage. The conduction (valence) band is marked in light (dark) grey with the conduction (valence) band maximum (minimum) indicated as CBM (VBM). The solid line marks the deduced position of the surface E_F: a.) Fe on p-InAs(110) ($N_\mathrm{A} = 3 \times 10^{18}/\mathrm{cm}^3$), Φ_0 is the work function at zero coverage; numbers in brackets are kinetic energy E_{kin} and escape depth λ of the photoelctrons; b.) Fe on n-InAs(110) ($N_\mathrm{D} = 1.1 \times 10^{16}/\mathrm{cm}^3$); c.) Nb on n-InAs(110) ($N_\mathrm{D} = 1.1 \times 10^{16}/\mathrm{cm}^3$); difference between work function and E_F shift caused by a change in surface dipole is marked. d.) Co on p-InAs(110) ($N_\mathrm{A} = 4.6 \times 10^{17}/\mathrm{cm}^3$).

the absolute, positive value is shown to ease comparison with the deduced E_F-shift. The P_{IV}-peak measured at $h\nu = 21$ eV indeed shows the strongest peak shift in all measurements. The lower shifts of the other peaks are largely due to the larger values of λ indicated in the insets. The black lines indicate the deduced surface E_F-shift.

In addition to the peak shifts, we always measured the work function Φ by monitoring the energy cut-off of secondary electrons. It is given with respect to the uncovered value being $\Phi = 4.8$ eV and $\Phi = 5.2$ eV for n-type and p-type material, respectively. In the case of Fe and Nb at a coverage of about 1 monolayer, the work function shift is larger than the E_F-shift indicating a change of the surfcae dipole. In both cases this change can be calculated to be about 10^{-30} Cm. It indicates a lifting of the InAs(110) reconstruction, which is associated with a surface dipole of -2.5×10^{-30} Cm. Indeed, such a lifting has been found in LDA (local density approximation) calculations of the Fe covered InAs(110) surface.

Most obviously, the coverage dependence of the E_F-shift is different for the different adsorbates. Comparing Fig. 3.86a, c and d shows that Fe exhibits a maximum in the surface E_F-shift at a coverage of about 3 %, while Nb and Co does not show a maximum up to a coverage of about 1 monolayer. Moreover, by comparing Fig. 3.86b and c, which are measured on the identical substrate, one notices, that the highest E_F-shift, in both cases being about 300 meV above the conduction band maximum, is reached after 0.7 % Fe deposition and 15 % Nb deposition, respectively. Obviously, these numbers differ by a factor of 20. Also in the case of Co, the maximum of the E_F shift needs a rather high coverage of about 1 monolayer. The possible reasons for these differences are discussed below.

As shown in Fig. 3.84 the surface E_F shift results in a band bending confining a 2DES. The expected subband energies E_n can be calculated by solving the Poisson-Schrödinger equation [48]. However, one should keep in mind that such a calculation is one-dimensional thus assuming a laterally homogeneous surface E_F. Anyway, the occupied part of the 2DES can be measured by ARUPS. Results for different Nb coverages, measured normal to the surface, are shown in Fig. 3.87a . The calculated subband energies are indicated as lines. A rough correspondence with the data can be seen. Also the peak intensity fits with the expected electron density n in the 2DES, which is calculated by $n = m_{eff}/(\pi\hbar^2) \cdot (E_F - E_0)$ (Fig. 3.87b). Notice the strong angular dependence of the 2DES peak shown in Fig. 3.87c. It is related to the strong dispersion of the InAs conduction band. The occupied part of a 2DES with $E_0 - E_F = -50$ meV (4 % coverage) is restricted to the inner ± 0.03 Å^{-1} of the surface Brillouin zone, i.e. an area 500 times smaller than the whole surface Brillouin zone. The angular dependence of the 2DES peak can be reproduced straightforwardly by considering the InAs dispersion, the temperature dependent Fermi level broadening and the instrumental resolution [9]. A comparison between measurement and calculation is shown in Fig. 3.87d and e exhibiting reasonable agreement. The expected intensity of the 2DES peak with respect to bulk peaks can be estimated taking electron density, k space volume and escape depth into account. At 8 % Nb coverage and

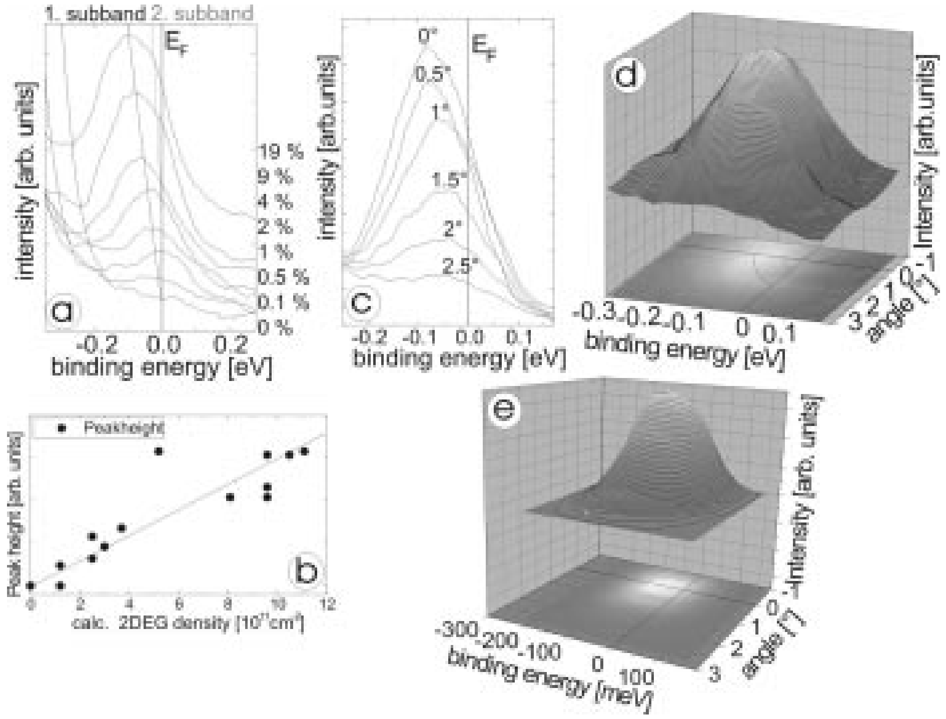

Figure 3.87: a.) 2DES peak measured for different Nb coverages on n-InAs(110), hν=13 eV, θ= 0^o. Some curves are slightly offset corresponding to the increasing coverages labelled on the right. The two lines mark the subband energies resulting from a solution of the Poisson-Schrödinger-equation taking the measured surface E_F shifts as a parameter. b.) Measured height of the 2DES peak as a function of expected 2DES density deduced from the measured E_F shift. Partly different measurements with the nominally identical coverage are shown to give an impression of the error bars. The line is a guideline to the eye. c.) Angular dependence of the 2DES peak measured at 8 % Nb coverage, hν=13 eV, θ as indicated. d.) 3D representation of the same data set as shown in c.). The (x,y)-plane gives an intensity plot of the 2DES peak. Straight lines mark Fermi energy and normal emission. The curved lines show the expected dispersion of the two subbands of the 2DES used for the simulation in e.). e.) 3D representation of the simulated 2DES peak using the two subbands indicated in d.) and the energy and angular resolution from the experimental setup.

$h\nu$ = 13 eV, the 2DES peak is expected to be 35 times smaller than the PIII peak in reasonable agreement with the factor of 50 in experiment [10]. For Nb we conclude that the relation between the measured surface E_F and the subband energies of the 2DES is adequately described by a one-dimensional model of the band bending as depicted in Fig. 3.84. The same agreement has been found for Fe. In particular, a 2DES peak has not been found for p-InAs(110) in agreement with the calculation, which exhibits subband energies only largely above E_F. Similar results also exist for other adsorbates [49]. Obvious deviations from results of the 1D model have been found for Co, which we attribute to lateral inhomogenities of the surface potential [11].

To understand the coverage dependence of the E_F shift shown in Fig. 3.86, it is crucial

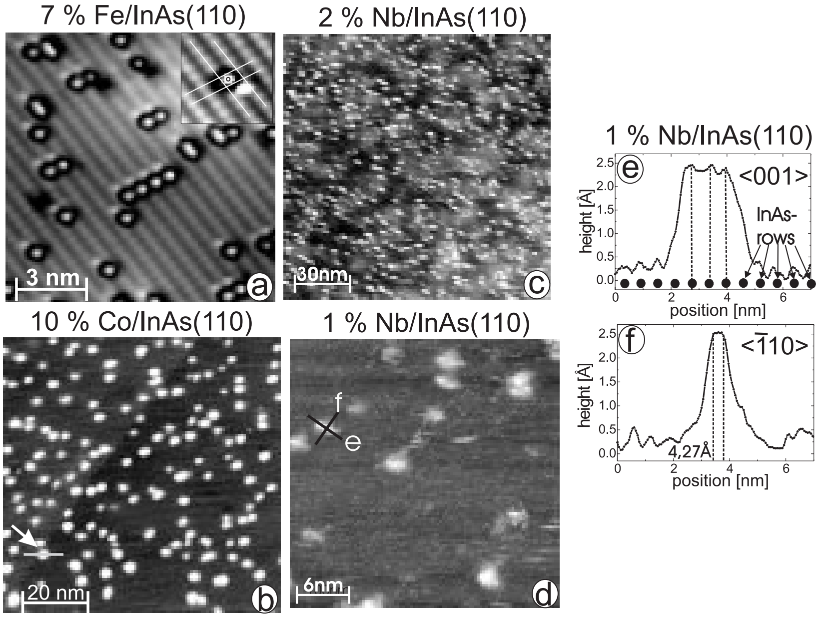

Figure 3.88: a.) STM-image of 7.5 % Fe on InAs(110), V=-50 mV, I=100 pA; atomic rows run diagonally through the image; the average cluster size is two; inset: magnification; lines indicate visible atomic rows and the circle marks the Fe atom b.) STM-image of 10 % Co on InAs(110), V=-1.0 V, I=30 pA; the average cluster size is 25 as estimated from the ratio of island density to deposited adsorbate density; from the apparent size of the islands the Co density in the islands is estimated to be close to the bulk Co value [11]. c.) STM-image of 2 % Nb on InAs(110), V=-500 mV, I=50 pA; the average cluster size is 3. d.) STM image of 1 % Nb on InAs(110), V=-1.8 V, I=25 pA; the atomic rows of InAs(110) run from the lower left to the upper right. Line scans along marked black lines are shown in e.) and f.); e.) and f.) lines scans along the black lines; atomic rows are symbolized in e.) as dark dots and the interatomic distance is shown in f.) by vertical lines demonstrating that this particular cluster is a trimer. Crystallographic directions are indicated.

to know the lateral distribution of the adsorbates. Fig. 3.88 shows STM images of the InAs(110) surface covered with Fe, Nb and Co, all deposited at room temperature. In the case of Fe, it is obvious that monomers, dimers, trimers and tetramers are formed on the surface. In the case of Nb, the adsorbate distribution is less evident, but by line scans as shown in Fig. 3.88 e and f, an assignment of the clusters is possible. They also mainly contain one to four atoms. In both cases a mean value of $2-3$ atoms per cluster can be deduced from the ratio of found clusters to deposited adsorbates. The very similar arrangement of Fe and Nb atoms is surprising regarding the fact that the coverage dependence of the E_F shift is so different. As visible in Fig. 3.88b, Co forms islands on the surface, which contain 25 atoms at 10 % coverage but up to 70 atoms at higher coverage.

A detailed description of the coverage dependence of the E_F shift is behind the scope of this review. It can be found in [9–11]. In short, we believe that Fe acts as a surface donor with a donor level 300 meV above the conduction band minimum. This level donates electrons to the substrate, if the local E_F is lower than the energy of the donor level E_{Don}. Taking the mutual Coulomb interaction of charged donors into account, such a model can reproduce the coverage dependence of the E_F shift up to about 10 %. Thus the formation of clusters does not change E_{Don} of an individual Fe atom, but only the lateral distribution of the donor levels. At higher coverage, metallic Fe islands are formed indicated by the appearance of a Fermi level in the ARUPS spectra. These islands pin the surface E_F close to the conduction band minimum, thus reducing the surface E_F shift as found experimentally [9]. For Nb such a model is not sufficient to explain the data. This becomes evident from Fig. 3.89. The simple model described above is used to calculate the ionization probability of the adsorbates assuming a random lateral distribution of the adsorbates (model). For comparison the measured ionization probability, which is simply the ratio between 2DES density and adsorbate density, is shown for Fe and Nb. While the Fe data only slightly deviate from the model, which can be explained by the non-random distribution caused by cluster formation, the Nb data strongly deviate at low coverage. We believe that the deviation is caused by hybridization of the donor levels in Nb clusters. LDA calculations to prove such a behaviour are currently under way. In the case of Co, the coverage dependence can be explained by assuming that each Co island provides a donor level, which is the charge neutrality level of the sample. Consequently each island is ionized once or less, which explains the slow saturation of the surface E_F shift (Fig. 3.89b). The singly charged islands also explain, that a 2DES subband at $E_0 - E_F = -7$ meV is found experimentally, while a 2DES subband at $E_0 - E_F = 30$ meV is expected from the one-dimensional model. The large inhomogenieties of the potential caused by the sparsely distributed Coulomb potentials around the islands lead to the formation of electron droplets in areas of high island density [11].

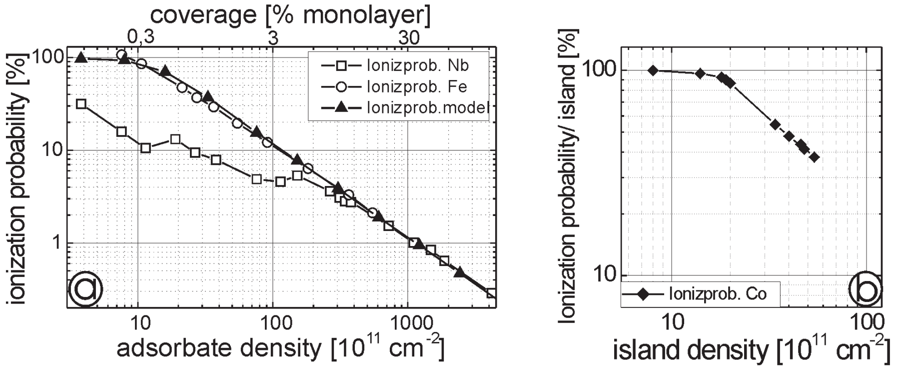

Figure 3.89: a.) Ionization probability of Fe and Nb adsorbates on n-InAs(110); the ionization probability is the ratio between the calculated 2DES density and the adsorbate density. The model assumes random distribution of the adsorbates, a position independent donor level of 300 meV and mutual Coulomb interactions between ionized adsorbates. b.) Ionization probability for Co on p-InAs(110) calculated as the ratio between acceptors in the space charge region and Co islands [11]. The saturation value of E_F is taken as the donor level of the islands.

For the following, the most important point is that the adsorbate induced 2DES can be characterized by ARUPS. Especially the subband energies can be determined experimentally by the described fit procedure. The accuracy of the subband determination depends on the angular and energy resolution of the ARUPS setup.

STS measurements at $B = 0$ T

For 2DES systems, which are investigated in detail by STS, we performed high resolution ARUPS measurements. The 2DES peak at 4.5 % Fe coverage is shown in Fig. 3.90a in comparison with three different fit curves. The 2DES peak consists of two smaller peaks attributed to the two subbands of the 2DES. A straightforward fit of the data with the subband energies E_n as the only fitting parameters [9] leads to $E_1 = -105 \pm 5$ meV and $E_2 = -40 \pm 5$ meV, i.e. only the fitting curve in the middle of Fig. 3.90a fits the data. The resulting E_n's are additionally validated by measuring the angular dependence of the 2DES peak at different energies and fitting the data with the same procedure. The knowledge of the subband energies is an important requirement to investigate the influence of the STM tip on the LDOS data [7, 12].

Next, we compare the ARUPS data with STS. Fig. 3.90b and d show spatially averaged dI/dV-curves representing the macroscopic average of the LDOS: the DOS [54]. The curves in Fig. 3.90b are measured with the same microtip before and after Fe-deposition. Without Fe, two peaks caused by the tip-induced quantum dot (QD) appear [7, 12]. With Fe, the lower peak shifts to lower energies while the other disappears. The shift of the lower peak by 80 mV is in quantitative agreement with the peak shift expected from an adsorbate induced band shift of 300 mV [9, 12]. The disappearance of the second peak is most likely caused by the reduction in QD size due to screening by the 2DES.

Additional rather flat dI/dV-intensity with two step-like features at -105 mV and -40 mV is found in between the QD peak and E_F. Since the features are located close to the E_n's determined by ARUPS, we identify them with E_1 and E_2. Additional evidence comes from Fig. 3.90c, a grey-scale plot of $dI/dV(V)$ along a substrate line. In the 2DES region intensity fluctuations are visible, whose fluctuation length along the y-axis changes abruptly at E_2. This result is straightforwardly explained by the fact that the DOS doubles at E_2: Doubling the number of states, each contributing with a different spatial phase to the LDOS, decreases the apparent fluctuation length. Fig 3.90d shows another spatially averaged dI/dV-curve recorded with a different tip at slightly lower coverage. E_n's are marked again. Obviously, the QD states are absent and clear step-like structures as expected from a 2DES DOS are visible. We conclude that the presence of the QD does not change the energies in the step-like DOS, but slightly influences the intensity distribution. Thus the influence of the QD on the 2DES DOS is weak.

A unique advantage in these measurements is provided by the presence of the QD. As described elsewhere, the energy of the lowest QD state follows the electrostatic potential in the center of the QD [7, 12]. Since the extension of the QD state perpen-

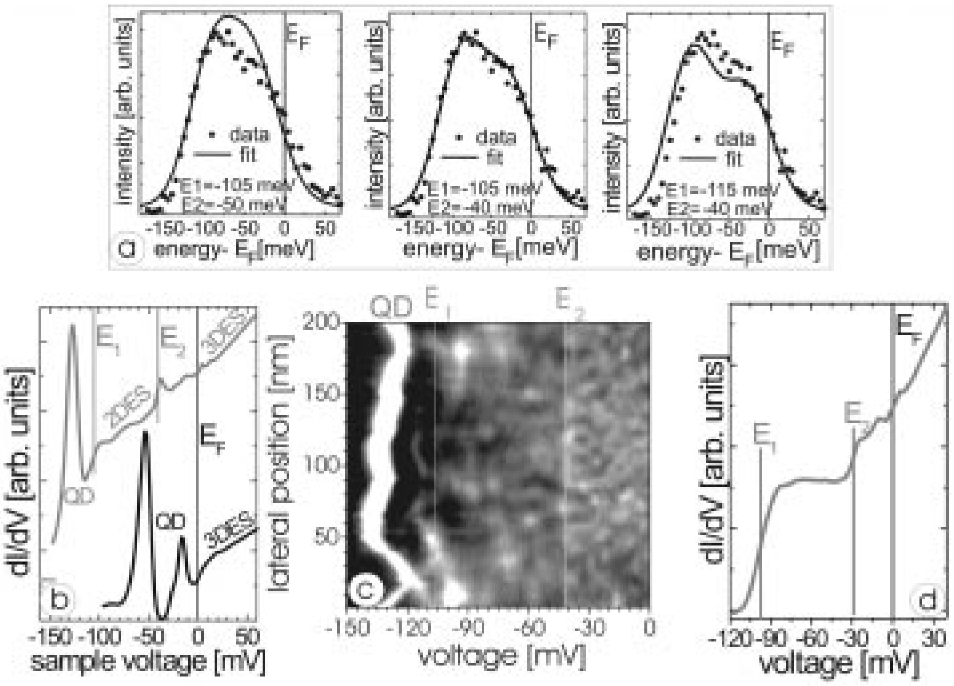

Figure 3.90: a.) ARUPS-spectrum of 4.5 % Fe/n-InAs(110), hν = 10 eV, E_{pass} = 4 eV (points) compared with fits for different subband energies E_1, E_2 as indicated (lines). Only the central curve fits the data. b.) Spatially averaged $dI/dV(V)$-curves of n-InAs(110) (lower curve) and 4.5 % Fe/n-InAs(110) (upper curve); both curves are taken with the same tip, $V_{stab} = 100$ mV, $I_{stab} = 500$ pA; peaks of the tip-induced quantum dot (QD), E_1, E_2 of the 2DES determined by ARUPS as well as the 3DES region are indicated. c.) Greyscale plot of $dI/dV(V)$-intensity as a function of position along a scan line, $V_{stab} = 100$ mV, $I_{stab} = 500$ pA; sample and tip as in the upper curve of b.); E_1, E_2 and QD peak are indicated. d.) Spatially averaged $dI/dV(V)$-curve of 2.7 % Fe/n-InAs(110), $V_{stab} = 100$ mV, $I_{stab} = 300$ pA; notice the absence of QD peaks.

dicular to the surface is the same as the extension of the 2DES, the QD state monitors the local 2DES potential. Indeed, the QD energy fluctuates with position as visible in Fig. 3.90c (curved line QD along y-axis). A plot of the QD energy as a function of position is shown in Fig. 3.91a. Four troughs about 20 meV in depth are visible. This is exactly the number of substrate donors located in the 2DES area and exactly the maximum attractive potential of a single donor averaged over the extension of the 2DES. We take both as strong evidence that the QD state indeed maps the 2DES potential.

The image of the potential can be used to estimate the mobility of the 2DES [55]. It is $\mu \simeq 5 \times 10^6$ cm^2/Vs indicating a mean free path in the large μm range. Notice, that the potential landscape is rather similar to potential landscapes in high-mobility 2DES's [53], thus allowing a direct comparison of STS results with usual transport measurements.

What is the influence of the Fe atoms ? An STM-image of a small area of Fig. 3.91a

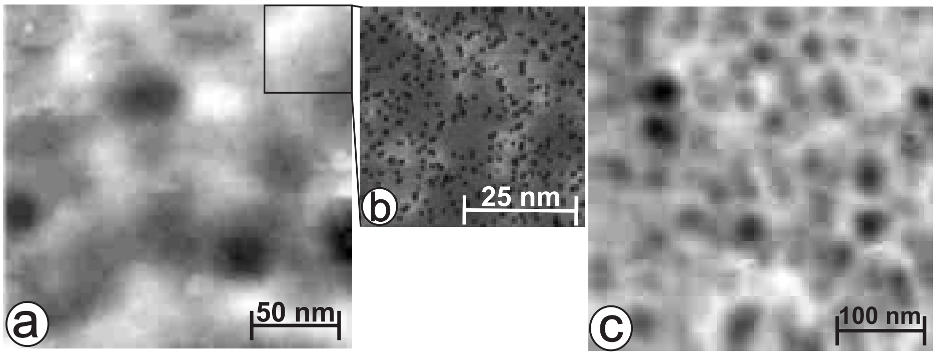

Figure 3.91: a.) Potential landscape as determined from laterally fluctuating peak voltage of the lowest-energy QD state, 4.5 % Fe/n-InAs(110). b.) Constant-current image of the area marked in a.), $V = 100$ mV, $I = 50$ pA; dark spots are Fe-atoms c.) Potential landscape at 0.8 % Fe/n-InAs(110). Both potential images cover a potential range of 20 meV.

is given in Fig. 3.91b. It shows several Fe atoms (black dots), but no correspondence between the Fe positions and the measured potential. This might be surprising, since the adsorbate layer donates electrons to the 2DES and is thus positively charged [9]. However, in the area of Fig. 3.91b only 700 electrons are donated, but 7000 Fe atoms are deposited. Assuming that each Fe atom provides an electron, an electron density of $1.5 \times 10^{13}\text{cm}^{-2}$ remains in the Fe layer sufficient to screen the positive charge of the ionized Fe atoms on small length scales.

Fig. 3.91c shows the more irregular potential at 0.8 % coverage exhibiting more troughs than expected from 16 bulk donors. In that case, the remaining electron density in the Fe layer of $2 \times 10^{12}/\text{cm}^{-2}$ is obviously not sufficient to screen the positive charge of 8×10^{11} e/cm^{-2}.

Next, we discuss the LDOS data. Fig. 3.92a–g show some of the LDOS images recorded at 2.7 % coverage in the absence of a QD. The data correspond to the spatially averaged dI/dV curve in Fig. 3.90d. The spatial resolution is 5 nm well below the Fermi wave length of 23 nm. The total intensity in each image corresponds to 40 complete electronic states [56]. However, since the scattering length and thus the localization length of individual states is larger than the image size, more states might contribute to the LDOS with part of its intensity distribution.

The LDOS images exhibit corrugations decreasing in length scale with increasing voltage as expected from the InAs dispersion. The corrugation patterns are rather complicated and do not exhibit the circular ring structures found in the InAs 3DES around individual dopants [2]. Moreover, the corrugation strength defined by the ratio between spatially fluctuating dI/dV-intensity and total dI/dV-intensity is 60 ± 5 %, much larger than the corrugation strength in the 3DES (3 ± 0.5 %) [2]. Both results reflect the tendency of the 2DES to weakly localize [51]. Many different scattering paths containing each many scattering events contribute to the LDOS leading to more intricate patterns, and, due to the tendency for localization, to a stronger corrugation.

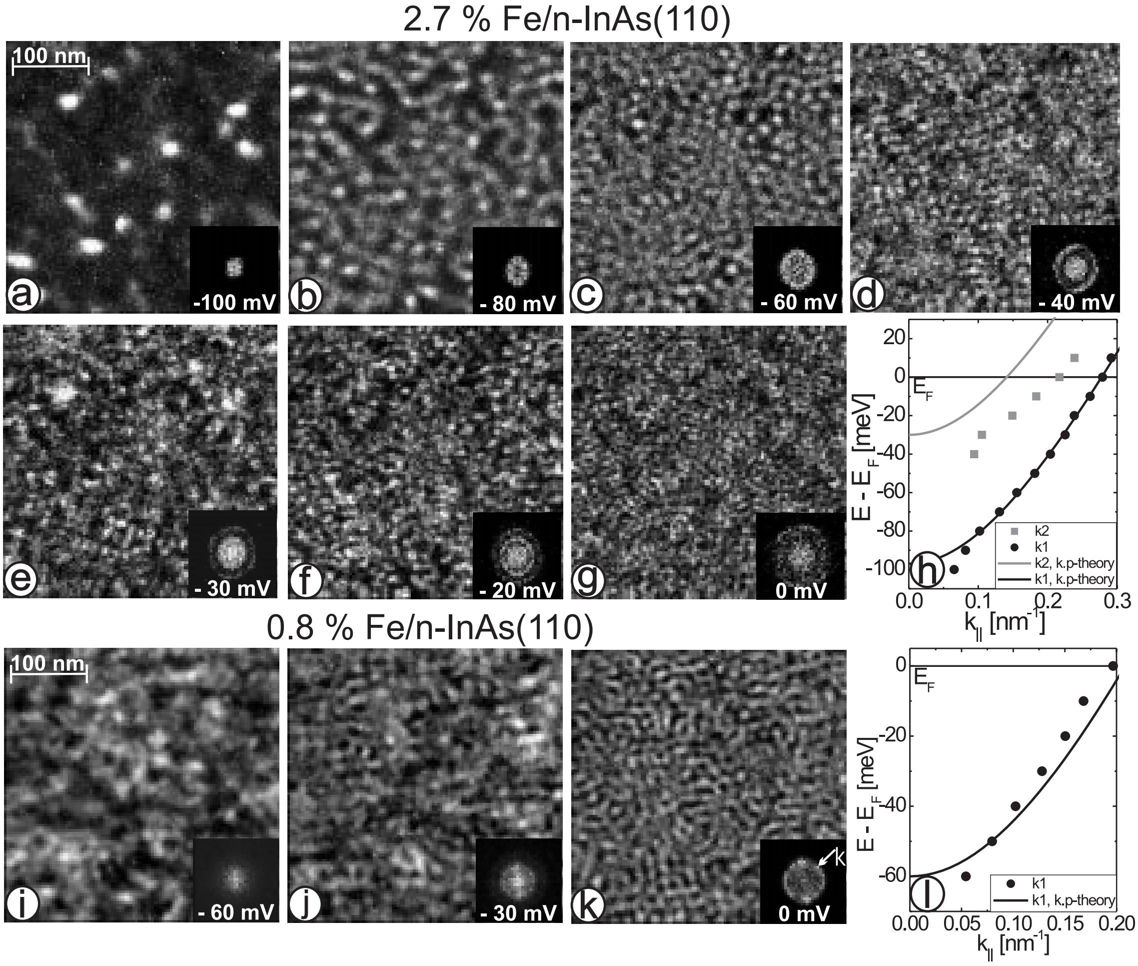

Figure 3.92: a.–g.) dI/dV-images (LDOS-images) of 2.7 % Fe/n-InAs(110) recorded at different V as indicated; $V_{stab} = 100$ mV, $I_{stab} = 300$ pA; the bright spikes in the images are the Fe-atoms. Insets: Fourier transformations (FT) of dI/dV-images. h.) dominating $|k|$-values corresponding to rings in FT's (symbols) in comparison with the dispersion curve of unperturbed InAs (lines) [57]. i.–l.) Same as a.–h.) but for 0.8 % Fe/n-InAs(110); the dominating ring structure ($|k|$) is marked once in k.); the investigated surface area belongs to the potential shown in Fig. 3.91c.

The fact that the measured corrugation is not 100 % is either caused by the finite phase coherence due to finite temperature or caused by the overlap of several states due to the finite energy resolution of the experiment.

Fourier transforms (FT's) of the LDOS (insets) reveal the distribution of contributing k-values. At low voltages a circle is visible, which at higher voltages is confined by a ring. At even higher voltages ($V > -40$ mV) a second smaller ring appears indicating the occupation of the second subband. A plot of the k-values corresponding to the rings, which obviously dominate the spectrum, is shown in Fig. 3.92h. At low voltages, where the ring is not apparent, the outer diameter of the circle is taken. For comparison the $E(k)$-dispersion of the unperturbed InAs conduction band is drawn [57]. The correspondence of the dispersion curve with the data is excellent for the lower subband and slightly worse for the second subband showing that the unperturbed k-values dominate the spectrum. Interestingly, additional k-space intensity not compatible with the unperturbed dispersion exists in the FT's. It is strongest at low k-values, but also exists faintly at k values larger than the ring structure [58]. Its origin will be discussed below.

For 0.8 % coverage, we find exactly the same tendencies as for 4.5 % coverage (Fig. 3.92i–l). Here, only one subband is occupied ($E_1 = -60$ meV) and the tip exhibits a QD state leading to the potential shown in Fig. 3.91c. Consequently, potential and LDOS can be directly compared. This is a crucial result, since effective mass, potential landscape and electron density completely determine the LDOS. All ingredients determining the physics of the 2DES become experimentally accessible. To demonstrate the relevance of this result, we give a simple analysis of the LDOS patterns. A first attempt to describe the LDOS is solving the Schrödinger equation for non-interacting particles in the measured disorder potential [59]. We solve it numerically using periodic boundary conditions [60]. There is no fit parameter in the calculation. To construct the LDOS, the resulting squared wave functions are weighted corresponding to the energy resolution of the experiment. The resulting LDOS for a particular energy is shown in Fig. 3.93a in comparison with the measured one (Fig. 3.93b). The correspondence is reasonable, i.e. several features as the central ring structure or the arc in the central bottom marked by arrows appear in both images. The FT's (insets) and the intensity distributions of the LDOS (Fig. 3.93c) show nearly perfect agreement. We found similar results at different energies and at a coverage of 4.5 % and conclude that the potential landscape indeed largely determines the LDOS by mixing different k-states [61]. Remaining discrepancies between measurement and calculation may be either caused by scattering centers outside the measured region or by electron-electron interactions.

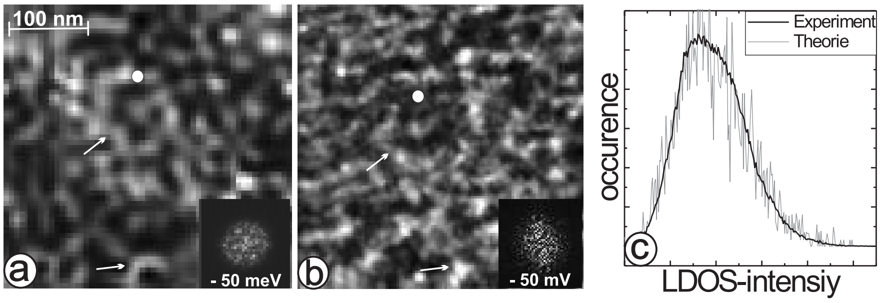

Figure 3.93: a.) LDOS calculated from the potential landscape in Fig. 3.91c [60]; $E = -50$ meV. b.) Normalized dI/dV-image of the same area; $V = -50$ mV, $V_{stab} = 100$ mV, $I_{stab} = 300$ pA. Insets are FT's. White dots mark identical sample positions as deduced from constant-current images. Arrows mark similar structures. c.) Intensity distribution of the LDOS in a.) and b.); for the sake of comparison the experimental curve is stretched by a factor of 1.5.

STS measurements in magnetic field

Applying a magnetic field to a 2DES leads to the well known Quantum Hall effect [43]. Basically, this is a repeating metal-insulator transition of the 2DES, with the metal only present exactly at half filling of each individual Landau level. The microscopic origin is a transition between localized states and extended states at the Fermi level. The proposed meachnism is visualized in Fig. 3.94 [33]. A potential landscape of the 2DES is shown in Fig. 3.94a. Classically, the electrons bounce in skipping orbits along equipotential lines, if the cyclotron radius is smaller than the correlation length of the potential (inset). Consequently electron states are located along individual equipotential lines, each line resulting in a state at different energy. These states are called drift states. Two of the drift states originating from the center and the tail of a Landau level are shown in Fig. 3.94c and d. Its width is about the magnetic length. In the center of the Landau level the state corresponds to the percolating equipotential line at about the mean value of the potential and is thus extended, while in the tails the state corresponds to a closed equipotential line and is thus localized. The width of the Landau level is basically the height of the potential fluctuations (see Fig. 3.94b).

Fig. 3.95 shows experimental results for a 2DES at $B = 6$ T. The same surface area is studied in Fig. 3.92i–k at $B = 0$ T. The spatially averaged dI/dV-curve in Fig. 3.95e clearly exhibits two occupied Landau levels marked LLn. Their widths correspond to the height of the potential fluctuations of about ±10 meV. LDOS images from LL2 are shown in Fig. 3.95a-d. The corrugation strength increases with respect to the LDOS at $B = 0$ T towards 95 %. Serpentine structures resembling the expected drift states are indeed visible in Fig. 3.95a, c and d. Their width is, as expected, close to the magnetic length $l_B = 10.5$ nm (see bar in a). Some of the structures can be directly identified with potential structures (see circle in c and f). These states exist on a rim of the potential. The drift states appear rather isolated in Fig. 3.95d, but dense in Fig. 3.95b, where the assignment of individual states is not possible. Unfortunately

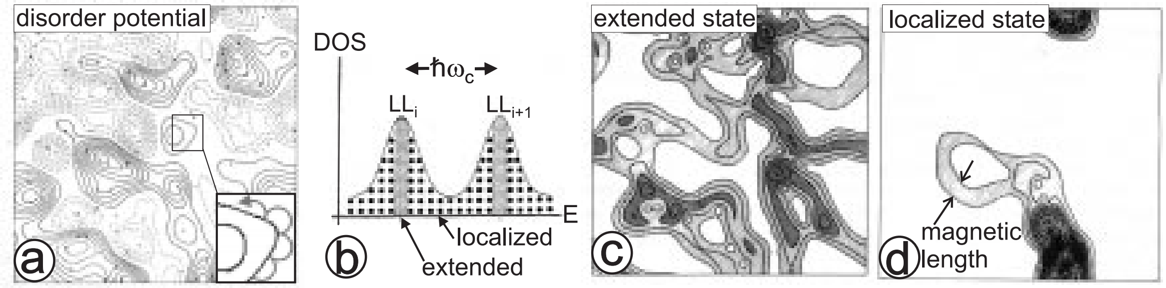

Figure 3.94: a.) Disorder potential of a 2DES showing equipotential lines; inset: schematic representation of an electron path in magnetic field. b.) DOS of the 2DES in magnetic field with energy regions of localized and extended states indicated; LL$_i$ are the Landau levels and $\hbar\omega_c$ is the Landau energy. c.) and d.) $|\Psi|^2$ of extended and localized state in greyscale representation; the magnetic length being the average width of the drift states is indicated. [33]

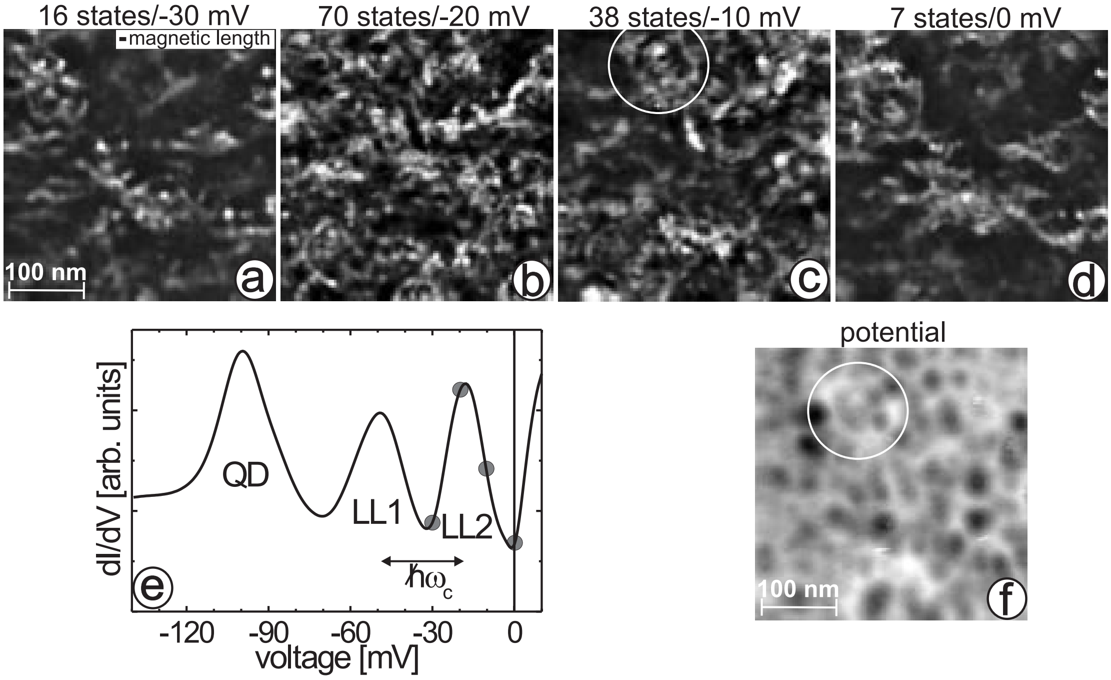

Figure 3.95: a.–g.) dI/dV-images of 0.8 % Fe/n-InAs(110) recorded at different V as indicated; $B = 6$ T, $V_{stab} = 100$ mV, $I_{stab} = 300$ pA; the average number of contributing states is indicated; black bar in a.) marks the magnetic length. e.) spatially averaged dI/dV-curve; $V_{stab} = 100$ mV, $I_{stab} = 300$ pA; quantum dot peak (QD), Landau level (LLn) and Landau energy $\hbar\omega_c$ are marked; dots mark the voltages of the images a–d.). e.) potential of measured area (same as Fig. 3.91c). The white circle marks the same area in c.) and f.).

the transition from localized to extended states is not obvious from the data. The fact that the LDOS appears more dense in Fig. 3.95b is most likely a result of the large number of states contributing to the image in the center of the Landau level [56]. This makes it difficult to deduce an extended character of the states from the image. An increase of the energy resolution from the actual value of 0.5 meV is desirable to decrease the number of contributing states.

3.4.4 One-dimensional electron systems

One-dimensional electron systems are particularly interesting, since they are the limiting case where interactions lead generally to a brekdown of the single particle description of the electron system [62]. Charge density waves and spin density waves are the basic excitations close to the Fermi level. They exhibit different dispersion. The resulting 1DES is called a Luttinger liquid [63] in contrast to the well known Fermi liquid, where single particle excitations remain valid. The different dispersion of spin and charge excitations is called spin-charge separation, refering to the fact that putting an electron into the 1DES would lead to different spreading velocities of its charge and its spin. Although we measured the LDOS of a 1DES, we did not find any indications of Luttinger liquid behaviour. The reason is currently unknown and requires further studies.

Here, we present the measured LDOS of a 1DES confined below a charged [112] step edge on InAs(110). The electron density of the 1DES is 2.4×10^6 cm^{-1}. The 1DES is confined in an irregular potential along the step edge.

Fig. 3.96a shows a constant-current image of the n-InAs(110) surface containing four step edges, which run diagonally across the image. The higher resolution image in the inset shows that the step edge does not run along a high symmetry direction of the sample parallel or perpendicular to the visible atomic rows, but along a different direction, which turns out to be [112]. The atoms directly at the step edge appear brighter than the surrounding atoms indicating some rearrangement of the atoms at the step edge. It has been proposed that As dimers are formed [64]. Around the step edge a bright stripe is faintly visible. It becomes more apparent in the line section shown in Fig. 3.95b. Besides the expected step edge morphology (grey line), additional intensity is visible at the step edge related to an additional density of states (DOS). Since the corresponding constant-current image is recorded at positive sample bias, this additional intensity indicates an attractive electron potential at the step edge [65]. The shape of this potential can be estimated from the appearance of the step edge using the formula for the tunneling current $I(V,z,x) \propto \int_0^V DOS(E,x) \cdot e^{-\kappa z(x)} dE$. Here, $z(x)$ is the apparent height as a function of position x after subtracting the morphologic height of the step edge (grey line in Fig. 3.96b), κ is the attenuation factor of the current, which is directly measured by $I(z)$ curves to be $\kappa = 1.2/\text{Å}$, and $DOS(E,x) \propto \sqrt{E - E_{CBM}(x)}$ is the position dependent density of states of the sample [38]. The conduction band minimum $E_{CBM}(x)$ depends on the position x and thus tracks the potential [38]. For the second step edge from the left in Fig. 3.96a, the resulting potential is shown in Fig. 3.96c. It has a depth of about 200 meV and a FWHM of 15 nm. Two subbands are confined in this potential as indicated by the two grey lines E_1 and E_2. They should both exhibit the typical 1DES DOS $\propto (E - E_n)^{-0.5}$. This 1DES DOS is indeed found as demonstrated by the two dI/dV curves in Fig. 3.96d. One is recorded above the step edge and one is recorded about 200 nm away from any step edge. Away from the step edge, the dI/dV intensity increases at the onset of the bulk conduction band $V = -10$ mV and resembles the $\sqrt{E}$ shape of the DOS in this

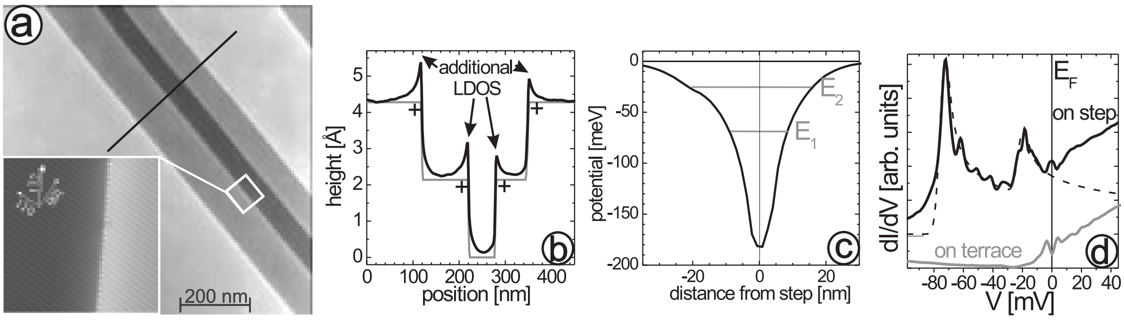

Figure 3.96: a.) Constant-current image of n-InAs(110) ($N_\mathrm{D} = 1.1 \times 10^{16}/\mathrm{cm}^3$), $V = 200$ mV, $I = 90$ pA; black line marks direction of line section shown in b.); inset: magnification of the area marked by the white rectangle, $V = 200$ mV, $I = 500$ pA; crystallographic directions are indicated. b.) Line section along black line in a.) (black line) in comparison with step edge morphology (grey line); additional height due to additional LDOS and the deduced attractive potential (+) is indicated. c.) Deduced potential across the step edge according to the method described in [38] (black line); expected confined subband energies E_n are marked as grey lines. d.) dI/dV spectra measured on the step edge (black) and 200 nm away from each step edge (grey), $V_{stab} = 50$ mV, $I_{stab} = 1.2$ nA; dashed line is a fit corresponding to the 1DES DOS with two subbands $DOS_n(E) \propto (E - E_n)^{-0.5}$ taking $E_1 = -76$ meV and $E_2 = -23$ meV and assuming a Gaussian broadening of the DOS with $\sigma = 3$ meV.

band. Above the step edge additional dI/dV intensity is found at negative sample voltage, corresponding to the region, where tunneling is related to the bulk band gap. Nevertheless, two peaks with a high energy tail are visible. They are compatible with the expected $(E - E_n)^{-0.5}$ shape of the 1DES DOS as evidenced by the fit shown as a dashed line. For the fit, a Gaussian broadening of the DOS of 3 meV has been folded to the bare 1DES DOS and the subband energies E_n are taken as fit parameters. They turn out to be $E_1 - E_F = -76$ meV and $E_2 - E_F = -23$ meV corresponding to an electron density of $2.4 \cdot 10^6$ cm^{-1} as calculated from $DOS_n(E) = 2/h\sqrt{m_{eff}/(E - E_n)}$ valid for each subband. Thus the average distance between electrons is $r = 4$ nm corresponding to a bare Coulomb repulsion of $E_{Coul} = 1/(4\pi\epsilon\epsilon_0 r) \simeq 25$ meV. Also the average kinetic energy of the electrons can be straightforwardly calculated to be $E_{kin} = \sum_n \int_{-\infty}^{E_F} DOS_n(E)E\, dE \simeq 20$ meV.

The lateral confinement energies E_n are related to confined states $\Psi_n(x)$ as indicated by the dotted lines in Fig. 3.97a. Since the $dI/dV(x)$ signal is proportional to the LDOS, the square of the wave function $|\Psi_n(x)|^2$ is relevant for the experiment (eq. 3.14). Consequently, we expect a Gaussian distribution of $dI/dV(x)$ for the first subband and a more extended double hill structure for the second subband (solid lines in Fig. 3.97a). Spectra taken at different positions x are shown in Fig. 3.97b. The first subband disappears about 10 nm away from the step edge, while the second subband extends up to more than 20 nm. The dI/dV intensity as a function of position x is plotted for two voltages in Fig. 3.97c. The voltages belong to the first and the second subband, respectively. The distribution at $V = -60$ mV indeed exhibits the expected

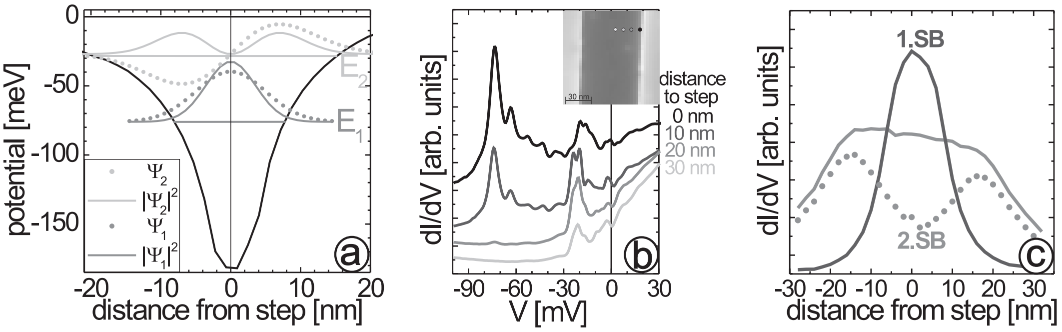

Figure 3.97: a.) Schematic representation of the expected confined states in the calculated potential; wave functions Ψ_n (dotted lines) and squared wave functions $|\Psi_n|^2$ (solid lines) are shown. b.) dI/dV curves taken at different distance from the step edge as indicated on the right and as dots in the constant-current image of the inset, $V_{stab} = 50$ mV, $I_{stab} = 1.2$ nA. c.) $dI/dV(x)$ at $V = -60$ mV corresponding to the first 1DES subband (dark grey) and $V = -20$ mV corresponding to the first and the second subband (light grey, solid line); to deduce the shape of the second subband, the intensity of the first subband at $V = -20$ mV is subtracted according to $DOS_n(E) \propto (E - E_n)^{-0.5}$ resulting in the dotted line.

Gaussian shape (dark grey line). The shape recorded at $V = -20$ mV above E_2, appears as a mesa (light grey line). Here, one has to take into account that also the first subband contributes to dI/dV. After subtracting this part, the expected double hill structure becomes visible as shown by the dotted line.

The most interesting part is the behaviour of the 1DES in the direction along the step edge, y. Its LDOS is measured over a distance of 800 nm. To get an impression of the potential along this step edge we apply the following procedure. First we subtract the average apparent shape of the step edge along x, called $\overline{z}(x)$, from the constant-current image $z(x, y)$ shown in Fig. 3.98a. This results in Fig. 3.98b. Dark and bright spots of a FWHM of 10 nm becone visible along y. They have to be attributed to positively and negatively charged point defects [65]. To Fig. 3.98b we apply the same method discussed with respect to the potential determination in Fig. 3.96c resulting in the potential $V(y)$ shown in Fig. 3.98c. The potential fluctuates irregularly by about ±30 meV. The standard deviation of the potential along y is $\sigma(V) \simeq 9$ meV.

The corresponding LDOS is shown for different energies in Fig. 3.98d−o. It exhibits strong fluctuations with a corrugation strength of 90 %. The fluctuation length decreases with increasing energy as expected from the InAs dispersion. At $V = -25$ mV, the appearance of the second subband is visible as dI/dV intensity at larger distances from the step edge. Also this intensity fluctuates along the step edge and its fluctuation length decreases with increasing V. Notice that the distribution of dI/dV intensity of the second subband at $V = -25$ mV is rather similar to the distribution of the first subband at $V = -75$ mV. This indicates the influence of the same disturbing potential on the two subbands. In both cases, the LDOS starts to appear at rather flat potential regions and not in deep potential valleys, which demonstrates that the

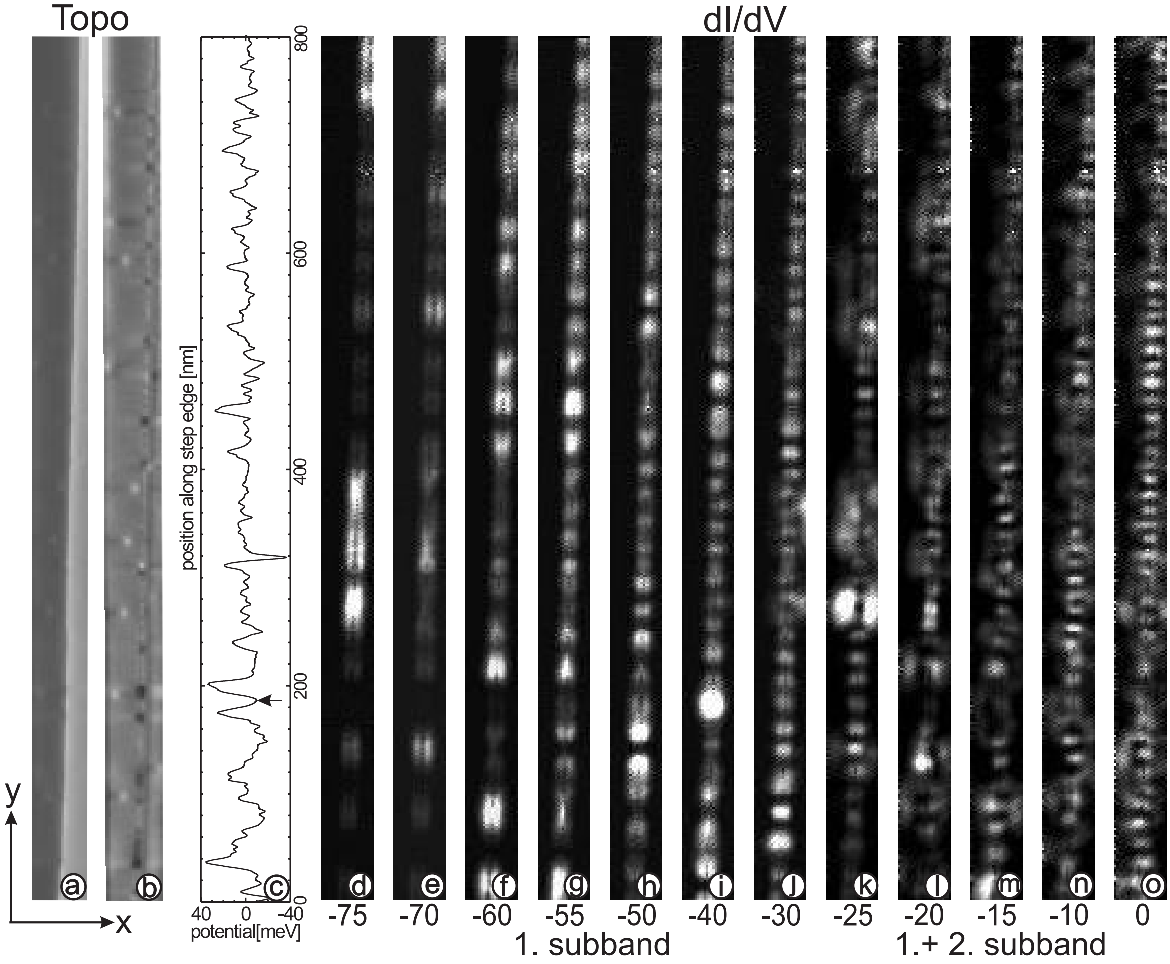

Figure 3.98: a.) Constant-current image of the investigated step edge, $V = 200$ mV, $I = 1.2$ nA. b.) Same as a.) after subtracting the average apparent height $\overline{z}(x)$ of the step edge. c.) Resulting potential along the step edge according to [38]; arrow marks a position discussed in the text. d–o.) dI/dV-images recorded at different V as indicated below in mV; $V_{stab} = 50$ mV, $I_{stab} = 1.2$ nA.

gain in kinetic energy dominates with respect to the possible gain in potential energy. Particularly interesting is the LDOS in the steep valley region marked by an arrow in Fig. 3.98c. Here, the LDOS is zero up to an energy of $V = -55$ mV. Then a bright spot appears with a maximum at $V = -40$ mV resembling a resonant state confined in the deep valley.

Figure 3.99 shows a grey-scale plot of the Fourier transformation of the dI/dV data. For comparison the expected unperturbed InAs dispersion of the two subbands is shown (white lines) [57]. As in the case of the 2DES the unperturbed dispersion is still faintly visible, but obviously additional intensity, mainly at lower k values, is present. An understanding of the origin of this additional intensity requires calculations similar to the ones presented in Fig. 3.93, which are currently under way.

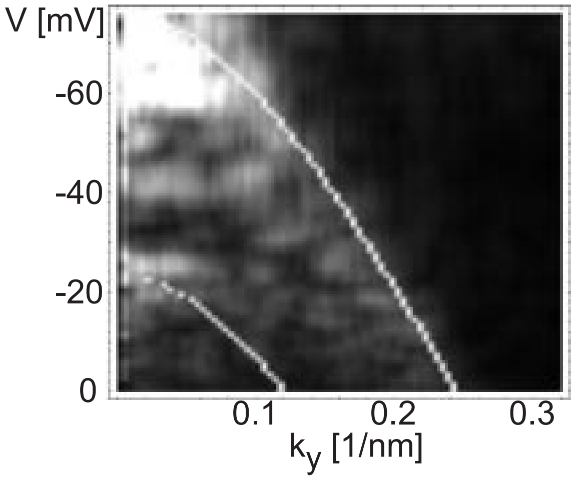

Figure 3.99: Grey scale representation of the Fourier transforms of dI/dV images as shown in Fig. 3.98d−o. The dispersion curves of unperturbed InAs corresponding to the two subbands are shown as white lines for comparison [57].

3.4.5 Zero-dimensional electron systems

Zero-dimensional electron systems confined in semiconductors are called quantum dots or artificial atoms. They have been investigated extensively in the past, since their increased size with respect to atoms allows to study the influence of strong magnetic fields and correlation effects on the electronic structure of a system confined in all three dimensions [66]. In particular, the reduced electron density of quantum dots favors the influence of electron-electron interactions, e.g. the exchange interaction. The last is a puzzling quantity, since its many-particle character leads to a non-local correlation with perturbations.

The aim of this section is to probe this non-locality. We use the recently discovered tip-induced quantum dot (QD) [7, 12], which is introduced into a semiconductor surface by the tip of a scanning tunneling microscope (STM). The tip acts as a local gate movable over the surface and the QD probes different potential environments of the surface. Thus the potential fluctuations of the sample act as spatially varying perturbations on the confinement potential. The resulting exchange interaction is probed by measuring the spin splitting of the QD, i.e we record dI/dV-curves in magnetic field exhibiting spin split states [13]. A comparison of the resulting spatial map of the spin splitting with the surface potential map answers the question, if the exchange interaction reacts locally or non-locally on potential perturbations. As expected, we find a non-local correlation, which, to our knowledge, is the first real-space visualization of the non-local character of the exchange interaction.

Besides this physical aspect, the study has also a technological aspect: the spin of a quantum dot has been proposed as a basic unit (qubit) in quantum computation [67]. The approach can be extended to a large number of qubits and the spin degree of freedom provides a reasonable coherence time [68]. However, in contrast to atoms, quantum dots suffer from their imperfections in the confinement potential leading to slightly varying level schemes between nominally identical dots [69]. Hence, the influence of potential perturbations on the spin splitting has to be understood to realize controllable devices. This study is a first step in that direction, although we did not find a quantitative model to explain our data.

To make a quantitative comparison between the confinement potential and the resulting energy levels, we first determine the QD potential. It consists of a position independent part provided by the potential of the tip (*averaged* QD potential) and a position dependent part given by the potential fluctuations of the sample. To reconstruct the QD potential, we use several results from previous publications [2, 7, 12]. The determination of the *averaged* QD potential is described in [12]. The QD states visible in dI/dV-curves at $B = 0$ T are measured. To get rid of influences of potential fluctuations of the sample, the QD spectrum is averaged over a $(200\ \text{nm})^2$-area. Fig. 3.100 shows the spectrum of the QD used in these experiments. Peak voltages are marked by vertical lines. It has been checked, that the spectrum does not change during the experiment by measuring it before and after recording the presented results. The measured energy states are compared with Hartree calculations for

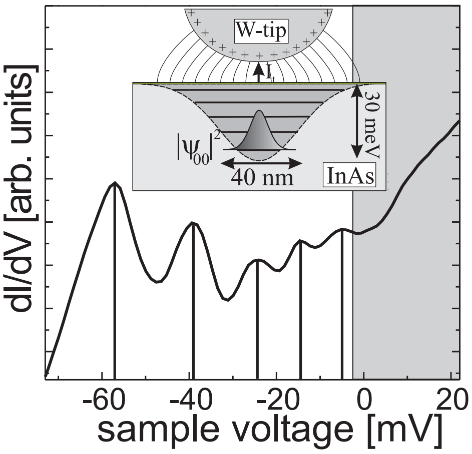

Figure 3.100: Spatially averaged dI/dV-spectrum of n-InAs(110) ($N_D = 2.0 \cdot 10^{16}$ cm^{-3}), $B = 0$ T, $I_{stab} = 300$ pA , $V_{stab} = 100$ pA; vertical lines mark peak positions, the grey area corresponds to the bulk conduction band. Inset: sketch of the corresponding *averaged* quantum dot potential (dark grey area); horizontal lines mark the quantized states and Ψ_{00} depicts the shape of the lowest energy state.The arrow labeled I_t marks the position of the tunneling current.

different trial potentials. In general, it turns out that a circular symmetric Gaussian shaped QD gives a reasonable description of the found states [12]. Hence the QD is described by the potential depth and the σ-width of a Gaussian. For the spectrum of Fig. 3.100 the resulting confinement potential (present at $V = 0$ mV) is shown as an inset.

Next, we determine the potential of the sample. Its spatial dependence results from additive contributions of the screened Coulomb potentials of all dopants $V_{Coul}(r) = -e/(4\pi\epsilon r) \cdot exp(-r/\lambda)$ (r: distance from dopant, ϵ: dielectric constant, λ: screening length (16 nm)). The dopant positions can be determined. Lateral (x, y) positions are directly visible from constant-current images [35, 38]. To determine the dopant depth below the surface (z), we use our previously described analysis of the scattering states visible in dI/dV-images [2]. The procedure is visualized in Fig. 3.101. Fig. 3.101a shows a dI/dV-image, which, as usual, is normalized to get a map of the local density of states (LDOS) in Fig. 3.101b [2]. The scattering states of individual dopants appear as ring structures. These scattering states recorded at different voltages are compared with WKB-calculations using *one* fitting parameter: the depth of the dopant below the surface. To perform the comparison with high accuracy we zoom to individual dopants and measure the scattering states at several voltages [2]. Having thus determined the position of each dopant, screened Coulomb potentials are fixed at each position and the Coulomb potentials are added up to get the surface potential depicted in Fig. 3.101c. Of course, the potential at other depth levels is also obtained from this method. We like to point out that this new method to determine the surface potential is not meant to be quantitative on a meV-scale, since the depth determination has an error bar of 20 %, dopants located deeper than

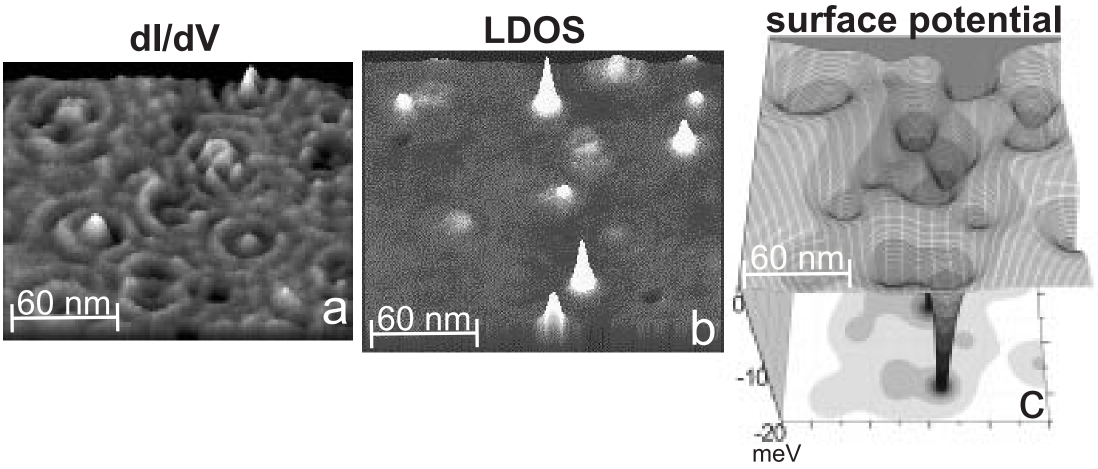

Figure 3.101: a.) dI/dV-image, $B = 0$ T, $V = 50$ mV, $I = 400$ pA; b.) normalized LDOS-image corresponding to a.): $\mathrm{LDOS}(x,y) = dI/dV(x,y)/I(z(x,y))$. Here $z(x,y)$ is the constant current image recorded in parallel with $dI/dV(x,y)$ and $I(z)$ is measured with the same tip afterwards [2]; c.) surface potential map resulting from an analysis of the scattering states (see text).

25 nm below the surface can not be evaluated and the influence of the surface on ϵ is neglected. But, important for these experiments, none of the restrictions influences the general shape of the surface potential. Obviously, the sum of the surface potential and the *averaged* QD potential centered at the measurement position gives the QD potential present during the measurement of an individual dI/dV-curve. It is different at each position. Knowing the QD potential, we now discuss the resulting energy levels. Since we are interested in the spin splitting data, we concentrate on the energy levels in magnetic field. The black line in Fig. 3.102a shows *one* dI/dV-curve recorded at $B = 6$ T at the position marked by the dot in Fig. 3.102c . The spectrum is reproducable on the time scale of weeks, if the same measurement position is used. It is independent of I_{stab} excluding influences of charging of the sample by the tunneling current. The spectrum exhibits three prominent peaks identified as different Landau levels. In addition, the peaks show a substructure consisting of two peaks, which is attributed to the spin splitting of the Landau levels. Both is discussed extensively in [13]. A fit of the dI/dV-curve is shown in Fig. 3.102a as a grey line. It is obtained with the assumption that the spectrum consists of six Gaussian shaped peaks of a σ-width of 3.2 meV (thin lines). Obviously, the fit is excellent. All 10^4 spectra recorded on a (200 nm)^2-area are reasonably fitted in that way. The maxima of the Gaussians are identified with the energies of the Landau and spin levels of the QD at an individual measurement position.

With these results (reconstruction of the QD potential, identification of probed energy levels), we can discuss the main result of the section shown in Fig. 3.102. Maps of the determined peak energies of the four low energy peaks are shown in Fig. 3.102c-f. Spin splitting maps obtained by subtracting Fig. 3.102e from c and Fig. 3.102f

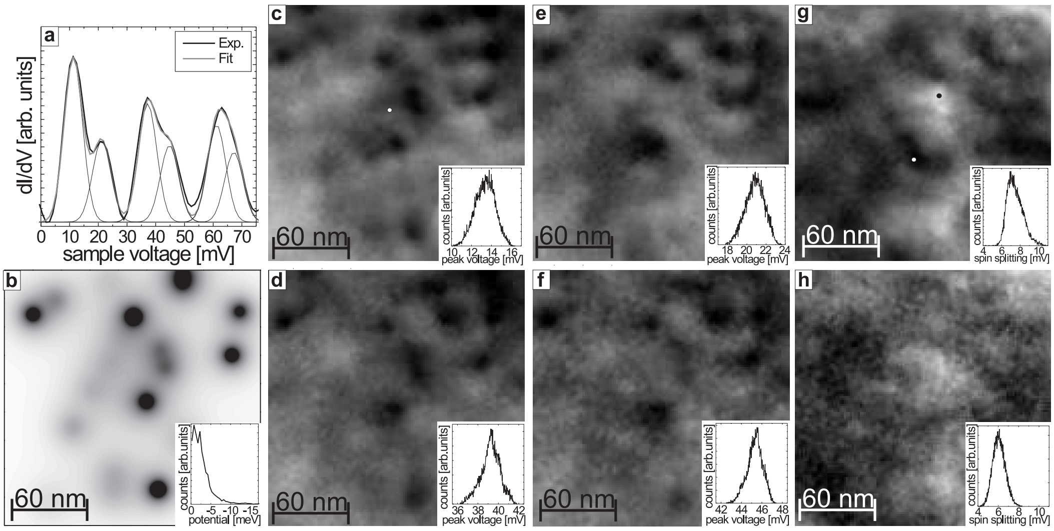

Figure 3.102: a.) Black line: dI/dV-curve from the position marked by a white dot in c.), $B = 6$ T, $I_{stab} = 300$ pA, $U_{stab} = 200$ mV; grey line: fit of the dI/dV-curve assuming six Gaussian peaks (thin, black lines) of a σ-width of 3.2 meV. b.) surface potential map of the investigated area (same as Fig. 3.101c), c.)–f.) maps of peak voltages of the four low voltage peaks fitted for 10^4 curves as shown in a.). They correspond to the two spin levels ($\uparrow,\downarrow$) of two Landau levels (LL1,LL2); c.) LL1, $\downarrow$; d.) LL1, $\uparrow$; e.) LL2, $\downarrow$; f.) LL2, $\uparrow$; g.)–h.) spin splitting maps obtained by subtracting e.) from c.), respectively f.) from d.). Insets in b.)–h.): histograms of obtained potential values, peak voltages and spin splittings. The positions marked by a black and a white dot in g.) are analyzed in Fig. 3.103.

from d, respectively, are shown in Fig. 3.102g and h. For comparison, Fig. 3.102b shows the surface potential map of the investigated area. As insets histograms of the obtained potential values, peak energies and spin splittings are given.

The energy maps are similar to the surface potential map. Fluctuations on small length scales due to individual dopants as well as large scale fluctuations, e.g. the bright area in the lower left part, appear to be similar in all energy maps (c$-$f) and in the potential map (b). Having in mind that the probed QD potential is the sum of the surface potential and the *averaged* QD potential centered at the measurement position, one has to conclude that the potential in the center of the QD is decisive for the state energies. This is not surprising, since Hartree-Fock calculations of the QD reveal that the states probed by STS have their main weight in the inner 20 nm of the QD [13]. Thus the surface potential acts as a local perturbation on the QD states. Of course, potential fluctuations on very small length scales smaller than the extension of the QD states do not lead to a linear change in QD state energy. These potential regions close to individual dopants are smeared out in the energy maps. Consequently, the tail in the surface potential histogram up to -15 meV is not reproduced by the energy histograms.

We now focus on the discussion of the spin splitting maps in Fig. 3.102g and h. They show a similar pattern for both Landau levels, but strongly differ from the surface potential map. Consequently, the local perturbation by the surface potential, describing the behaviour of individual energy states reasonably (see above), is not sufficient to explain the spin splitting of the same states. The reason is the non-locality of the exchange interaction. The large g-factor of bulk InAs resulting in a spin splitting of 5 meV at $B = 6$ T is caused by spin-orbit interaction. In contrast, the additionally enhanced spin splitting of the QD is due to the exchange interaction. This is evidenced by Hartree-Fock calculations of the QD performed by V. Gudmundsson (Science Institute, Reykjavik). He used different configurations of an impurity in the QD to reproduce the experimentally observed additional g-enhancement [13]. Since the exchange interaction mixes all QD states and thus depends in a non-local way on the surface potential, it naturally explains the differences in shape between the spin splitting maps and the surface potential map. In turn, the measured spin splitting maps compared with the surface potential map represent, to our knowledge, the first visualization of the non-local character of the exchange interaction. This is the central result of the present section.

Importantly, we can directly compare the complete QD potential with the resulting spin splitting. Especially, in view of possible applications [67], this promises to get a quantitative understanding of the non-local influence of potential perturbations on the exchange interaction. We did not succeed so far, but we like to present the lines of our first analysis. The analysis of the Hartree-Fock data implies that the total spin of the QD (sum of the spin of all occupied levels) fluctuates between 0 and 1 and is decisive for the observed spin splitting. However, only a limited number of QD-potentials have been calculated and thus an experimental test of this prediction is needed. We can not measure the total QD spin directly, but we can analyze the QD potentials present at different measurement positions. The QD potentials at positions of low and high spin splitting (marked by a white and a black dot in Fig.

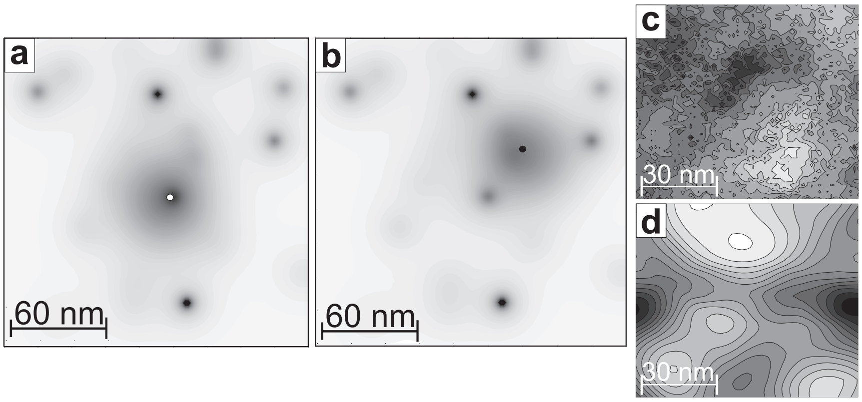

Figure 3.103: a.)–b.) Quantum dot potential present during the measurement at the positions marked by a black and white dot in Fig. 3.102g. c.) spin splitting map (inner part of Fig. 3.102g) spanning a spin splitting range from 4–12 meV; d.) map of the averaged quantum dot potential in a (10 nm)-ring 70 nm away from the center of the quantum dot; same area as in c.). The grey-scale spans a potential range from $-5 - -1.5$ meV.

3.102g) are depicted in Fig. 3.103a and b. An obvious difference between the two potentials is the different number of dopants at the QD rim, i.e. the QD extension. A simple argument would be that an extended state close to the Fermi level is changed from being unoccupied to being occupied by the slight blow up of the QD. This changes the QD spin and thereby the exchange interaction as proposed by the Hartree-Fock calculations. To be more quantitative we tried to estimate changes in the QD occupation from the QD potential. Therefore we used the knowledge provided by the Hartree-Fock calculations that the QD states have a ring-like shape with a width of about 10 nm. We divided each QD potential in 10 nm rings and calculated the average ring potential, thereby assuming that the ring potential determines the energy of the state with respect to the Fermi level and thus its occupation. Mapping the resulting data for different ring diameters, we unfortunately did not find strong correlations with the measured spin splitting map (Fig. 3.103c). However, some similarities in shape are found as e.g. at a ring radius of 70 nm shown in Fig. 3.103d: the grey areas in Fig. 3.103d (intermediate ring potential) partly correlate with bright areas in Fig. 3.103c (high spin splitting), while bright and dark areas in Fig. 3.103d (high and low ring potential) correspond more to dark areas in Fig. 3.103c (low spin splitting). However, several details in the two images are quite different. From this and the complete analysis of the QD potentials, we conclude that our simple model is not sufficient to explain the spin splitting data. Consequently, more intricate effects, as the overlap of different wave functions have to be considered.

Notice that QD's, proposed as qubits for quantum computation, will probably suffer from the same imperfections as studied here. Thus, tuning of the spin splitting in an assembly of quantum dots remains a difficult task, worthwile some additional considerations. The introduced method, up to now exclusively, can deliver the needed experimental information.

Summary

The preceding chapters underline the enormous potential of scanning tunneling spectroscopy applied to dilute electron systems. By detecting the LDOS a basic property of the system is visualized. That leads to a completely new understanding of the behaviour of a 3DES in the extreme quantum limit. The peculiar shape of the Hall curve known for more than 40 years has been found to be related to the appearance of drift like states, usually expected in a 2DES in magnetic field. A tentative explanation of this behaviour as well as of the shape of the Hall curve has been deduced from the data.

Two-dimensional electron systems accesible for STS have been prepared, thus allowing to tackle the paradigmatic case of electron systems. The 2DES has been characterized by ARUPS and exhibits electron densities between 10^{11} cm^{-2} and 10^{12} cm^{-2}. The LDOS of some particular 2DES's has been measured by STS. The presence of the tip-induced quantum dot during these measurements allowed to map the potential landscape of the 2DES area in parallel. Thus the complete ingredients of the Schrödinger equation describing the 2DES are known and the resulting LDOS is measured, an important requirement for fundamental studies. As a first result, we presented a numerical solution of the Schrödinger equation including the measured inhomogeneous potential, which was able to largely reproduce the measured LDOS. In magnetic field, the LDOS dramatically changes exhibiting the drift states expected for a 2DES in the quantum Hall regime. Notice, that the LDOS measurements of a 2DES in magnetic field is very promising, since it allows to directly detect the different predicted electron phases as, e.g., the recently proposed stripe phase appearing at half filling.

A one-dimensional system has been found below a charged step edge and its LDOS as well as the underlying potential have been mapped.

Finally, we used the tip-induced quantum dot to probe the influence of residual disorder on the exchange interaction in the quantum dot. A rather complex behaviour has been found, which is not completely understood, but nicely demonstrates the non-locality of the exchange interaction.

References

[1] M. F. Crommie *et al.*, Nature **363**, 524 (1993); E.J. Heller *et al.*, Nature **369**, 464 (1994); Y. Hasegawa *et al.*, Phys. Rev. Lett. **71**, 1071 (1993); Ph. Avouris *et al.*, Science **264**, 942 (1994); Ph. Avouris *et al.*, Chem. Phys. Lett. **240**, 423 (1995); Ph. Hoffmann *et al.*, Phys. Rev. Lett. **79**, 265 (1997). M.C.M.M. van der Wielen *et al.*, Phys. Rev. Lett. **76**, 1075 (1996).

[2] Chr. Wittneven *et al.*, Phys. Rev. Lett. **81**, 5616 (1998).

[3] J. Li *et al.*, Phys. Rev. Lett. **81**, 4464 (1998); L. Bürgi *et al.*, Phys. Rev. Lett. **82**, 4561 (1999).

[4] A. Yazdani *et al.*, Science **275**, 1767 (1997); S. H. Pan *et al.*, Nature, **413**, 6853 (2001); E. W. Hudson **et al.**, Nature, **411**, 6840 (2001); S. H. Pan *et al.*, Nature, **403**, 746 (2000); E. W. Hudson **et al.**, Science, **285**, 5424 (1999).

[5] S. Heinze, M. Bode, A. Kubetzka, O. Pietzsch, X. Nie, S. Blügel, and R. Wiesendanger, Science **288**, 1805 (2000); O. Pietzsch, A. Kubetzka, M. Bode, and R. Wiesendanger, Science **292**, 2053 (2001); M. Bode, O. Pietzsch, A. Kubetzka, S. Heinze, and R. Wiesendanger, Phys. Rev. Lett. **86**, 2142 (2001); M. Kleiber, M. Bode, R. Ravlic, and R. Wiesendanger, Phys. Rev. Lett. **85**, 4606 (2000); R. Wiesendanger, M. Bode, and M. Getzlaff, Appl. Phys. Lett. **75**, 124 (1999); M. Bode, M. Getzlaff, and R. Wiesendanger, Phys. Rev. Lett. **81**, 4256 (1998); O. Pietzsch, A. Kubetzka, M. Bode, and R. Wiesendanger, Phys. Rev. Lett. **84**, 5212 (2000).

[6] J. Li *et al.*, Phys. Rev. Lett. **80**, 2893 (1998); V. Madhavan *et al.*, Science, **280**, 567 (1998); H. C. Manoharan *et al.*, Nature, 403, 512 (2000).

[7] M. Morgenstern *et al.*, J. Electr. Micr. Rel. Phen., **109**, 127 (2000).

[8] D. Haude *et al.*, Phys. Rev. Lett. **86**, 1582 (2001); M. Morgenstern *et al.*, Phys. Rev. B, **64**, 205104 (2001).

[9] M. Morgenstern *et al.*, Phys. Rev. B, **61**, 13805 (2000).

[10] M. Getzlaff *et al.*, Phys. Rev. B, **763**, 205305 (2001).

[11] M. Morgenstern *et al.*, Phys. Rev. B, submitted (2001).

[12] R. Dombrowski *et al.*, Phys. Rev. B. **59**, 8043 (1999).

[13] M. Morgenstern *et al.*, Phys. Rev. B. **62**, 7257 (2000).

[14] M. Morgenstern *et al.*, Phys. Rev. B. **59**, 201301(R) (2001).

[15] M. Morgenstern *et al.*, Phys. Rev. Lett. **84**, 5588 (2000).

[16] Chr. Wittneven *et al.*, Rev. Sci. Instr. **68**, 3806 (1997).

[17] B. Voigtländer, G. Meyer, and N. M. Amer, Phys. Rev. B **44**, 10354 (1991); R. Allensbach, M. Stampanoni, and A. Bischof, Phys. Rev. Lett. **65**, 3344 (1990).

[18] K. Rossnagel *et al.*, Nucl. Instrum. Methods Phys. Res. A, **467-8**, 1485 (2001).

[19] S.D. Jog *et al.*, J. Phys. C **11**, 2763 (1978).

[20] P. Skudlarsky *et al.*, Phys. Rev. B **48**, 8547 (1993).

[21] Y. Yafet *et al.*, J. Phys. Chem. Solids **1**, 137 (1956).

[22] S.T. Pavlov *et al.*, Sov. Phys. JETP **21**, 1049 (1965).

[23] S.S. Murzin, JETP Lett. **44**, 56 (1986); F.F. Egorov *et al.*, Sov. Phys. JETP **67**, 1045 (1988).

[24] M. Shayegan *et al.*, Phys. Rev. B **32**, 6952 (1985); Phys. Rev. B **38**, 5585 (1988) V.J. Goldman *et al.*, Phys. Rev. Lett. **57**, 1056 (1986).

[25] P. Vasilopoulos *et al.*, J. Math. Phys. **25**, 1391 (1984).

[26] R.G. Mani, Phys. Rev. B **90**, 7922 (1990).

[27] O. Viehweger *et al.*, Phys. Rev. B **43**, 6840 (1991); U. Zeitler *et al.*, J. Phys. Cond. Mat. **6**, 4289 (1994).

[28] A. Chabra and R. V. Jensen, Phys. Rev. Lett. **62**, 1327 (1989); F. Milde, R. A. Römer, and M. Schreiber, Phys. Rev. B **55**, 9463 (1997).

[29] B. Huckestein, B. Kramer, and L. Schweitzer, Surf. Sci. **263**, 125 (1992); R. Klesse and M. Metzler, Europhys. Lett. **32**, 229 (1995).

[30] B.A. Aronzon *et al.*, phys. stat. sol. (b) **157**, 17 (1990); Philos. Mag. B **67**, 847 (1992); Sov. Phys. JETP **62**, 71 (1985); J. Mosc. Phys. Soc. **2**, 33 (1992).

[31] S.S. Murzin *et al.*, Phys. Rev. Lett. **80**, 2681 (1998).

[32] J.T. Chalker *et al.*, Phys. Rev. Lett. **75**, 4496 (1995).

[33] R. Joynt *et al.*, Phys. Rev. B **29**, 3303 (1984); R.E. Prange *et al.* (eds.,) "The Quantum Hall Effect", Springer Verlag, New York 1990.

[34] M.Ya Azbel *et al.*, Phys. Rev. B **32**, 562 (1985).

[35] R.M Feenstra *et al.*, J. Vac. Sci. Technol. B **5**, 923 (1987).

[36] V. Ramachandran *et al.*, Phys. Rev. Lett. **82**, 1000 (1999).

[37] D. Vion *et al.*, J. Appl. Phys. **77**, 2519 (1995).

[38] M. Morgenstern *et al.*, phys. stat. sol. (b) **210**, 845 (1998).

[39] D. Haude *et al.*, Phys. Rev. Lett. **86**, 1582 (2001).

[40] S.H. Tessmer *et al.*, Nature, **392**, 6671 (1998); G. Finkelstein *et al.*, Science, **289**, 90 (2000); possibly readers might identify the structures found there with our structures, but Finkelstein *et al.* measure capacitance in a 2D system thus being sensitive to charging of their tip-induced quantum dot in the fluctuating 2D potential, while we measure tunneling current being sensitive to the LDOS of the 3D system investigated here.

[41] N.B. Zhitenev *et al.*, Nature, **404**, 473 (2000); A, Yacobi *et al.*, Sol. State Com. **111**, 1 (1999).

[42] A. L. Efros *et al.*, J. Phys. C, **8**, L49 (1975).

[43] K. v. Klitzing *et al.*, Phys. Rev. Lett. **45**, 494 (1980); D. C. Tsui *et al.*, Phys. Rev. Lett. **48**, 1599 (1982). R. E. Prange *et al.*, "The Quantum Hall Effect", Springer 1987.

[44] Y. Chen *et al.*, Phys. Rev. B **39**, 12682 (1989); H.U Baier *et al.*, Solid State Com. **58**, 327 (1986); H.U Baier, *et al.*, J. Vac. Sci. Technol. B **4**, 1086 (1986); T. van Gemmeren *et al.*, Appl. Surf. Sci. **65/66**, 625 (1993); K. Smit *et al.*, J. Vac. Sci. Technol. B **7**, 888 (1989); V.Yu Aristov *et al.*, Phys. Rev. B **47**, 2138 (1993); V.Yu Aristov, Physica Scripta **T39**, 333 (1991); W.N. Rodrigues *et al.*, Chemistry and Defects in Semiconductor Heterostructures Symposium, eds: M. Kawabe, T.D. Sands, E.R. Weber, and R.S. Williams, Mater. Res. Soc., Pittsburgh, USA , 197 (1989); V.Yu Aristov *et al.*, Surf. Sci. **251/252**, 453 (1991); V.Yu Aristov *et al.*, J. Vac. Sci. Technol. B **12**, 2709 (1994); V.Yu Aristov *et al.*, Surf. Sci. **331-333**, 641 (1995); C. Nowak *et al.*, Surf. Sci. **331-333**, 619 (1995); V. Yu Aristov *et al.*, Appl. Surf. Sci. **104/105**, 73 (1996); V.Y. Aristov *et al.*, Europhys. Lett. **26**, 359 (1994).

[45] C.B.M Andersson *et al.* Surf. Sci. **398**, 395 (1998); C.B.M. Andersson *et al.*, Phys. Rev. B, **47**, 2427, (1993).

[46] W. Mönch, "Semiconductor Surfaces and Interfaces", Springer Series in Surface Science 26, Springer, Berlin, 1993; W. Mönch, "Electronic Structure of Metal-Semiconductor Contacts", Perspectives in Condensed Matter Physics, Kluver Academic Publishers, Milano, 1990.

[47] J.C Riviere, "Surface Analytical Techniques", Oxford University Press, 1990, p. 100.

[48] T. Ando *et al.*, Rev. Mod. Phys. **54**, 437 (1982).

[49] M.G. Betti *et al.*, Solid State Com. **110**, 661 (1999); V. Yu Aristov *et al.*, Surf. Rev. and Lett. **5**, 235 (1998); M.G. Betti *et al.*, Phys. Rev. B **63**, 155315 (2001).

[50] see e.g. T. Ando *et al.*, Rev. Mod. Phys. **54**, 437 (1982); P. A. Lee *et al.*, Rev. Mod. Phys. **57**, 287 (1985).

[51] E. Abrahams *et al.*, Phys. Rev. Lett. **42**, 673 (1979).

[52] K. Kanisawa *et al.*, Phys. Rev. Lett. **86**, 3384 (2001).

[53] J. J Koonen *et al.*, Phys. Rev. Lett. **84**, 2473 (2000); R. Joynt *et al.*, Phys. Rev. B **29**, 3303 (1984).

[54] LDOS and dI/dV coincide as long as V is small [12] and electron-electron interactions are negligible.

[55] K. Hirakawa *et al.*, Phys. Rev. B **33**, 8291 (1986).

[56] The number of contributing states is simply the product of DOS, image size and energy resolution of the experiment.

[57] U. Merkt *et al.*, Phys. Rev. B **35**, 2460 (1987).

[58] The experimental noise is considerably smaller than the intensities depicted in the FT's.

[59] The contributing energy scales are roughly given by the average kinetic energy $E_{kin} = 30$ meV, the σ-value of the potential fluctuations $\sigma(V) = 5$ meV and the electron-electron repulsion of regularly distributed point charges $E_{Coul} = 5$ meV. This indicates that away from E_F electron-electron interactions might be neglected.

[60] C. Metzner *et al.*, Phys. Rev. B **58**, 7188 (1996).

[61] J. Klijn *et al.*, to be published.

[62] J. Voit, Rep. Prog. Phys. **57**, 977 (1994); H. J. Schulz *et al.*, cond-mat/9807366 (1998).

[63] J. M. Luttinger, J. Math. Phys. **4**, 1154 (1963).

[64] Y. Liang *et al.*, Phys. Rev. B **48**, 11942 (1993).

[65] J. A. Stroscio *et al.*, J. Vac. Sci. Technol B **6**, 1472 (1988).

[66] R.C. Ashoori, Nature **379**, 413 (1996); L.P. Kouwenhoven *et al.*, Science **278**, 1788 (1997); C.W.J. Beenakker, Rev. Mod. Phys. **69**, 731 (1997).

[67] D. Loss *et al.*, Phys. Rev. A, **57**, 120 (1998); B.E. Kane, Nature, **393**, 133 (1998)

[68] J.M. Kikawa *et al.*, Phys. Rev. Lett. **80**, 4313 (1998); A. Inamoglu *et al.*, Phys. Rev. Lett. **83**, 4204 (1999).

[69] S.A. Empedocles *et al.*, Phys. Rev. Lett. **77**, 3873 (1996); B.T. Miller *et al.*, Physica B **249-251**, 257 (1998).

3.5 Nanomechanics

High resolution force microscopy developed rapidly since the end of 1995, the year in which true atomic resolution with dynamic force microscopy (DFM), also known as non-contact atomic force microscopy (NCAFM) was obtained for the first time in ultrahigh vacuum [1]. We participated in this field from the very beginning [2]. Due to our development of a very stable low temperature force microscope optimized for atomic resolution [3] we could contribute many important experimental results on various samples [4]. The distance dependence of the tip-sample interaction (dynamic force spectroscopy (DFS)) from the non-contact to the contact regime has been studied. The experimental data as well as analytical and numerical models were used to get a deeper understanding of the physical origin of the contrast formation and the role of dissipation during the tip-sample interaction. By comparison of DFM experiments and simulation the contrast mechanisms on the atomic scale and the differences between atomic resolution in the static mode contact force microscopy and DFM were clarified. Our experimental studies covered conductors (graphite) [5–7], semiconductors (indium arsenide) [8–10], insulators (nickel oxide) [11] and noble gas crystals (xenon) [12]. The experimental results have been successfully simulated for DFM [13,14] and DFS [6,7]. Moreover, thorough analysis gave a deeper insight into the measurement process itself [6,15–17].

All experimental data, which we well show in the following sections, were obtained with our low temperature ultrahigh vacuum force microscope [3]. The dynamic mode implemented in our instrument is based on the frequency modulation technique introduced by Albrecht et al. [18]. In this mode of operation the cantilever oscillates with its resonance frequency at an amplitude A, which is kept constant by a regulator. The frequency shift Δf between the eigenfrequency f_0 and the actual resonance frequency f of the cantilever is the measured quantity. A larger attractive tip-sample interaction results in a larger negative Δf. This frequency shift is a measure for the magnitude of the tip-sample interaction. In the spectroscopy mode (DFS) this signal is directly recorded to obtain the distance dependence of the tip-sample interaction. In the microscopy mode (DFM) this signal is used to adjust the tip-sample distance accordingly.

3.5.1 Direct Observation of Tip Induced Relaxation in Force Microscopy

A. Schwarz, W. Allers and U. D. Schwarz

Dynamic force microscopy (DFM) can be used to image the atomic structure of surfaces, because it is sensitive to short range forces between the foremost tip atom and the surface atom underneath. We will present experimental evidence that the interaction during atomic scale imaging can lead to a tip induced relaxation of surface atoms.

The sample was an n-InAs single crystals (doping concentrations $N_D \approx 3 \times 10^{18}$ cm^{-3}) cleaved in situ parallel to the (110) surface. InAs crystallizes in the ZnS structure, showing zigzag chains of alternating In (cations) and As (anions) atoms along the $[1\bar{1}0]$-direction (see Fig. 3.104a). The (110) cleavage plane of InAs is electrically neutral and (1×1) relaxed with a surface unit cell size of 0.606 nm × 0.427 nm [19]. According to the bond rotation model, which is valid for most III-V semiconductors, the As atoms move outwards and the In atoms inwards. Therefore, the (110) surface is As terminated (see Fig. 3.104b). Since the relaxation is accompanied by a charge transfer from the cation to the anion, the total valence charge has its maximum above the As atoms. Negative frequency shifts were used for imaging, which means that the total tip-sample interaction was attractive.

On atomic-scale images (cf. Fig. 3.105), usually only the As atoms are visible as protrusions in DFM images. Note, that experimentally other contrasts have been observed with some tips [8, 9], but As atoms always appear as protrusions. This is supported by theoretical ab initio calculations on similar III-V semiconductors [20,21]. Using this information, missing protrusions, as marked by arrows in Fig. 3.105), can be easily identified as As vacancies. In the line section of Fig. 3.105 no relaxation of the As atoms around a vacancy is detectable, which has been confirmed in higher magnification images [9]. A relaxation of the surrounding In atoms is likely, but since the In sublattice is not imaged here, no certain assertions are possible.

In Fig. 3.106 a different point defect is studied. As in Fig. 3.105 protrusions reflect the position of the As atoms. Both images in Fig. 3.106 show the same point defect at two different frequency shifts. The corrugation amplitude in $[1\bar{1}0]$-direction is 11 pm in a) and 20 pm in b), except above the two As lattice sites, which are marked byX” (X-sites). Furthermore, the contrast is inverted relative to the other As lattice sites.

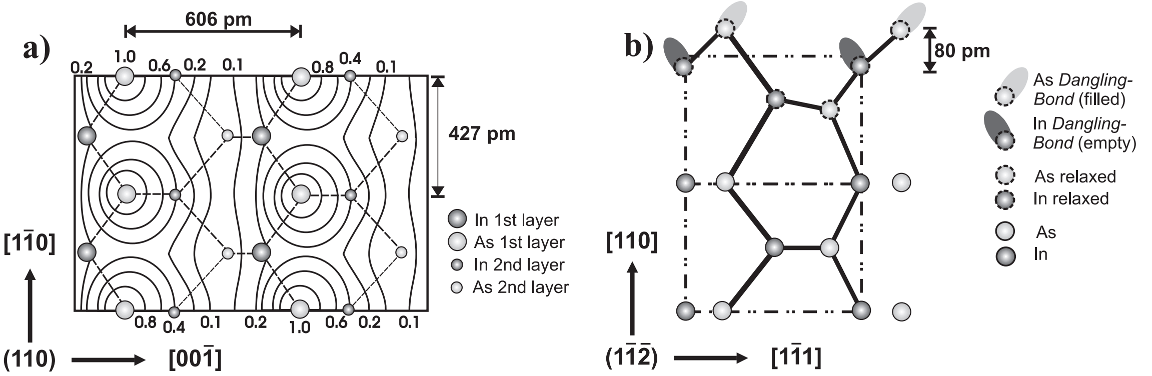

Figure 3.104: (a) Top view on the (110) cleavage plane of InAs. Bonds are indicated by dashed lines. Solid lines with small numbers represent the contour lines of the normalized total valence charge density 0.3 nm above the surface. (b) Side view of the relaxed surface. Due to the relaxation, which is accompanied by a charge transfer from the In atoms to the As atoms, the (110) surface becomes As terminated.

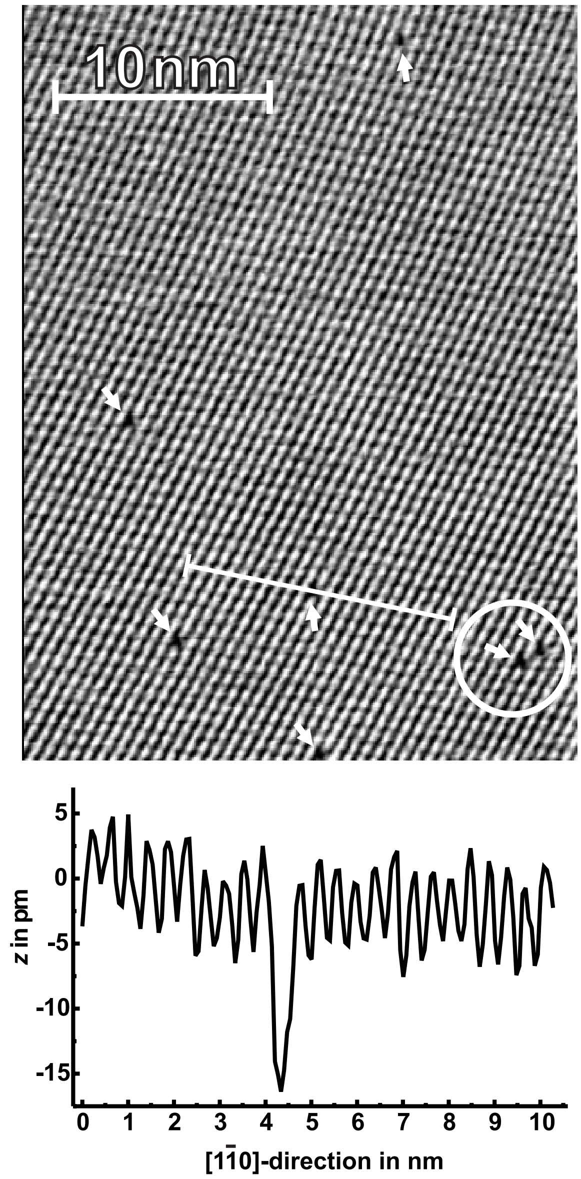

Figure 3.105: Typical DFM image of InAs(110) with a Si tip. The seven missing protrusions marked by white arrows can be identified as As vacancies. The line section shows a depression of about 15 pm instead of a protrusion at the position of the As vacancy. Parameters: $T = 14$ K, $k \approx 36$ N/m, $f_{\mathrm{res}} = 160$ kHz, $A = \pm 12.7$ nm, $\Delta f = -63.2$ Hz.

In a) the corrugation amplitude is only 5 pm and the X-sites appear 6 pm lower. In b) the corrugation amplitude is 30 pm and the X-sites appear elevated by 10 pm.

As mentioned before a larger adjusted frequency shift results in a smaller tip-sample distance and consequently in an increased tip-sample interaction. Therefore, the corrugation amplitude of the As sublattice in b) is larger than in a). Additionally, from the symmetry of the point defect with respect to the As sublattice it can be concluded

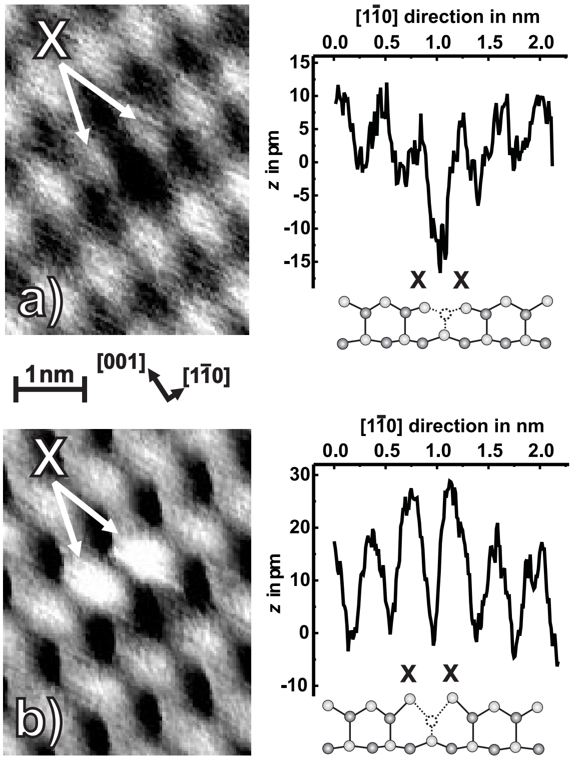

Figure 3.106: DFM images of an In-vacancy at two different tip-sample distances. The position of the defect is slightly shifted due to a different xy-offset voltage at the scan piezos. The two As lattice sites, which are influenced by the In-site defect are marked with X (X-sites). In a), the X-sites appear displaced by 6 pm into the bulk (see the line section for illustration). In b), the tip-sample distance is reduced by adjusting a larger negative frequency shift Δf, and now, the X-site As atoms appear to be 10 pm higher than the surrounding As atoms (see line section). This change is attributed to a stronger tip-sample interaction caused by the reduced tip-sample distance, which pulls the two weakly bound As atoms into the vacuum region. Parameters: $T = 14$ K, $k \approx 36$ N/m, $f_{\mathrm{res}} = 160$ kHz, $A = \pm 12.7$ nm, a) $\Delta f = -39.5$ Hz and b) $\Delta f = -44.7$ Hz.

that the point defect is located on the In sublattice. The observed distance dependence of the contrast indicate the presence of an In vacancy in the surface layer. A missing In atom reduces the number of bonds of two neighboring surface As atoms from three to two. According to calculations done by G. Schwarz et al. for GaAs(110) [22], this results in an inward relaxation of the neighboring anions for surface cation vacancies. Such an inward relaxation is observed in a) at a relatively small tip-sample interaction. An increased tip-sample interaction as in b) might provide enough energy to pull the two weakly bonded As atoms towards the tip. The presence of this additional interaction could reverse the relaxation. Consequently, the two weakly bonded As atoms would appear elevated as indeed observed in b). Note, that other possible point defects cannot be ruled out completely, but are very unlikely as explained in Ref. [9].

This experimental result strongly suggests, that relaxation is present even during measurements in the attractive force regime. Although only the relaxation of sample atoms around a defect can be directly observed, all other surface atoms of the sample will also relax. Due to its exposed position relaxation has to be considered for the foremost tip apex atom as well. This has been confirmed by ab initio calculation on GaAs(110), where the tip atoms as well as the atoms of the defect free surface were allowed to relax [21]. It appears that DFM has the capability to directly measure site specific elastic properties on the atomic scale. Moreover, the investigation of such point defects can help to understand how relaxation processes influence the tip-sample interaction.

3.5.2 Imaging of Dopants in n- and p- Doped InAs Single Crystals with Force Microscopy

A. Schwarz, W. Allers and U. D. Schwarz

Force microscopy is in principle sensitive to different types of forces, like van der Waals forces, magnetic forces, electrostatic forces and short range chemical forces. In particular, many schemes have been adopted to separate the electrostatic part of the tip-sample interaction from topographic effects [23–28]. In the following we will demonstrate that on atomically flat and clean semiconductors electrostatic interactions due to the presence of near surface ionized doping atoms can be directly observed with dynamic force microscopy (DFM). The contrast mechanisms due to electrostatic interactions between a metallic-like tip and a semiconducting sample is discussed.

Experimental

In DFM the sum of all tip-sample interactions is detected with a cantilever that oscillates with a constant amplitude at its resonance frequency. The measured quantity is the frequency shift Δf between the eigenfrequency f_0 and the actual resonance frequency f. If the tip-sample distance is kept constant the frequency shift is negative for attractive interactions and positive for repulsive interactions . In the constant frequency shift mode a feedback adjusts tip-sample distance accordingly. Thereby, the total tip-sample interaction is kept constant. The magnitude of the electrostatic tip-sample interaction can be influenced by the bias voltage (U_{bias}), which in our instrument is applied to the sample with respect to the grounded cantilever. For imaging, tips made from highly doped silicon (antimony, $N_D \approx 8\times10^{17}-5\times10^{18}$ cm^{-3}) were cleaned by argon ion sputtering before the measurements on n-InAs, whereas they remained untreated for measurements on p-InAs. The n- (sulphur) and p- (zink) doped InAs single crystals (doping concentrations $N_D \approx 3\times10^{18}$ cm^{-3} and $N_A \approx 4-6\times10^{18}$ cm^{-3}, respectively) used in this study were cleaved in situ ($p < 1\times10^{-7}$ Pa) parallel to the

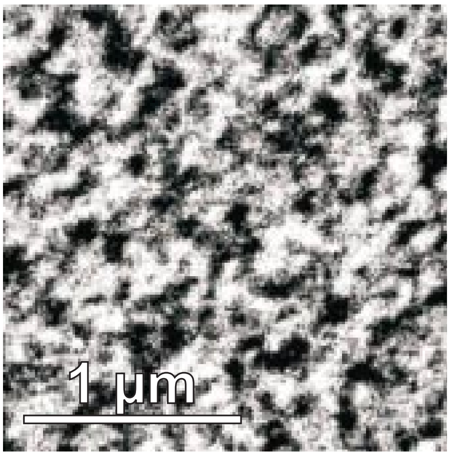

Figure 3.107: Long-range contrast on a large-scale DFM image acquired with constant frequency shift on an atomically flat terrace of n-InAs(110). The image has been taken directly after cleavage under UHV conditions. The observed corrugation is on the order of 0.1-0.2 nm and can be attributed to the presence of near surface doping atoms, which lead to a locally varying electrostatic tip-sample interaction. Parameters: T = 300 K, $k \approx 38$ N/m, f_{res} = 177 kHz, $A = \pm 10.2$ nm, image size 2.0 μm × 2.0 μm, $\Delta f = -62.5$ Hz, $U_{\mathrm{bias}} = 0$ V.

(110) surface. The (110) surface of InAs is electrically neutral and (1×1) relaxed with a surface unit cell size of 0.606 nm × 0.427 nm [19]. The band gap has a width of 360 meV at room temperature. No intrinsic band bending occurs at the clean defect-free surface, and no surface states are present in the forbidden band gap [29]. The Fermi level is unpinned at the surface and lies for our n-InAs (p-InAs) samples $\approx$ 290 meV ($\approx$ 18 meV) above (below) the conduction (valence) band edge. The electron gas is degenerated for both samples at all relevant temperatures.

Results

On large scale images of the n-doped sample, as in Fig. 3.107, a long range contrast with a corrugation of 0.2 nm could be observed. To investigate the nature and origin of this contrast, we explored its bias dependence using the following technique. First, the tip-sample distance was stabilized at an image point with $\Delta f = -12.5$ Hz and $U_{\mathrm{bias}} = +0.50$ V. Then, the feedback was switched off, and while the bias voltage was ramped in 10 s from -2.5 V to +3.5 V, the frequency shift Δf was recorded. Applying this method at each image point of a regular raster, we could generate a series of Δf-maps of the same surface area at different, but fixed bias voltages. The four images displayed in Fig. 3.108 represent such Δf-maps at $U_{\mathrm{bias}} = -2.22$ V, -0.25 V, +0.50 V, and +2.75 V. Bright (dark) areas in the images correspond to a increased (reduced) frequency shift. The encircled area illustrates the influence of the bias voltage: The contrast inverts from large negative to large positive bias voltages. At the +0.50 V, the contrast vanishes, which means that the interaction is the same at every point.

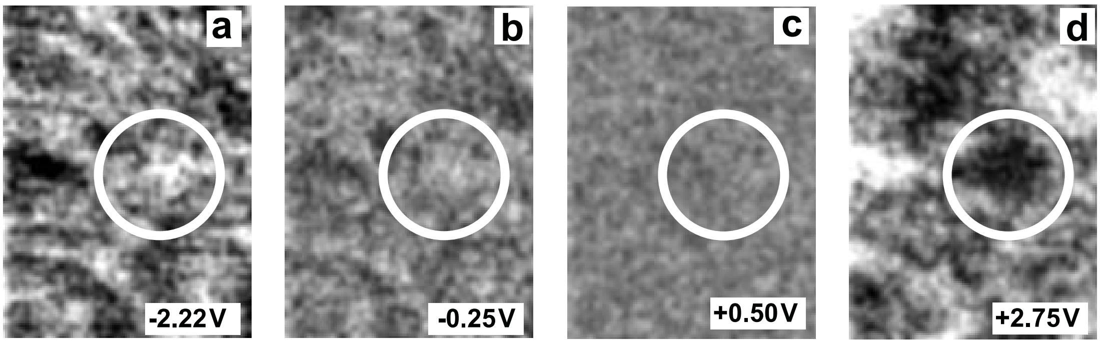

Figure 3.108: Series of images demonstrating the bias dependence of the frequency shift at identical sample locations. A detailed description of the technique used to generate these images can be found in the text. The encircled area illustrates the bias dependent contrast variations, which correspond to the fluctuations in the density distribution of doping atoms . (a) At $U_{\mathrm{bias}} = -2.22$ V, electrons (majority carriers) are accumulated at the surface. Bright areas correspond to a high density of doping atoms. (b) The contrast becomes weaker at smaller absolute values of U_{bias}. (c) At $U_{\mathrm{bias}} = +0.50$ V, the contrast vanishes. The surface is depopulated of mobile charge carriers. (d) At $U_{\mathrm{bias}} = +2.75$ V, holes (minority carriers) are generated near the surface. Inversion occurs and the contrast inverts. Parameters: $T = 300$ K, $k \approx 37$ N/m, $f_{\mathrm{res}} = 166$ kHz, $A = \pm 12.4$ nm, image size 300 nm × 400 nm, bias ramp at each point performed between -2.5 V and 3.0 V with 0.1 Hz sweep rate, stabilization values at each point: $\Delta f = -12.5$ Hz and $U_{\mathrm{offset}} = 0.5$ V.

Exactly this bias voltage was used when the feedback was turned on for stabilization at a new raster point. Therefore, the tip-sample distance was identical at each raster point before the bias ramp was started.

Directly after cleavage of the p-doped sample bright spots are visible as shown in Fig. 3.109. Approximately 150 of these spots can be counted on an area of 14400 nm^2. Images on the atomic scale, as in Fig. 3.110, reveal more features. Firstly, the As sublattice, which is represented by protrusions [12], is clearly resolved. Secondly, there are bright circular areas with diameters between 2 nm to 4 nm which possess an intact atomic structure. The upper line section in Fig. 3.110 along the [001]-direction across such a bright area shows that the corrugation amplitude between the maxima remains constant, but the envelope has approximately a gaussian shape. Thirdly, there are dark areas with diameters around 3 nm. The corresponding lower line section in Fig. 3.110 indicates that one corrugation maximum is missing in the center of this dark area. The same holds for all regions, which appear depressed in Fig. 3.110. Note, that we never could observe such features on the atomic scale images recorded on the n-doped sample.

Discussion

As a starting point of our discussion, we stress that the distribution of bright and dark areas in the Figs. 3.107, 3.108, and 3.109 does not reflect topographic features, because cleaved InAs(110) is atomically flat and under UHV conditions adsorbates should not be present immediately after cleavage. Instead, the bias dependence of the contrast, as visible in the image series of Fig. 3.108, strongly suggests that the contrast is of electrostatic origin.

To understand the observed effects, the electrostatic properties of the tip/sample system have to be taken into account. The tips used in our experiments can be considered to behave essentially as a metallic electrode. This assertion is justified by their high doping level. The second electrode of the system is represented by the semiconducting InAs sample. Any potential difference between tip and sample results in an electric field, which penetrates into the bulk. Therefore, the density of mobile charge carriers near the InAs surface is influenced in a more complex way by an electric field than it is in the metallic-like tip. It is important to note, that the potential difference between tip and sample is not only determined by the external applied bias voltage U_{bias}, but also depends on the difference between the work functions of tip (Φ_{tip}) and sample (Φ_{sample}). However, for a qualitative analysis of our experimental results, it is not necessary to know the absolute work function of the tip, but to realize the potential difference is in general not zero at $U_{\mathrm{bias}} = 0$ V.

Let us now recall the effect of a potential difference on the band structure at the surface of a semiconductor. For n-doped material, the electric field due to a negative potential with respect to the tip causes a downward band bending, which attracts majority carriers (electrons) towards the surface, i.e., an accumulation layer will form underneath the tip. At positive sample potentials, however, the bands bend upwards and electrons are repelled from the surface. If the conduction band crosses the Fermi level, no mobile charge carriers are available any more at the surface, and a depletion layer emerges. At the transition from accumulation to depletion the band bending is zero, i.e., the flat band condition is realized. If $\Phi_{\mathrm{tip}} \neq \Phi_{\mathrm{sample}}$, zero band bending is not achieved at $U_{\mathrm{bias}} = 0$, but at the so called flat band voltage U_{FB}. The actual value of U_{FB} depends on the tip geometry as well as on the tip-sample distance. Upon further upward band bending the depletion layer becomes thicker, until the valence band also crosses the Fermi level. At such a large positive potential difference, the depletion layer width remains constant and minority carriers (holes) are generated near the surface, which lead to the formation of an inversion layer directly at the surface below the tip. The same line of arguments is valid for p-doped material, in which the mobile charge carriers behave in an analogous way.

The electrostatic interaction described above is always attractive, independent of the polarity of the charge carriers (electrons or holes), because the mirror charges induced in a metallic tip are always of opposite polarity. The magnitude of the electrostatic interaction depends on the amount of band bending, which depends on the effective voltage between tip and sample (bias voltage plus contact potential differ-

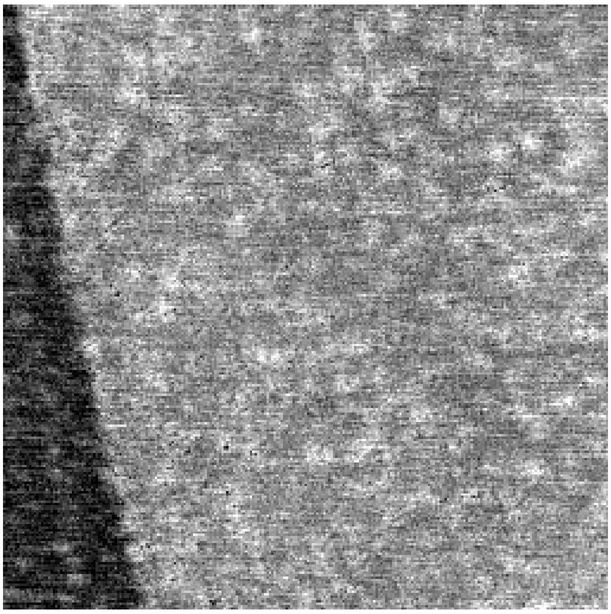

Figure 3.109: DFM image of the (110) p-InAs surface with a monoatomic step on the left hand side. The approximately 150 bright spots can be identified as individual doping atoms. Parameters: $T = 300$ K, $k \approx 34$ N/m, $f_{\mathrm{res}} = 149$ kHz, $A = \pm 15.3$ nm, image size 120 nm×120 nm, $\Delta f = -110.0$ Hz, $U_{\mathrm{bias}} = 0$ V.

ence). Locally, the band bending is modified by the presence of doping atoms or other charged defects. The volume in which the band structure is influenced underneath the tip depends on the tip-sample distance as well as on the tip radius and the screening length. The latter determines how deep the electric field penetrates the semiconductor. The screening length λ_{S} for degenerate semiconductors can be calculated from

$$\lambda_{\mathrm{S}} = 4(3/\pi)^{-\frac{1}{6}}\, N_{\mathrm{D,A}}^{-\frac{1}{6}}\, \epsilon^{-\frac{1}{2}}\, (m^*_{\mathrm{e,h}}/m_{\mathrm{e}})^{-\frac{1}{2}}\, a_{\mathrm{B}}{}^{\frac{1}{2}}, \tag{3.17}$$

where $a_{\mathrm{B}} = 0.053$ nm is the Bohr radius, $\epsilon = 14.55$ the dielectric constant of InAs, and m_{e} is the mass of the free electron. $m^*_{\mathrm{e,h}}$ represent the effective masses of the majority charge carriers (electrons and holes, respectively), and $N_{\mathrm{D,A}}$ correspondingly the concentration of either donator or acceptor doping atoms. Since both samples are degenerated, these values are identical with the majority charge carrier concentrations in thermal equilibrium. Note that λ_{S} depends only weakly on $N_{\mathrm{D,A}}$, but strongly on the effective masses $m^*_{\mathrm{e,h}}$. For InAs, the holes ($m^*_{\mathrm{h}} = 0.41 m_{\mathrm{e}}$) are about sixteen times heavier than the electrons ($m^*_{\mathrm{e}} = 0.026 m_{\mathrm{e}}$), leading to a four times smaller screening length in p-InAs ($\lambda^{\mathrm{p}}_{\mathrm{S}} \approx 2$ nm) than in n-InAs ($\lambda^{\mathrm{n}}_{\mathrm{S}} \approx 8$ nm). The screening length determines also the spherical volume in which the charge of a doping atom or any other defect is screened . While the screening length is quite different for the n- and p-doped sample, another important quantity to understand the electrostatic tip-sample interactions is the mean distance $\bar{r}$ between doping atoms. Its value can be calculated from the doping concentration and is very similar in both samples ($\bar{r}_{\mathrm{D}} \approx 7$ nm for n-InAs and $\bar{r}_{\mathrm{A}} \approx 6$ nm for p-InAs). Since they are not arranged into a regular lattice, their distribution fluctuates.

By comparing $\bar{r}$ and λ_{S} the different behavior of n- and p-InAs can be explained as follows. For the n-InAs sample there is a significant overlap of the Coulomb clouds around neighboring doping atoms ($\bar{r}_{\mathrm{D}} < \lambda_{\mathrm{S}}^{\mathrm{n}}$). Therefore, only the fluctuations of doping atoms are visible in Fig. 3.107. Bright and dark areas reflect high and low concentrations of mobile charge carriers, respectively. The contrast inversion in the image series presented in Fig. 3.108 illustrates how the observed contrast depends on sign and magnitude of the applied bias voltage. The magnitude changes the number of charge carriers, while the sign determines the type of charge carriers present at the surface. In accumulation, the area underneath the tip is populated by electrons, which are attracted by the positively charged doping atoms. The increased density of electrons around doping atoms causes locally a stronger electrostatic tip-sample interaction, which in turn leads to a larger frequency shift. Therefore, bright areas in Fig. 3.108a at large negative bias voltages correspond to a relatively large concentration of near surface doping atoms. Towards zero volts, the concentration of electrons decreases and consequently the contrast diminishes (see Fig. 3.108b). At the point of maximum depletion, approximately at $U_{\mathrm{bias}} = 0.5$ V, ionized doping atoms are the only charges present near the surface. Since they cannot sufficiently be screened by mobile charge carriers, the long-range electrostatic potentials overlap strongly and the contrast vanishes (see Fig. 3.108c). Finally, at large positive voltages holes are generated underneath the tip. Since the holes are repelled by the positively charged doping atoms, the contrast reverses. Thus, bright areas in Fig. 3.108d correspond to regions of reduced doping density.

For the p-InAs sample the overlap is very small ($\bar{r}_{\mathrm{A}} > \lambda_{\mathrm{S}}^{\mathrm{p}}$). Therefore, individual doping atoms are distinguishable (bright circular spots in Fig. 3.109. Close to the surface the screening sphere is cut and becomes visible as a circular spot, in which the the band bending is locally modified. Assuming that each spot in Fig. 3.109 could be identified with one ionized doping atom and taking the concentration of doping atoms given by the manufacturer, it follows that doping atoms up to a depth of 1.7 nm to 2.5 nm can be detected. This is in good agreement with the calculated screening length, which is a measure of the depth in which doping atoms should be detectable with a surface sensitive method like force microscopy.

In Fig. 3.110 the atomic structure at the surface is resolved. Bright areas can be identified as doping atoms which are negatively charged and surrounded by holes. The missing protrusions in the centers of the dark areas indicate the presence of As vacancies [9]. Scanning tunneling microscopy experiments on p-InAs samples with a similar doping concentration indicate that such vacancies are positively charged and surrounded by an electron cloud [30]. In addition to the band bending due to an effective voltage between tip and sample, the charged point defects modify the band bending at the surface locally in an area with a radius λ_{S}. For one type of defects the local modification results in a small upward band bending, for the other type the

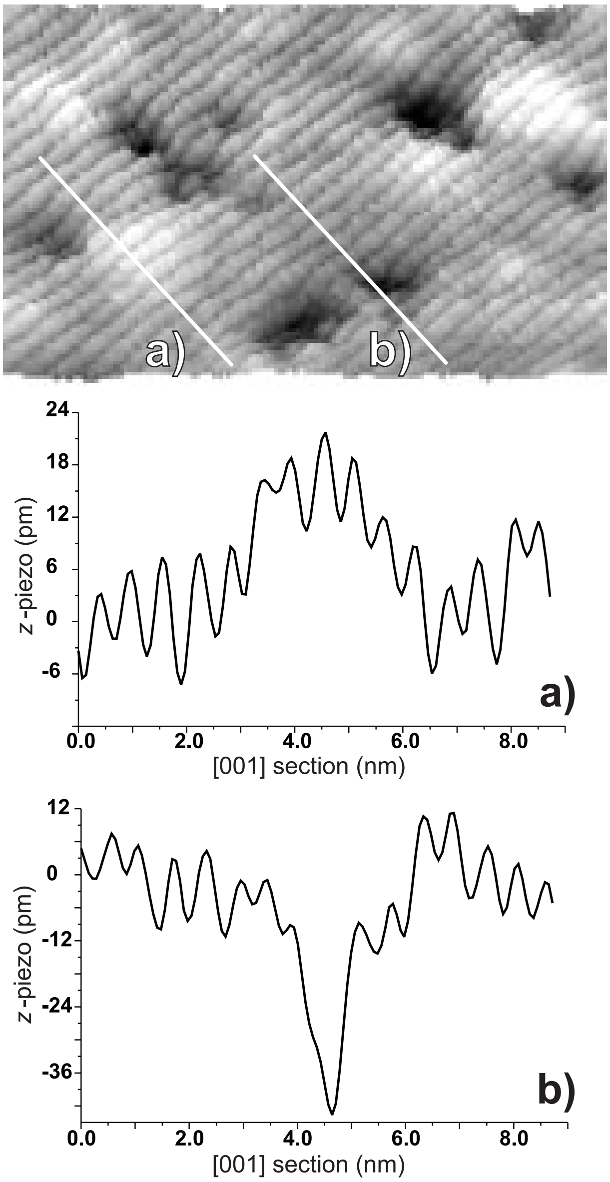

Figure 3.110: Atomically resolved DFM image of p-InAs(110) acquired with constant frequency shift and displayed in a quasi 3D-representation. Bright areas with an intact atomic structure correspond to ionized (negatively charged) near surface doping atoms (acceptors). They attract holes (majority carriers) and thereby the corrugation amplitudes appear elevated (see section a). Dark areas have at least one missing protrusion in their center (see section b), which can be identified as As vacancies. They are positively charged on p-InAs and repel holes. Parameters: T = 300 K, $k \approx 34$ N/m, $f_{\mathrm{res}} = 149$ kHz, $A = \pm 15.3$ nm, image size 16 nm×10 nm, $\Delta f = -495.0$ Hz, $U_{\mathrm{bias}} = 0$ V.

direction of the band bending is downwards. Consequently, the area around a charged defect is either elevated or depressed with respect to defect free parts of the surface.

Summary

In conclusion, we demonstrated that DFM can not only obtain atomic resolution but also is able to identify individual single charged defects. In the case of atomically flat surfaces the separation of electrostatic from topographic effects is straightforward. However, to obtain quantitative results more elaborated schemes like Kelvin probe microscopy has to be adopted. For semiconductors the lateral resolution depends critically on the distance between doping atoms (or other charged defects) and the screening length. If the latter is larger than the mean distance it is still possible to measure the distribution of doping atoms.

3.5.3 Towards Exchange Force Microscopy: Imaging of the Antiferromagnetic Insulator Nickel Oxide (001) with a Ferromagnetic Tip

W. Allers, S. Langkat, and R. Wiesendanger

Nickel oxide has been subject of intense research for more than half a century, since it belongs to the group of transition metal oxides, which are used in a wide range of applications such as catalysis or exchange coupled devices [31]. Only recently the NiO(001) surface has been analyzed in ultra high vacuum (UHV) by elevated temperature STM [32] and DFM at room temperature [33]. The goal of our investigation was to directly image the antiferromagnetic spin structure via the magnetic exchange interaction between the nickel atoms at the surface and a ferromagnetic tip. We succeeded to atomically resolve nickel oxide (001) at low temperatures with dynamic force microscopy (DFM) using pure silicon tips and iron coated silicon tips. Point defects could be imaged with high lateral and vertical resolution. Moreover, atomic resolution across step edges could be obtained. However, although the RMS noise level was as small as $\approx 1.5\,\mathrm{pm}$ no spin contrast could be observed so far.

NiO is a $3d$-transition metal oxide which crystallizes in the rocksalt structure with a lattice constant of 4.17 Å, as shown in Fig. 3.111. Below its Néel temperature of 525 K NiO is antiferromagnetic. In this phase the nickel atoms line up in a ferromagnetic sublattice along $\{111\}$-planes with their spins lying in plane in one of the six possible $\langle 1\bar{2}1\rangle$-directions. These planes couple antiferromagnetically, giving rise to a slight rhombohedral distortion of $\alpha = 90°3.8'$ at room temperature. The (001) surface is bulk terminated and only slightly (2%) relaxed inward. The spin structure at the surface is made up of ferromagnetic rows of Ni atoms in $\langle 110\rangle$-directions, which couple antiferromagnetically. The spins are slightly inclined towards the incident direction.

Although the Néel temperature is above room temperature, simple estimations [11] and more thorough theoretical calculations [34] indicate, that a very good stability and a very low noise is necessary to detect the short range weak exchange force. The signal modulation between parallel and antiparallel spin configuration at tip-sample distances

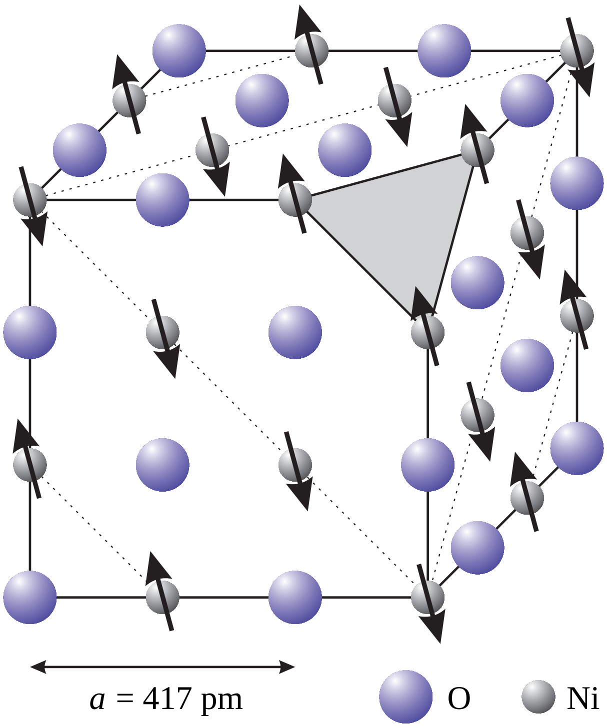

Figure 3.111: NiO crystalizes in the rocksalt structure with a unit cell length of 4.17 Å. The spins of the nickel atoms are aligned in ferromagnetic sublattices along {111}-planes, as indicated by the dotted lines. The (001) surface is an almost perfect bulk termination with the outermost atoms slightly relaxed inwards by 2 %.

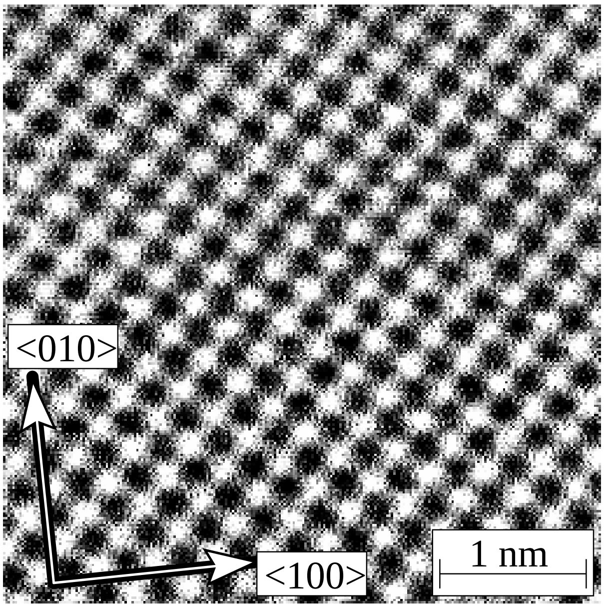

Figure 3.112: Dynamic mode image of NiO(001) acquired with a sputtered silicon tip.The corrugation amplitude is 40 pm along the $\langle 100\rangle$-direction and the RMS noise level is approximately 5 pm. Parameters: $T = 10\,\mathrm{K}$, $k \approx 60\,\mathrm{N/m}$, $f_0 = 198\,\mathrm{kHz}$, $A = \pm 20\,\mathrm{nm}$, $\Delta f = -24\,\mathrm{Hz}$, image size: $4\,\mathrm{nm} \times 4\,\mathrm{nm}$.

below 0.4 nm is expected to be in the picometer range. Up to now such requirements are only met by low temperature force microscopy.

For the DFM experiments we used silicon tips, which were cleaned by argon ion sputtering first. Some of the tips were then coated with iron, to find out about the influences on the imaging mechanisms and parameters, and the resulting data. The samples used in these experiments were NiO single crystalline rods purchased from MaTeck [35]. Gold was evaporated onto their sides to reduce the risk of static charges evolving on the surface during cleavage. They were cleaved *in situ* at room temperature along their [001] plane just before being inserted into the already cold microscope, which was then transferred into the cryostat.

Figure 3.112 shows an atomically resolved image of NiO(001) obtained with a silicon tip. It was taken at a temperature of 10 K with an oscillation amplitude of 20 nm at a constant frequency shift $\Delta f = -24\,\mathrm{Hz}$. This corresponds to a normalized frequency shift $\gamma = \Delta f \times kA^{3/2}/f_0$ [36] of $-2.0610^{-14}\,\mathrm{N}\sqrt{\mathrm{m}}$, where $k = 60\,\mathrm{N/m}$ is the cantilever's spring constant. The distance of two maxima in $\langle 100\rangle$-direction is $\approx 4.2\,\text{Å}$, which corresponds well to the lattice constant of 4.17 Å. This also means that only one type of atoms is imaged as maxima, and there is no straightforward conclusion if these are the oxygen or nickel sites. The corrugation amplitude along the $\langle 100\rangle$-direction is typically 40 pm, which is comparable to the value found by Hosoi et al. [33]. The noise level was determined to $\approx 5\,\mathrm{pm}$ RMS.

Figure 3.113 was acquired at a temperature of 13.7 K with a similar cantilever.

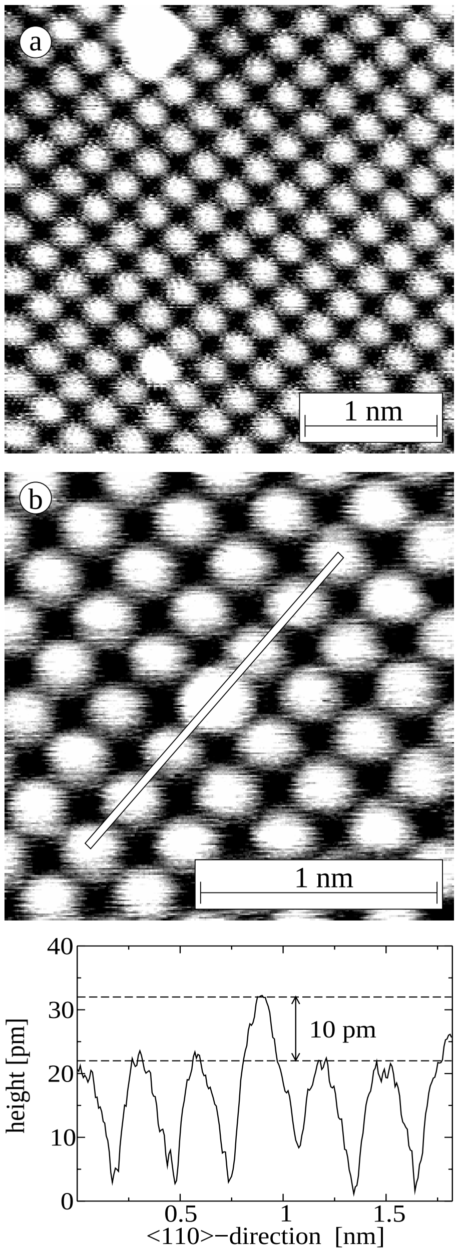

Figure 3.113: Dynamic mode images of NiO(001) acquired with an iron coated silicon tip. Image a) shows the surface with an adsorbate of approximately 0.5 Å height and less than 4 Å diameter close to the upper edge. The monoatomic defect,which can be seen in the lower half, has been scanned in the close-up view b). The cross section along the line in b) shows the corrugation amplitude of 20 pm in $\langle 110 \rangle$-direction and the monoatomic defect elevated 10 pm above the surrounding atoms. The RMS noise level amounts to 1.5 pm. Parameters: $T = 13.7\,\mathrm{K}$, $k \approx 60\,\mathrm{N/m}$, $f_0 = 201\,\mathrm{kHz}$, $A = \pm 7.5\,\mathrm{nm}$, $\Delta f = -51\,\mathrm{Hz}$.

Here the tip was coated with $\approx 30\,\mathrm{nm}$ iron. With this coating, atomic resolution was achieved at a frequency shift $\Delta f = -51\,\mathrm{Hz}$ and amplitude $A = 7.5\,\mathrm{nm}$. These parameters give a considerably smaller normalized frequency shift $\gamma = -9.8910^{-15}\,\mathrm{N}\sqrt{\mathrm{m}}$. A further reduction of the oscillation frequency usually resulted in a tip crash, after which the atomic resolution on this portion of the surface was lost. It could frequently be regained immediately afterwards though by simply moving to a different position nearby on the surface. It can therefore be concluded that a small region of the surface was usually destroyed while the tip kept its imaging qualities. This is in contrast to our experiences with pure Si-tips, which were usually destroyed by tip crashes. Also, the RMS-noise of $\approx 1.5\,\mathrm{pm}$ in images acquired with iron coated tips was considerably lower than in those acquired with silicon tips. The corrugation amplitude along the $\langle 100\rangle$-direction is again 40 pm and 20 pm along the$\langle 110\rangle$-direction. Similarly to Fig. 3.112 only one type of atom was imaged as a protrusion. However, this does not mean that these are the same, since the contrast formation might be different for a semiconductor and a metal tip. In many cases, when transition metal atoms are adsorbed on transition metal oxides, they react strongly with the lattice oxygen [37]. It is therefore quite possible that with an iron coated tip the oxygen atoms will be imaged as maxima and the nickel atoms as depressions. Moreover, the image features a defect in the middle where one of the maxima is 10 pm higher than the surrounding ones. As this defect is located exactly at the position of one single maximum, it is probably a monoatomic defect located either at the surface or the layer directly underneath, otherwise an effect should be seen in the surrounding. This defect demonstrates not only the high lateral “true atomic” resolution, but also the possibility of distinguishing features well below 10 pm.

The image displayed in Fig. 3.114 shows a monoatomic step edge of the same surface with atomic corrugation on both terraces. Again this image was acquired at a temperature of 13.7 K and with a sputtered Si-cantilever coated with a iron film of approximately 30 nm thickness. The amplitude$A = 7.5\,\mathrm{nm}$ was the same, however the frequency shift $\Delta f = -25\,\mathrm{Hz}$ was significantly lower. This was necessary to avoid crashing the tip into the step and resulted in a smaller corrugation amplitude of only ≈ 20 pm. The step height of 220 pm corresponds well to the half of a unit cell(208 pm). Consequently, the maxima on the upper terrace are in registry with the minima on the lower terrace. The defect in the upper right quadrant of the image consists of three missing protrusions which are surrounded by elevated maxima.

So far, none of the images have yielded any exchange force signal. Even Fourier analysis never revealed peaks, that could correspond to the larger antiferromagnetic unit cell. However, the reasons for this may not only lie in the noise level, but also quite possibly the choice of tip material, the spin alignment between tip and sample or a too high estimate for the magnetic exchange interaction. The main reason might be the short range of the exchange force in conjunction with the strong chemical affinity between the oxygen sites and the iron atoms at the tip apex. On one hand this would mean, that the nickel atoms are imaged as minima. On the other hand, it could

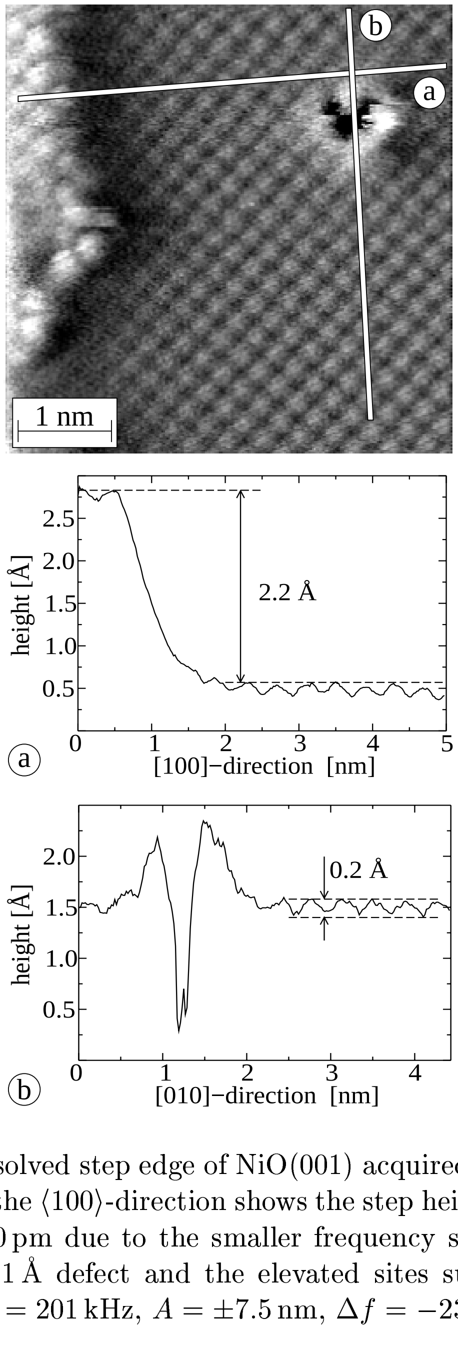

Figure 3.114: Atomically resolved step edge of NiO(001) acquired with an iron coated silicon tip. Cross section (a) along the ⟨100⟩-direction shows the step height of 0.22 nm. The reduced corrugation amplitude of 20 pm due to the smaller frequency shift is documented in cross section (b), as well as the 1 Å defect and the elevated sites surrounding it. Parameters: $T = 13.7\,\mathrm{K}$, $k \approx 60\,\mathrm{N/m}$, $f_0 = 201\,\mathrm{kHz}$, $A = \pm 7.5\,\mathrm{nm}$, $\Delta f = -23\,\mathrm{Hz}$.

be difficult to establish a stable tip-sample distance that is small enough to detect exchange forces before a tip crash occurs.

3.5.4 Dynamic Force Microscopy on Van der Waals Surfaces: Experiment and Simulation

H. Hölscher, W. Allers, A. Schwarz and U. D. Schwarz

Atomically resolved images of graphite (0001) and xenon(111) obtained by dynamic force microscopy (DFM) are simulated. Both materials are important model systems: Graphite has been a standard sample in force microscopy since its invention by Binnig et al. [41], and xenon is a pure very weakly bonded van der Waals crystal. We found that all features of the experimental images for both samples could be successfully reproduced. Moreover, the comparison between experiment and simulation allows the identification of the maxima and minima in the experimental images with the actual positions of the surface atoms, which gives some insight about the contrast formation in DFM.

Figure 3.115 shows a schematic view of the principle of a DFM and the notations in the following. During measurements, a cantilever with spring constant c_z and eigenfrequency f_0 is oscillated near the sample surface at its resonance frequency f with the fixed amplitude A using the frequency modulation technique [18]. As a result of the tip-sample interaction, the cantilever oscillates with its actual resonance frequency $f := f_0 + \Delta f$, which is shifted by Δf from the eigenfrequency of the cantilever. While imaging a sample surface, this frequency shift is kept constant by a feedback loop, which varies the cantilever-sample distance along the z-direction, i.e. the nearest tip-sample distance D. Consequently, the recorded data represents surface maps of constant frequency shifts: $\Delta f(D) = const.$

Simulation Method

The simulation method focuses on the atomic-scale corrugation of DFM images rather than on the absolute value of the frequency shift. Therefore, we restrict ourselves to the calculation of the short-range tip-sample interaction, which is the main origin of the observed contrast [38]. The introduction of long-range forces like *van der Waals* or electrostatic forces is, of course, possible, but we did not find a significant effect on the overall structure of the simulated images.

For the specific case of a non-reactive *van der Waals* surface like Xe(111) and HOPG(0001) – the short-range interaction force between the tip apex and the sample

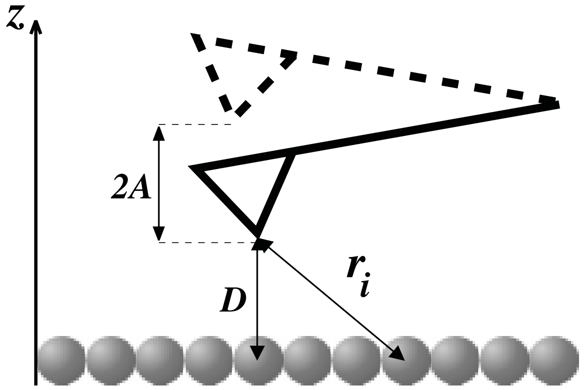

Figure 3.115: Illustration of the experimental set-up and the notations used. The cantilever oscillates with the amplitude A. The nearest distance between the tip apex and the sample surface during these oscillations is D and r_i denotes the actual distance between the tip apex and the ith surface atom.

surface can be sufficiently described by the sum of pair-wise Lennard-Jones potentials

$$\begin{aligned} V_{\mathrm{ts}} &= \sum_{i=1}^{N} V_{\mathrm{LJ}}(r_i) \\ &= \sum_{i=1}^{N} E_0 \left(\left(\frac{r_0}{r_i} \right)^{12} - 2 \left(\frac{r_0}{r_i} \right)^{6} \right). \end{aligned} \tag{3.18}$$

In this equation, E_0 is the binding energy, r_0 the equilibrium distance of the Lennard-Jones potential, and

$$r_i := \sqrt{(x - x_i)^2 + (y - y_i)^2 + (z - z_i)^2}$$

represents the distance between the point-like tip apex and the ith surface atom (see Fig. 3.115). Consequently, the tip-sample interaction force F_{ts} is given by

$$\begin{aligned} F_{\mathrm{ts}}(z) &= \sum_{i=1}^{N} \frac{\partial V_{\mathrm{LJ}}}{\partial r_i} \frac{\partial r_i}{\partial z} \\ &= \frac{12\, E_0}{r_0} \sum_{i=1}^{N} \left(\left(\frac{r_0}{r_i} \right)^{13} - \left(\frac{r_0}{r_i} \right)^{7} \right) \frac{z}{r_i}, \end{aligned} \tag{3.19}$$

and the frequency shift can now be calculated from the the well-known expression [36,39,40]

$$\Delta f = \frac{1}{\sqrt{2\pi}} \frac{f_0}{c_z A^{3/2}} \int_{D}^{\infty} \frac{F_{\mathrm{ts}}(z)}{\sqrt{z - D}} \, dz. \tag{3.20}$$

For the simulation of DFM images and line sections, we choose a certain feedback parameter Δf_{const} and determine the corresponding nearest distance D at different scan positions (x, y), i.e. we solve numerically the equation $\Delta f(D) = \Delta f_{const}$. This procedure models the behavior of the feedback in the experimental set-up and results in maps of constant frequency shifts similar to the experiment. Due to the comparably simple form of the tip-sample force Eq. (3.19), complete DFM images can be calculated in this way with acceptable computer time.

Since $\Delta f \propto f_0/(c_z A^{3/2})$ and $F_{\mathrm{ts}} \propto E_0$, it is advantageous to use reduced units and to introduce a *reduced frequency shift* $\Delta f' := \Delta f \times (c_z\, A^{3/2})/(E_0\, f_0)$. The benefit of this definition is that $\Delta f'$ depends only on the atomic structure of the sample surface, i.e. on the r_i's and the equilibrium distance of the Lennard-Jones potential r_0. Therefore, it is not necessary to determine the binding energy E_0. Consequently, only the parameter r_0 has to be estimated. However, the simulations depend only slightly on the exact value of r_0. In a more detailed analysis of this topic, we found that the results are primarily determined by the specific surface structure, which is well known for HOPG(0001) and Xe(111), and are indeed independent of the chosen parametrisation of the tip-sample force F_{ts}.

HOPG(0001)

Highly oriented pyrolytic graphite (HOPG) was cleaved *in situ* under UHV-conditions and immediately inserted into the microscope. The experiments were then performed at liquid helium temperature. The HOPG(0001) surface consists of hexagons of carbon atoms as depicted in Fig. 3.116. A-site carbon atoms have a neighbor in the graphite layer below, B-site carbon atoms do not. The carbon-carbon distance is only 1.42 Å. The center of the hexagons are denoted as hollow sites (H-sites). Equivalent lattice sites (A-, B- and H-sites, as marked in Fig. 3.116 exhibit a trigonal symmetry and are 2.46 Å apart. An example for a DFM image of an HOPG(0001) surface is shown in Fig. 3.117a). As reported by Allers *et al.* [5,12] all DFM images of HOPG exhibit a trigonal structure of maxima and minima with a distance of 2.46 Å. At first sight this result may correspond to the finding of the contact mode images which also show a trigonal structure of maxima [41]. In contact mode, however, the observed contrast is caused by the lateral “stick-slip” movement of the tip on the sample surface [42–44], which can be ruled out in non-contact mode, since the trigonal structure observed in DFM is independent of the scan angle [5].

The line section in Fig. 3.117a) reveals that the contrast in high resolution images is dominated by two maxima (M1 and M2) and two corresponding minima (m1 and m2). The observed corrugation amplitude between the higher maxima M1 and lower minima m1 is $\approx$ 12 pm. The lateral distance between the higher maxima and the intermediate maxima M2 is about 1.42 Å, which corresponds to the nearest-neighbor distance between the carbon atoms. Thus, with the assumption that protrusions represent atomic lattice sites, the main maxima may be classified as the A-type and the lower maxima as the B-type atom (or vice versa). However, the distance between

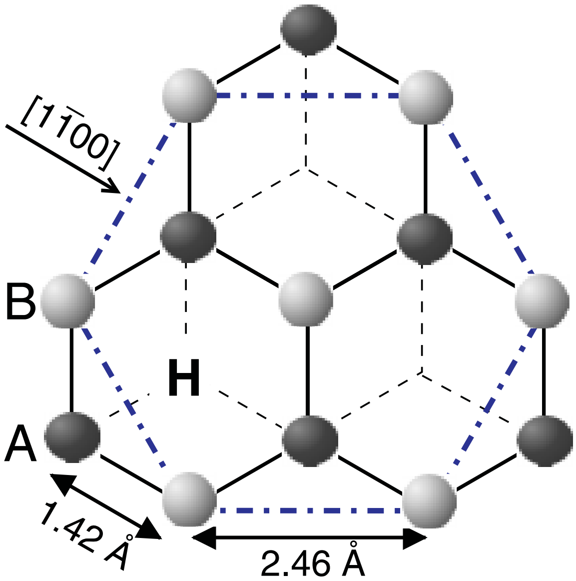

Figure 3.116: The hexagonal structure of the graphite (0001) surface. First layer bonds are indicated by solid lines, second layer bonds by dashed lines. Since neighboring layers are shifted relatively to each other, there are two different sites for carbon atoms: A-type atoms have a direct neighbor in the layer underneath (dark spheres), whereas B-type atoms do not (lighter spheres). The so-called "hollow site" (H-site) represents the center of the hexagon. As shown at the example of B-type atoms, the sublattice of only one specific position (A-, B-, or H-site) forms a trigonal pattern with a lattice constant of 2.46 Å (dash-dotted lines). The nearest distance between two carbon atoms is 1.42 Å. The arrow marks the [1$\bar{1}$00]-direction of the scan lines shown in Fig. 3.117.

the lower minima and the intermediate minima m2 is also 1.42 Å. Therefore, all specific features of the experimental image – minima and maxima – would fit to the lattice positions of the carbon atoms. Consequently, it is not *a priori* clear which features of the image correspond to the actual positions of the carbon atoms.

To reproduce the experimental observations, we set up a cluster of $N = 540$ carbon atoms with the atomic structure of graphite(0001) (see Fig. 3.116). Equations (3.19) and (3.20) are used to calculate the tip-sample force and frequency shift in reduced units. Furthermore, we have to estimate the parameter r_0. This is done by a comparison with experimental frequency shift versus distance curves and gives an approximate value of $r_0 \approx 3.4$ Å [7]. Finally, the structural difference between the A- and B-type atoms has to be considered. Due to this effect, various authors have already predicted different tip-sample forces at these two sites by theoretical calculations [45–47]. We take these results into account by the variation of the parameter r_0 for the two different types of atoms, i.e. $r_A = r_0 - 0.025$ Å $= 3.375$ Å and $r_B = r_0 + 0.025$ Å $= 3.425$ Å for the A- and B-type atoms, respectively. However, we would like to emphasize that this approach is not necessarily unique, but using these values for Eq. (3.18), the overall

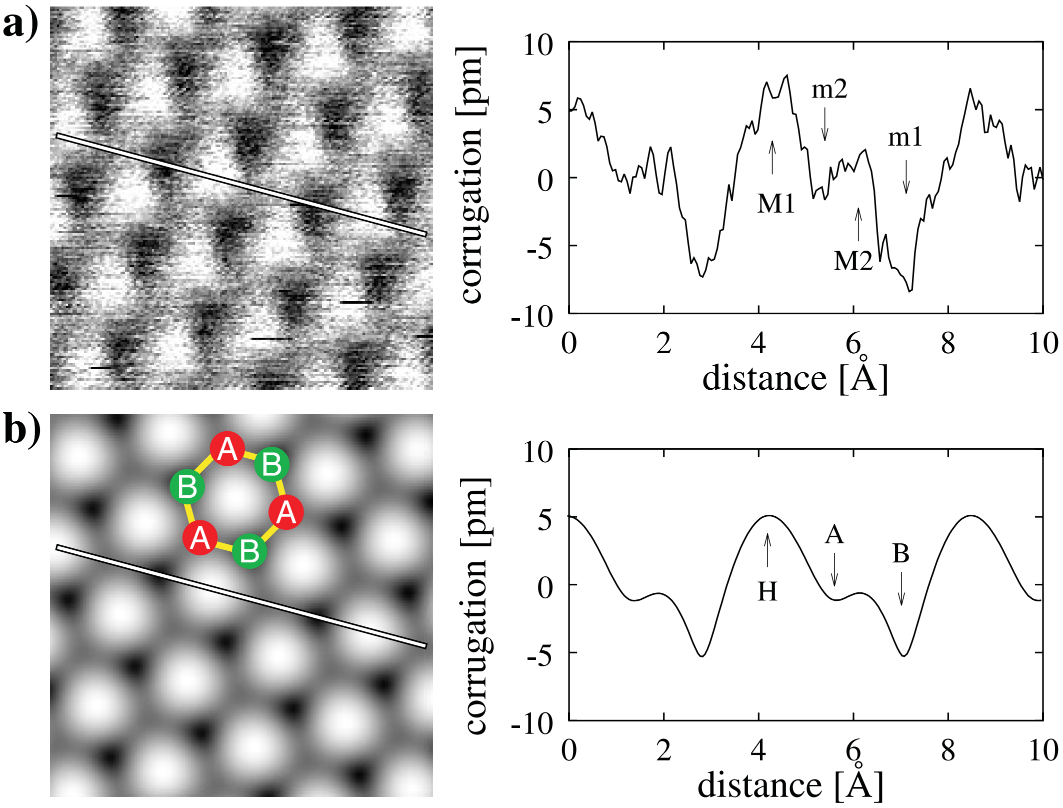

Figure 3.117: A comparison between the experimental and theoretical DFM images of graphite(0001) (image size: 10 Å × 10 Å) and their corresponding line sections along the $[1\bar{1}00]$-direction (see Fig. 3.116). **a)** An experimental image of HOPG obtained in the non-contact mode in UHV at low temperatures. Experimental parameters: $f_0 = 160\,\mathrm{kHz}$, $\Delta f = -63\,\mathrm{Hz}$, $c_z = 35\,\mathrm{N/m}$, $A = 88\,\text{Å}$, $T = 22\,\mathrm{K}$. The line section demonstrates that the experimental DFM image of graphite(0001) exhibits two different types of minima and maxima (see text). **b)** A simulated image where the A- and B-sites are assumed to be different. The simulation shows the same features as the experiment and enables the identification of the positions of the carbon atoms. The corresponding line section reveals that the H-sites are imaged as the higher maxima, whereas the positions of the carbon atoms appear as two different minima.

shape of the resulting force curves at the A, B, and H-sites is fully consistent with the findings of Refs. [46–49]: (i) Before the minimum of $F_{\mathrm{ts}}(z)$-curves the tip-sample force at the H-sites is lower than above the carbon atoms. This causes a contrast inversion in the *attractive regime*, i.e. before the minimum of $F_{\mathrm{ts}}(z)$ the H-sites are higher than the carbon atoms [47–49]. (ii) In the *repulsive regime* of F_{ts} the corrugation between the H-site and the carbon atoms is about 0.2 Å and the B-type atom is slightly higher than the A-type atom [46].

The reduced frequency shift at a hollow site and above the carbon atoms is plotted in Fig. 3.118. The curves are nearly identical and differ only close to the sample surface

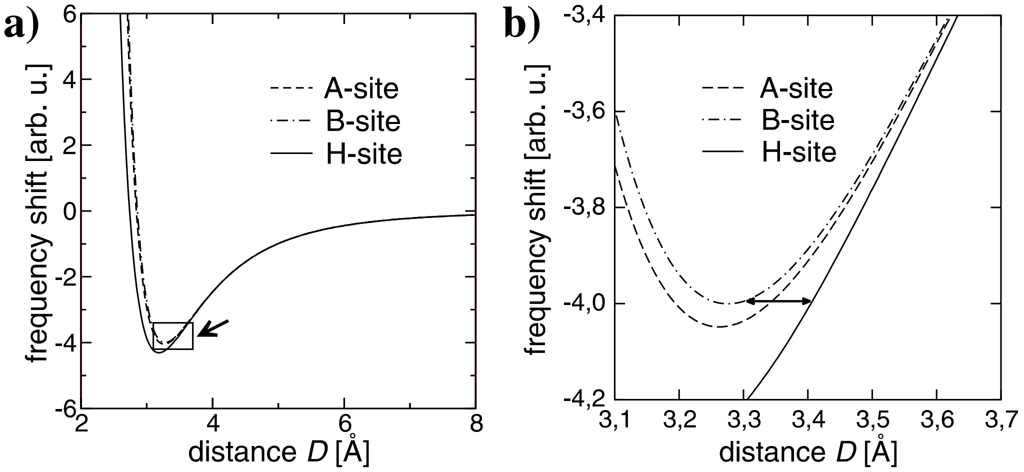

Figure 3.118: A plot of the reduced frequency shift $\Delta f'$ at a hollow site (solid line) and above the A- (dashed line) and B-type (dash-dotted line) carbon atoms. The arrow in a) marks the magnification shown in b). The largest possible corrugation of 10 pm is indicated by the arrow in b).

for $D < 4$ Å, as shown in the magnification (Fig. 3.118b). However, the frequency shift at the H-sites is lower than above the carbon atoms and it is largest above the B-sites for all distances D. A stable feedback operation of the microscope is only possible in the regime on the right hand side of the minimum of the $\Delta f'$-curves, where the frequency shift curve has negative slope [39, 50]. Therefore, the largest possible corrugation can be obtained in the regime which is indicated by the arrow in Fig. 3.118b).

A simulated image for this frequency shift is displayed in Fig. 3.117b). It shows a trigonal structure of maxima and minima with a distance of 2.46 Å and is quite comparable to the experiment. A closer look at the corresponding line section along the [$1\bar{1}00$]-direction (Fig. 3.117b) demonstrates that the simulation exhibits the same features as the experiment. In particular, the appearance of two types of minima and maxima corresponds well to the data presented in Fig. 3.117a) and even the corrugation of 10 pm agrees reasonably with the experimental values of 10-15 pm [5, 12].

In contrast to the experiment, the simulation enables the direct comparison of the DFM image with the atomic structure of the HOPG(0001) surface, allowing an identification of the actual positions of the carbon atoms in the DFM images. As indicated in Figs. 3.117b), the H-sites appear as maxima, whereas the A- and B-type atoms are imaged as two different minima. Consequently, the real atomic structure of HOPG appears as the inversion of the topography in DFM. For HOPG(0001) this contrast inversion occurs, since the tip-sample force F_{ts} is more attractive above the H-site than above the carbon atoms. This is a characteristic feature of the surface structure of HOPG(0001), which is caused by the fact that the tip apex interacts with the six nearest carbon atoms if it is located at the H-sites, but only with one plus

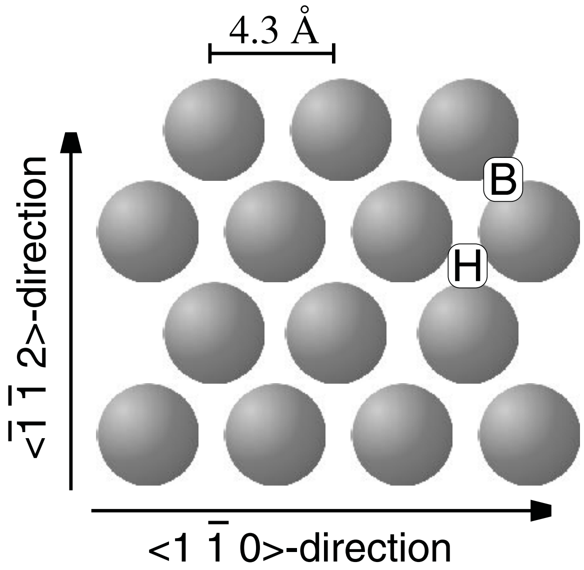

Figure 3.119: The surface structure of xenon(111). The arrows indicate the $\langle 1\bar{1}0\rangle$ and $\langle \bar{1}\bar{1}2\rangle$-direction used for the line section shown in Fig. 3.117. The hollow site and the bridge site are labeled as "H" and "B".

three carbon atoms if it is placed directly above a carbon atom [48].

Xe(111)

To study Xe(111) graphite was used as substrate, and prepared as described above. After precooling the HOPG(0001) substrate at liquid helium temperature the surface was exposed to a 1.3×10^{-5} mbar atmosphere of xenon gas for three minutes, while the temperature was kept well below 50 K. In this way a Xe(111) film could be grown on the graphite substrate. A sketch of the well-known surface structure of xenon is displayed in Fig. 3.119. Xenon atoms condense in a close-packed *fcc* structure, which reflects the characteristic three-fold symmetry of the (111) surface. The nearest neighbor distance between two xenon atoms is 4.3 Å. An example of a DFM image of Xe(111) recorded with a silicon tip oxide is shown in Fig. 6a (to get a clean Si tip, it was sputtered with argon ions prior to the measurement). It is made up of hexagonally arranged maxima with a nearest neighbor distance of ≈ 4.5 Å $\pm 10\,\%$ and has a corrugation of ≈ 25 pm along the $[1\bar{1}0]$-direction [12]. To simulate the experimental results, reduced frequency shift versus distance curves $\Delta f(D)$ were computed at specific sites with Eq. (3.19) and (3.20), where we used a fixed monolayer of $N = 1080$ xenon atoms with the atomic structure of xenon(111) (see Fig. 3.119). For the Xe-Si pair potential we apply the simple combining rule $r_0 = (1/2)(r_{\mathrm{Xe}} + r_{\mathrm{Si}})$ and obtain $r_0 = 3.3$ Å as an estimation (Xe-Xe: 4.3 Å and Si-Si: 2.3 Å).

The $\Delta f(D)$-curves calculated directly above a xenon atom, between two atoms (B-site; cf. Fig. 3.116) and at a H-site turned out to be nearly identical and differ only

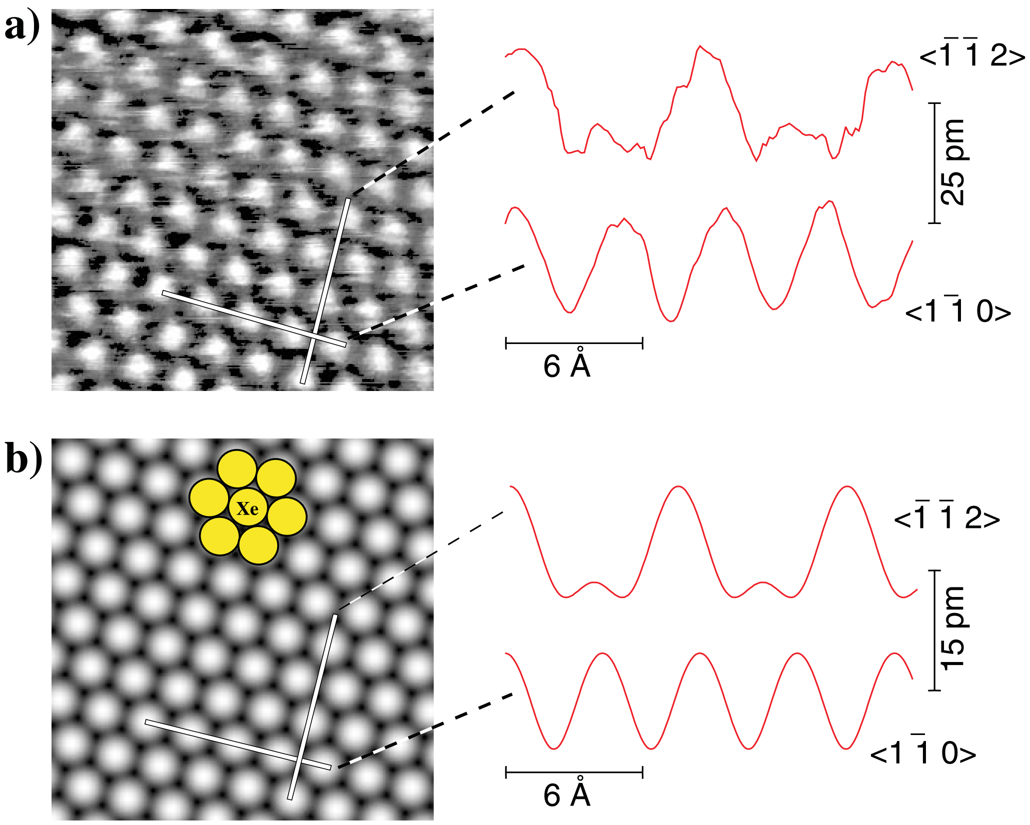

Figure 3.120: A comparison between an experimental **(a)** and a simulated **(b)** DFM image of xenon(111) (image size: $36\,\text{Å} \times 36\,\text{Å}$). The corresponding line sections are taken along the $\langle 1\bar{1}0\rangle$- and $\langle \bar{1}\bar{1}2\rangle$-directions (see Fig. 3.116). Experimental parameters: $f_0 = 160\,\text{kHz}$, $\Delta f = -92\,\text{Hz}$, $c_z = 40\,\text{N/m}$, $A = 94\,\text{Å}$, $T = 22\,\text{K}$.

close to the sample surface for $D < 5\,\text{Å}$ as for HOPG (cf., Fig. 3.118). Therefore, the largest possible corrugation can be obtained on the right hand side close to the minima of the $\Delta f'$-curves, where the frequency shift curve has negative slope [39, 50]. 256×256 image points for a reduced frequency $\Delta f' = -0.4$ were calculated for the simulated DFM image in Fig. 3.117b). It shows a trigonal structure of maxima with a distance of 4.3 Å and is quite comparable to the experimental image. The simulation enables a direct comparision of the DFM image with atomic surface structure, which shows that the positions of the maxima coincide with the positions of the xenon atoms, in contrast to the situation found on graphite(0001).

A closer look at the corresponding line sections along the $\langle \bar{1}\bar{1}2\rangle$- and $\langle 1\bar{1}0\rangle$-directions additionally demonstrates that the simulation exhibits the same features as the experiment. In particular, the appearance of two maxima along the $\langle \bar{1}\bar{1}2\rangle$-direction corresponds well to the equivalent experimental line section presented in Fig. 3.120a). Considering experimental uncertainties and the simplicity of the introduced model the corrugations of the experiment (25 pm) and the simulation (15 pm) are comparable. However, the slight disagreement may have several origins; the two most likely ones are: (i) The Xe(111) sample surface may be deformed, since its bonding is quite soft compared to the covalent bonding of the tip, i.e. the atoms directly below the tip might be "pulled out" from the surface [39]. (ii) In our approach to calculate the tip-sample force, we assumed implicitly that the Lennard-Jones potential V_{LJ} between an individual Xe atom and the tip apex is only a function of the tip sample distance r_i, i.e. that the pair potential is isotropic. In general, however, this interaction may be anisotropic due to a non-spherical electronic density of the apex of the Si-tip. This concept has been successfully applied to describe the interaction between noble gases and graphite [51].

Summary

For both van der Waals surfaces a simple model successfully reproduced all features in the experimental DFM data. Experimental and theoretical corrugation amplitudes are in good agreement. On Xe(111) the maxima correspond to the positions of the xenon atoms, while the situation for graphite is more complex. The real atomic structure of graphite appears as inversion of the topography.

3.5.5 Analysis of the Contact and Non-Contact Regimes with Dynamic Force Spectroscopy

H. Hölscher, A. Schwarz, W. Allers, and U. D. Schwarz

Since "true" atomic resolution has been achieved in non-contact force microscopy the transition from non-contact to contact is an important issue. Another question might be, whether the high resolution is really obtained in a "true" non-contact mode [52]. For a deeper understanding we present a comparative experimental and theoretical study of the frequency shift Δf in ultrahigh vacuum dynamic force microscopy at 80 K on graphite(0001) measured as a function of the tip-sample distance ($\Delta f(z)$-curves) for different resonance amplitudes A in the repulsive and attractive regime of the tip-sample forces.

It was suggested that strong interactions through dangling bonds between the foremost tip atoms and the surface atoms are responsible for the observed contrast [53, 54]. However, it is also possible to obtain atomic-scale contrast on *van der Waals* surfaces like graphite(0001) [5] and xenon(111) [12]. Since it was the aim of this study to measure the tip-sample interaction in the *non-contact* and in the *contact* regime, we chose (0001) oriented graphite as a sample. It is well-known that this material consists of individual layers of hexagonally arranged carbon atoms; within these layers each atom is strongly bound by sp^2-bonds. Therefore, we expect no damage of the sample surface, if the tip touches the sample only slightly. Analyzing the measured frequency shift versus distance curves, we found that the frequency shift scales with $1/A^{3/2}$ as predicted earlier [36]. To fit the experimental data to specific force laws (van der Waals, Lennard-Jones, Hertz/DMT), we calculated the tip-sample interaction force from the frequency shift curves. The subsequent analysis demonstrates that *dynamic force spectroscopy* (DFS) can be used to measure tip-sample interactions including elastic contact forces with high precision.

The tip used for this study was made of mono-crystalline silicon (the tip was sputtered *in situ* with Ar^+-ions prior to the measurements) with a spring constant of 38 N/m and an eigenfrequency of 171 kHz. The graphite sample was cleaved *in situ* at room temperature at a pressure below 10^{-9} mbar and immediately inserted into the pre-cooled microscope (base pressure below 10^{-10} mbar). After the sample reached an equilibrium temperature at $T = 80\,\mathrm{K}$ (liquid nitrogen cooling), series of experiments were performed measuring $\Delta f(z)$-curves (DFS) for different resonance amplitudes A. The experimental data presented here was recorded with grounded tip and sample.

The obtained frequency shift versus distance curves are presented in Fig. 3.121a) by symbols for resonance amplitudes between 54 Å and 180 Å. All curves show a similar overall shape. During the approach of the cantilever to the sample surface, the frequency shift decreases and reaches a minimum. With a further reduction of the nearest tip-sample distance, the frequency shift increases again and becomes positive. For smaller resonance amplitudes, the minimum of the $\Delta f(z)$-curves is deeper and the slope after the minimum is steeper than for larger amplitudes.

The frequency shift versus distance curves can be rescaled to a *normalized frequency shift* curve [36]

$$\gamma(z) := \frac{c_z\, A^{3/2}}{f_0}\,\Delta f(z), \tag{3.21}$$

which should be independent of the spring constant c_z, the eigenfrequency f_0, and the amplitude A of the cantilever. The dependence of the frequency shift on these parameters has first been calculated for the specific case of inverse power and exponential force laws [36], but the same result can be obtained for arbitrary tip-sample forces [40]. The application of this scaling law to our experimental data is plotted in Fig. 3.121b). All data points perfectly fit to a single curve within the full range, demonstrating the validity of the predicted $1/A^{3/2}$-dependence of the frequency shift. This result verifies that γ is a useful quantity to compare frequency shift versus distance curves acquired with different amplitudes.

However, to obtain more information on the tip-sample interaction from the $\Delta f(z)$-curves, it is useful to calculate the frequency shift for suitable tip-sample interaction forces and to compare these results with the experiment. Giessibl [36] suggested to describe the force between the tip and the sample by a combination of a long-range (van der Waals) and a short-range (Lennard-Jones) term. For a tip with the radius R, this assumption results in the tip-sample force

$$F_{\mathrm{ts}}(z) = -\frac{A_{\mathrm{H}}R}{6z^2} + \frac{12E_0}{r_0}\left(\left(\frac{r_0}{z}\right)^{13} - \left(\frac{r_0}{z}\right)^{7}\right), \tag{3.22}$$

where A_H is the Hamaker constant, E_0 the binding energy, and r_0 the equilibrium distance of the Lennard-Jones potential. Since this approach does not explicitly consider elastic contact forces, it is only valid as long as tip and sample are not in contact. Therefore, we will call the force law Eq. (3.22) "non-contact" force in the following to distinguish it from the other force law used below to explicitly describe elastic tip-sample forces. With the formulas given in Ref. [36], the normalized frequency shift for this specific tip-sample force can be calculated in the limit of large amplitudes from

$$\gamma_\mathrm{ts}(D) = \\ -\frac{A_\mathrm{H}R}{12\sqrt{2}D^{1.5}} + \frac{12E_0}{\sqrt{2r_0}}\left[0.16\left(\frac{r_0}{D}\right)^{12.5} - 0.23\left(\frac{r_0}{D}\right)^{6.5}\right], \tag{3.23}$$

where D is the nearest tip-sample distance during the oscillations of the cantilever (D and $D + 2A$ are the lower and upper turnaround point, respectively)

A fit of this equation to the experimentally obtained normalized frequency shift is plotted in Fig. 3.121b) by a solid line; the parameters are $A_\mathrm{H}\,R = 2.4 \cdot 10^{-27}\,\mathrm{Jm}$, $r_0 = 3.4\,\mathrm{Å}$, and $E_0 = 3\,\mathrm{eV}$. The regime right from the minimum of the calculated curve fits well to the experimental data, but the deep and wide minimum of the experimental curves cannot be described accurately with the non-contact force Eq. (3.22). This is caused by the steep increase of the Lennard-Jones force in the repulsive regime ($F_\mathrm{ts} \propto 1/r^{12}$ for $z < r_0$). The specific choice of the short-range force does not matter; the obtained agreement is not significantly better with other choices (e.g., a Morse potential).

To analyze the frequency shift curves behind the minimum of F_ts, it is useful to change our approach to data analysis. So far, we assumed a certain tip-sample force, calculated the frequency shift caused by this force, and compared the result with the experimental data. An alternative and probably more instructive way is to directly calculate the interaction force from the frequency shift, which can be done either by the analysis of the frequency shift as a function of the distance [40, 55] or of the amplitude [6]. Here, we determine the tip-sample force using the approach of Dürig [40] leading to the formula

$$F_\mathrm{int}(D) = \sqrt{2}\frac{c_z A^{3/2}}{f_0}\frac{\partial}{\partial D}\int_D^\infty \frac{\Delta f(z)}{\sqrt{z-D}}\,dz, \tag{3.24}$$

which allows the calculation of the tip-sample interaction force from the frequency shift versus distance curves.

The application of this method results in identical tip-sample force curves for the different resonance amplitudes, as shown in Fig. 3.121c). This demonstrates that the tip-sample interaction did not change during the measurement, i.e., inelastic deformations of the sample and/or tip changes during the recording of the presented data can be excluded. The comparision with the force law F_ts Eq. (3.22) (dashed-dotted line) confirms our former result that this force law fits the tip-sample interaction force quite

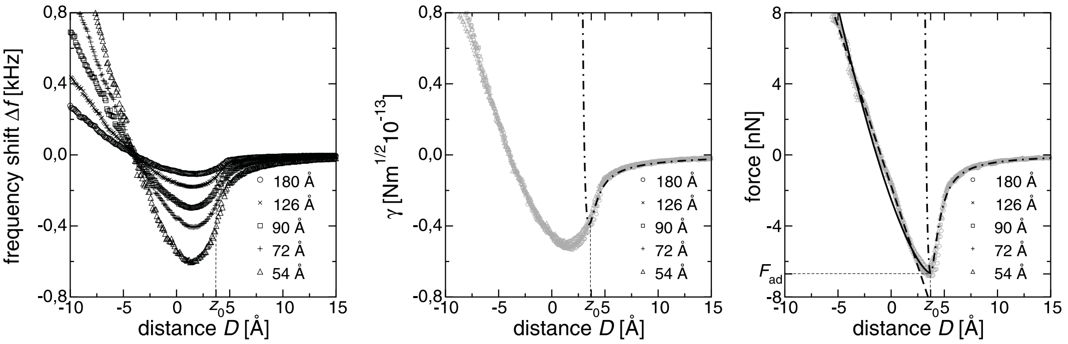

Figure 3.121: **a)** The experimental frequency shift versus distance curves acquired with a silicon tip and a graphite sample for different amplitudes A are displayed by symbols. D is the nearest tip-sample distance at the lower turnaround point. All curves are shifted along the x-axes. The zero point is defined by the force law Eq. (3.22). **b)** The normalized frequency shift γ as a function of D obtained from the experimental data presented in a). The dashed-dotted line represents the best fit using Eq. (3.23). **c)** The tip-sample force calculated with the experimental data given in a) using the formula Eq. (3.24) is shown by symbols. The force F_{ts} Eq. (3.22) is plotted by a dashed-dotted line. The best fit using the force law F_c is displayed by a solid line; a linear fit for $D < 0$ Å is drawn by a dashed line. To indicate the border between "contact" and "non-contact" force, the position z_0 is marked in all plots.

well, but only to the "right" of the minimum of F_{ts}. If the tip comes closer to the sample surface, the repulsive forces between tip and sample become more pronounced. Consequently, tip and sample are deformed by elastic contact forces, which we will discuss in the following.

To obtain a contact force law, we assume that the form of tip and sample changes only slightly until point contact is reached and that, after the formation of this point contact, the tip-sample forces are given by the Hertz theory [57, 58]. This approach coincides with DMT model [59] and has been successfully used to describe the tip-sample contact of an AFM [60, 61]. It results in a force law of the type

$$F_{\text{c}} = g_0(z_0 - z)^{3/2} + F_{\text{ad}} \quad \text{for} \quad \text{z} \leq \text{z}_0. \tag{3.25}$$

The first term in this equation describes the elastic behavior of a Hertzian contact, where z_0 is the point of contact, and g_0 is a constant which depends on the elasticity of tip and sample, and on the shape of the tip. If the tip is exactly spherical with the radius R, the constant g_0 is given by $g_0 = K\sqrt{R}$, where $K = \frac{4}{3}\left(\frac{1-\nu_1^2}{E_1} + \frac{1-\nu_2^2}{E_2}\right)^{-1}$ describes the elasticity of tip and sample ($E_{1,2}$ = Young's moduli, $\nu_{1,2}$ = Poisson's ratio of tip and sample, respectively). If the exact geometry of the tip is unknown, the constant g_0 cannot be determined *a priori*, but it can be shown that Eq. (3.25) still holds [58]. The offset F_{ad} is the adhesion force between tip and sample surface. Since the experimental tip-sample force shows a reasonable agreement with the non-contact force [Eq. (3.22)] until its minimum, we defined the contact point by this minimum, i.e., $z_0 := min\{F_{\mathrm{ts}}(z)\} = 3.7\,\text{Å}$ and therefore, $F_{\mathrm{ad}} := F_{\mathrm{ts}}(z_0) = -6.7\,\mathrm{nN}$. With this choice, we get not only a continuous connection between the non-contact and contact force, but also between their force gradients.

A fit of Eq. (3.25) to the experimental data is shown in Fig. 3.121c) by a solid line ($g_0 = 5.8 \times 10^5\,\mathrm{nN/m^{3/2}}$). The good agreement with the experimental force curves demonstrates that the contact force describes the tip-sample interaction much better than the repulsive part of the non-contact force F_{ts}, since contact forces obviously dominate the tip-sample interaction for $D < z_0$. It is additionally interesting to note that the described analysis allows us to identify the border between the non-contact and contact regime in the frequency shift versus amplitude curves. As shown in Fig. 3.121a), the contact point z_0 is near the point of inflection of the $\Delta f(z)$-curves, well before the minimum of the $\Delta f(z)$-curves.

Although the DMT model gives reasonable agreement with the overall behavior of the measured data for $D < z_0$, it should be mentioned that the experimental force curve looks quite linear for $D < 0\,\text{Å}$. Fitting a linear force law to the measured data within this range [see the dashed line in Fig. 3.121c)] leads to a contact stiffness of $\approx 18\,\mathrm{N/m}$. A similar behavior has been reported for the single asperity contact investigated in Ref. [62], whereas other authors [60,61] found a better agreement with the Hertz/DMT force law as already mentioned above. The main reason for these different results might be the specific choice of the tip/sample materials used in each case. However, another possible reason is that the consideration of the attractive adhesion forces by a constant offset is incomplete. Consequently, in order to examine the validity of specific force laws describing the contact mechanics of a single asperity contact, it will be the aim of future research to use well-defined (e.g., spherical [63]) tips on different samples, and to compare the experimental results with models considering the adhesion forces in a more sophisticated way, see, e.g., Refs. [64–66].

In summary, we verified experimentally that frequency shift versus distance curves obtained with different amplitudes scale with $1/A^{3/2}$ and can therefore be condensed to a single normalized frequency shift curve. To fit the experimental data to specific force laws, we determined the tip-sample force from the frequency shift versus distance curves. This experimental force curve shows good agreement with specific force laws for long-range (van der Waals), short-range (Lennard-Jones), and contact (Hertz/DMT) forces. The result demonstrates that not only non-contact, but also elastic contact forces can be quantitatively measured by DFS opening a new and direct way to the verification of contact mechanical models of nanoasperities.

3.5.6 Determination of Tip-Sample Interaction Potentials by Dynamic Force Spectroscopy

H. Hölscher, W. Allers, U. D. Schwarz and A. Schwarz

With the invention of the *atomic force microscope* (AFM) in 1986 [67], it became possible to measure the interaction forces between a sharp tip and a sample surface on the nanometer scale by recording the deflection of a cantilever. The distance dependence is measured by approaching and retracting the cantilever to and from the surface, respectively ($F(z)$-curves). Unfortunately, such investigations in this "static" mode are often strongly hindered close to the sample surface by an instantaneous jump of the tip to the sample surface. Due to this so called “jump to contact” of the tip to the sample surface, not every distance between tip and surface is stable and consequently it is usually not possible to obtain continuous $F(z)$-curves. We introduce a new method which allows the precise determination of the tip-sample interaction potentials with a force microscope and avoids the “jump to contact” . The method is based on the measurement of the resonance frequency as a function of the resonance amplitude of the oscillated cantilever. The application of this method to model potentials and to experimental data, obtained for a graphite sample and a silicon tip in ultrahigh vacuum, demonstrates its reliability.

The origin of the *“jump to contact”* is an instability in the effective tip-sample potential at the position where the actual force gradient of the tip-sample interaction is larger than the spring constant of the cantilever. This effect leads to a hysteresis and discontinuities in the measured force-distance curves ($F(z)$-curves) and complicates the interpretation [68,69]. Using harder cantilevers can avoid such an instability, but at the cost of force resolution. One way to circumvent this effect is to perform experiments in liquid [70]. However, for several reasons this is not always desirable.

Another way to avoid this problem is to oscillate the cantilever ("dynamic mode") [36,71]. If the oscillation amplitude is large enough, the “jump to contact” of the tip is prevented by the restoring force of the cantilever. This feature is used in the dynamic force microscopy (DFM), where the cantilever is vibrated with its *resonance frequency* f near the sample surface (see Fig. 3.122) [1]. In contrast to the type of experiments described above, the tip-sample force is not directly detected in this mode. Instead, the measured quantity is the change of the resonance frequency – the *frequency shift* Δf – caused by the tip-sample interaction. The distance dependence of the frequency shift in this "dynamic" mode ($\Delta f(z)$-curves) can be measured analogous to $F(z)$-curves in the "static" mode. For a given tip-sample interaction law, various methods were suggested to calculate this frequency shift [15, 36, 72–74] In general, however, the inversed problem will be of more interest: *How can the tip-sample interaction be determined from frequency shift data?* A first step towards the answer of this question has been done by Gotsmann *et al.* [55]. who developed a fully numerical algorithm to fit the results of a computer simulation to experimental frequency shift versus distance

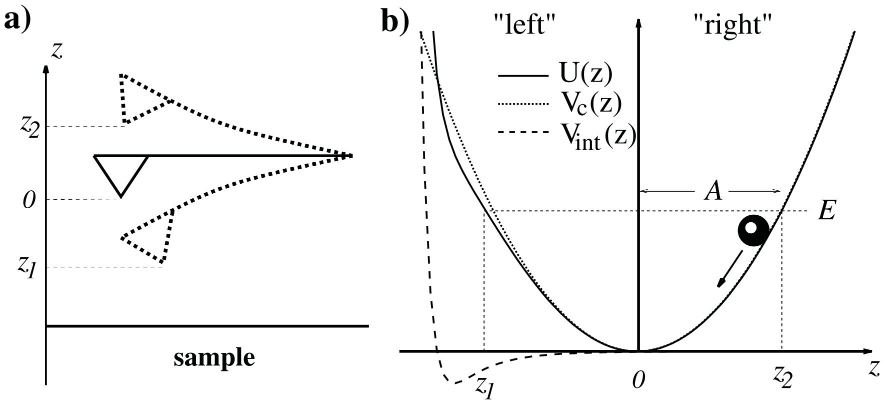

Figure 3.122: A schematic view of the experimental set-up and the used definitions. **a)** A cantilever with integrated tip oscillates with its resonance frequency and a well-defined amplitude near the sample surface. **b)** The effective tip-potential (solid line) is the sum of the parabolic cantilever potential (dotted line) and the tip-sample interaction potential (dashed line). To calculate the tip-sample potential from the frequency shift, it is assumed that the "right" part of the effective potential ($z > 0$) can be replaced by the original parabolic cantilever potential in good approximation (see text).

data.

In the following, we show how the tip-sample interaction potential (and force) can be precisely determined from the analysis of the frequency shift Δf as a function of the resonance amplitude A ($\Delta f(A)$-curves) . Note that in contrast to $\Delta f(z)$-curves the distance between sample and cantilever stage is kept constant during $\Delta f(A)$-curves, but that the distance between tip and sample at the lower turnaround point changes. The advantage of this method is that comparatively simple analytical formulas are used to compute the tip-sample potential from $\Delta f(A)$-curves allowing a quick and direct access to the tip-sample interaction without a "jump-to-contact". Moreover, errors introduced by creep of the piezoelectric scanner used to change the tip-sample distance are eliminated.

The main idea of this new method can be understood by taking a closer look at the reason for the shift of the resonance frequency in the dynamic mode (see Fig. 3.122). If the cantilever oscillates far away from the sample surface, the tip moves in the parabolic cantilever potential V_c (dotted line in Fig. 3.122b), and its oscillation is harmonic. In such a case, the tip motion is sinusoidal, and the resonance frequency is given by the eigenfrequency of the cantilever f_0 which is independent of the oscillation amplitude. If the vibrating cantilever is brought close to the sample surface, the potential which determines the oscillation is modified. The resulting effective potential U (solid line) is given by the sum of the parabolic potential and the tip-sample interaction potential V_int (dashed line). This effective potential has an asymmetric shape due to the tip-sample interaction. Consequently, the resulting tip oscillation becomes anharmonic, and the resonance frequency of the oscillation now depends on the resonance amplitude. The

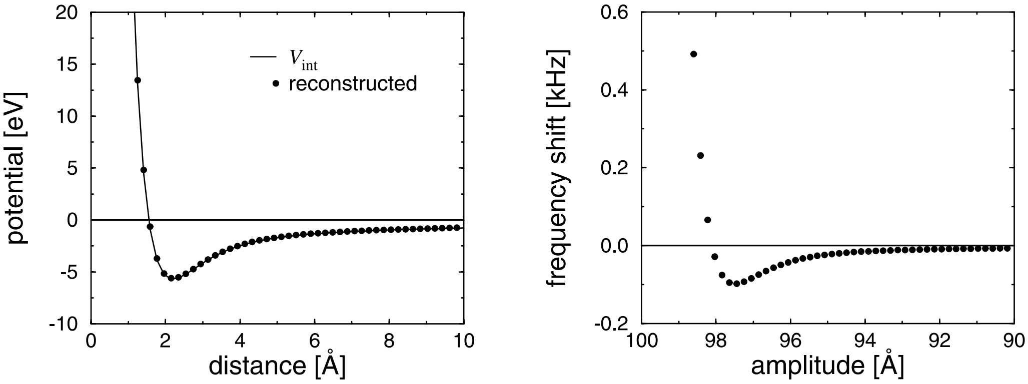

Figure 3.123: A simulation of the proposed method. **a)** The tip-sample potential given by Perez *et al.* [17] (solid line) used for the calculation of the $\Delta f(A_{\text{exp}})$-curve shown in b). The reconstructed potential computed from the $\Delta f(A_{\text{exp}})$-data given in b) is plotted by symbols. **b)** The frequency shift versus amplitude curve $\Delta f(A_{\text{exp}})$ calculated with the tip-sample potential shown in a).

effective potential experienced by the tip changes also with the cantilever-sample distance (distance between tip and sample, if the cantilever is undeflected). Therefore, the frequency shift depends on two parameters: the cantilever-sample distance and the resonance amplitude. The changes of the frequency shift caused by the damping of the cantilever can be neglected in ultrahigh vacuum, if the energy loss due to the damping of the cantilever is compensated using the frequency modulation scheme described in Ref. [18]. As a result, the resonance frequency can be measured independently from the actual damping [18, 75].

For a given effective potential $U(z)$, the period of oscillation T can be calculated as a function of the energy of the system E by the integral

$$T(E) = \sqrt{2m} \int_{z_1}^{z_2} \frac{dz}{\sqrt{E - U(z)}}, \tag{3.26}$$

where m is the effective mass of the oscillating system [16]. Unfortunately, it is not possible to solve the inverted problem. The effective potential $U(z)$ cannot be determined from the function $T(E)$ without further assumptions about the potential $U(z)$, since the inverted function $z(U)$ is two-valued: Each value of U corresponds to two different values of z [76].

However, in our special case, this problem can be solved by dividing the potential $U(z)$ into two parts, "left" and "right" of its minimum as indicated in Fig. 3.122b). Since the tip-sample interaction potential $V_{\text{int}}(z)$ is usually very small on the "right" side for typical cantilever-sample distances, it can be assumed that this part of $U(z)$ is nearly parabolic

$$U(z) \approx \frac{1}{2} c\, z^2 \quad \text{for} \quad \text{z} \geq 0, \tag{3.27}$$

where c is the spring constant of the cantilever. For convenience, we define the origin of the z- and U-axes at the position of the minimum of the effective potential. As a result of the assumption Eq. (3.27), the integration of Eq. (3.26) from 0 to z_2 leads to

$$T(E) = \frac{T_0}{2} + \sqrt{2m} \int\limits_{z_1}^{0} \frac{dz}{\sqrt{E - U(z)}}, \tag{3.28}$$

where $T_0 = 1/f_0 = 2\pi\sqrt{m/c}$ is the period of oscillation of the free cantilever. Now the function $U(z)$ is reversible for all $z \leq 0$, and the integral in Eq. (3.28) can be inverted. Following Ref. [76], we obtain

$$z_1(U) = \frac{1}{\pi\sqrt{2m}} \int\limits_{0}^{U} \frac{\frac{T_0}{2} - T(E)}{\sqrt{U - E}}\, dE. \tag{3.29}$$

Usually, it is the frequency shift $\Delta f := f_0 - f$ and not the period of oscillation $T = 1/f$ which is measured in DFM. Therefore, it is advantageous to transform Eq. (3.29) to

$$z_1(A) = -\int\limits_{0}^{A} \frac{f_0 - \Delta f(A')}{f_0 + \Delta f(A')} \frac{A'}{\sqrt{A^2 - A'^2}}\, dA', \tag{3.30}$$

where A represents the amplitude in the parabolic part of the effective potential (see Fig. 3.122). Using this formula it is straightforward to calculate the position $z_1(A)$ from a frequency shift versus amplitude curve $\Delta f(A)$, and to determine the tip-sample interaction potential from

$$V_{\mathrm{int}}(z_1) = \frac{1}{2} c \left(A(z_1)^2 - z_1^2\right). \tag{3.31}$$

If this method is applied to experimental frequency shift versus amplitude curves, it has to be taken into account that it is the amplitude

$$A_{\mathrm{exp}} := \frac{1}{2}(A - z_1) \tag{3.32}$$

– and *not* the amplitude A sketched in Fig. 3.122 – which is measured in the real experiment. This is considered in the following by a simple search algorithm, which varies the amplitude until condition Eq. (3.32) is fulfilled.

To prove the reliability of this new method, we computed a frequency shift versus amplitude curve for a given tip-sample interaction potential by solving numerically the corresponding equation of motion [15]. Afterwards we have calculated the reconstructed potential with the described method from the frequency shift versus amplitude data and compared the original and reconstructed potential. This simulation is shown in Fig. 3.123 with the example of the potential given by Perez *et al.* [77], which

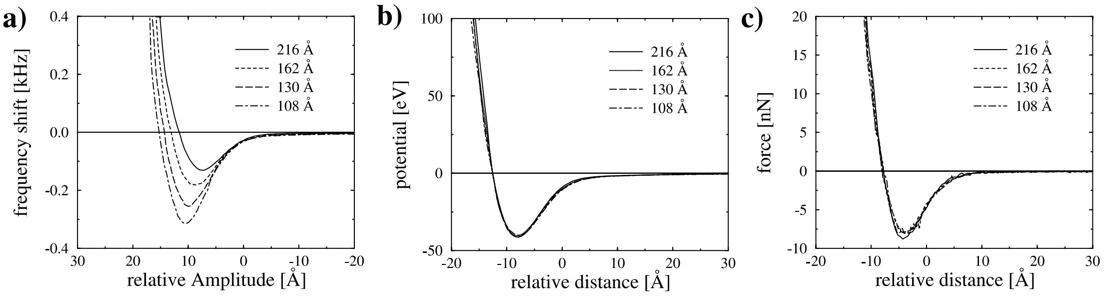

Figure 3.124: Experimental results obtained with the proposed method. **a)** Four measured $\Delta f(A_{\text{exp}})$-curves recorded in ultrahigh vacuum with a silicon tip and a graphite sample for various cantilever-sample distances. The curves are individually shifted along the x-axes in order to fit all into the same graph. The subtracted offset is 216 Å, 162 Å, 130 Å, and 108 Å, respectively. **b)** The tip-sample potential calculated from the experimental data shown in a). Note that all curves are nearly identical despite of the different $\Delta f(A_{\text{exp}})$-curves. The zero point of the x-axis is arbitrarily chosen. **c)** The corresponding tip-sample forces.

describes the interaction between a mono-atomic silicon tip and an adatom of the Si(111)-5×5 surface [solid line in Fig. 3.123a); both short-range and long-range (van-der-Waals) forces are included]. The $f(A_{\text{exp}})$-curve calculated with this potential at a typical cantilever-sample distance of 100 Å is plotted in Fig. 3.123b) for discrete values. A comparison between the original (solid line) and the reconstructed tip-sample potential (symbols) plotted in Fig. 3.123a) demonstrates the quality of the proposed method.

The same high agreement between original and reconstructed potentials is obtained for other tip-sample interactions and different cantilever-sample distances, as long as the assumption Eq. (3.27) applies. The detailed analysis shows that the method is unique. Moreover, the systematic error made by assumption Eq. (3.27) can be neglected for realistic tip-sample potentials if the cantilever-sample distance is large enough.

An application of the new method to experimental data is shown in Fig. 3.124 for a clean oxygen-free silicon tip (k =38 N/m, f_0 = 177 kHz) and an *in situ* cleaved graphite sample (HOPG). Series $\Delta f(A)$-curves were taken at different distances between cantilever stage and sample. The experimental $\Delta f(A_{\text{exp}})$-curves displayed in Fig. 3.124a) were measured for four different distances at room temperature. All curves show the same typical overall behavior, but differ significantly in quantity, depending on the cantilever-sample distance.

Despite these differences, the reconstruction of the tip-sample potential using these experimental data sets leads to identical results [see Fig. 3.124b)]. The corresponding tip-sample forces are shown in Fig. 3.124c). The depth of the measured potential is $\sim$ 40 eV, which is much more than the expected binding energy between a sharp mono-atomic tip and a sample surface ($<$ 6 eV, see Fig. 3.123). This feature indicates that more than one tip atom interacts with the sample surface, which can be caused by two reasons: (i) the tip is blunt and/or (ii) elastic tip-sample forces deform the shape of the tip.

Using this new method it is possible to precisely determine the tip-sample potentials and forces without "jump-to-contact" and hysteresis. Compared to the $F(z)$-curves measured in the static mode every tip-sample distance in the non-contact and contact regime can be adjusted, which demonstrates clearly the advantage of this method. The presented formulas give a quick and direct access to the tip-sample interaction potential and forces.

3.5.7 Measurement of Conservative and Dissipative Tip-Sample Interactions in Dynamic Force Microscopy

H. Hölscher and U. D. Schwarz

Forces can be conservative and non-conservative. In the latter case energy is dissipated. Dynamic force microscopy (DFM) is in principle sensitive to dissipative interactions, because the tip moves periodically in the force field of the sample. In the following the measurement of tip-sample interaction forces with DFM using the frequency modulation (FM) detection scheme [18] is studied. Since this method is based on the properties of a self-driven oscillator, we discuss the main differences to an externally driven oscillator. An analytical expression is derived, which clarifies how the measured quantities of the FM technique, the frequency shift and the gain factor (or "excitation amplitude"), are influenced by the time ("phase") shift and how these quantities are related to conservative and dissipative forces.

Force microscopes using detection schemes working with a vibrating cantilever ("dynamic" modes of operation) are often based on an experimental set-up where the cantilever is driven by an external oscillator with a fixed excitation frequency, if they are run under ambient conditions (e.g.,"tapping" mode). The equation of motion of the cantilever is then given by the differential equation of a driven damped oscillator with the (non-linear) tip-sample force F_{ts} [74, 78–85].

$$m\ddot{z}(t) + \frac{2\pi f_0 m}{Q}\dot{z}(t) + c_z\, z(t) = F_{\mathrm{ts}}\left[z(t), \dot{z}(t)\right] + \underbrace{a_d\, c_z\, \cos(2\pi f_d t)}_{\text{external excitation}}, \tag{3.33}$$

where $z(t)$ is the position of the tip at the time t; c_z, m, Q, and $f_0 = \sqrt{(c_z/m)}/(2\pi)$ are the spring constant, the effective mass, the quality factor, and the eigenfrequency of the cantilever, respectively. The external excitation of the cantilever with the excitation amplitude a_d at a fixed frequency f_d is described by the term on the right side of Eq. (3.33).

In DFM one is mainly interested in steady state solutions, where the cantilever oscillations are nearly sinusoidal. In this case, the oscillation frequency is given by the

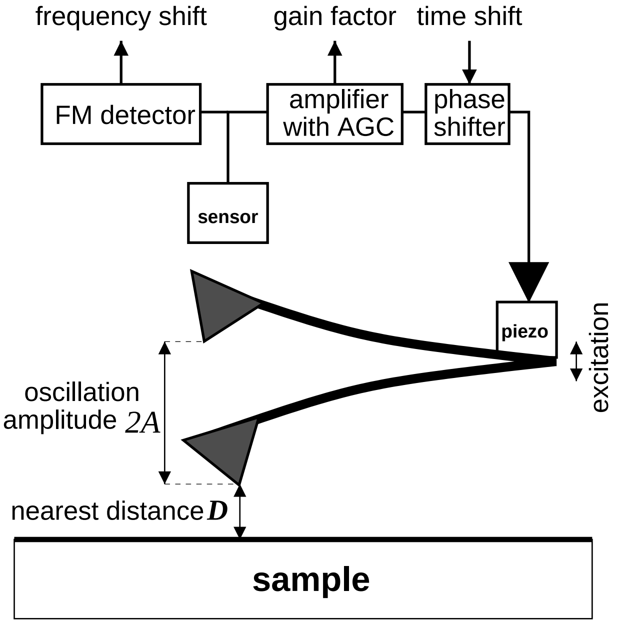

Figure 3.125: The schematic set-up of a dynamic force microscope operated in UHV using the frequency modulation technique (constant amplitude mode) introduced by Albrecht *et al.* [18]. A significant feature of this set-up is the positive feedback of the self-driven cantilever (see text).

external frequency f_d, and the solution of Eq. (3.33) is given by

$$z(t \gg 0) \cong A(f_d, a_d) \cos(2\pi f_d t + \phi_0(f_d, a_d)), \tag{3.34}$$

where the oscillation amplitude and the phase shift are functions of the excitation frequency and the excitation amplitude. The explicit form of these functions depends on the tip-sample interaction force F_{ts} [81]. Thus, different detection schemes, which use either the oscillation amplitude A or the phase shift ϕ for distance control, have been established for DFM with an externally driven cantilever [86].

However, as it has been pointed out by Albrecht *et al.* [18], an experimental set-up based on an externally driven cantilever has a principle limitation of the sensitivity if it is run in ultra-high vacuum. Due to the high Q-values of cantilevers in UHV ($Q \approx 10\,000 - 100\,000$), the response of the system during data acquisition is very slow, restricting the bandwidth of the experimental set-up.

This problem does not exist for the frequency modulation technique, where the sensitivity of the microscope increases with the Q-value of the cantilever without limiting the bandwidth. Using this method, “true” atomic resolution has been obtained on clean surfaces in UHV, where the tip is believed to vibrate without touching the sample surface (“non-contact”- force microscopy)

The key feature of FM detection is the positive feedback, which ensures that the cantilever oscillates always at its resonance frequency. The reason for this behavior is that the cantilever serves as the frequency determining element. This is in contrast to an externally driven cantilever: Such a cantilever oscillates in steady state with its excitation frequency, which is not necessarily its resonance frequency [see Eq. (3.34)].

A schematic set-up of a DFM using the FM technique is shown in Fig. 3.125. The movement of the cantilever is measured with a displacement sensor. This signal is then fed into an amplifier possessing an *automatic gain control* (AGC) and is subsequently used to excite the piezo driving the cantilever. The phase shift between the excitation signal and cantilever deflection is adjusted by a phase (or time) shifter to a value corresponding to ≈ 90°, since this ensures an oscillation near resonance. Two different modes have been established for use with the FM detection: The *constant amplitude mode*, where the oscillation amplitude is kept at a constant value by the AGC [18], and the *constant excitation mode* [50], where the excitation amplitude is kept constant. In this article, however, we focus on the original constant amplitude mode.

With such an experimental set-up, the corresponding equation of motion of a DFM with FM technique driven in the constant amplitude mode is different to Eq. (3.33). It is now a differential equation with a *time delay* t_0 [55, 73, 87]

$$m\ddot{z}(t) + \frac{2\pi f_0 m}{Q}\dot{z}(t) + c_z\, z(t) = F_{\mathrm{ts}}\left[z(t), \dot{z}(t)\right] + \underbrace{g\, c_z\, z(t - t_0)}_{\text{driving}}. \tag{3.35}$$

The term on the right side of this equation differs from the external driving term in Eq. (3.33) and describes the active feedback of the system by the amplification of the displacement signal, i.e., the tip position z, measured at the retarded time $t - t_0$ by the *gain factor* g.

Due to the obvious difference in the equations of motion of the driven and the self-driven oscillator, it is quite clear that both have different features which have to be taken into account for the analysis of experimental data. To give insight into the properties of a self-driven oscillator, we discuss the solutions of Eq. (3.35) with and without tip-sample force.

Far away from the sample surface (at infinity) are no tip-sample forces ($F_{\mathrm{ts}} \equiv 0$), and Eq. (3.35) simplifies to

$$m\ddot{z}(t) + \frac{2\pi f_0 m}{Q}\dot{z}(t) + c_z\, z(t) = g\, c_z\, z(t - t_0). \tag{3.36}$$

In the steady state the cantilever oscillations is sinusoidal and the amplitude is constant. Therefore, we make the ansatz

$$z(t \gg 0) = A\cos(2\pi f t), \tag{3.37}$$

introduce it into Eq. (3.36), and finally get a set of two coupled trigonometric equations:

$$g\,\cos(2\pi f t_0) = \frac{f_0^2 - f^2}{f_0^2}, \tag{3.38}$$

$$g\,\sin(2\pi f t_0) = -\frac{1}{Q}\frac{f}{f_0}. \tag{3.39}$$

Since the amplitude A is held constant by the AGC and the time delay t_0 is a constant value set by the phase shifter, Eq. (3.5.7) must be solved for the oscillation frequency f and the gain factor g. However, before analyzing the general solution we examine the behavior of the system at resonance.

In this case, the trigonometric equations Eq. (3.5.7) can be simplified and decoupled with the assumption that the time shift t_0 is set to a value corresponding to

$$t_0 = \underbrace{\frac{1}{4}T_0}_{=90^\circ}, \underbrace{\frac{3}{4}T_0}_{=270^\circ}, \underbrace{\frac{5}{4}T_0}_{=450^\circ}, \ldots, \tag{3.40}$$

where $T_0 = 1/f_0$ is the period of oscillation of the free and undamped cantilever. For these values of t_0, the solution of Eq. (3.5.7) is given by

$$f = f_0, \tag{3.41}$$

$$|g| = 1/Q. \tag{3.42}$$

These simple calculations demonstrate the interesting and very specific behavior of a self-driven oscillator with velocity dependent damping: The cantilever oscillates exactly with its eigenfrequency f_0 and the gain factor g depends only on the Q-value of the cantilever, if the time delay is set to a value given by Eq. (3.40). Consequently, we define that the system is in *resonance*, if Eq. (3.40) is fulfilled.

In a real experiment, the time (or phase) shift between the excitation and the cantilever oscillations might be slightly detuned. Consequently, it is necessary to examine the impact of this effect on the oscillation frequency f and the gain factor g.

If the time delay is not given by the special values of Eq. (3.40), the system is out of resonance and the oscillation frequency shifts from the eigenfrequency of the cantilever by $\Delta f_{\mathrm{err}} := f - f_0$. The gain factor differs also from the value given by Eq. (3.42). The general behavior of the system can in this case be analyzed by the following approximate solution of Eq. (3.5.7): Since the frequency error is quite small ($\Delta f_{\mathrm{err}} \ll f_0$) for a small detuning of t_0, it can be shown that

$$\Delta f_{\mathrm{err}} \approx \frac{f_0}{2Q}\cot(2\pi f_0 t_0), \tag{3.43}$$

$$|g| \approx \frac{1}{Q}\frac{1}{\sin(2\pi f_0 t_0)}. \tag{3.44}$$

These two functions are plotted in Fig. 3.126 for typical parameters by solid lines. The left axis of the graph represents the values of the frequency error and the gain factor. (For our purposes, the sign of the gain factor can be arbitrarily defined, therefore we plot only its absolute value $|g|$.) The percental deviation from the optimal value at 90° is shown on the right axis. The corresponding values obtained from a numerical simulation of the whole system are marked by symbols. The excellent agreement between the simulation and the analytical solution demonstrates the reliability of both approaches to solve Eq. (3.36).

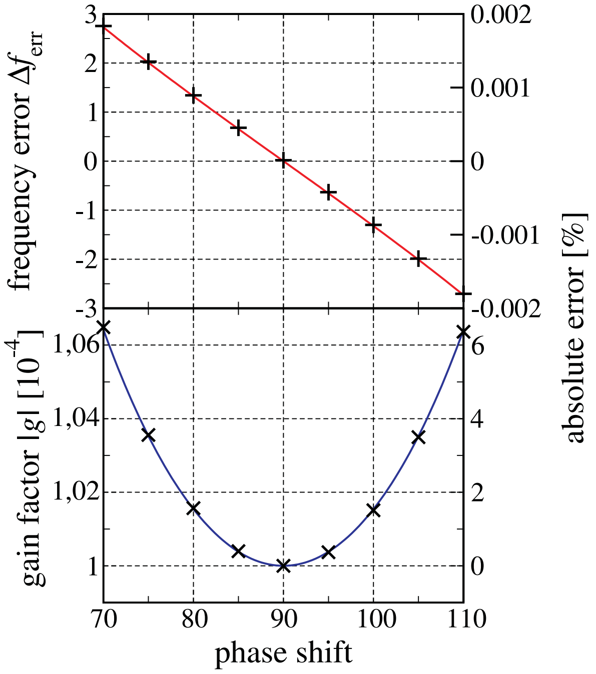

Figure 3.126: The shift of the frequency $\Delta f_{\rm err}$ and the gain factor g without a tip-sample force as a function of the phase shift, i.e., the time delay t_0, for the parameters: $f_0 = 150\,\rm kHz$, $c_z = 40\,\rm N/m$, $A = 100\,\rm Å$, and $Q = 10\,000$. The solid lines and the symbols mark the solution of Eq. (3.5.7) and the numerical simulation of the whole system, respectively. The left axis represents the shift of the frequency and the gain factor from the resonance values at 90°; the right axis shows the corresponding error.

Figure 3.126 and the analysis of Eq. (3.5.7) demonstrate that the frequency error caused by an improper adjustment of t_0 changes nearly linearly with the time delay and is quite small. Even for a large detuning of 20° the error is smaller than 0.002 %. The change in the gain factor is much larger than the frequency error: A detuning of 10° (20°) leads to an error of about 2 % (6 %). The absolute value of the gain factor, however, minimizes if the system is in resonance, and varies parabolically with t_0, if the system is out of resonance. Therefore, it is straightforward to determine the optimal values for t_0 in an experiment. If the cantilever is far away from the sample surface (i.e., zero tip-sample force), the optimal value for the time delay can easily be found by a minimization of the gain factor as a function of t_0.

Close to the sample (finite tip-sample distances) it can be assumed that the tip-sample interaction force is a function of the actual tip position $z(t)$ and its velocity $\dot{z}(t)$ ($\Rightarrow F_{\rm ts} := F_{\rm ts}\left[z(t), \dot{z}(t)\right]$). The exact form of this function, however, depends on many different parameters such as the material properties of tip and sample, the shape of the tip, the bias voltage, etc.

For such a force, the equation of motion Eq. (3.35) can again be solved with the ansatz Eq. (3.37). Then, the obtained equation is simplified in the following way [88]:

After a multiplication with $\cos(2\pi f t)$, the equation is integrated over one period of oscillation $t = [0, 1/f]$. The same procedure is repeated after a multiplication with $\sin(2\pi f t)$. The result is a set of two coupled trigonometric equations:

$$\begin{aligned} g\cos(2\pi f t_0) &= \\ \frac{f_0^2 - f^2}{f_0^2} &- \frac{2f}{Ac_z}\int_0^{1/f} F_{\text{ts}}\left[z(t), \dot{z}(t)\right]\cos(2\pi f t)\,dt, \end{aligned} \tag{3.45}$$

$$\begin{aligned} g\sin(2\pi f t_0) &= \\ -\frac{1}{Q}\frac{f}{f_0} &- \frac{2f}{Ac_z}\int_0^{1/f} F_{\text{ts}}\left[z(t), \dot{z}(t)\right]\sin(2\pi f t)\,dt. \end{aligned} \tag{3.46}$$

These equations may be solved numerically to determine the exact dependency of the tip-sample interaction force F_{ts} and the time delay t_0 on the oscillation frequency f and the gain factor g.

The detailed analysis, however, demonstrates that the results of a DFM experiment are mainly determined by the tip-sample force and only slightly by the time delay. This can be shown by an approximation of Eq. (3.5.7), which is based on the assumption that condition Eq. (3.40) is fulfilled. In this case, the time delay is set to an optimal value by the experimentalist before an approach of the tip towards the sample surface. Since the frequency shifts caused by the tip-sample interaction are usually quite small, the system is also nearly in resonance during the measurement of tip-sample forces. Therefore, it can be assumed that $\cos(2\pi f t_0) \approx 0$ and $\sin(2\pi f t_0) \approx \pm 1$.

With this assumption the two coupled equations (3.5.7a) and (3.5.7b) can be decoupled and we obtain

$$\Delta f \cong -\frac{f_0^2}{Ac_z}\int_0^{1/f_0} F_{\text{ts}}\left[z(t), \dot{z}(t)\right]\cos(2\pi f_0 t)\,dt, \tag{3.47}$$

$$|g| \cong \frac{1}{Q} + \frac{2f_0}{Ac_z}\int_0^{1/f_0} F_{\text{ts}}\left[z(t), \dot{z}(t)\right]\sin(2\pi f_0 t)\,dt. \tag{3.48}$$

Since we did not make any assumption about the specific force law describing the tip-sample interaction F_{ts}, these equations are valid for every type of interaction as long as the resulting cantilever oscillations are nearly sinusoidal. In this context, it is interesting to note that Eq. (3.47) coincides with the well-known result of Refs. [36,40], if F_{ts} is a conservative force.

To demonstrate the reliability of these formulas we compared them with numerical simulations of the system based on Eq. (3.35) using a purely conservative tip-sample force as shown in Fig. 3.127a). It describes the short- and long-range interaction between an atomically sharp silicon tip and an adatom of the Si(111)(5×5) surface as

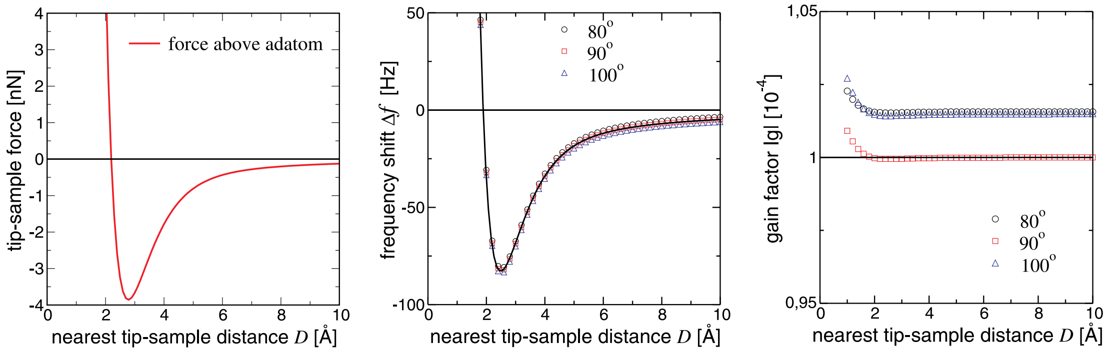

Figure 3.127: **a)** The tip-sample force between an adatom of the Si(111)(5×5) surface after Peréz *et al.* [19]. **b)** The frequency shift caused by the tip-sample force shown in a). The solid line is the result of Eq. (3.47). The symbols represent the numerical simulations calculated with different time delays t_0. The parameters are the same as in Fig. 3.126: $f_0 = 150\,\mathrm{kHz}$, $c_z = 40\,\mathrm{N/m}$, $A = 100\,\text{Å}$, and $Q = 10\,000$. **c)** The gain factor corresponding to the results shown in b). Since the used tip-sample force is purely conservative, the solution of Eq. (3.48) is a constant value $|g| = 1/Q = 10^{-4}$ (solid line). The comparison with the numerical simulations for different time delays t_0 (symbols) shows that the precision of this approximated formula is better than 3 %.

calculated by Peréz *et al.* [77]. The corresponding frequency shift is displayed in Fig. 3.127b). The solid line is calculated with Eq. (3.47). The symbols represent the results of numerical simulations, if the system is in resonance (90°) and for detuned time delays (80°, 100°). For resonance, the error of the approximation Eq. (3.47) is negligible. For a detuning of 10° it is smaller than 5 Hz. The approximation for the gain factor is also quite reasonable (see Fig. 3.127c). The calculation with Eq. (3.48) gives a constant value $|g| = 1/Q$ which depends only on the quality factor of the cantilever, since the integral on the right side is zero for conservative tip-sample forces. The deviation from the numerically obtained gain factor values can be neglected at resonance and it is smaller than 3 % for a detuning of 10°.

This example shows that a conservative tip-sample force influences mainly the frequency shift, but not the gain factor, which is nearly constant. All deviations displayed in Fig. 3.127c) are small effects mainly caused by the detuning of the time shift. However, experimental data obtained with the FM detection scheme show typically much larger variations of the gain factor towards the sample surface [87]. Various authors suggested physical mechanisms [89] and dissipative force laws [87, 90] to explain this behavior. To examine the physical significance of these approaches, we adopt our equations for the frequency shift and the gain factor to a force law including dissipation.

For this purpose, we assume the following force law to describe the tip-sample interaction

$$F_{\mathrm{ts}} := F_{\mathrm{int}}(z) + F_{\mathrm{diss}}(z, \dot{z}), \tag{3.49}$$

where the first term depends only on the tip-sample position and the actual movement direction of the tip

$$F_{\mathrm{int}}(z) := \begin{cases} F_{\rightarrow}(z)\dot{z} \leq 0 & \text{“forward”} \\ F_{\leftarrow}(z)\dot{z} > 0 & \text{“backward”}, \end{cases} \tag{3.50}$$

while the second term describes the energy dissipation due to a viscous damping

$$F_{\mathrm{diss}}(z, \dot{z}) := \gamma_1(z)\,\dot{z}, \tag{3.51}$$

where the damping coefficient γ is a function of the actual tip position.

For the application of these force laws to Eqs. (3.5.7) it is convenient to use the transformation $z(t) := A\cos(2\pi f_0 t)$ for the simplification of the integrals on the right side of these equations. We then find

$$\Delta f \cong -\frac{f_0}{\pi A^2 c_z} \int_{-A}^{A} \frac{F_{\rightarrow} + F_{\leftarrow}}{2} \frac{z}{\sqrt{A^2 - z^2}}\, dz, \tag{3.52}$$

$$\begin{aligned} |g| &\cong \frac{1}{Q} + \frac{1}{\pi A^2 c_z} \int_{-A}^{A} (F_{\rightarrow} - F_{\leftarrow})\, dz \\ &\quad + \frac{4 f_0}{A^2 c_z} \int_{-A}^{A} \gamma_1(z)\sqrt{A^2 - z^2}\, dz. \end{aligned} \tag{3.53}$$

This result demonstrates that the frequency shift depends only on the *average of the tip-sample force* between forward and backward movement, but is *independent* of the dissipative force Eq. (3.51). In contrast, the gain factor g is directly related to all energy dissipation processes: The intrinsic damping of the cantilever leads to a constant term $1/Q$. The second term is given by an integral over the difference of the tip-sample force between forward and backward movement, i.e., the hysteresis, whereas the third term is related to the viscous damping mechanism.

The analysis for DFM using the FM technique (self-driven oscillator) in the constant amplitude mode showed the following: (i) The cantilever oscillates always exactly with its eigenfrequency for a time delay corresponding to 90°. (ii) The adjustment of the correct time delay can easily be performed by the minimization of the gain factor. (iii) The frequency shift is given by the mean tip-sample force. (iv) The gain factor is directly related to dissipative forces.

References

[1] F.-J. Giessibl, Science **260**, 67 (1995).

[2] R. Wiesendanger, *Triannual Report 1996-1998*, Hamburg (1998).

[3] W. Allers, A. Schwarz, U. D. Schwarz, and R. Wiesendanger, Rev. Sci. Instrum. **69**, 221 (1998).

[4] W. Allers, A. Schwarz, H. Hölscher, U. D. Schwarz, R. Wiesendanger Jpn. J. Appl. Phys. **39**, 3701 (2000).

[5] W. Allers, A. Schwarz, U. D. Schwarz, and R. Wiesendanger, Appl. Surf. Sci. **140**, 247 (1999).

[6] H. Hölscher, W. Allers, U. D. Schwarz, A. Schwarz, and R. Wiesendanger, Phys. Rev. Lett. **83**, 4780 (1999).

[7] H. Hölscher, A. Schwarz, W. Allers, U. D. Schwarz, and R. Wiesendanger, Phys. Rev. B **61**, 12678 (2000).

[8] A. Schwarz, W. Allers, U. D. Schwarz, and R. Wiesendanger, Appl. Surf. Sci. **140**, 293 (1999).

[9] A. Schwarz, W. Allers, U. D. Schwarz, and R. Wiesendanger, Phys. Rev. B **61**, 2837 (2000).

[10] A. Schwarz, W. Allers, U. D. Schwarz, and R. Wiesendanger, Phys. Rev. B **62**, 13617 (2000).

[11] W. Allers, S. Langkat, and R. Wiesendanger, Appl. Phys, A **72** S27 (2001).

[12] W. Allers, A. Schwarz, U. D. Schwarz, and R. Wiesendanger, Europhys. Lett. **49**, 276 (1999).

[13] H. Hölscher, W. Allers, A. Schwarz, U. Schwarz, and R. Wiesendanger, Phys. Rev. B **62**, 6967 (2000).

[14] H. Hölscher, W. Allers, U. D. Schwarz, A. Schwarz, and R. Wiesendanger, Appl. Phys. A **72** S35 (2001).

[15] H. Hölscher, U. D. Schwarz, and R. Wiesendanger, Appl. Surf. Sci. **140**, 344 (1999).

[16] U.D. Schwarz, H. Hölscher, and R. Wiesendanger, Phys. Rev. B **62**, 13089 (2000).

[17] H. Hölscher, B. Gotsmann, W. Allers, U. D. Schwarz, H. Fuchs, and R. Wiesendanger, Phys. Rev. B **64**, 075402 (2001).

[18] T. R. Albrecht, P. Grütter, D. Horne, and D. Rugar, J. Appl. Phys. **42-44**, 668 (1991).

[19] C. B. Duke, C. Mailhot, A. Paton, D. J. Chadi, and A. Khan, J. Vac. Sci. Technol. B **3**, 1087 (1985).

[20] S. H. Ke, T. Uda, R. Perez, I. Stich, and K. Terakura, Phys. Rev. B **60**, 11631 (1999).

[21] J. Tobik, I. Stich, R. Perez, and K. Terakura, Phys. Rev. B **60**, 11639 (1999).

[22] G. Schwarz, A. Kley, J. Neugebauer, and M. Scheffler, Phys. Rev. B **58**, 1392 (1998).

[23] Y. Sugawara, T. Uchihashi, M. Abe, and S. Morita, Appl. Surf. Sci. **140**, 371 (1999).

[24] A. Kikukawa, S. Hosaka, and R. Imura, Appl. Phys. Lett. **66**, 3510 (1995).

[25] A. Kikukawa, S. Hosaka, and R. Imura, Rev. Sci. Instrum. **67**, 1463 (1996).

[26] T. Uchihashi, M. Ohta, Y. Sugawara, Y. Yanase, T. Sigematsu, M. Suzuki, and S. Morita, J. Vac. Sci. Technol. B **15**, 1543 (1999).

[27] S. Kitamura and H. Iwatsuki, Appl. Phys. Lett. **72**, 3154 (1998).

[28] C. Sommerhalter, T. W. Matthes, T. Glatzel, A. Jäger-Waldau, and M. C. Lux-Steiner, Appl. Phys. Lett. **66**, 3510 (1999).

[29] J. van Laar, A. Huijser, and T. L. van Rooy, J. Vac. Sci. Technol. **14**, 894 (1977).

[30] W. Kresse, Diploma Thesis, University of Hamburg, Hamburg (1997)

[31] P. A. Cox: *Transition Metal Oxides: an introduction totheir electronic structure and properties*, Clarendon Press, Oxford (1992).

[32] M. R. Castell, P. L. Wincott, N. G. Condon, C. Muggelberg,G. Thornton, S. L. Dudarev, A. P. Sutton, and G. A. D. Briggs, Phys. Rev. B**55**, 7859 (1997).

[33] H. Hosoi, K. Sueoka, K. Hayakawa, and K. Mukasa, Appl. Surf. Sci. **157**, 218 (2000).

[34] A. S. Foster, A. L Shluger, Surf. Sci. **490**, 211 (2001).

[35] Mateck, Im Langenbroich 20, Jülich, Germany.

[36] F. J. Giessibl, Phys. Rev. B **56**, 16010 (1997).

[37] V. E. Henrich and P. A. Cox: *The Surface Science of Metal Oxides*, Cambridge University Press, Cambridge (1994).

[38] L. N. Kantorovich, A. S. Foster, A. L. Shluger, A. M. Stoneham, Surf. Sci. **445**, 283 (2000).

[39] F.-J. Giessibl, H. Bielefeldt, Phys. Rev. B **61**, 9968 (2000).

[40] U. Dürig, Appl. Phys. Lett. **75**, 433 (1999).

[41] G. Binnig, Ch. Gerber, E. Stoll, T. R. Albrecht, and C. F. Quate, Europhys. Lett. **3**, 1281 (1987).

[42] S. Fujisawa, E. Kishi, Y. Sugawara, and S. Morita, Tribology Letters **1**, 121 (1996).

[43] N. Sasaki, K. Kobayashi, and M. Tsukada, Phys. Rev. B **54**, 2138 (1996).

[44] H. Hölscher, U. D. Schwarz, O. Zwörner, and R. Wiesendanger, Phys. Rev. B **57**, 2477 (1998).

[45] S. A. C. Gould, K. Burke, and P. K. Hansma, Phys. Rev. B **8**, 5363 (1989).

[46] N. Sasaki and M. Tsukada, Phys. Rev. B **52**, 8471 (1995).

[47] Inder P. Batra and S. Ciraci, J. Vac. Sci. Technol. A **6**, 313 (1988).

[48] S. Ciraci, A. Baratoff, and P. Batra, Phys. Rev. B **41**, 2763 (1990).

[49] E. Tekman and S. Ciraci, J. Phys.: Condens. Matter **3**, 2613 (1991).

[50] H. Ueyama, Y. Sugawara, S. Morita, Appl. Phys. A **66**, S295 (2001).

[51] L. W. Bruch, M. W. Cole, E. Zaremba, *Physical Adsorption: Forces and Phenomena*, Oxford Science Publications, Oxford (1997).

[52] I. Yu. Sokolov, G. S. Henderson, and F. J. Wicks, Surf. Sci. **381**, L558 (1997).

[53] R. Erlandsson, L. Olsson, and P. Mårtenson, Phys. Rev. B **54**, R8309 (1996).

[54] R. Peréz, M. C. Payne, I. Stich, and K. Terakura, Phys. Rev. Lett. **78**, 668 (1997).

[55] B. Gotsmann, B. Ancykowski, C. Seidel, and H. Fuchs, Appl. Surf. Sci. **140**, 314 (1999).

[56] G. Binnig, H. Rohrer, Ch. Gerber, and E. Weibel, Phys. Rev. Lett **50**, 120 (1983).

[57] H. Hertz, J. Reine Angew. Math. **92**, 156 (1882).

[58] L. Landau, E. M. Lifschitz, *Lehrbuch der Theoretischen Physik IV*, 7th ed., Akademie Verlag, Berlin (1991).

[59] B. V. Derjaguin, V. M. Muller, and Yu. P. Toporov, J. Colloid Interface Sci. **53**, 314 (1975).

[60] U. D. Schwarz, O. Zwörner, P. Köster, and R. Wiesendanger, Phys. Rev. B **56**, 6987 (1997).

[61] M. Enachescu, R. J. A. van den Oetelaar, R. W. Carpick, D. F. Ogletree, C.F.J. Flipse, and M. Salmeron, Phys. Rev. Lett. **81**, 1877 (1998).

[62] G. Cross, A. Schirmeisen, A. Stadler, P. Grütter, M. Tschudy, and U. Dürig, Phys. Rev. Lett. **80**, 4685 (1998).

[63] U. D. Schwarz, O. Zwörner, P. Köster, and R. Wiesendanger, J. Vac. Sci. Technol. B **15**, 1527 (1997).

[64] V. M. Muller, V. S. Yushchenko, and B. V. Derjaguin, J. Colloid Interface Sci. **77**, 91 (1980).

[65] V. M. Muller, V. S. Yushchenko, and B. V. Derjaguin, J. Colloid Interface Sci. **92**, 92 (1982).

[66] D. Maugis, J. Colloid Interface Sci. **150**, 243 (1991).

[67] G. Binnig, C. F. Quate, and Ch. Gerber, Phys. Rev. Lett. **68**, 930 (1986).

[68] N. A. Burnham and R. J. Colton, J. Vac. Sci. Technol. A **7**, 2906 (1989).

[69] S. P. Jarvis and H. Tokumoto, Probe Microscopy **1**, 65 (1997).

[70] F. Ohnesorge, G. Binnig, Science **260**, 1451 (1993).

[71] S. P. Jarvis, S. I. Yamamoto, H. Yamada, H. Tokumoto, and J. B. Pethica, Appl. Phys. Lett. **70**, 2238 (1997).

[72] N. Sasaki and M. Tsukada, Jpn. Appl. Phys. **37**, L533 (1998).

[73] B. Gotsmann, D. Krüger, and H. Fuchs, Europhys. Lett. **39**, 153 (1997); **41**, 581 (1998).

[74] R. Boisgard, D. Michel, J. P. Aime, Surf. Sci. **401**, 199 (1998).

[75] U. Dürig, O. Züger, and A. Stalder, J. Appl. Phys. **72**, 1778 (1992).

[76] L. Landau and E. M. Lifshitz, *Lehrbuch der Theoretischen Physik I*, Akademie-Verlag, 13th ed., Berlin (1990).

[77] R. Peréz, I. Štich, M. C. Payne, and K. Terakura, Phys. Rev. B **58**, 10835 (1998).

[78] B. Ancykowski, D. Krüger, and H. Fuchs, Phys. Rev. B **53**, 15485 (1996).

[79] A. Kühle, A. H. Sørensen, and J. Bohr, J. Appl. Phys. **81**, 6592 (1997).

[80] D. Krüger, B. Anczykowski, H. Fuchs, Ann. Phys. (Leipzig) **6**, 34 (1997).

[81] N. Sasaki and M. Tsukada, Jpn. J. Appl. Phys. **37**, L533 (1998).

[82] N. Sasaki, M. Tsukada, R. Tamura, K. Abe, N. Sato, Appl. Phys. A **66**, S287.

[83] O. Behrendt, F. Oulevey, D. Gourdon, E. Dupas, A. J. Kulik, G. Gremaud, N. A. Burnham, Appl. Phys. A **66**, S219 (1998).

[84] M. Labardi, Probe Microscopy **1**, 215 (1998).

[85] J. P. Aimé, R. Boisgard, L. Nony, G. Couturier, Phys. Rev. Lett. **82**, 3388 (1998).

[86] see, e.g., Y. Martin, C. C. Williams, and H. K. Wichramasinghe, J. Appl. Phys. **61**, 4723 (1987); R. Erlandsson, G. M. McClelland, C. M. Mate, and S. Chiang, J. Vac. Sci. Technol. A **6**, 266 (1988); P. Grütter, H. J. Mamin, and D. Rugar, in: *Scanning Tunneling Microscopy II*, ed. by R. Wiesendanger and H.-J. Güntherodt, pp. 151-207, Springer (1992)

[87] B. Gotsmann, B. Ancykowski, C. Seidel, and H. Fuchs, Phys. Rev. B **60**, 11051 (1999).

[88] A. I. Livshits, A. L. Shluger, A. Rohl, Appl. Surf. Sci. **140**, 327 (1999).

[89] M. Gauthier and M. Tsukada, Phys. Rev. B **60**, 11716 (1999).

[90] U. Dürig, N. J. of Phys. **2**, 5.1-5.12 (2000).

3.6 Instrumental Developments

O. Pietzsch, A. Kubetzka, and M. Bode

In our approach to spin-polarized scanning tunneling microscopy, there is, next to the application of a spectroscopic mode of STM operation, a second essential ingredient, namely the use of tunneling tips which are coated by thin films of magnetic material. This second component establishes an instrumental requirement which is non-trivial if the tip preparation is to be done *in situ*. In the following, the design of an STM is presented which meets three operational conditions: ultra-high vacuum, low temperatures, and high magnetic fields [1]. For the purpose of our special interest in investigations in surface magnetism we have supplied the instrument with some unique features, like sample rotation, easy tip exchange mechanism, and an arrangement for measurements of the magneto-optical Kerr effect (MOKE).

3.6.1 The Cryo-Magnet STM

Chamber system

The new cryo-magnet STM chamber is added to a four-chamber UHV system [2] consisting of a central distribution chamber, a preparation chamber equipped with resistive and electron beam heating and a sputter gun, an MBE chamber with five evaporators and a home built STM especially designed for growth studies described elsewhere [7], an analysis chamber containing facilities for standard surface characterization as, e.g. low energy electron diffraction (LEED), Auger electron spectroscopy (AES), and spin-resolved photoelectron spectroscopy (SP-PES), and, within an additional satellite chamber, a commercial variable-temperature STM [3] which can be operated in a temperature range of 30 K $< T <$ 1000 K. A load lock allows for fast introduction of samples and tips without venting the chamber system. To prevent from acoustical and low frequency building vibrations the whole system is installed in an acoustically shielded laboratory with a foundation being completely separated from the rest of the building. The UHV chamber system is supported by a table with additional pneumatic damping.

Magnet Cryostat System

The magnet cryostat system (Fig. 3.128) is a modified Spectromag ^{4}He bath cryostat with a LN$_2$ radiation shield [4]. The 2.5 T superconducting magnet is a split coil type with a 62 mm bore. Homogeneity of the field in a 10 mm diameter spherical volume at the sample location is specified to 1 part in 10^2. The maximum sweep rate accounts to 2.5 T per minute. The central region of the magnet (cf. Fig. 3.129) has two cutaways of 80° and 90°, respectively, and a minimum height of 42 mm thus providing two access openings to the microscope. Samples and tips are being exchanged through the 80°

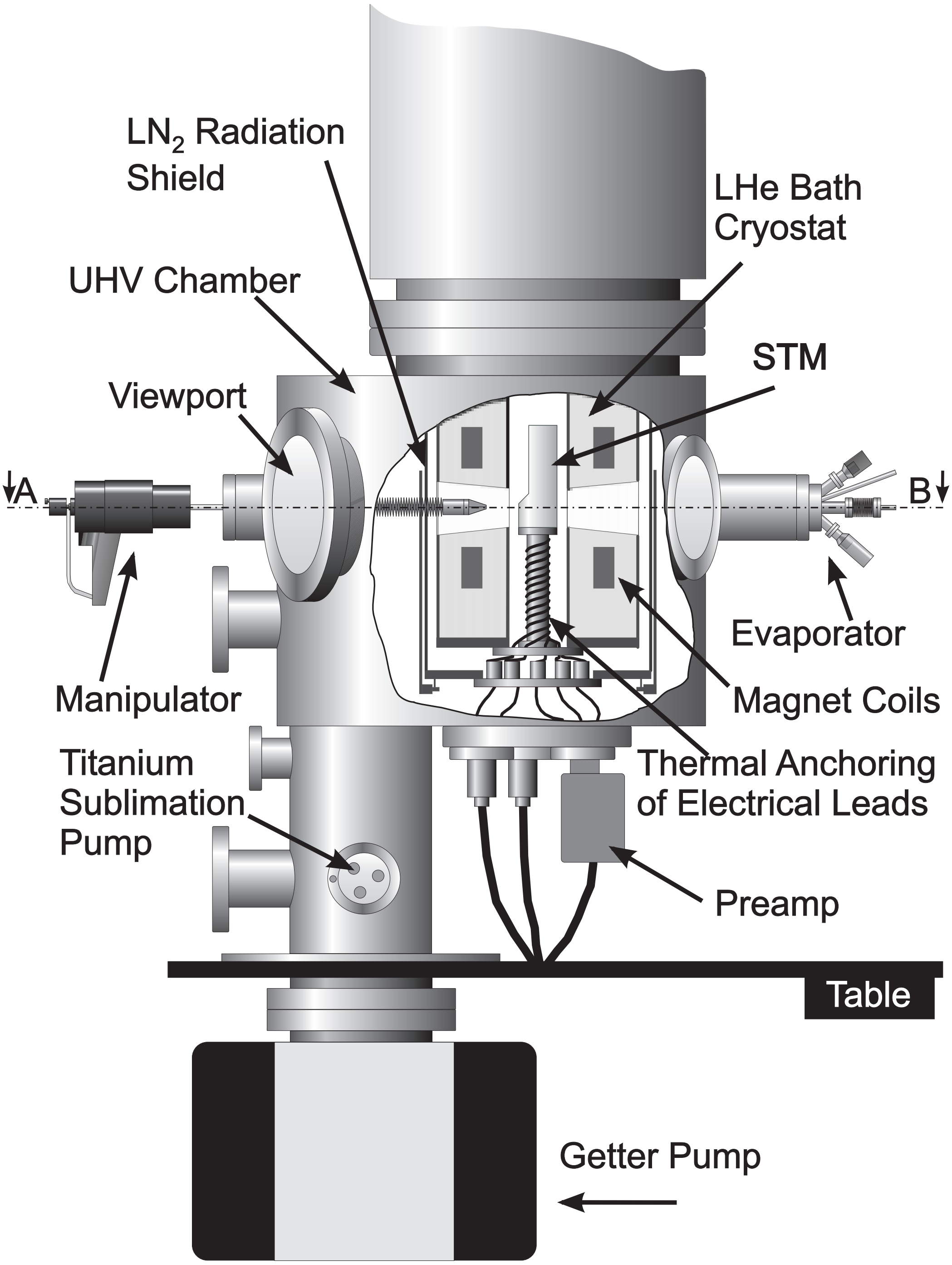

Figure 3.128: (a) Schematic drawing of the cryomagnet STM system (side view). The STM is inserted from the bottom through the base flange which also carries the electrical feedthroughs. For section A—B see Fig. 3.129.

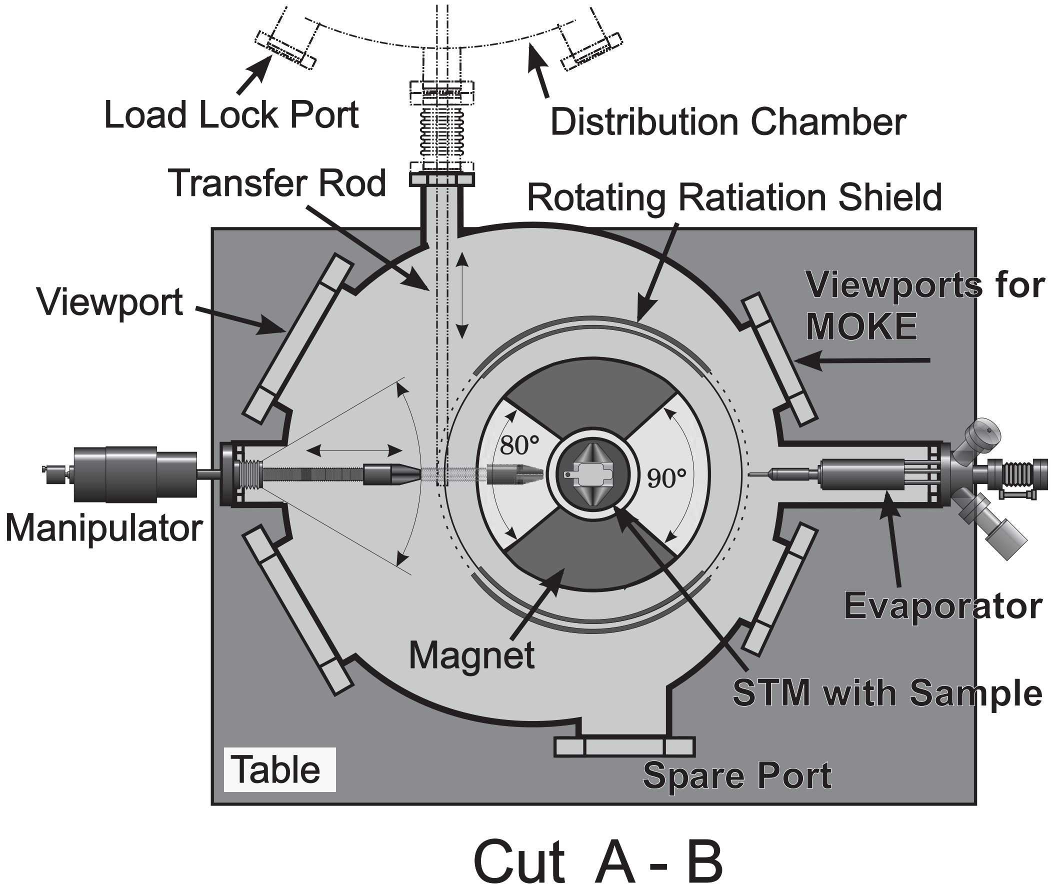

Figure 3.129: Section of the cryomagnet system at the sample plane.

window whereas the 90° window is used to carry out MOKE measurements, and to allow for metal or molecular beam evaporation onto the sample surface. To obtain proper UHV conditions the magnet is designed to safely endure bakeout at 120° C. In our bakeout procedure we keep the magnet at 115° C for 48 h. The temperature is measured by a platinum resistor sensor on top of the magnet. The signal of this sensor feeds a control unit that supplies a flow of cold nitrogen gas across the magnet if the temperature is about to surpass the set point value. Thus a safe bakeout operation is guaranteed over night. The helium reservoir of the cryostat has a useful capacity of 20 l giving a hold time in the low temperature regime of approx. 40 h between subsequent fills. The helium reservoir and the magnet are enclosed by a nitrogen radiation shield. Its 20 l volume provides a hold time of 36 h. At the lower end where the magnet has its above mentioned openings the shield has an additional rotating cylinder the purpose of which is to shut the access windows. This cylinder is thermally coupled to the main part of the shield by a number of copper braids. To avoid vibrations due to boiling nitrogen the LN_2 reservoir is pumped to a pressure $p < 5$ mbar so that the nitrogen solidifies. To cope with the initially huge amount of gas from the boiling liquid we use a rotary vane pump with a nominal pumping speed of 65 m^3/h. As the gas flow through the pumping line is very low we have no acoustic coupling of the pump. Having a radiation shield at a temperature as low as 63 K is of considerable advantage for minimizing the helium boil off.

The outer vacuum chamber of the cryostat unit has a DN 350 CF base flange which fits onto the appropriate top flange of our custom-made UHV chamber. Pumping is done by a turbo pump, an ion getter pump and a titanium sublimation pump. The base pressure after bakeout and cooldown is $p < 5 \times 10^{-11}$ mbar. The turn-around time for venting the system from low temperature, bake-out, and returning to low temperature accounts to several days. Thus it is essential that samples and tips can be introduced through the load-lock of the central distribution chamber without breaking the vacuum.

3.6.2 STM Design

The design of the STM was geometrically restricted by the 62 mm diameter of the magnet's core tube. The cylindrical body of the STM, machined from one piece of the glass ceramic Macor [5] has a diameter of 40 mm and a height of 110 mm. This body bears all parts of the microscope. It is mounted on top of an OFHC copper pedestal which serves both as the microscope's support and as the thermal anchoring for all electrical wirings. Together with this stand the microscope is installed as a unit into the magnet bore (cf. Fig. 3.130). To avoid any disturbance of the magnetic field the few metallic parts used are made from titanium, molybdenum, copper, or copper beryllium.

Approach Mechanism

At the center of the microscope one finds two moving parts, the approach sledge bearing the scanner tube at its lower end [(b) in Fig. 3.131], and the sample recectacle (i) which can be rotated about the y-axis. The coarse approach mechanism is based on Pan's design [6] that has proven to be stable enough to regain a microscopic location on the sample with an accuracy of less than 100 nm posterior to a macroscopic movement of 20 mm [7, 8]. The approach sledge is a polished sapphire prism placed in a V-shaped groove where it is rigidly clamped by two triplets of shear piezo stacks [9] [(c) in Fig. 3.131]. A 5 mm × 5 mm × 1 mm Al_2O_3 pad is glued on top of each shear piezo stack. These pads provide the actual contact areas between the stacks and the sapphire prism surfaces. Two of the piezo stacks are glued to a Macor beam (d) which is pressed onto the prism by means of a molybdenum leaf spring (f) and a ruby ball (e). The Macor beam functions as a balance and thus warrants an equal distribution of the spring force to all contact areas of the six shear piezo stacks and the prism surface. In contrast to previously presented designs [10–12] we do not employ walker stepping as a working mechanism but use inertial movement by applying an asymmetric saw-tooth voltage curve to all six stacks simultaneously (stick-slip). On the flat slope of the

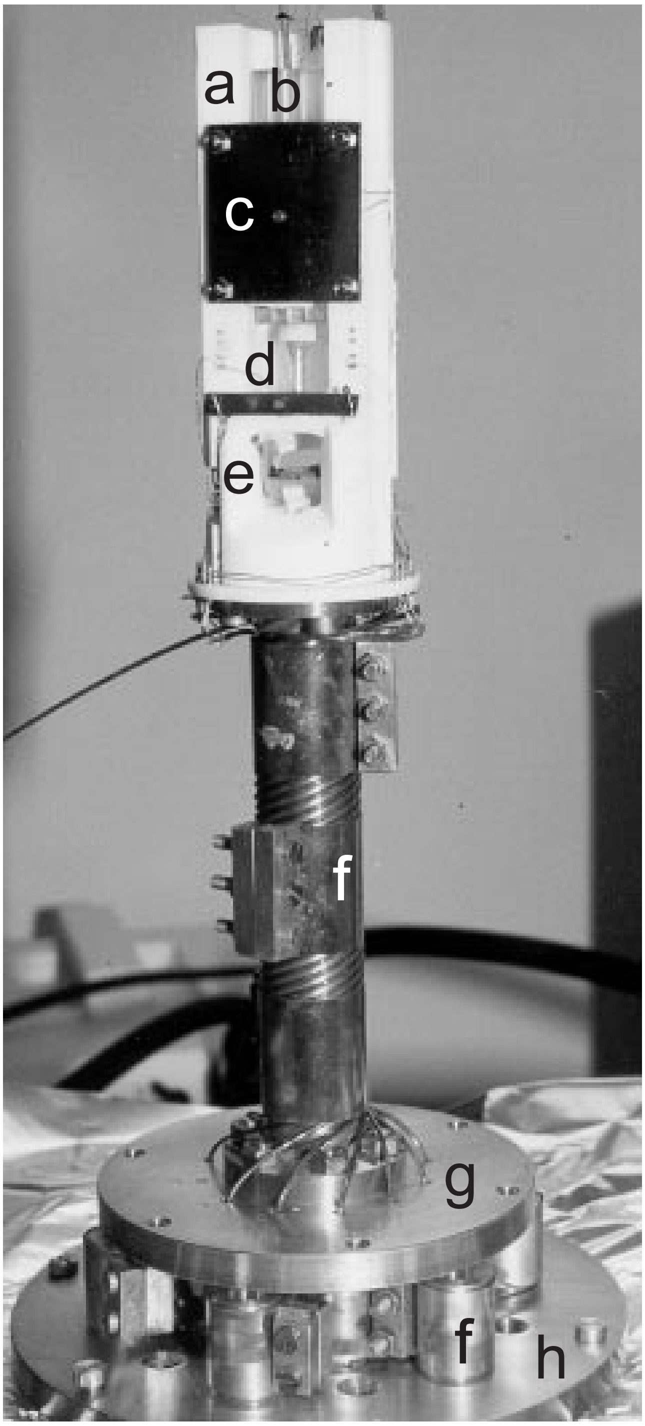

Figure 3.130: Photograph of the microscope on its pedestal. (a) Macor body, (b) sapphire prism, (c) leaf spring, (d) tube scanner with tip, (e) sample, (f) thermal anchoring of electrical leads to helium and nitrogen temperature, respectively. When mounted to the cryostat the helium flange (g) and the nitrogen flange (h) are mechanically disconnected.

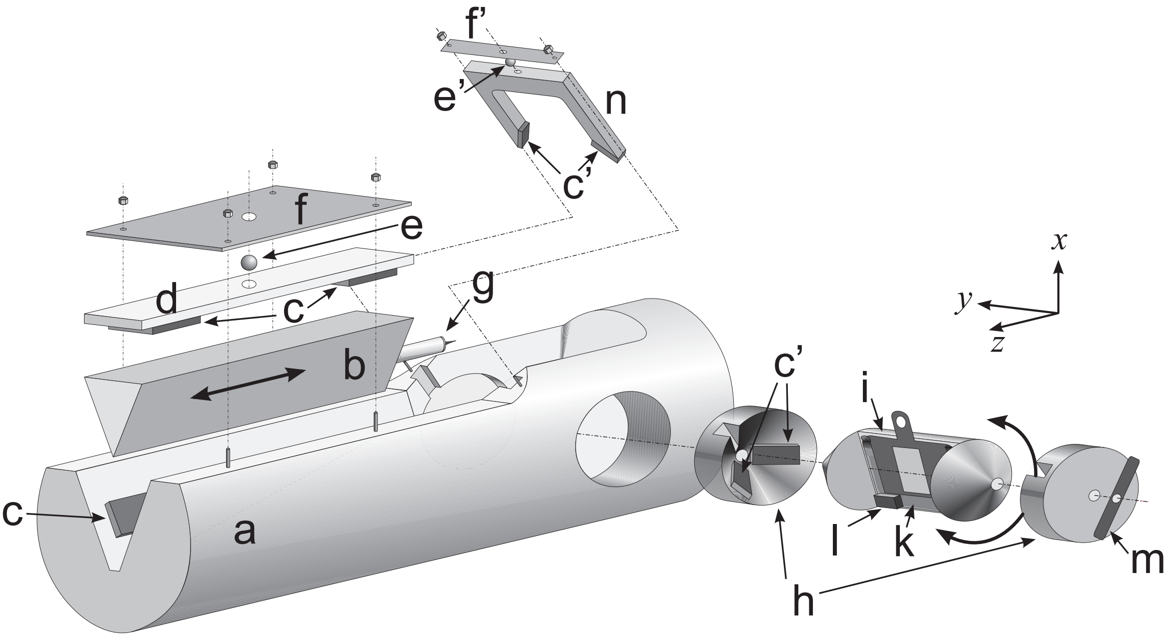

Figure 3.131: Schematic drawing of the STM (not to scale). (a) Macor body, (b) sapphire prism, (c) and (c') shear piezo stacks, (d) Macor beam,(e) and (e') ruby ball, (f) and (f') leaf spring, (g) scanner with tip, (h) stators for sample rotation, (i) rotor with sample, (k) spring, (l) temperature sensor, (m) leaf spring, (n) bridge.

voltage ramp the prism follows the shear movement (stick) while, due to its inertial mass, it is unable to follow the rapid relaxation of the piezos on the steep slope (slip), the result being one step of the prism per period. The mechanism is driven at 0.5–1 kHz; the step size can be tuned by varying the applied voltage amplitude. The scanner containing the tip is mounted to the lower end of the prism. The tip approach towards the sample to less than 0.2 mm distance is carried out manually using a remote control box; this operation can easily be controlled visually through one of the viewports with an *ex situ* located optical microscope. Only the fine approach is accomplished in automatic mode of the STM control unit. During a measurement the sapphire prism stays firmly clamped to the microscope body. The scanner in use is a 1/4” EBL #4 piezo tube [9] with a length of 31 mm. This length was chosen in order to allow for a scan range of 5 μm at low temperatures (10.5 μm at room temperature) and still having a sufficiently high resonance frequency ($f_{\mathrm{res}} = 2.2$ kHz). A large scan range is desirable for imaging of magnetic domains.

Sample Rotation

The sample is introduced into a receptacle [(i) in Fig. 3.131] which can be rotated by more than 270° about the y-axis. This rotor is a sapphire cylinder with the edges ground off to form two 90° cones. These cones are polished and again serve as the sur-

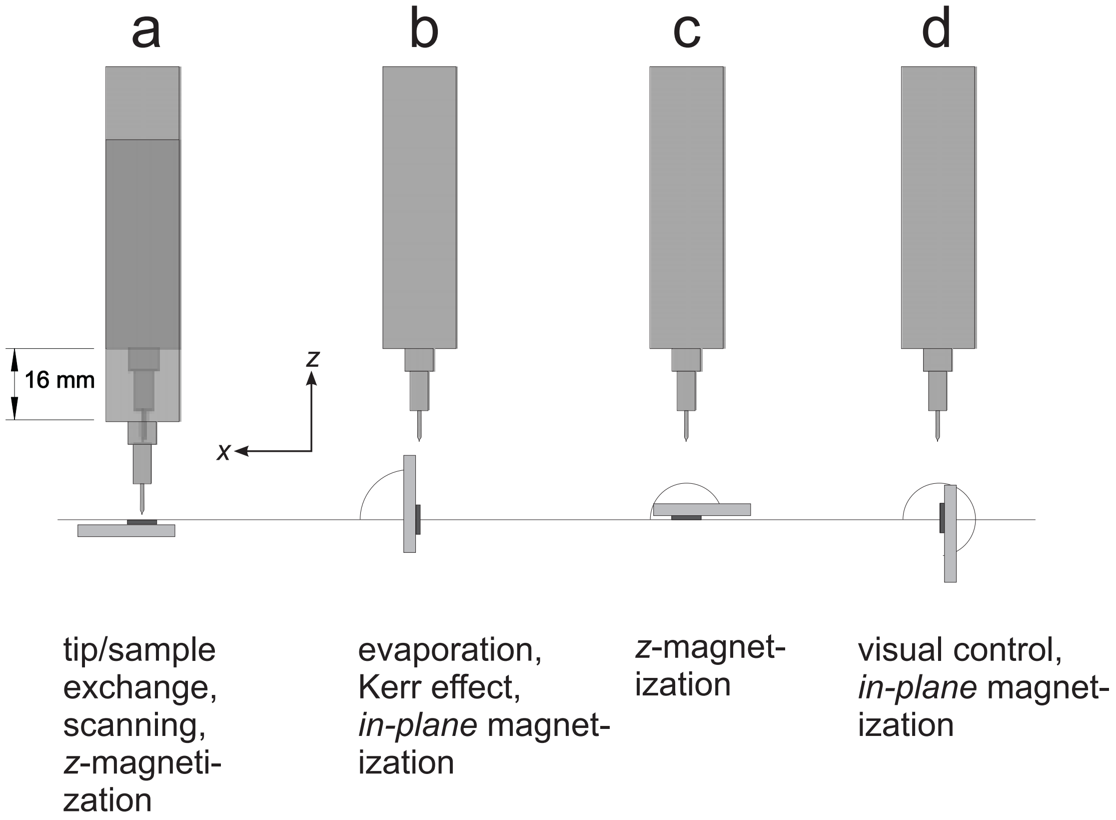

Figure 3.132: Principal geometrical configurations of the sample. For details on the particular use of each position see text.

faces for stick-slip movement. In close analogy to the arrangement described above for the linear movement there are six shear piezo stacks (c') two of which are pressed onto the cones by a bridge (n) with a leaf spring (f'). Due to the symmetry of this assembly it is self-centering in both radial and axial direction, and no additional bearings are required. When brought into place and turned for the first time the rotor, shaken by the rapid oscillatory piezo movements, takes on an equilibrium position and keeps it. Between the two cones a recess is ground into the cylinder deep enough to receive the sample tray such that the sample surface lies in the $x-y$-plane. The sample tray is kept in place by a copper beryllium spring (k). The gap voltage to the sample is applied through a contact soldered to the spring. Also, the sample temperature sensor (l), a GaAlAs diode [13], is glued onto the spring, and is thus in immediate proximity and in excellent thermal contact to the sample.

The capability to rotate the sample allows for some unique experimental arrangements, illustrated in Fig. 3.132. While the sample receptacle is in position (a) (i.e. the sample surface normal pointing in $+z$ direction) and the tip retracted, sample and tip exchange can be carried out. With the tip approached, this is also the position for STM measurements. After retraction of the tip a 90° rotation can be applied to the sample, thus turning the surface normal into the $-x$ direction [position (b)]. This position allows to direct a molecular beam from the evaporator (cf. Fig. 3.128 and Fig. 3.129) to impinge normal to the sample surface. The sample re-rotated back into position (a), STM imaging can, in principle, be applied for growth studies at low temperature and, if desired, in a magnetic field. Position (b) also allows for measurements of the magneto-optical Kerr effect (MOKE). The UHV chamber is supplied with two viewports at the appropriate sites (see Fig. 3.129), one for the incident beam, the other for the reflected beam.

Sample Magnetization

Though the external magnetic field vector at the sample location is restricted to the z direction, the sample can be magnetized in almost any appropriate direction by virtue of the rotor. If in-plane magnetization is desired this can be achieved by turning the sample into position (b) or position (d), respectively. Out-of-plane magnetization is accomplished in position (a) and position (c). This latter configuration provides a very elegant way to study certain surface magnetic phenomena: Suppose a ferromagnetic sample being in the upside down position (c), and the external field is applied in, e.g., the $+z$ direction. Having a ferromagnetic tip in use, both tip and sample will be magnetized according to the applied field. Now the field is switched off, and the sample is rotated by 180° into the scanning position, i.e. position (a). Tip and sample will now be in an *antiparallel* magnetic orientation. After taking a measurement *in remanence* the field is switched on again. The magnetization orientation of the tip will stay the same. The sample, however, will experience a reorientation of its magnetization, tip and sample magnetization thus ending up in a *parallel* configuration. With the external field switched off, again a measurement *in remanence* can be taken. Since, for the field sweep, the tip does not need to be retracted the second scan will image exactly the same location on the sample surface, thus allowing a one-to-one comparison of the two measurements.

Tip Exchange Mechanism

When working with ferromagnetically coated tips it is mandatory to have the possibility to prepare and exchange tips *in situ* in a short turn-around time. We use etched tungsten tips coated with 5–10 ML of Fe or Gd. A typical tip preparation procedure is as follows. The tungsten tip is cleaned by heating it to $T > 2000$ K by means of electron bombardment in the preparation chamber. Iron coating and subsequent annealing is performed in the MBE chamber. The tip has then to be introduced into the microscope. While a normal W or PtIr tip can repeatedly be sharpened by field emission and thus can be kept in the microscope for periods of months this is not possible for a tip carrying an ultrathin magnetic film. Thus a tip exchange mechanism is indispensable. Figure 3.133 shows the assembly schematically. The tip is fixed in a molybdenum tip holder. For inserting a tip into the scanner the tip holder is carried

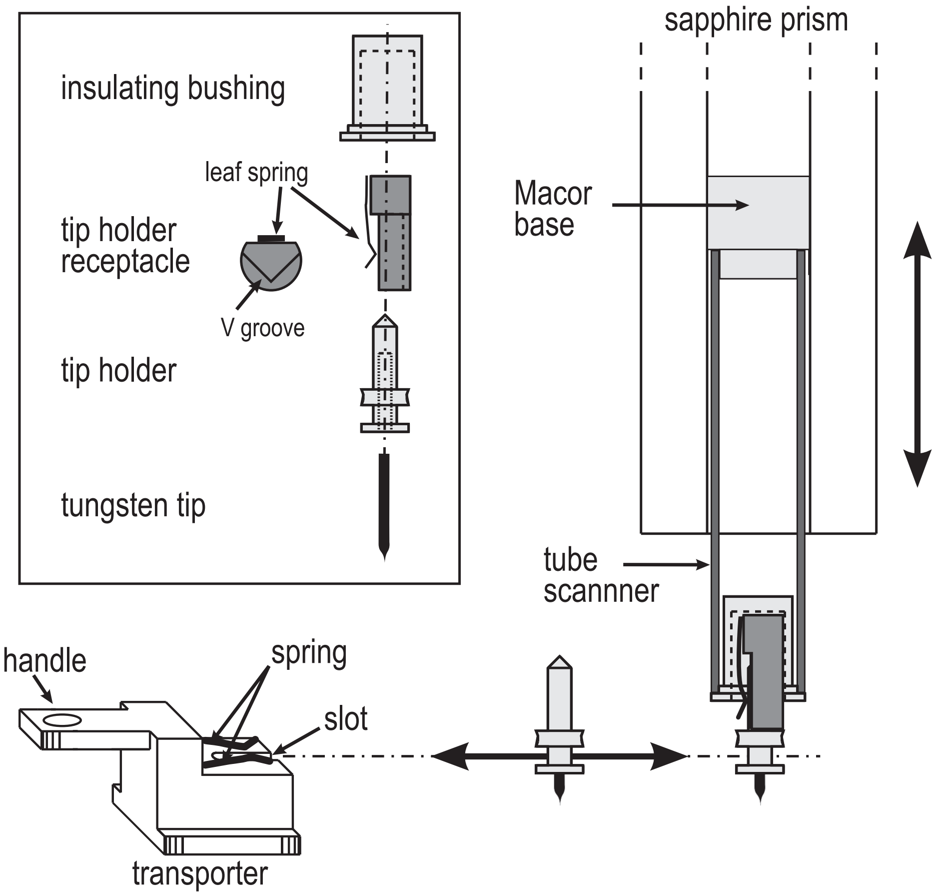

Figure 3.133: Schematic drawing of the tip exchange mechanism. Drawing from Ref. [14].

by means of the transporter which can be placed into the sample receptacle where it is positioned such that the tip holder ends up precisely below the retracted scanner. Driving down the linear motor lets the tip holder slip into a V–shaped groove of the tip receptacle which is mounted inside an insulating bushing within the lower end of the scanner tube. A small leaf spring clamps the tip holder. Now the transporter can be retracted, leaving holder and tip firmly attached to the scanner tube. Tip and sample exchange is carried out using a "Mechanical Hand" [15] which allows simple and safe operation. Tip exchange comes down to a matter of minutes, sample exchange being even faster. A whole tip preparation procedure, including fresh coating, accounts to less than one hour.

Electrical Connections

Since electrical leads introduce heat to the microscope special attention has to be paid to an optimum of thermal anchoring of all wirings. The leads for the magnet current supply, level meters, and temperature sensors are fed through the top side of the cryostat. They are effectively cooled by the flow of cold helium gas. The microscope wiring, however, is fed directly into UHV via several multipin feedthroughs at the bottom flange of the outer vacuum chamber (see Fig. 3.128). We use custom made Capton insulated shielded twisted pair VA steel cables with an overall diameter of 1 mm. They are thermally anchored to both the nitrogen and the helium stage (cf. Fig. 3.128 and 3.130). At the nitrogen stage every single lead is wound around a copper pole ten of which are mounted on top of a flange and thereby fixed to the base flange of the nitrogen shield. Anchoring to helium temperature is achieved in a similar way: a ten gear thread is cut into the microscope's pedestal such that all ten leads can be firmly wound around it, being held in place by appropriate clamps. When installed, the nitrogen and the helium flange are mechanically disconnected. For maintenance works they get coupled so that they form a unit with the microscope on top. Mounting and dismounting requires approx. 1/2 h.

3.6.3 Performance

Micro Positioning

Due to the very high stability of both the linear and the rotational drive one can regain a microscopic location on the sample after a macroscopic movement. This feature is illustrated in Fig. 3.134. The series of images was taken *ex situ* on Au(111)/mica in alphabetical order as indicated. Some islands of characteristic shape are shown which can easily be distinguished. After each scan the tip was retracted by 16 mm, followed by a rotation of the sample by 90°, re-rotation of the sample, and re-approach of the tip. The images have been taken without any correction of the scan position. The maximum lateral offset during subsequent scans was found to be $\Delta(x, y) < 280$ nm, and $\Delta(x, y) < 425$ nm during 7 cycles.

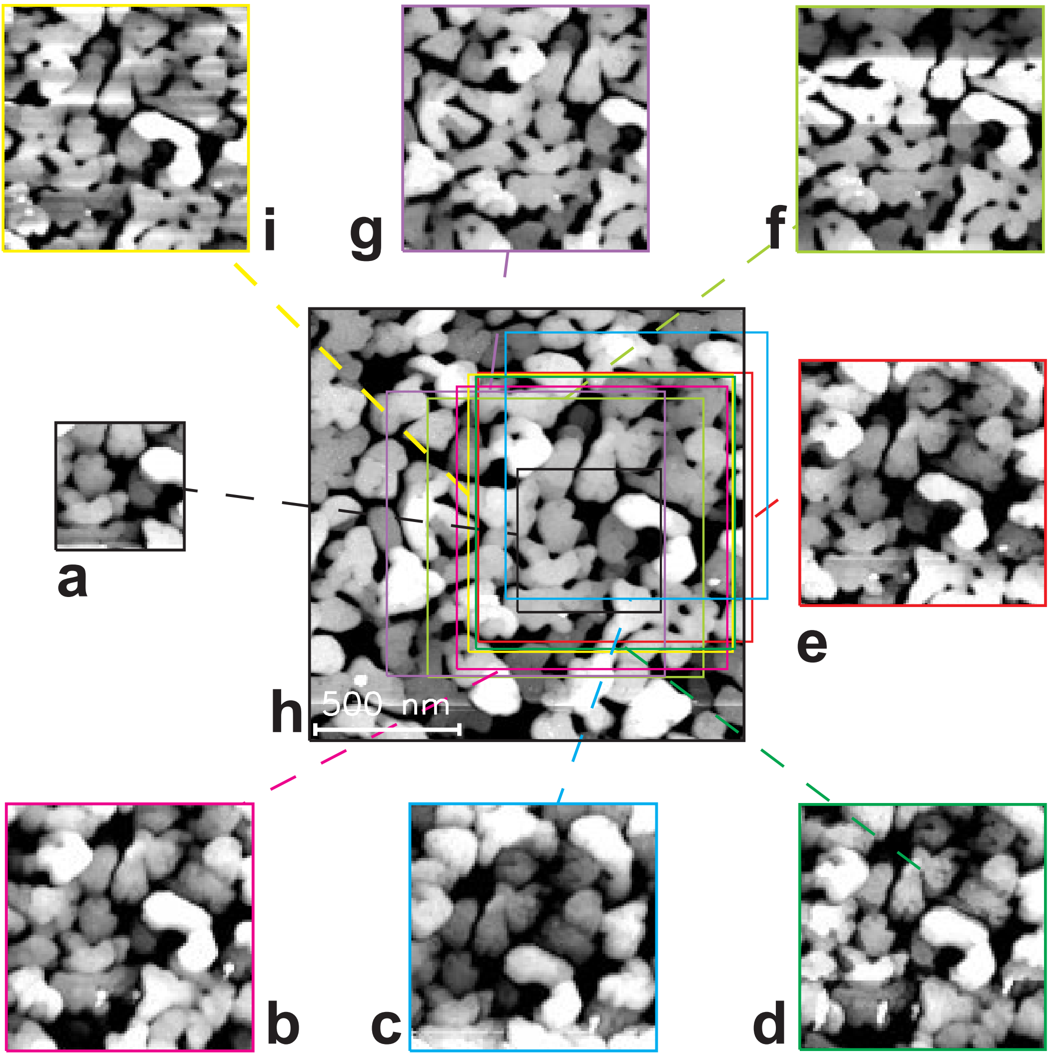

Figure 3.134: Sequence of images in alphabetical order demonstrating the microscope's ability to regain a microscopic location after a macroscopic movement. Au(111)/Mica, ambient condition. Each scan was followed by a retraction of the tip by 16 mm, rotation of the sample by 90°, re-rotation of the sample, re-approach of the tip. Maximum lateral offset during subsequent scans $\Delta(x, y) < 280$ nm, maximum lateral offset during 7 cycles $\Delta(x, y) < 425$ nm.

Spectroscopy in Applied Magnetic Fields

In order to test the microscope's performance in strong magnetic fields we prepared a 50 ML smooth Gd(0001) film by electron beam evaporation on a W(110) single crystal and subsequent annealing. A clean tungsten tip was coated with approx. 100 ML Fe. In a simultaneous measurement at a sample temperature of $T = 16.9$ K topographic, $I(U)$ and $dI(U)/dU$ data were obtained. Fig. 3.135(a) shows two curves of the differential conductance dI/dU, which is a measure of the local density of states, obtained by a lock-in technique. Black squares indicate the spectrum taken with a magnetic field of

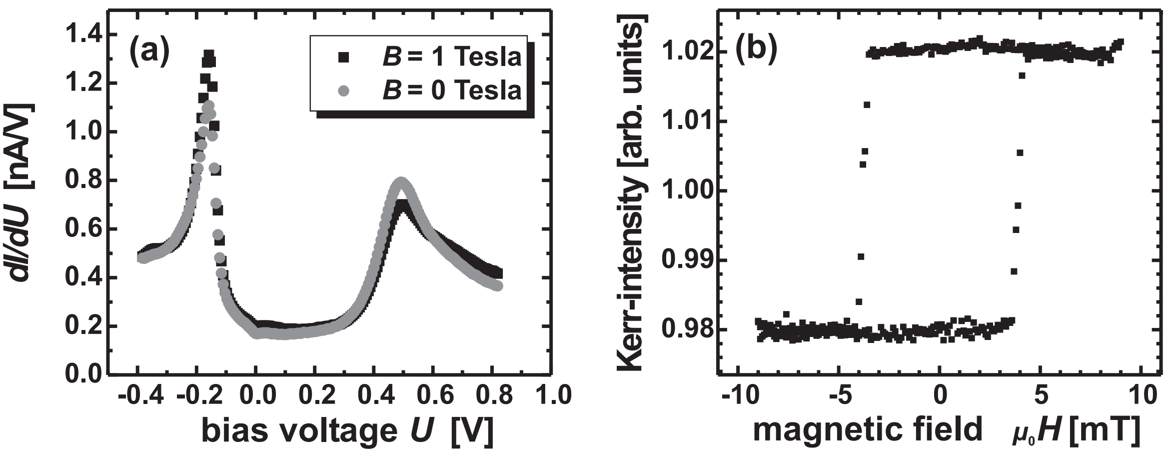

Figure 3.135: **(a)** Impact of an external magnetic field of $B = 1$ Tesla on the spin split surface state of 50 ML Gd(0001)/W(110) as measured with a Fe covered tungsten tip (Black squares: field applied; grey circles: no field applied). **(b)** Kerr-loops measured *in-situ* on a 50 ML Gd(0001)/W(110) film.

$B = 1$ Tesla applied perpendicular to the sample surface, whereas grey circles show the spectrum with no external field applied, i.e. in remanence. Both spectra were measured at exactly the same sample location. The well known spin split Gd surface state is clearly resolved. [16–18] By comparing the two spectra one can see the impact of the applied external magnetic field which forces the magnetization of tip and sample into a parallel configuration. The intensity of the occupied part of the surface state at a binding energy $E_{\text{bin}} = -160$ meV is enhanced by 22 percent at the expense of the unoccupied part, energetically located at a binding energy $E_{\text{bin}} = +500$ meV which is damped by 12.5 percent. There is no energy shift of the peaks due to the magnetic field.

By rotating the sample by 90° [cf. Fig 3.132] Kerr effect measurements can be carried out in the transverse geometry. Fig. 3.135(b) shows results measured *in-situ* on an identically prepared 50 ML Gd thin film. The obtained easy axis Kerr-loop confirms the in-plane anisotropy of the film at the chosen coverage.

References

[1] O. Pietzsch, A. Kubetzka, D. Haude, M. Bode, and R. Wiesendanger, Rev. Sci. Instrum. **71**, 424 (2000).

[2] Omicron Multiprobe *MX*.

[3] Omicron Variable Temperature STM.

[4] Oxford Instruments, Cambridge CB4 4WZ, United Kingdom.

[5] Ceramic Products, Palisades Park, NJ 07650, USA.

[6] S.H. Pan, S. Behler, M. Bernasconi, and H.-J. Güntherodt, Bull. Am. Phys. Soc. **37**, 167 (1992).

[7] Ch. Witt, U. Mick, M. Bode, and R. Wiesendanger, Rev. Sci. Instrum. **68**, 1455 (1997).

[8] M. Bode, M. Hennefarth, D. Haude, M. Getzlaff, and R. Wiesendanger, Surf. Sci. **432**, 8 (1999).

[9] Staveley Sensors, East Hartford, CT 06108, USA.

[10] Ch. Wittneven, R. Dombrowski, S.H. Pan, and R. Wiesendanger, Rev. Sci. Instrum. **68**, 3806 (1997).

[11] S.H. Pan, E.W. Hudson, and J.C. Davis, Rev. Sci. Instrum. **70**, 1459 (1999).

[12] W. Allers, A. Schwarz, U.D. Schwarz, and R. Wiesendanger, Rev. Sci. Instrum. **69**, 221 (1998).

[13] Lakeshore Cryotronics, Westerville, OH 43081, USA.

[14] A. Kubetzka, Diploma thesis, University of Hamburg, Germany (1999).

[15] Vacuum Generators, Hastings, E Sussex, England.

[16] M. Bode, M. Getzlaff, and R. Wiesendanger, Phys. Rev. Lett. **81**, 4256 (1998).

[17] M. Getzlaff, M. Bode, S. Heinze, R. Pascal, and R. Wiesendanger, J. Magn. Magn. Mat. **184**, 155 (1998).

[18] R. Wiesendanger, M. Bode, and M. Getzlaff, Appl. Phys. Lett. **75**, 124 (1999).

Chapter 4

Collaborations

4.1 Research Partners

- Institute of Applied Physics and MARCH, University of Hamburg:
  Prof. R. Anton, Prof. W. Hansen, Prof. D. Heitmann, Prof. J. Kötzler, Prof. U. Merkt, Prof. H. P. Oepen, Dr. D. Grundler, Dr. T. Matsuyama, Dr. I. Meinel, Dr. Chr. Steinebach

- HASYLAB at DESY, Hamburg:
  Prof. R. L. Johnson, Prof. G. Materlik

- Institute for Laser Physics, University of Hamburg:
  Prof. G. Huber

- I. Institute for Theoretical Physics, University of Hamburg:
  Prof. D. Pfannkuche

- Institute for Inorganic and Applied Chemistry, University of Hamburg:
  Prof. D. Rehder

- Institute for Physical Chemistry, University of Hamburg:
  Prof. H. Weller, Prof. S. Förster

- Cognitive Systems Research Group, Computer Science, University of Hamburg:
  Prof. H. S. Stiehl

- Beiersdorf AG, Hamburg:
  Dr. U. Hintze, Dr. R. Wepf

- Forschungszentrum Jülich, University of Osnabrück:
  Prof. S. Blügel

- University of Mainz:
  Prof. H. J. Elmers, Prof. G. Schönhense

- University of Göttingen:
  Prof. R. Kirchheim, Dr. A. Pundt
- University of Rostock:
  Prof. K.H. Meiwes-Broer, Dr. J. Bansmann
- University of Kiel:
  Prof. M. Skibowski, Dr. L. Kipp
- University of Bonn:
  Prof. K. Wandelt
- University of Munich:
  Prof. H. Gaub, Prof. W. Heckl
- University of Münster:
  Prof. H. Fuchs, Dr. B. Gotsmann
- University of Bielefeld:
  Prof. G. Reiss
- University of Saarbrücken:
  Prof. U. Hartmann
- TU Chemnitz:
  Dr. R.A. Römer
- Siemens, Erlangen:
  Dr. J. Wecker
- PTB Braunschweig:
  Dr. M. Albrecht
- IMEC, Leuven, Belgium:
  Prof. W. Vandervorst
- TU Delft, The Netherlands:
  Prof. C. Dekker, Dr. S. Lemay
- Institute of Physics, Poznan University of Technology, Poland:
  Prof. B. Susla, Dr. R. Czajka
- Institute of Physics, Polish Academy of Sciences, Warsaw, Poland:
  Prof. J. Rauluszkiewicz
- Kazan Physical Technical Institute of Russian Academy of Sciences, Kazan, Russia: Prof. A. A. Bukharaev, Dr. D. V. Ovchinnikov

- Ukrainian Academy of Sciences, Kiev, Ukraine:
  Prof. S. Nepijko
- University of Reijkjavik, Iceland:
  Prof. V. Gudmundsson
- University College London, U.K.:
  Prof. A. Shluger
- Ben-Gurion University of the Negev, Israel:
  Prof. Y. Manassen
- Seoul National University, South Korea:
  Prof. Z. G. Khim, U. H. Pi
- Graduate School of Engineering, Tohoku University, Japan:
  Prof. T. Miyazaki, Dr. N. Tezuka

4.2 Industrial Partners

- Beiersdorf, Hamburg
- Digital Instruments, Mannheim
- Exabyte Magnetics, Nürnberg
- Focus, Hünstetten–Görsroth
- GST mbH, Mainz
- IBM Deutschland Speichersysteme, Mainz
- Nanosensors, Aidlingen
- OMICRON Vakuumphysik, Taunusstein
- Oxford Instruments, Cambridge
- Siemens, Erlangen
- Infineon Technologies, München
- Surface Imaging Systems, Herzogenrath

Chapter 5

Theses

5.1 Diploma Theses

1. André Kubetzka (1999):
   Optimierung eines Rastertunnelmikroskops für die Durchführung spinpolarisierter Rastertunnelspektroskopie

2. Johannes Isenbart (1999):
   Simulationen zur Rasterkapazitätsmikroskopie

3. Volker Hagen (1999):
   Entwicklung eines Tieftemperatur-Kapazitätssensors und zweidimensionale Dotierprofilanalyse von Halbleitermikrostrukturen

4. Jan Peter Podsiadly (1999):
   Aufbau eines Systems zur Messung des magneto-optischen Kerr-Effektes an dünnen Schichten

5. Robert Ravlić (1999):
   Herstellung von mikrostrukturierten ferromagnetischen Filmen und Untersuchung mittels Magnetkraftmikroskopie

6. Marcus Liebmann (2000):
   Aufbau und Charakterisierung eines Rasterkraftmikroskops für den Einsatz im Ultrahochvakuum, bei tiefen Temperaturen und im Magnetfeld

7. Christian Meyer (2000):
   Untersuchung des Wachstums von Niob auf InAs(110) mittels Rastertunnelmikroskopie

8. Leif Busse (2000):
   Rastertunnel-Mikroskopie und -Spektroskopie an binären Schichten aus Eisen und Gadolinium auf W(110)

9. Oliver Krause (2000):
   Simulationen zur Bestimmung von 2D-Dotierprofilen mittels Rasterkapazitätsmikroskopie
10. Carsten Bartsch (2000):
    Rastersondenmikroskopie an ligandenstabilisierten Metallclustern
11. Theophilos Maltezopoulos (2000):
    Deposition von ligandenstabilisierten InAs-Clustern auf HOPG
12. Tobias Richter (2000):
    Quellverhalten von menschlichen Corneozyten in verschiedenen Medien
13. Richard Werner (2000):
    Präparation von T4-Bakteriophagen und Aufbau einer neuen Rastereinheit zu deren Untersuchung mittels Nicht-Kontakt-Rasterkraftmikroskopie
14. Anja Wehner (2001):
    Bestimmung der Gleichstromstärke in integrierten Schaltungen mittels Magnetkraftmikroskopie
15. Georg Greve (2001):
    Systematische Problemanalyse der Bildgebung in der Rastersondenmikroskopie (SXM) und anwendungsorientierte Analyse der Anforderungen an die digitale Verarbeitung von SXM-Bildern
16. Lutz Tröger (2001):
    Aufbau eines Tieftemperatur-Rasterkraftmikroskops
17. Christian-Dennis Rahn (2001):
    Experimentelle Analyse der Eignung problemorientierter Verarbeitungsmethoden für SXM-Bilder

5.2 Ph. D. Theses

1. René Pascal (1999):
   Rastertunnelmikroskopie und Rastertunnelspektroskopie an dünnen Filmen der Seltenerdmetalle Gd und Tb sowie GdFe2 Legierungen
2. Michael Dreyer (1999):
   Untersuchungen ultradünner Kobaltfilme mittels Magnetkraftmikroskopie im Ultrahochvakuum
3. Hendrik Hölscher (1999):
   Kontrastmechanismen in der Rasterkraftmikroskopie

4. Axel Born (2000):
   Nanotechnologische Anwendungen der Rasterkapazitätsmikroskopie und verwandter Rastersondenmethoden

5. Stefan Heinze (2000):
   First-Principles Theory of Scanning Tunneling Microscopy Applied to Transition-Metal Surfaces

6. Alexander Kelch (2000):
   Nahfeldoptische Untersuchungen an biologischen Systemen im ultravioletten und sichtbaren Wellenlängenbereich

7. Michael Kleiber (2000):
   Untersuchung ultradünner magnetischer Filme mittels Magnetkraftmikroskopie und spinpolarisierter Rastertunnelmikroskopie im Ultrahochvakuum

8. Jens Müller (2000):
   Kryo-Rasterkraftmikroskopie an biologischen Systemen

9. Christoph Zarnitz (2000):
   Rastertunnelmikroskopie und -spektroskopie von Fe- und Gd-Clustern sowie GdFe2-Mischfilmen

10. Daniel Haude (2001):
    Rastertunnelspektroskopie auf der InAs(110)-Oberfläche: Untersuchungen an drei-, zwei- und nulldimensionalen Elektronensystemen im Magnetfeld

11. Oswald Pietzsch (2001):
    Magnetic imaging by spin-polarized scanning tunneling spectroscopoy applied to ultrathin Fe/W(110) films

5.3 Habilitation Theses

1. Udo Schwarz (1999):
   Nanomechanics – Nanomechanical Investigations with the Scanning Force Microscope

2. Mathias Getzlaff (2000):
   Surface Magnetism – From the Spin Resolved Band Structure to the Imaging of Magnetic Domains on the Nanometer Scale

Chapter 6

Scientific Publications

6.1 Books

1. U.D. Schwarz, H. Hölscher, and R. Wiesendanger (eds.), Proc. 3rd International Conference on Non-Contact Atomic Force Spectroscopy, Springer 2001
2. M. Getzlaff, M. Morgenstern, and R. Wiesendanger (eds.), Proc. 2nd International Conference on Scanning Probe Spectroscopy, Springer 2001

6.2 Book Contributions and Review Articles

1. R. Wiesendanger, M. Bode, and M. Getzlaff, J. Magn. Soc. Jpn. **23** (S1), 195 (1999): *Recent advances in spin-polarized scanning tunneling spectroscopy for imaging of magnetic domains.*
2. A. Born and R. Wiesendanger, Appl. Phys. A **68**, 131 (1999): *Present and future developments of SPM systems as mass storage devices.*
3. M. Bode, M. Dreyer, M. Getzlaff, M. Kleiber, A. Wadas, and R. Wiesendanger, Journ. Phys.: Cond. Matter **11**, 9387 (1999): *Recent progress in high-resolution magnetic imaging using scanning probe techniques.*
4. R. Wiesendanger, Current Opinion in Solid State & Materials Science **4**, 435 (1999): *Surface magnetism at the nanometer and atomic scale.*
5. M. Getzlaff, M. Bode and R. Wiesendanger, Physik in unserer Zeit **31**, 110 (2000): *Nanomagnetische Domänen mit dem Rastertunnelmikroskop.*
6. R. Wiesendanger, in: Encyclopedia of Analytical Chemistry, eds. R.A. Meyers et al., John Wiley & Sons Ltd, Chichester (2000), 9232: *Proximal Probe Techniques.*
7. A. Born and R. Wiesendanger, Proc. ISTFA 2000, Bellevue/Washington, p. 521: *Guidelines for two-dimensional dopant profiling using SCM.*

8. A. Born, Encyclopedia of Analytical Chemistry: Instrumentation and Application, R. A. Meyers (Hrsg.), Wiley, Chichester (2000): *Industrial Application of Scanning Probe Microscopy.*

9. A. Born and R. Wiesendanger, Bericht zum 152. PTB-Seminar, M. Albrecht (Hrsg.), Braunschweig (2000): *Rastersondenmethoden und Datenspeichertechnik.*

10. W. Allers, A. Schwarz, H. Hölscher, U. D. Schwarz, and R. Wiesendanger, Jpn. J. Appl. Phys. **39**, 3701 (2000): *Dynamic Scanning Force Microscopy at Low Temperatures.*

11. M. Morgenstern, D. Haude, V. Gudmundsson, Chr. Wittneven, R. Dombrowski, Chr. Steinebach, and R. Wiesendanger, J. Electr. Spectr. Rel. Phen. **109**, 127 (2000): *Low Temperature Scanning Tunneling Spectroscopy on InAs(110).*

12. R. Wiesendanger, Ann. Phys. **9**, 895 (2000): *Nano-scale studies of quantum phenomena by scanning probe spectroscopy.*

13. U. D. Schwarz, H. Hölscher, W. Allers, A. Schwarz, and R. Wiesendanger, In: Fundamentals of Tribology and bridging the gap between macro- and micro/nanoscale tribology, B. Bushan (ed.), NATO ASI Series E: Appl. Phys., Kluwer Academic Publishers, Dordrecht, The Netherlands (2001): *Investigation of the mechanics of Nanocontacts using a vibrating cantilever technique.*

14. U. D. Schwarz and H. Hölscher, In: CRC Handbook of Modern Tribology, 1st edition, CRC Press, Inc., Boca Raton, FL. (appears 2001): *Atomic-scale friction studies using scanning force microscopy.*

15. K. Schoepe and R. Wiesendanger, in: ... und Er würfelt doch!, eds. H. Müller-Krumbhaar, H.F. Wagner, Wiley-VCH, Berlin (2001), p.521: *Faszinierende Einblicke in den Nanokosmos.*

16. R. Wiesendanger and M. Bode, in: Spin Effects in Mesoscopic Systems, eds. E. Molinari, V. Pellegrini, and A. Pinczuk, Special Issue of Sol. State Commun. Vol. 119 (2001), p.341: *Nano- and atomic-scale magnetism studied by spin-polarized scanning tunneling microscopy and spectroscopy.*

17. M. Getzlaff, Appl. Phys. A **72**, 455 (2001): *Surface magnetism: from the spin resolved density of states to magnetic domain imaging on the nanometer scale.*

6.3 Original Articles

1. M. Getzlaff, M. Bode, R. Pascal, and R. Wiesendanger, Phys. Rev. B **59**, 8195 (1999): *Adsorbates on Gd (0001) - a combined STM/UPS study.*

2. M. Getzlaff, M. Bode, R. Pascal, and R. Wiesendanger, Appl. Surf. Sci. **142**, 63 (1999): *The adsorption process of hydrogen on Gd (0001).*
3. M. Getzlaff, M. Bode, and R. Wiesendanger, Appl. Surf. Sci. **142**, 428 (1999): *Coadsorption of H and CO on Gd (0001).*
4. M. Getzlaff, R. Pascal, H. Tödter, M. Bode, and R. Wiesendanger, Appl. Surf. Sci. **142**, 543 (1999): *$GdFe_2$ alloy formation observed by STM.*
5. M. Getzlaff, M. Bode, S. Heinze, and R. Wiesendanger, Appl. Surf. Sci. **142**, 558 (1999): *New insight into the surface magnetic properties of Gd(0001).*
6. M. Bode, M. Hennefarth, D. Haude, M. Getzlaff, and R. Wiesendanger, Surf. Sci. **432**, 8 (1999): *Growth of thin Mn-films on W(110) studied by means of in-situ scanning tunneling microscopy.*
7. M. Bode, M. Getzlaff, and R. Wiesendanger, J. Vac. Sci. Technol. A. **17**, 2228 (1999): *Quantitative aspects of spin-polarized scanning tunneling spectroscopy of Gd(0001).*
8. R. Wiesendanger, M. Bode, and M. Getzlaff, Appl. Phys. Lett. **75**, 124 (1999): *Vacuum-tunneling magnetoresistance: the role of spin-polarized surface states.*
9. M. Getzlaff, R. Pascal, H. Tödter, M. Bode, and R. Wiesendanger, Surf. Rev. Lett. **6**, 741 (1999): *Preparation of highly ordered $GdFe_2$ alloys.*
10. M. Getzlaff, M. Bode, and R. Wiesendanger, Surf. Rev. Lett. **6**, 591 (1999): *Spin polarized vacuum tunneling: correlation of electronic and megnetic properties on the nanometer scale.*
11. S. Heinze, X. Nie, S. Blügel, and M. Weinert, Chem. Phys. Lett. **315**, 167 (1999): *Electric-field induced changes in STM images of metal surfaces.*
12. S. Heinze, R. Abt, S. Blügel, G. Gilarowski, and H. Niehus, Phys. Rev. Lett. **83**, 4808 (1999): *STM-Images of transition-metal structures buried below noble-metal surfaces.*
13. M. Dreyer, M. Kleiber and R. Wiesendanger, Appl. Phys. A **69**, 359 (1999): *Simultaneous observation of atomic step and domain wall structure of ultrathin Co films by magnetic force microscopy.*
14. H. Hölscher, W. Raberg, U. D. Schwarz, A. Hasbach, K. Wandelt, and R. Wiesendanger, Phys. Rev. B **59**, 1661 (1999): *Imaging of sub-unit-cell structures in the contact mode of the scanning force microscope.*
15. W. Allers, A. Schwarz, U. D. Schwarz, and R. Wiesendanger, Appl. Surf. Sci. **140**, 247 (1999): *Dynamic scanning force microscopy at low temperatures on a van der Waals surface: graphite(0001).*

16. H. Hölscher, U. D. Schwarz, and R. Wiesendanger, Appl. Surf. Sci. **140**, 344 (1999): *Calculation of the frequency shift in dynamic scanning force microscopy.*

17. A. Schwarz, W. Allers, U. D. Schwarz, and R. Wiesendanger, Appl. Surf. Sci. **140**, 293 (1999): *Simultaneous imaging of the In and As sublattice on InAs(110)-(1x1) with dynamic scanning force microscopy.*

18. W. Allers, A. Schwarz, U. D. Schwarz, and R. Wiesendanger, Europhys. Lett. **48**, 276 (1999): *Dynamic scanning force microscopy at low temperatures on a noble gas crystal: Atomic resolution on the xenon(111) surface.*

19. A. Born, M. Kleiber, G. Meier, D. Heitmann, and R. Wiesendanger, Werkstoffe für die Informationstechnik, K. Kempter und J. Haußelt (Hrsg.), 155, Wiley-VCH, Weinheim (1999): *Nanostrukturierung und Charakterisierung von magnetischen Materialien.*

20. T. Asada, G. Bihlmayer, S. Handschuh, S. Heinze, Ph. Kurz, and S. Blügel, Journal of Physics (Cond. Mat.) **11**, 9347 (1999): *First-principles theory of ultra-thin magnetic films.*

21. M. Dreyer, M. Kleiber, A. Wadas, and R. Wiesendanger, Phys. Rev. B **59**, 4273 (1999): *Composition driven change of magnetic anisotropy of ultrathin Co/Au (111) films studied by magnetic force microscopy under ultrahigh vacuum.*

22. R. Dombrowski, Chr. Steinebach, Chr. Wittneven, M. Morgenstern, and R. Wiesendanger, Phys. Rev. B **59**, 8043 (1999): *Determining the tip induced band bending by scanning tunneling spectroscopy of the states of the tip induced quantum dot on InAs(110).*

23. R. Pascal, M. Getzlaff, H. Tödter, M. Bode, and R. Wiesendanger, Phys. Rev. B **60**, 16109 (1999): *GdFe2 alloy formation studied on the atomic scale by scanning tunneling microscopy.*

24. M. Bode, M. Getzlaff, A. Kubetzka, R. Pascal, O. Pietzsch, and R. Wiesendanger, Phys. Rev. Lett. **83** , 3017 (1999): *Temperature-dependent exchange splitting of a surface state on a local-moment magnet: Tb(0001).*

25. S. A. Nepijko and R. Wiesendanger, Semiconductor Physics (Quantum Electronics and Optoelectronics) **2**, 5 (1999): *Size dependence of magnetic characteristics measured on separate nickel particles.*

26. H. Hölscher, W. Allers, U. D. Schwarz, A. Schwarz, and R. Wiesendanger, Phys. Rev. Lett. **83**, 4780 (1999): *Determination of tip-sample interaction potentials by dynamic force spectroscopy.*

27. J. Bansmann, L. Lu, V. Senz, A. Bettac, M. Getzlaff, and K.H. Meiwes-Broer, Eur. Phys. J. D. **9**, 461 (1999): *Structure and magnetism of self-organized Co islands.*

28. M. Getzlaff, M. Morgenstern, R.L. Johnson, and R. Wiesendanger, HASYLAB annual report 1999, p. 251: *Dispersion behavior of a two-dimensional electron gas.*

29. M. Getzlaff, J. Bansmann, and G. Schönhense, J. Magn. Magn. Mater. **192**, 458 (1999): *Oxygen on Fe(110): Magnetic properties of the adsorbate system.*

30. O. Pietzsch, A. Kubetzka, M. Bode, and R. Wiesendanger, Rev. Sci. Instr. **71**, 424 (2000): *A Low-Temperature UHV Scanning Tunneling Microscope with a Split-Coil Magnet and a Rotary Motion Stepper Motor for High Spatial Resolution Studies of Surface Magnetism.*

31. O. Pietzsch, A. Kubetzka, M. Bode, and R. Wiesendanger, Phys. Rev. Lett. **84**, 5212 (2000): *Real-Space Observation of Dipolar Antiferromagnetism in Magnetic Nanowires by Spin-Polarized Scanning Tunneling Spectroscopy.*

32. S.Heinze, M.Bode, A.Kubetzka, O.Pietzsch, X.Nie, S.Blügel, and R.Wiesendanger, Science **288**, 1805 (2000): *Real-Space Imaging of Two-Dimensional Antiferromagnetism on the Atomic Scale.*

33. D. Wortmann, S. Heinze, G. Bihlmayer, and S. Blügel, Phys. Rev. B **62**, 2862 (2000): *Interpreting STM-Images of the MnCu/Cu(100) Surface Alloy.*

34. N. Papanikolaou, B. Nonas, S. Heinze, R. Zeller, and P. H. Dederichs, Phys. Rev. B **62**, 11118 (2000): *Scanning tunneling spectra of impurities in the Fe(001) surface.*

35. S.A.Nepijko, M.Getzlaff, R.Pascal, Ch.Zarnitz, M.Bode and R.Wiesendanger, Surf. Sci. **466**, 89 (2000): *Lattice relaxation of Gd on W(110).*

36. M. Morgenstern, M. Getzlaff, D. Haude, R.L. Johnson, and R. Wiesendanger, Phys. Rev. B **61**, 13805 (2000): *Coverage dependence of the Fe-induced Fermi level shift and the two dimensional electron gas on InAs(110).*

37. J. Bansmann, L. Lu, M. Getzlaff, M. Fluchtmann, and J. Braun, Surf. Sci. **454**, 686 (2000): *Epitaxial cobalt films on W(110) an experimental and theoretical photoemission study with polarized synchrotron radiation.*

38. M. Getzlaff, C. Westphal, J. Bansmann, and G. Schönhense, J. Electr. Spectr. Relat. Phen. **107**, 293 (2000): *Chalcogen adsorption and surface magnetism.*

39. M. Morgenstern, M. Getzlaff, J. Klijn, Ch. Meyer, A. Wachowiak, J. Wiebe, L. Plucinski, R.L. Johnson, R. Adelung, K. Roßnagel, and R. Wiesendanger, HASYLAB annual report 2000, p. 297: *Photoemission on two-dimensional electron systems.*

40. A. Schwarz, W. Allers, U.D. Schwarz, and R. Wiesendanger, Phys. Rev. B **61**, 2837 (2000): *Dynamic mode scanning force microscopy study of n-InAs(110)-(1x1) at low temperatures.*

41. A. Pundt, M. Getzlaff, M. Bode, R. Kirchheim, and R. Wiesendanger, Phys. Rev. B **61**, 9964 (2000): *H-induced plastic deformation of Gd thin films studied by STM.*

42. H. Hölscher, A. Schwarz, W. Allers, U. D. Schwarz, and R. Wiesendanger, Phys. Rev. B **61**, 12678 (2000): *Quantitative Analysis of Dynamic-Force-Spectroscopy Data on Graphite (0001) in the Contact and Noncontact Regimes.*

43. M. Getzlaff and R. Wiesendanger, European Microscopy and Analysis **68**, 7 (2000): *STM Study of Hydrogen on and in Gadolinium Films.*

44. M. Morgenstern, Chr. Wittneven, R. Dombrowski, and R. Wiesendanger, Phys. Rev. Lett. **84**, 5588 (2000): *Spatial fluctuations of the density of states in magnetic fields observed with scanning tunneling spectroscopy.*

45. H. Hölscher, W. Allers, A. Schwarz, U. Schwarz, and R. Wiesendanger, Phys. Rev. B **62**, 6967 (2000): *Interpretation of 'true atomic resolution' images of graphite(0001) in non-contact atomic force microscopy.*

46. M. Kleiber, M. Bode, R. Ravlic, and R. Wiesendanger, Phys. Rev. Lett. **85**, 4606 (2000): *Topology-induced spin frustrations at the Cr(001) surface studied by spin-polarized scanning tunneling spectroscopy.*

47. A. Schwarz, W. Allers, U. D. Schwarz, and R. Wiesendanger, Phys. Rev. B **62**, 13617 (2000): *Detection of doping atom distributions and individual dopants in InAs(110) by dynamic mode scanning force microscopy in ultrahigh vacuum.*

48. U.D. Schwarz, H. Hölscher, and R. Wiesendanger, Phys. Rev. B **62**, 13089 (2000): *Atomic resolution in scanning force microscopy: Concepts, requirements, contrast mechanisms, and image interpretation.*

49. M. Morgenstern, D. Haude, V. Gudmundsson, Chr. Wittneven, R. Dombrowski, and R. Wiesendanger, Phys. Rev. B **62**, 7257 (2000): *Origin of Landau oscillations observed in scanning tunneling spectroscopy on n-InAs(110).*

50. A. Kelch, S. Wessel, T. Will, U. Hintze, R. Wepf, and R. Wiesendanger, J. Microsc. **200**, 179 (2000): *Penetration pathways of fluorescent dyes in human hairfibres investigated by scanning near-field optical microscopy.*

51. A. Pundt, U. Laudahn, U. v. Hülsen, U. Geyer, T. Wagner, M. Getzlaff, M. Bode, R. Wiesendanger, and R. Kirchheim, Mat. Res. Soc. Symp. Proc. **594**, 75 (2000): *Hydrogen induced plastic deformation of thin films.*

52. H. Hölscher, W. Allers, U. D. Schwarz, A. Schwarz, and R. Wiesendanger, Appl. Phys. A **72**, S35 (2001): *Simulation of Non-contact atomic force microscopy images of Xenon(111).*

53. T. Richter, J. Müller, U. D. Schwarz, R. Wepf, and R. Wiesendanger, Appl. Phys. A **72**, S125 (2001): *Investigation of the swelling of human skin cells in liquid media by tapping mode scanning force microscopy.*

54. M. Bode, O. Pietzsch, A. Kubetzka, and R. Wiesendanger, J. Electr. Spectr. Relat. Phenom. **114**, 1055 (2001): *Imaging Magnetic Nanostructures by Spin-Polarized Scanning Tunneling Spectroscopy.*

55. A. Kubetzka, O. Pietzsch, M. Bode, and R. Wiesendanger, Phys. Rev. B **63**, 140407 (2001): *Magnetism of nanoscale Fe islands studied by spin-polarized scanning tunneling spectroscopy.*

56. M. Bode, O. Pietzsch, A. Kubetzka, S. Heinze, and R. Wiesendanger, Phys. Rev. Lett. **86**, 2142 (2001): *Experimental Evidence for Intra-Atomic Non-Collinear Magnetism at Thin Film Probe Tips.*

57. D. Haude, M. Morgenstern, I. Meinel, and R. Wiesendanger, Phys. Rev. Lett. **86**, 1582 (2001): *Local Density of States of a Three-Dimensional Conductor in the Extreme Quantum Limit.*

58. M. Getzlaff, M. Morgenstern, Chr. Meyer, R. Brochier, R.L. Johnson, and R. Wiesendanger, Phys. Rev. B **63**, 205305 (2001): *Nb-induced two-dimensional electron gas on n-InAs (100):Anomalous coverage dependence.*

59. M. Morgenstern, V. Gudmundsson, R. Dombrowski, Chr. Wittneven, and R. Wiesendanger, Phys. Rev. B **63**, 201301 (2001): *Nonlocality of the exchange interaction probed by scanning tunneling spectroscopy.*

60. W. Allers, S. Langkat, and R. Wiesendanger, Appl. Phys. A **72**, S27 (2001): *Low-temperature dynamic force microscopy on nickel oxide(001).*

61. M. Bode, O. Pietzsch, A. Kubetzka, and R. Wiesendanger, Appl. Phys. A **72**, S149 (2001): *Spin-polarized scanning tunneling spectroscopy on Fe-nanowires.*

62. J. Isenbart, A. Born, and R. Wiesendanger, Appl. Phys. A **72**, S243 (2001): *Physical Principles of Scanning Capacitance Microscopy.*

63. M. Getzlaff, M. Bode, A. Kubetzka, O. Pietzsch, and R. Wiesendanger, Chin. Phys. **10**, S186 (2001): *Spin-dependent tunneling effects on magnetic nanostructures.*

64. O. Pietzsch, A. Kubetzka, M. Bode, and R. Wiesendanger, Science **292**, 2053 (2001): *Observation of Magnetic Hysteresis at the Nano-Scale by Spin Polarized Scanning Tunneling Spectroscopy.*

65. H. Hölscher, B. Gotsmann, W. Allers, U. D. Schwarz, H. Fuchs, and R. Wiesendanger, Phys. Rev. B **64**, 075402 (2001): *Measurement of conservative and dissipative tip-sample interaction forces with a dynamic force microscope using the frequency modulation technique.*

66. M. Pratzer, H.J. Elmers, M. Bode, O. Pietzsch, A. Kubetzka, and R. Wiesendanger, Phys. Rev. Lett. **87**, 127201 (2001): *Atomic-scale magnetic domain walls in quasi-one-dimensional Fe nanostripes.*

67. G. Kuri, G. Materlik, V. Hagen, and R. Wiesendanger, Appl. Phys. A **73**, 265 (2001): *Surface morphology of MgO(100) crystals implanted with MeV.*

68. M. Morgenstern, D. Haude, Chr. Meyer, and R. Wiesendanger, Phys. Rev. B **64**, 205104 (2001): *Experimental evidence for edge-like states in three-dimensional electron systems.*

69. H. Hölscher, B. Gotsmann, W. Allers, U.D. Schwarz, H. Fuchs, and R. Wiesendanger, Phys. Rev. Lett. (in press): *Comment on ”Damping mechanism in dynamic force microscopy”.*

70. M. Kleiber, M. Bode, R. Ravlic, N. Tezuka, and R. Wiesendanger, J. Magn. Magn. Mater. (in press): *Magnetic properties of the Cr(001) surface studied by spin-polarized scanning tunneling spectroscopy.*

71. A. Kubetzka, M. Bode, O. Pietzsch, and R. Wiesendanger, Phys. Rev. Lett. (in press): *Spin-polarized Scanning Tunneling Microscopy with Antiferromagnetic Probe Tips.*

Chapter 7

Talks

7.1 Invited Talks

13.01.99: R. Wiesendanger, Monterey, USA (MORIS'99): *Recent Advances in Spin-Polarized Scanning Tunneling Spectroscopy for Imaging of Magnetic Domains.*

23.03.99: U. D. Schwarz, Frühjahrstagung der Deutschen Physikalischen Gesellschaft, Münster, Germany: *Reibung auf der Nanometerskala - Nanotribologie mit dem Rasterkraftmikroskop.*

24.03.99: R. Wiesendanger, Atlanta, USA (APS Centennial Meeting): *Spin Polarized Scanning Tunneling Spectroscopy with Magnetic Probe Tips.*

25.03.99: M. Bode, M. Getzlaff, and R. Wiesendanger, Frühjahrstagung der Deutschen Physikalischen Gesellschaft, Münster, Germany: *Spinpolarisiertes Vakuumtunneln in den Oberflächenzustand von Gd(0001).*

25.03.99: R. Wiesendanger, Atlanta, USA (APS Centennial Meeting): *Low-Temperature Scanning Tunneling Spectroscopy on n-InAs(110) at High Magnetic Fields: Landau Level Quantization and Scattering of Electron Waves at Dopant Atoms.*

19.07.99: M. Bode, M. Getzlaff, and R. Wiesendanger, 10th International Conference on Scanning Tunneling Microscopy/Spectroscopy and Related Techniques, Seoul (South Korea): *Spin-polarized vacuum tunneling into the exchange-split surface state of Gd(0001).*

21.07.99: M. Getzlaff, Cortona, Italy: (1st IUVSTA *Summer School on Quantum Devices and Nanostructures): STM / AFM of magnetic structures.*

27.09.99: R. Wiesendanger, Chemnitz, Germany (WE-Heraeus-Ferienkurs "Moderne Fernfeld- und Nahfeld-Mikroskopien"): *Raster-Tunnel-Mikroskopie: Grundlagen und Anwendungen.*

28.09.99: M. Getzlaff, Workshop "Cluster 1999", Sassnitz, Germany: *Spinpolarisiertes Vakuumtunneln: strukturelle, elektronische und magnetische Eigenschaften von Nanostrukturen.*

29.09.99: M. Getzlaff, Workshop "Magnetische Nanostrukturen: Physikalische Grundlagen und Anwendungen", Hamburg, Germany: *Bestimmung elektronischer und magnetischer Eigenschaften mittels spinauflösender Photoelektronenspektroskopie und spinpolarisierter Rastertunnelspektroskopie.*

07.10.99: R. Wiesendanger, Dresden, Germany (WE-Heraeus-Ferienkurs "Festkörperspektroskopie"): *Raster-Tunnel-Spektroskopie: Grundlagen und Anwendungen.*

22.10.99: R. Wiesendanger, Groningen, The Netherlands (Symposium "Magnetism at Surfaces and Interfaces"): *Spin-polarized vacuum tunneling spectroscopy: Correlation of structural, electronic, and magnetic properties of surfaces at the nanometer scale.*

28.10.99: R. Wiesendanger, Seattle, USA (AVS'99): *Spin-polarized scanning tunneling spectroscopy: Magnetic domain imaging and beyond.*

30.11.99: A. Pundt, U. Laudahn, U. v. Hülsen, U. Geyer, T. Wagner, M. Getzlaff, M. Bode, R. Wiesendanger, and R. Kirchheim, MRS-meeting (1999), Boston, USA: *Hydrogen induced plastic deformation of thin films.*

10.12.99: M. Morgenstern, Osaka, Japan (2nd Int. Symposium on Atomic Scale Processing and Novel Properties in Nanoscopic Materials): *Scanning Tunneling Spectroscopy at low temperatures and high magnetic fields: a nanoscale view to Landau oscillations, spin splittings and spin-polarized tunneling.*

11.12.99: W. Allers, A. Schwarz, H. Hölscher, U. D. Schwarz, and R. Wiesendanger, Seventh International Conference on Scanning Probe Methods (ICSPM-7), Atagawa, Shizouka, Japan: *Dynamic scanning force microscopy at low temperatures.*

23.02.00: A. Born and R. Wiesendanger, 152. PTB-Seminar: Technologien für Datenspeicher der Zukunft, Braunschweig, Germany: *Rastersondenmethoden und Datenspeichertechnik.*

08.03.00: R. Wiesendanger, Sendai, Japan (Int. Symp. on Nanoscale Magnetism and Transport): *A Nano- and Atomic-Scale View of Surface Magnetism by Spin-Polarized Scanning Tunneling Spectroscopy.*

14.03.00: R. Wiesendanger, Montreux, Switzerland (EPS-CMD18): *Scanning Tunneling Spectroscopy at Low Temperatures and High Magnetic Fields: a Nanoscale View of Landau Quantization, Spin Splittings and Spin-Polarized Tunneling Effects.*

27.03.00: U. D. Schwarz, Nancy, France, 7*th* International Symposium on Trends and Applications of Thin Films (TATF'2000): *Study of microfriction by AFM.*

28.03.00: M. Getzlaff, Frühjahrstagung der Deutschen Physikalischen Gesellschaft Regensburg 2000, Symposium Oberflächenmagnetismus: *Oberflächen-Magnetismus: Von der spinaufgelösten Zustandsdichte zur Abbildung magnetischer Domänen auf der nm-Skala.*

31.03.00: R. Wiesendanger, Namur, Belgium (IUVSTA Divisional Highlight Seminar): *Magnetic Nanostructures probed by Spin-Polarized Scanning Tunneling Spectroscopy.*

13.04.00: R. Wiesendanger, London, U.K. (UK SPM 2000 Meeting): *Low-Temperature Scanning Tunneling Spectroscopy of Electronic States at Semiconductor and Ferromagnet Surfaces in External Magnetic Fields.*

13.04.00: M. Bode, S. Heinze, A. Kubetzka, O. Pietzsch, X. Nie, S. Blügel, and R. Wiesendanger, International Symposium on Physical Properties of Structured Thin Metallic Films, FU Berlin, Germany: *Domain-Imaging of Nanostructured Magnetic Thin Films.*

13.05.00: M. Bode, S. Heinze, A. Kubetzka, O. Pietzsch, X. Nie, S. Blügel, and R. Wiesendanger, ESF Workshop on Magnetic Imaging of Nanostructures, Regensburg, Germany: *Imaging of Nanostructured Thin Films by Spin-Polarized STM.*

23.05.00: M. Getzlaff, Achema 2000, Frankfurt, Germany: *The scanning tunneling microscope as a nanoanalytical tool.*

22.06.00: M. Getzlaff, Ameland, The Netherlands: Summer School on Spectroscopies of inorganic, organic and biological material *STM and MFM of magnetic nanostructures.*

05.07.00: R. Wiesendanger, University of Konstanz, Germany (SFB-Workshop on Nanostructures at Surfaces and Interfaces): *Magnetic nanostructures at surfaces probed by spin-polarized scanning tunneling spectroscopy.*

20.07.00: M. Bode, S. Heinze, A. Kubetzka, O. Pietzsch, X. Nie, S. Blügel, and R. Wiesendanger, 2nd International Conference on Scanning Probe Spectroscopy, Hamburg, Germany: *Spin-polarized STM/STS on magnetic thin films.*

21.07.00: M. Morgenstern, Second International Conference on Scanning Probe Spectroscopy, Hamburg, Germany: *Scanning Tunneling Spectroscopy of Landau States.*

26.07.00: M. Bode, 4th International School on the Applications of Surface Science Techniques, Erice, Italy: *Nano-Scale Surface Magnetism Studied by Spin-Polarized STM.*

11.08.00: M. Bode, M. Getzlaff, S. Heinze, O. Pietzsch, A. Kubetzka, R. Ravlic, M. Kleiber, X. Nie, S. Blügel, and R. Wiesendanger, 8th International Conference on Electronic Spectroscopy, Berkeley, USA: *Atomic-scale magnetic imaging of ultrathin films by scanning tunneling microscopy and spectroscopy.*

19.08.00: U. D. Schwarz, H. Hölscher, W. Allers, A. Schwarz, and R. Wiesendanger, NATO-ASI-Workshop "Fundaments of and Bridging the Gap between Macro- and Micro/Nanoscale Tribology", Keszthely, Hungary: *Investigation of the mechanics of nanocontacts using a vibration cantilever technique.*

06.09.00: U. D. Schwarz, Jahrestreffen der Französischen Gesellschaft für Mikroskopie, Toulouse, France: *New applications of scanning force microscopy: From the microscopic origins of friction to high-resolution imaging and spectroscopy at low temperatures.*

14.09.00: R. Wiesendanger, Hamburg, Germany (MNU-Tag 2000): *Neue Einblicke in den Nanokosmos.*

26.09.00: R. Wiesendanger, Münster, Germany (SXM4): *Magnetic imaging at the atomic level.*

27.09.00: M. Getzlaff, Physik Event "ÖPG 2000", Graz, Austria: *Surface magnetism: from the spin resolved density of states to magnetic domain imaging on the nanometer scale.*

28.09.00: R. Wiesendanger, Paris, France (2nd LEEM/PEEM workshop): *Scanning Tunneling Microscopy (STM) and Spin-Resolved STM.*

27.10.00: M. Getzlaff, 2. Europäisches Rastersondenmikroskopie User Meeting 2000, Dresden, Germany: *Das UHV - STM: Möglichkeiten und Perspektiven der Korrelation von strukturellen, elektronischen und magnetischen Eigenschaften auf der nm-Skala.*

31.10.00: R. Wiesendanger, Berlin, Germany (Japanese-German Symposium on Strategies in Nanotechnology): *Nanoprobe Analysis in Physical Based Sciences.*

01.11.00: M. Getzlaff, Peking, China, Workshop "Characterization and Development of Nanosystems" (2000): *Spin dependent tunneling effects on magnetic nanostructures.*

09.11.00: H. Hölscher and U. D. Schwarz, Hückelhoven, Germany, European Symposium on Nanomechanical Testing: *Friction at the nanometer scale - nanotribology studied with the atomic force microscope.*

11.12.00: R. Wiesendanger, Berlin, Germany (Symposium on 100 Years of Quantum Theory): *Nano-Scale Studies of Quantum Phenomena by Scanning Probe Spectroscopy.*

14.12.00: R. Wiesendanger, Berlin, Germany (Public Lecture to the Year of Physics): *Neue faszinierende Einblicke in den Nanokosmos.*

19.12.00: M. Bode, S. Heinze, O. Pietzsch, A. Kubetzka, R. Ravlic, M. Kleiber, X. Nie, S. Bügel, and R. Wiesendanger, Condensed Matter & Materials Physics Conference 2000, Bristol (Great Britain): *Atomic Resolution Imaging of Surface Spin-Structures by Spin-Polarized Scanning Tunneling Microscopy.*

20.01.01: U. D. Schwarz, Uhldingen-Mühlhofen, Germany, Diskussionsworkshop über Reibung und Verschleiß: *Reibung auf der Nanometerskala - Nanotribologie mit dem Rasterkraftmikroskop.*

21.02.01: R. Wiesendanger, 158. PTB-Seminar: Technologien für Datenspeicher der Zukunft II, PTB Braunschweig, Germany: *Neue Entwicklungen auf dem Gebiet magnetischer Datenspeicher.*

01.03.01: R. Wiesendanger, DFG-Rundgespräch: Chemie und Physik an Grenzflächen, Bad Honnef, Germany: *Quantenphänomene auf der Nanometerskala: Neue Einblicke mittels Rastertunnelspektroskopie.*

27.03.01: M. Bode, O. Pietzsch, A. Kubetzka, S. Heinze, M. Kleiber, R. Ravlic, X. Nie, S. Blügel, and R. Wiesendanger, 65. Frühjahrstagung der Deutschen Physikalischen Gesellschaft, Hamburg, Germany: *Spin-polarisierte Rastertunnelmikroskopie.*

06.04.01: M. Getzlaff, 4th Workshop on Functional Materials, Synthesis and Characterization of Mesoscalic Systems, Geesthacht, Germany: *The interaction of hydrogen with Gd thin films.*

19.05.01: R. Wiesendanger, Sackler Colloquium of the National Academy of Sciences on "Nanoscience", Washington D. C., USA: *Nano-scale Studies of Quantum Phenomena by Scanning Probe Spectroscopy.*

25.06.01: R. Wiesendanger, Laserion-Workshop, Schloß Ringberg, Tegernsee, Germany: *Scanning Probe Based Science and Technology.*

11.07.01: R. Wiesendanger, European Summer School on Nanotechnology, University of Würzburg, Germany: *Scanning Probe Spectroscopy of Semiconductor Nanostructures.*

11.07.01: R. Wiesendanger, European Summer School on Nanotechnology, University of Würzburg, Germany: *Scanning Probe Spectroscopy of Magnetic Nanostructures.*

16.07.01: R. Wiesendanger, STM ‘01, Vancouver, Canada: *Nano-Scale Studies of Quantum Phanomena by Scanning Probe Spectroscopy.*

25.07.01: R. Wiesendanger, VUV XIII Congress, Trieste, Italy: *Spin-Resolved Spectro-Microscopy at the Atomic Level.*

09.08.01: R. Wiesendanger, ICAS 2001, Tokyo, Japan: *Contributions of Scanning Probe Spectroscopy to Analytical Sciences.*

02.09.01: A. Schwarz, U.D. Schwarz, S. Langkat, H. Hölscher, W. Allers, and R. Wiesendanger, 4th International Conference on Noncontact Atomic Force Microscopy, Kyoto, Japan: *Dynamic Force Microscopy and Spectroscopy at Low Temperatures.*

05.09.01: R. Wiesendanger, Sino-German Symposium on Micro Systems and Nano Technology, PTB Braunschweig, Germany: *Semiconductor and magnetic nanostructures.*

21.09.01: R. Wiesendanger, 3. Workshop on Quantum Hall Systems, Gedern, Germany: *Nano-Science: the Beauty of Being Small.*

17.10.01: M. Morgenstern, 3rd International Conference "Physics of Low Dimensional Structures", Chernogolovka, Russia: *Scanning Tunneling Spectroscopy of Dilute Electron Systems in different Dimensions.*

18.10.01: M. Bode, 3rd International Conference "Physics of Low-Dimensional Structures", Chernogolovka, Russia: *Imaging magnetic nanostructures by spin-polarized scanning tunneling microscopy.*

26.10.01: O. Pietzsch, European Science Foundation, Final Nanomag Meeting, Anglet, France: *Spin-Polarized Scanning Tunneling Microscopy in Applied Magnetic Fields.*

01.11.01: M. Bode, A. Kubetzka, O. Pietzsch, and R. Wiesendanger, 48th Intl. Symposium of the American Vacuum Society, San Francisco, USA: *Domain imaging of magnetic nanostructures by spin- polarized scanning tunneling microscopy.*

01.11.01: M. Morgenstern, V. Gudmundsson, and R. Wiesendanger, AVS, 48th International Symposium of the American Vacuum Society, San Francisco, USA: *Probing the Dependence of the Spin Splitting in Quantum Dots on Residual Disorder.*

09.11.01: R. Wiesendanger, Medienfestival "Bilder aus der Physik", Göttingen, Germany: *Das Unsichtbare wird sichtbar – Nutzung neuer Medien bei der Vermittlung nanotechnologischer Forschung.*

15.11.01: R. Wiesendanger, LVII Yamada Conference on Atomic-scale surface designing for functional low-dimensonal materials, Tsukuba, Japan: *Spin-resolved spectro-microscopy at the atomic level.*

05.12.01: M. Getzlaff, US/Germany Joint Meeting on Nanoscale Science and Engineering, Boston, USA: *Recent Highlights of Scanned Probe Based Research at the Nanoscale.*

11.12.01: M. Morgenstern, Scanning Probe Microscopy in Biology, Chemistry and Physics, SPM 2001, Santa Fé, USA: *Probing the local density of states of dilute electron systems in different dimensions.*

7.2 Conference Contributions and Talks at Other Institutes

7.2.1 Talks

04.01.99: S. Heinze and S. Blügel, 211. WE-Heraeus Seminar (Magnetic Nanostructures), Physikzentrum Bad Honnef, Germany: *Theorectical analysis of STM and STS of thin magnetic films.*

07.01.99: H. Hölscher, U. D. Schwarz, and R. Wiesendanger, University of Cologne, Germany (Seminar): *Reibung auf der Nanometerskala - Nanotribologie mit dem Rasterkraftmikroskop*

14.01.99: A. Born and R. Wiesendanger, Leoben, Austria: *Einsatz der Rastersondenmikroskopie in der Halbleiteranalytik.*

15.01.99: R. Wiesendanger, Berkeley, USA (Seminar): *From Micro- to Nanoelectronics: Novel Insight into the Microscopic Nature of Electronic States in Semiconductors and Ferromagnets.*

26.01.99: R. Wiesendanger, University of Hannover, Germany (Kolloquium): *Von der Mikroelektronik zur Nanoelektronik: Neue faszinierende Einblicke in das Mikroskopische Verhalten von Festkörperelektronen.*

02.02.99: M. Kleiber, International Symposium on Magnetic Nanostructures, Hamburg, Germany: *Magnetization switching of nanometer-scale magnetic dots induced by a magnetic force microscope tip.*

15.02.99: M. Morgenstern, Ch. Wittneven, R. Dombrowski, V. Gudmundsson, and R. Wiesendanger, Status Seminar "Quantenmaterialien", Hamburg, Germany: *Die Ursache langreichweitiger Kontraste in der Rastertunnelspektroskopie im Magnetfeld auf InAs(110).*

22.03.99: M. Getzlaff and R. Wiesendanger, Frühjahrstagung der Deutschen Physikalischen Gesellschaft, Münster, Germany: *Magnetische Eigenschaften dünner Pd-Schichten auf Fe(110).*

22.03.99: J. Bansmann, L. Lu, M. Getzlaff, K.-H. Meiwes-Broer, M. Fluchtmann, and J. Braun, Frühjahrstagung der Deutschen Physikalischen Gesellschaft, Münster, Germany: *Magnetischer zirkularer und linearer Dichroismus im Co 3d Valenzband - ein Vergleich zwischen Experiment und Theorie -.*

22.03.99: M. Morgenstern, Chr. Wittneven, R. Dombrowski, V. Gudmundsson, and R. Wiesendanger, Frühjahrstagung der Deutschen Physikalischen Gesellschaft, Münster, Germany: *Der Einfluß ionisierter Dotieratome auf die Landauquantisierung: Eine Rastertunnelspektroskopieanalyse auf InAs(110).*

22.03.99: M. Getzlaff, A. Pundt, M. Bode, R. Kirchheim, and R. Wiesendanger, Frühjahrstagung der Deutschen Physikalischen Gesellschaft, Münster, Germany: *Abbildung der wasserstoffinduzierten plastischen Verformung von Gd-Schichten mittels STM.*

23.03.99: M. Getzlaff, M. Bode, and R. Wiesendanger, Frühjahrstagung der Deutschen Physikalischen Gesellschaft, Münster, Germany: *Bestimmung von Radialmatrixelementen und Phasenverschiebungen in der Photoemission.*

24.03.99: A. Schwarz, W. Allers, U. D. Schwarz, and R. Wiesendanger, Frühjahrstagung der Deutschen Physikalischen Gesellschaft, Münster, Germany: *Untersuchung von Punktdefekten auf InAs(110) mittels dynamischer Rasterkraftmikroskopie im UHV bei tiefen Temperaturen.*

24.03.99: M. Kleiber, M. Dreyer, and R. Wiesendanger, Frühjahrstagung der Deutschen Physikalischen Gesellschaft, Münster, Germany: *Untersuchung des Einflußes von Kohlenstoff auf die Anisotropie ultradünner Kobaltfilme auf Gold(111) mittels Magnetkraftmikroskopie im Ultrahochvakuum.*

25.03.99: H. Hölscher, W. Allers, U. D. Schwarz, A. Schwarz, and R. Wiesendanger, Frühjahrstagung der Deutschen Physikalischen Gesellschaft, Münster, Germany: *Rekonstruktion des Spitzen/Proben-Potentials aus der Frequenzverschiebung im dynamischen Modus des Rasterkraftmikroskops.*

25.03.99: M. Bode, M. Getzlaff, and R. Wiesendanger, Frühjahrstagung der Deutschen Physikalischen Gesellschaft, Münster, Germany: *Temperaturabhängige Austauschaufspaltung des Oberflächenzustandes von Tb(0001).*

25.03.99: S. Heinze, X. Nie, S. Blügel, and M. Weinert, Frühjahrstagung der Deutschen Physikalischen Gesellschaft, Münster, Germany: *Einfluß des elektrischen Feldes auf STM-Bilder von Metalloberflächen.*

09.04.99: V. Hagen, A. Born, and R. Wiesendanger, 5. DI-User Meeting, 07.-09.04.99 Dresden, Germany: *Simulation zur Rasterkapazitätsmikroskopie.*

13.04.99: R. Wiesendanger, TU Ilmenau, Germany (Kolloquium): *Von der Mikroelektronik zur Nanoelektronik: Neue faszinierende Einblicke in das mikroskopische Verhalten von Festkörperelektronen.*

20.04.99: R. Wiesendanger, Hannover, Germany (Messe): *Die Augen des Nanokosmos - das Kompetenzzentrum 'Nanoanalytik'.*

03.05.99: S. Heinze, R. Abt, S. Blügel, Institut für Oberflächenphysik und Atomstoßprozesse (Seminar), Humboldt Universität Berlin, Germany: *Interpretation von STM-Bildern von Übergangsmetallstrukturen auf der Basis der Elektronentheorie.*

05.05.99: R. Wiesendanger, University of Essen, Germany (Kolloquium): *Spinpolarisierte Rastertunnelspektroskopie: Ein neuer Zugang zum Nanomagnetismus.*

07.05.99: U. D. Schwarz, W. Allers, H. Hölscher, A. Schwarz, and R. Wiesendanger, Freie Universität Berlin, Germany: *Dynamische Rasterkraftmikroskopie bei tiefen Temperaturen: Physikalische Prinzipien und ausgewählte, bei tiefen Temperaturen erhaltene Resultate.*

10.05.99: U. D. Schwarz, Rheinisch-Westfälische Technische Hochschule Aachen, Germany: *Neue Anwendungen der Rasterkraftmikroskopie: Von den mikroskopischen Ursachen der Reibung zur hochauflösenden Mikroskopie/Spektroskopie bei tiefen Temperaturen.*

12.05.99: U. D. Schwarz, Technische Universität Berlin, Germany: *Reibung auf der Nanometerskala - Neue Einblicke in ein altes Problem.*

18.05.99: M. Morgenstern, Hamburg, Germany (Seminar über Quantenoptik und Spektroskopie): *Auf dem Weg zur Kartierung der elektronischen Struktur von Halbleitersystemen mittels Rastertunnelspektroskopie.*

20.05.99: U. D. Schwarz, University of Hamburg, Germany: *Nanomechanik - Nanomechanische Untersuchungen mit dem Rasterkraftmikroskop.*

21.05.99: M. Getzlaff, Seminarvortrag, University of Göttingen: *STM an Selten-Erdsystemen.*

25.05.99: J. Wiebe, Niederkleveez, Germany (Workshop des Graduiertenkollegs Physik nanostrukturierter Festkörper): *Planning of a 300 mK-UHV-Scanning Tunneling Microscope.*

27.05.99: R. Wiesendanger, WISTA, Berlin-Adlershof, Germany: *Die Augen des Nanokosmos - das Kompetenzzentrum 'Nanoanalytik'.*

08.06.99: U. D. Schwarz, A. Schwarz, H. Hölscher, W. Allers, and R. Wiesendanger, University of Halle, Germany: *Abbildung von Punktdefekten mit dem Rasterkraftmikroskop.*

14.06.99: U. D. Schwarz, Technische Universität Ilmenau, Germany: *Reibung auf der Nanometerskala - Neue Einblicke in ein altes Problem.*

18.06.99: W. Allers, Eidgenössisch-Technische Hochschule Zürich, Switzerland: *Dynamische Rasterkraftmikroskopie auf atomarer Skala.*

24.06.99: U. D. Schwarz, University of Essen, Germany: *Schichtdickenmessung mit dem Rasterkraftmikroskop.*

18.07.99: H. Hölscher, W. Allers, U. D. Schwarz, and R. Wiesendanger, 10th International Conference on Scanning Tunneling Microscopy/Spectroscopy and Related Techniques, Seoul, South Korea: *Analysis of the frequency shift in dynamic force microscopy.*

18.07.99: U. D. Schwarz, W. Allers, H. Hölscher, A. Schwarz, and R. Wiesendanger, 10th International Conference on Scanning Tunneling Microscopy/Spectroscopy and Related Techniques, Seoul, South Korea: *Dynamic scanning force microscopy in UHV: Physical principles and exemplary experimental results obtained a low temperatures.*

19.07.99: M. Kleiber, M. Dreyer, A. Wadas, and R. Wiesendanger, 10th International Conference on Scanning Tunneling Microscopy/Spectroscopy and Related Techniques, Seoul, South Korea: *Composition driven change of the magnetic anisotropy of ultrathin Co/Au(111) films studied by means of magnetic force microscopy in ultrahigh vacuum.*

20.07.99: M. Morgenstern, V. Gudmundsson, Chr. Wittneven, R. Dombrowski, and R. Wiesendanger, 10th International Conference on Scanning Tunneling Microscopy/Spectroscopy and Related Techniques, Seoul, South Korea: *The influence of Potential Fluctuations on Landau Quantization and Spin Splitting studied by Low Temperature Scanning Tunneling Spectroscopy.*

21.07.99: M. Bode, M. Getzlaff, A. Kubetzka, R. Pascal, O. Pietzsch, and R. Wiesendanger, 10th International Conference on Scanning Tunneling Microscopy/Spectroscopy and Related Techniques, Seoul, South Korea: *Temperature dependent surface electronic structure of a local-moment magnet: Tb(0001).*

28.07.99: M. Getzlaff, M. Bode, and R. Wiesendanger, ICSOS-6 (1999), Vancouver, Canada: *Spin polarized vacuum tunneling: Correlation of electronic and magnetic properties on the nanometer scale.*

01.09.99: A. Schwarz, W. Allers, U. D. Schwarz, and R. Wiesendanger, Pontresina, Switzerland, Second International Workshop on Noncontact Atomic Force Microscopy: *Atomic-scale dynamic mode scanning force microscopy study on n-InAs(110)-(1x1) at low temperatures.*

02.09.99: U. D. Schwarz, H. Hölscher, and R. Wiesendanger, Pontresina, Switzerland, Second International Workshop on Noncontact Atomic Force Microscopy: *Towards the understanding of dynamic scanning force microscopy: Analysis of the contrast mechanism and interpretation of atomic-scale images.*

03.09.99: H. Hölscher, W. Allers, U. D. Schwarz, A. Schwarz, and R. Wiesendanger, Pontresina, Switzerland, Second International Workshop on Noncontact Atomic Force Microscopy: *Simulation of NC-AFM results for graphite(0001).*

21.09.99: M. Morgenstern, V. Gudmundsson, Chr. Wittneven, R. Dombrowski, and R. Wiesendanger, European Conference of Surface Science, Vienna, Austria: *The Influence of Potential Fluctuations on Landau Quantization and Spin Splitting studied by Low Temperature Scanning Tunneling Spectroscopy on InAs(110).*

23.09.99: M. Getzlaff, M. Bode, R. Pascal, O. Pietzsch, A. Kubetzka, and R. Wiesendanger, European Conference of Surface Science, Vienna, Austria: *Surface electronic properties of Tb(0001): a variable-temperature STM study.*

29.09.99: S. Heinze, R. Wiesendanger, and S. Blügel, Workshop on "Magnetische Nanostrukturen: Physikalische Grundlagen und Anwendungen", Hamburg, Germany: *Ab initio Bandstrukturrechnungen zum spinpolarisierten Tunneln.*

29.09.99: M. Bode, M. Getzlaff, and R. Wiesendanger, Workshop on "Magnetische Nanostrukturen: Physikalische Grundlagen und Anwendungen", Hamburg, Germany: *Spin-polarized vacuum tunneling into exchange-split surface state of Gd(0001): a new concept for high-resolution imaging of magnetic domains.*

29.09.99: M. Kleiber, Workshop on "Magnetische Nanostrukturen: Physikalische Grundlagen und Anwendungen", Hamburg, Germany: *Magnetische Domänenstrukturuntersuchungen ultradünner magnetischer Schichten mittels UHV-Magnetkraftmikroskopie.*

21.10.99: O. Krause, A. Born, and R. Wiesendanger, Infineon Technologies Munich, Germany: *SCM-Simulationen.*

25.10.99: R. Wiesendanger, Seattle, USA (AVS'99): *Low-temperature tunneling spectroscopy of the tip-induced quantum dot on n-InAs(110).*

08.11.99: M. Bode, M. Getzlaff, R. Pascal, O. Pietzsch, A. Kubetzka, and R. Wiesendanger, University of Mainz, Germany: *Rastertunnelspektroskopie an dünnen magnetischen Filmen.*

09.11.99: U. D. Schwarz, University of Hamburg, Germany: *Reibung auf der Nanometerskala - Neue Einblicke in ein altes Problem.*

29.11.99: R. Wiesendanger, University of Hamburg, Germany (Kolloquium, FB Informatik): *Nanotechnologie und ihre Bedeutung für die Informationstechnik.*

30.11.99: J. Klijn, Graduiertenkolleg "Felder und lokalisierte Atome - Atome und lokalisierte Felder. Spectroscopy an localisierten atomaren Systemen", Travemünde, Germany: *Scanning Tunneling Spectroscopy on single adsorbed atoms on semiconducting surfaces.*

02.12.99: M. Morgenstern, University of Göttingen, Germany (Seminar): *Scanning Tunneling Spectroscopy of Landau Quantization and Spin Splitting.*

03.12.99: A. Born and R. Wiesendanger, Infineon Technologies AG, (Seminar) Munich, Germany: *Strom- und Dotierungsmessung von integrierten Schaltkreisen mit Nanometer-Auflösung.*

16.12.99: U. D. Schwarz, Eidgenössisch-Technische Hochschule Zürich, Switzerland: *Neue Anwendungen der Rasterkraftmikroskopie: Von den mikroskopischen Ursachen der Reibung zur hochauflösenden Mikroskopie/Spektroskopie bei tiefen Temperaturen.*

05.01.00: M. Morgenstern, M. Getzlaff, D. Haude, R. L. Johnson, and R. Wiesendanger, Workshop "Metal-Nonmetal Structures for Magnetoelectronics" , Bad Honnef, Germany: *Fe on InAs(110): A combined study using scanning tunneling microscopy and photoelectron spectroscopy.*

15.01.00: U. D. Schwarz, Rheinisch-Westfälische Technische Hochschule Aachen, Germany: *Strukturanalyse und ortsaufgelöste Messung von Materialeigenschaften mittels dynamischer Rasterkraftmikroskopie.*

19.01.00: S.Heinze, Research Institute for Materials, University of Nijmegen, The Netherlands: *Interpretation of STM Experiments on Transition-Metal Structures by ab initio Calculations.*

28.01.00: M. Morgenstern, Seminar ETH Zürich, Switzerland: *Scanning tunneling spectroscopy of zero, two and three dimensional electron systems.*

13.03.00: C. Bartsch, A. Born, and R. Wiesendanger, Cluster-Workshop, Kochel am See, Germany: *Rastersonden-Mikroskopie und -Spektroskopie an Metallclustern zur Erforschung von Einzelelektronen- und Quantengrößen-Effekten.*

28.03.00: M. Morgenstern, D. Haude, V. Gudmundsson, R. Dombrowski, Chr. Wittneven, Chr. Steinebach, and R. Wiesendanger, Frühjahrstagung der Deutschen Physikalischen Gesellschaft, Regensburg, Germany: *Die Ursache der Beobachtung von Landau-Oszillationen in der Rastertunnelspektroskopie.*

28.03.00: A. Born, O. Krause, J. Isenbart, and R. Wiesendanger, Frühjahrstagung der Deutschen Physikalischen Gesellschaft, Regensburg, Germany: *Quantitative Rasterkapazitätsmikroskopie für die Fehleranalyse von Halbleiterbauelementen.*

28.03.00: V. Hagen, A. Born, J. Isenbart, and R. Wiesendanger, Frühjahrstagung der Deutschen Physikalischen Gesellschaft, Regensburg, Germany: *Dotierprofilanalyse von Halbleitermikrostrukturen mittels Scanning Spreading Resistance Microscopy.*

28.03.00: C. Bartsch, A. Born, and R. Wiesendanger, Frühjahrstagung der Deutschen Physikalischen Gesellschaft, Regensburg, Germany: *Untersuchung von ligandenstabilisierten Metallclustern mittels SPM.*

28.03.00: M.Bode, O.Pietzsch, A.Kubetzka, and R.Wiesendanger, Frühjahrstagung der Deutschen Physikalischen Gesellschaft, Regensburg, Germany: *Anisotropie dünner magnetischer Schichten an Tunnelspitzen.*

28.03.00: M. Morgenstern, M. Getzlaff, D. Haude, R.L. Johnson, and R. Wiesendanger, Frühjahrstagung der Deutschen Physikalischen Gesellschaft, Regensburg, Germany: *ARUPS-Untersuchung der Bedeckungsabhängigkeit des Nb-induzierten zweidimensionalen Elektronengases auf InAs(110).*

28.03.00: S. Heinze, R. Abt, S. Blügel, G. Gilarowski, and H. Niehus, Frühjahrstagung der Deutschen Physikalischen Gesellschaft, Regensburg, Germany: *STM-Bilder von vergrabenen Übergangsmetallstrukturen.*

28.03.00: S. Heinze, D. Wortmann, Ph. Kurz, X. Nie, S. Blügel, M. Bode, A. Kubetzka, O. Pietzsch, and R. Wiesendanger, Frühjahrstagung der Deutschen Physikalischen Gesellschaft, Regensburg, Germany: *Ab initio Rechnungen zum spin-polarisierten Tunneln.*

28.03.00: J. Isenbart, A. Born, and R. Wiesendanger, Frühjahrstagung der Deutschen Physikalischen Gesellschaft, Regensburg, Germany: *Aufbau eines Prototyps für die Massenspeicherung basierend auf Rastersondenverfahren.*

28.03.00: O. Krause, A. Born, and R. Wiesendanger, Frühjahrstagung der Deutschen Physikalischen Gesellschaft, Regensburg, Germany: *Simulationen zur Rasterkapazitätsmikroskopie.*

28.03.00: O. Pietzsch, A. Kubetzka, M. Bode, and R. Wiesendanger, Frühjahrstagung der Deutschen Physikalischen Gesellschaft, Regensburg, Germany: *Direkte Visualisierung von dipolar antiferromagnetisch gekoppelten Nanostreifen mittels spinpolarisierter Rastertunnelspektroskopie.*

28.03.00: R. Pascal, H. Tödter, M. Bode, M. Getzlaff, and R. Wiesendanger, Frühjahrstagung der Deutschen Physikalischen Gesellschaft, Regensburg, Germany: *Tunnelspektroskopische Detektion von Stapelwechselfehlern auf Tb(0001).*

28.03.00: D. Haude, I. Meinel, M. Morgenstern, and R. Wiesendanger, Frühjahrstagung der Deutschen Physikalischen Gesellschaft, Regensburg, Germany: *Abbildung magnetfeldinduzierter Lokalisierung mit Rastertunnelspektroskopie.*

28.03.00: M. Kleiber, M. Bode, R. Ravlic, and R. Wiesendanger, Frühjahrstagung der Deutschen Physikalischen Gesellschaft, Regensburg, Germany: *Untersuchung ultradünner Eisenfilme auf Cr(001) mit MFM und STM im UHV.*

29.03.00: H. Hölscher, W. Allers, U. D. Schwarz, A. Schwarz, and R. Wiesendanger, Frühjahrstagung der Deutschen Physikalischen Gesellschaft, Regensburg, Germany: *Simulation und Analyse von NC-AFM-Bildern: Abbildung der A- und B-Atome der Graphit-(0001)-Oberfläche.*

29.03.00: A. Schwarz, W. Allers, U. D. Schwarz, and R. Wiesendanger, Frühjahrstagung der Deutschen Physikalischen Gesellschaft, Regensburg, Germany: *Die Rolle der dangling bonds bei atomarer Auflösung im dynamischen Modus der Rasterkraftmikroskopie.*

30.03.00: A. Kubetzka, M. Bode, O. Pietzsch, and R. Wiesendanger, Frühjahrstagung der Deutschen Physikalischen Gesellschaft, Regensburg, Germany: *Korrelation struktureller und magnetischer Eigenschaften dünner Fe-Filme auf W(110) mittels spinpolarisierter Rastertunnelspektroskopie.*

03.04.00: H. Hölscher, Seminar talk, Jülich, Institut für Festkörperforschung des Forschungszentrums Jülich, Germany: *Physical Mechanisms of Atomic Force Microscopy.*

19.04.00: Chr. Meyer, Ringvorlesung: Graduiertenkolleg, "Physik nanostrukturierter Festkörper", Hamburg, Germany: *Untersuchung des Wachstums von Niob auf InAs(110).*

08.05.00: H. Hölscher, Seminar talk, Mainz, Germany, Institut für Physik, University of Johannes Gutenberg, Germany: *Reibung auf der Nanometerskala - Nanotribologie mit dem Rasterkraftmikroskop.*

30.05.00: M. Morgenstern, Kolloquium Uni Leiden, Germany: *Scanning tunneling spectroscopy of zero, two and three dimensional electron systems.*

05.06.00: R. Wiesendanger, University of Regensburg, Germany (Kolloquium): *Neue Einblicke in den Nanokosmos.*

06.06.00: R. Wiesendanger, University of Stuttgart, Germany (Kolloquium): *Neue Einblicke in den Nanokosmos.*

15.06.00: R. Wiesendanger, IFW Dresden, Germany (BMBF-Seminar "Magnetoelektronik"): *Observation of in-plane and out-of-plane magnetization in magnetic nanostructures.*

30.06.00: R. Wiesendanger, University of Hamburg, Germany (Workshop on Nanomagnetism, Magneto- and Spinelectronics): *Messung magnetischer Dipolkräfte, quantenmechanischer Austauschkräfte und spinpolarisierter Tunneleffekte an den Grenzen des technisch Möglichen.*

03.07.00: M.Bode, S.Heinze, O.Pietzsch, A.Kubetzka, R.Ravlic, M.Kleiber, X.Nie, S.Blügel, and R.Wiesendanger, Symposium on Spin-Electronics, Halle, Germany: *Imaging of surface spin-structures: pushing the limits.*

05.07.00: J. Wiebe, Ringvorlesung: Graduiertenkolleg "'Physik nanostrukturierter Festkörper"' (Physik der Mikrostrukturen), Hamburg, Germany: *Planung und Aufbau einer 300mK-UHV-Rastertunnelmikroskopie-Anlage mit 14T-Magnet.*

05.07.00: U. D. Schwarz, University of Johannes-Gutenberg Mainz, Germany: *Neue Anwendungen der Rasterkraftmikroskopie: Von den atomistischen Ursachen der Reibung zur hochauflösenden Mikroskopie/Spektroskopie bei tiefen Temperaturen.*

07.07.00: S. Heinze, IBM Research Division, T. J. Watson Research Center, Yorktown Heights, N.Y. , USA: *Interpretation of STM Experiments on Transition-Metal Structures by ab initio Calculations.*

10.07.00: R. Wiesendanger, University of Bielefeld, Germany (Kolloquium): *Neue Einblicke in den Nanokosmos.*

11.07.00: S. Heinze, M. Bode, A. Kubetzka, O. Pietzsch, X. Nie, D. Wortmann, Ph. Kurz, S. Blügel, and R. Wiesendanger, 10th International Conference on Solid Films and Surfaces, Princeton, N.J. , USA: *Real Space Imaging of Two-Dimensional Antiferromagnetism on the Atomic Scale.*

17.07.00 W. Allers, S. Langkat, and R. Wiesendanger, 3rd International Conference on Non-Contact Atomic Force Microscopy, Hamburg, Germany: *Dynamic scanning force microscopy on transition metal oxides.*

18.07.00: H. Hölscher, B. Gotsmann, A. Schwarz, W. Allers, U. D. Schwarz, H. Fuchs, and R. Wiesendanger, Third International Workshop on Non-Contact Atomic Force Microscopy, Hamburg, Germany: *On the measurement of the energy dissipation in dynamic force spectroscopy.*

22.07.00: A. Born and R. Wiesendanger, 2*nd* International Conference on Scanning Probe Spectroscopy, Hamburg, Germany: *The physical priniciples of scanning capacitance microscopy.*

10.08.00: M.Bode, S.Heinze, O.Pietzsch, A.Kubetzka, R.Ravlic, M.Kleiber, X.Nie, S.Blügel, and R.Wiesendanger, Sandia Nat. Lab., Sandia, USA: *Imaging of surface spin-structures: pushing the limits.*

21.08.00: M. Morgenstern, D. Haude, I. Meinel, and R. Wiesendanger, 25th International Conference on the Physics of Semiconductors, Osaka, Japan: *Magnetic field induced localization in three dimensions.*

24.08.00: S. Heinze, Ph. Kurz, G. Bihlmayer, D. Wortmann, X. Nie, S. Blügel, M. Bode, A. Kubetzka, O. Pietzsch, and R. Wiesendanger, Second International Conference of the Psi-k Network, August 2000, Schwäbisch–Gmünd, Germany: *Resolving Complex Atomic-Scale Spin-Structures by Spin-Polarized STM.*

08.09.00: M. Morgenstern, Colloqium TU Delft, The Netherlands: *Scanning tunneling spectroscopy: three, two and zero dimensional electron systems.*

19.09.00: R. Wiesendanger, University of Twente, Enschede, The Netherlands (Kolloquium): *Novel Insight into the Nanoworld.*

03.10.00: O. Pietzsch, A. Kubetzka, M. Bode, and R. Wiesendanger, 47th International Symposium, American Vacuum Society, and NANO 6, Boston, USA: *Direct Visualization of Magneitc Nanowires by Spin Polarized Scanning Tunneling Spectroscopy.*

03.10.00: M. Kleiber, R. Ravlic, M. Bode, and R. Wiesendanger, 47th International Symposium, American Vacuum Society, and NANO 6, Boston, USA: *Correlation of Structural and Magnetic Properties of Fe/Cr(001) Studied by Combined SP-STM and MFM.*

03.10.00: M. Bode, S. Heinze, A. Kubetzka, O. Pietzsch, X. Nie, S. Blügel, and R. Wiesendanger, 47th International Symposium, American Vacuum Society, and NANO 6, Boston, USA: *Real-Space Imaging of Two-Dimensional Antiferromagnetism on the Atomic Scale.*

05.10.00: A. Kubetzka, O. Pietzsch, M. Bode, and R. Wiesendanger, 47th International Symposium, American Vacuum Society, and NANO 6, Boston, USA: *Correlation of Structural and Magnetic Properties of Ultra-Thin Fe-Films on W(110) by Spin-Polarized STM/STS.*

16.10.00: J. Isenbart, A. Born, and R. Wiesendanger, 4. Workshop des Graduiertenkollegs "Physik nanostrukturierter Festkörper", Schwerin, Germany: *From Scanning Capacitance Microscopy to high speed Scanning Capacitance Spectroscopy.*

17.10.00: A. Wachowiak, J. Wiebe, 4. Workshop des Graduiertenkollegs "Physik nanostrukturierter Festkörper", Schwerin, Germany: *Planning and Assembly of a 300mK-UHV-Scanning-Tunneling-Microscope with 14T-magnet.*

17.10.00: Ch. Meyer, 4. Workshop des Graduiertenkollegs "Physik nanostrukturierter Festkörper", Schwerin, Germany: *Scanning tunneling spectroscopy of the Fe-induced two dimentional electron gas on InAs(110).*

18.10.00: M. Bode, S. Heinze, O. Pietzsch, A. Kubetzka, R, Ravlic, M. Kleiber, X. Nie, S. Blügel, and R. Wiesendanger, Allgemeines Physikalisches Kolloquium, Universität Münster, Germany: *Spinpolarisierte Rastertunnelmikroskopie: Visualisierung magnetischer Domänen mit atomarer Auflösung.*

10.11.00: M. Getzlaff, Physikalisches Kolloquium der Universität Düsseldorf, Germany: *Oberflächen-Magnetismus und Adsorbate - Korrelation struktureller, elektronischer und magnetischer Eigenschaften.*

13.11.00: J. Klijn, Graduiertenkolleg "Felder und lokalisierte Atome - Atome und lokalisierte Felder. Spectroscopy an localisierten atomaren Systemen", Schwerin, Germany: *Interaction between single Fe adsorbates and InAs.*

14.11.00: M. Bode, S. Heinze, O. Pietzsch, A. Kubetzka, R. Ravlic, M. Kleiber, X. Nie,
S. Blügel, and R. Wiesendanger, Kolloquium zur Physik der kondensierten Materie, University of Ulm, Germany: *Spinpolarisierte Rastertunnelmikroskopie: Visualisierung magnetischer Domänen mit atomarer Auflösung.*

16.11.00: A. Born and R. Wiesendanger, 26 *th* International Symposium for Testing and Failure Analysis, Bellevue/Washington, USA: *Guidelines for Two-Dimensional Dopant Profiling using SCM.*

05.12.00: M. Getzlaff, Ringvorlesung "2000 - Das Jahr der Physik", Hamburg, Germany: *Neue Einblicke in den Magnetismus auf mikroskopischer Skala.*

12.12.00: J. Wiebe, M. Morgenstern, A. Wachowiak, D. Haude, and R. Wiesendanger, 1st International Workshop on Nano-scale Spectroscopy and its Applications to Semiconductor Research, Trieste, Italy: *An Ultra High Vacuum-300mK-Scanning Tunneling Microscope for Local Measurements of the Density of States on InAs(110)*

15.12.00: M. Getzlaff, Physikalisches Kolloquium der Universität Halle-Wittenberg, Germany: *Adsorbate auf Oberflächen: Korrelation struktureller und elektronischer Eigenschaften.*

15.12.00: U. D. Schwarz, Martin-Luther-Universität Halle-Wittenberg, Germany: *Dynamische Rasterkraftmikroskopie: Eine neue Methode zur hochauflösenden Untersuchung von Festkörperoberflächen.*

19.12.00: M. Bode, S. Heinze, O. Pietzsch, A. Kubetzka, R. Ravlic, M. Kleiber, X. Nie, S. Blügel, and R. Wiesendanger, Condensed Matter & Materials Physics Conference 2000, Bristol, Great Britain: *Atomic-Resolution Imaging of Surface Spin-Structures by Spin-Polarized Scanning Tunneling Microscopy.*

05.01.01: M. Bode, O. Pietzsch, A. Kubetzka, and R. Wiesendanger, 248. WE-Heraeus-Seminar on Spin Dynamics, Bad Honnef, Germany: *Visualization of Magnetic Hysteresis in Fe-Nanowires by Spin-Polarized Scanning Tunneling Spectroscopy.*

08.01.01: M. Getzlaff, Physikalisches Kolloquium der Universität Osnabrück, Germany: *Atome und Moleküle auf Oberflächen: Korrelation struktureller und elektronischer Eigenschaften.*

10.01.01: M. Getzlaff, Physikalisches Kolloquium der Universität Dortmund, Germany: *Oberflächen-Magnetismus: Korrelation struktureller, elektronischer und magnetischer Eigenschaften.*

22.01.01: M. Morgenstern, D. Haude, Chr. Meyer, J. Klijn, I. Meinel, and R. Wiesendanger, Workshop DFG-Schwerpunkt "Quantenhalleffekt", Bad Honnef, Germany: *Scanning Tunneling Spectroscopy on InAs(110): A possible Quantum Hall Effect in the Extreme Quantum Limit of a 3DES.*

22.01.01: R. Wiesendanger, Kolloquium, München, Germany: *Neue Einblicke in den Nanokosmos.*

31.01.01: M. Bode, S. Heinze, O. Pietzsch, A. Kubetzka, R. Ravlic, M. Kleiber, X. Nie, S. Blügel, and R. Wiesendanger, Max-Planck-Institut für Festkörperforschung, Stuttgart (Germany): *Imaging of magnetic nanostructures by spin-polarized STM.*

01.02.01: R. Wiesendanger, Kolloqium, University of Düsseldorf, Germany: *Quantenphañomene auf der Nanometerskala: Neue Einblicke mittels Rastertunnelspektroskopie.*

06.02.01: R. Wiesendanger, Kolloqium, University of Amsterdam, The Netherlands: *Novel isight into the nanoworld.*

08.02.01: M. Morgenstern, Kolloquium der Universität Kiel, Germany: *Rastertunnelspektroskopie an Elektronensystemen in verschiedenen Dimensionen.*

26.03.01: J. Klijn, Chr. Meyer, D. Haude, M. Getzlaff, M. Morgenstern, R. Adelung, L. Kipp, M. Skibowski, and R. Wiesendanger, Frühjahrstagung der Deutschen Physikalischen Gesellschaft, Hamburg, Germany: *UHV-Rastertunnelspektroskopie am adsorbatinduzierten 2DES auf InAs(110).*

26.03.01: M. Morgenstern, M. Getzlaff, J. Klijn, Chr. Meyer, R. Wiesendanger, R. Adelung, K. Roßnagel, L. Kipp, M. Skibowski, L. Plucincks, R. Brochier, and R. L. Johnson, Frühjahrstagung der Deutschen Physikalischen Gesellschaft, Hamburg, Germany: *Photoelektronenspektroskopie am adsorbatinduzierten zweidimensionalen Elektronengas: Grenzen des Oberflächendotierungsmodells.*

27.03.01: M. Bode, O. Pietzsch, A. Kubetzka, S. Heinze, M. Kleiber, R. Ravlic, X. Nie, S. Blügel, and R. Wiesendanger, Frühjahrstagung der Deutschen Physikalischen Gesellschaft, Hamburg, Germany: *Spin-polarisierte Rastertunnelmikroskopie.*

27.03.01: M. Morgenstern, D. Haude, I. Meinel, Chr. Meyer, and R. Wiesendanger, Frühjahrstagung der Deutschen Physikalischen Gesellschaft, Hamburg, Germany: *Rastertunnelspektroskopie an InAs(110): Ein Quanten-Hall-Effekt in drei Dimensionen?*

29.03.01: O. Pietzsch, A. Kubetzka, M. Bode, and R. Wiesendanger, Frühjahrstagung der Deutschen Physikalischen Gesellschaft, Hamburg, Germany: *Ummagnetisierung von Fe-Nanodrähten beobachtet mit dem Rastertunnelmikroskop.*

29.03.01: M. Bode, O. Pietzsch, A. Kubetzka, and R. Wiesendanger, Frühjahrstagung der Deutschen Physikalischen Gesellschaft, Hamburg, Germany: *Experimentelle Evidenz für intra-atomaren nicht-kollinearen Magnetismus an STM Sondenspitzen.*

29.03.01: H. Hölscher, B. Gotsmann, U. D. Schwarz, W. Allers, H. Fuchs, and R. Wiesendanger, Frühjahrstagung der Deutschen Physikalischen Gesellschaft, Hamburg, Germany: *Messung konservativer und dissipativer Spitzen-Proben-Kräfte in der dynamischen Rasterkraftmikroskopie mittels Frequenzmodulationstechnik.*

29.03.01: M. v. Sprekelsen, J. Isenbart, and R. Wiesendanger, Frühjahrstagung der Deutschen Physikalischen Gesellschaft, Hamburg, Germany: *Hochgeschwindigkeit-Rasterkapazitätsspektroskopie an Halbleitermikrostrukturen - Apparativer Aufbau und Messungen.*

29.03.01: A. Kubetzka, O. Pietzsch, M. Bode, and R. Wiesendanger, Frühjahrstagung der Deutschen Physikalischen Gesellschaft, Hamburg, Germany: *Untersuchung der magnetischen Domänenstruktur von 2 ML Fe/W(110) mittels SP-STM/STS.*

29.03.01: R. Ravlic, M. Kleiber, M. Bode, and R. Wiesendanger, Frühjahrstagung der Deutschen Physikalischen Gesellschaft, Hamburg, Germany: *Untersuchung der Cr(001)-Oberfläche mittels SP-STS/STM.*

29.03.01: S. Heinze, D. Wortmann, and S. Blügel, Frühjahrstagung der Deutschen Physikalischen Gesellschaft, Hamburg, Germany: *Ab-initio Rechnungen zur elektronischen Struktur von magnetischen STM-Spitzen.*

29.03.01: S. Langkat, W. Allers, and R. Wiesendanger, Frühjahrstagung der Deutschen Physikalischen Gesellschaft, Hamburg, Germany: *Nichtkontakt-Rasterkraftmikroskopie auf Übergangsmetalloxiden.*

29.03.01: J. Isenbart, A. Born, and R. Wiesendanger, Frühjahrstagung der Deutschen Physikalischen Gesellschaft, Hamburg, Germany: *Hochgeschwindigkeit-Rasterkapazitätsspektroskopie an Halbleitermikrostrukturen - Grundprinzip und Simulationen.*

30.03.01: A. Schwarz, M. Liebmann, U. H. Pi, Z. G. Khim, and R. Wiesendanger, Frühjahrstagung der Deutschen Physikalischen Gesellschaft, Hamburg, Germany: *Temperatur- und dickenabhängige Domänenstruktur dünner Manganperowskitschichten.*

20.04.01: R. Wiesendanger, Kolloquium, University of Bonn, Germany: *Quantenphänomene auf der Nanometerskala: Neue Einblicke mittels Rastertunnelspektroskopie.*

22.04.01: M. Bode, R. Pascal, M. Getzlaff, and R. Wiesendanger, Ben-Gurion-University of the Negev, Beer Sheva (Israel): *Correlation of structural, electronic and magnetic properties by STM/STS: rare-earth metals.*

02.05.01: M. Bode, S. Heinze, O. Pietzsch, A. Kubetzka, R. Ravlic, M. Kleiber, X. Nie, S. Blügel, and R. Wiesendanger, Ben-Gurion-University of the Negev, Beer Sheva (Israel): *Imaging of surface magnetic structures by spin-polarized STM.*

10.05.01: R. Wiesendanger, Kolloquium, University of Duisburg, Germany: *Von der Mikro- zur Nanoelektronik: Beiträge der Rastersondenspektroskopie.*

06.06.01: M. Morgenstern, SFB-Workshop "Quantenmaterialien", Hamburg, Germany: *Scanning Tunneling Spectroscopy on InAs(110): Low Density Electron Systems in Different Dimensions.*

11.06.01: M. Getzlaff, Kolloquium, University of Kaiserslautern, Germany: *OBERFLÄCHEN-Magnetismus: Korrelation struktureller, elektronischer und magnetischer Eigenschaften.*

13.06.01: M. Getzlaff, Seminar, University of Göttingen, Germany: *Niederdimensionale Systeme: Korrelation struktureller, elektronischer und magnetischer Eigenschaften auf der Nanometerskala.*

19.06.01: R. Wiesendanger, SFB-Seminar, University of Saarbrücken, Germany: *Spinaufgelöste Spektroskopie auf atomarer Skala.*

24.06.01: M. Bode, O. Pietzsch, A. Kubetzka, M. Kleiber, R. Ravlic, and R. Wiesendanger, 4th International Symposium on Metallic Multilayers, Aachen, Germany: *Imaging antiferromagnetic surface spin-structures by spin-polarized STM.*

11.07.01: M. Getzlaff, Seminar, University of Rostock, Germany: *Adsorbate auf dünnen Seltenerdschichten: strukturelle und elektronische Modifikationen.*

16.07.01: D. Haude, 11th International Conference on Scanning Tunneling Microscopy/Spectroscopy and Related Techniques, Vancouver, Canada: *Experimental evidence of edge-like states in three-dimensional electron systems observed with scanning tunneling microscopy.*

17.07.01: M. Bode, A. Kubetzka, O. Pietzsch, S. Heinze, and R. Wiesendanger, 11th International Conference on Scanning Tunneling Microscopy/Spectroscopy and Related Techniques, Vancouver, Canada: *Magnetic properties of Fe, Gd, and Cr thin film probe tips.*

17.07.01: S. Heinze, D. Wortmann, Ph. Kurz, G. Bihlmayer, and S. Blügel, 11th International Conference on Scanning Tunneling Microscopy/Spectroscopy and Related Techniques, Vancouver, Canada: *Resolving Complex Atomic-Scale Spin-Structures by Spin-Polarized STM.*

17.07.01: M. Getzlaff, R. Pascal, and R. Wiesendanger, 11th International Conference on Scanning Tunneling Microscopy/Spectroscopy and Related Techniques, Vancouver, Canada: *Magnetic thin film alloy formation:* $GdFe_2$ *and* $GdFe_3$.

17.07.01: O. Pietzsch, A. Kubetzka, M. Bode, and R. Wiesendanger, 11th International Conference on Scanning Tunneling Microscopy/Spectroscopy and Related Techniques, Vancouver, Canada: *Spin Polarized Scanning Tunneling Spectroscopy in an Applied Magnetic Field: Hysteresis at the Nano-Scale.*

19.07.01: H. Hölscher, B. Gotsmann, W. Allers, U.D. Schwarz, H. Fuchs, and R. Wiesendanger, 11th International Conference on Scanning Tunneling Microscopy/Spectroscopy and Related Techniques, Vancouver, Canada: *Analysis and Simulation of Dynamic Force Microscopy and Spectroscopy.*

31.07.01: Chr. Meyer, J. Klijn, M. Morgenstern, and R. Wiesendanger, 14th International Conference on the Electronic Properties of Two-dimensional Systems, Prag, Czech Republic: *Local density of states of a one dimensional conductor confined below a charged step edge.*

04.09.01: M. Getzlaff, A. Kubetzka, O. Pietzsch, M. Bode, and R. Wiesendanger, European Conference on Surface Science ECOSS-20, Krakow, Poland: *Self-assembled Fe nano-particles on Cu templates.*

04.09.01: A. Schwarz, M. Liebmann, U.H. Pi, D.W. Kim, T.W. Noh, Z.G. Khim, and R. Wiesendanger, 4th International Conference on Noncontact Atomic Force Microscopy, Kyoto, Japan: *Dynamic Mode Magnetic Force Microscopy at Low Temperatures on Perovskite Manganites.*

19.09.01: M. Getzlaff, Seminar at the Department of Chemistry, Hamburg, Germany: *Characterization of functional materials by electron spectroscopic methods.*

21.09.01: J. Klijn, Ch. Meyer, D. Haude, M. Morgenstern, M. Getzlaff, R. Adelung, L. Kipp, M. Skibowski, and R. Wiesendanger, Workshop Schwerpunkt "Quantum Hall Systems", Gedern, Germany: *Scanning tunneling spectroscopy on an adsorbate induced two-dimensional electron system in zero and high magnetic field.*

25.09.01: M. Morgenstern, 2. Symposium on Interdisciplinary Nanoscience, Hamburg, Germany: *Rastertunnelspektroskopie: Ein Werkzeug für die Nanowissenschaft.*

09.10.01: M. Bode, O. Pietzsch, A. Kubetzka, and R. Wiesendanger, Joint Research Center for Atom Technology, Tsukuba (Japan): *Recent progress in spin-polarized STM.*

14.10.01: K. v. Bergmann, , Workshop "Functionalized Materials", Weißenhäuser Strand, Germany: *Spinpolarisierte Rasterunnelmikroskopie und –spektroskopie.*

15.10.01: M. Getzlaff, , Workshop "Functionalized Materials", Weißenhäuser Strand, Germany: *SURFACE – Magnetism.*

17.10.01: J. Klijn, Ch. Meyer, L. Plucinski, D. Haude, M. Morgenstern, M. Getzlaff, R. Adelung, L. Kipp, M. Skibowski, R.L. Johnson, and R. Wiesendanger, Workshop "Spectroscopy on localized atomic systems", Weißenhäuser Strand, Germany: *Scanning tunneling spectroscopy on adsorbate induced two-dimensional systems.*

18.10.01: Chr. Meyer, J. Klijn, M. Morgenstern, and R. Wiesendanger, SFB 508 Statusseminar, Hamburg, Germany: *Local density of states of a one dimensional conductor confined below a charged step edge.*

19.10.01: J. Wiebe, J. Klijn, A. Wachowiak, M. Morgenstern, D. Haude, Chr. Meyer, F. Meier, and R. Wiesendanger, Status-Seminar SFB 508 "Quantenmaterialien", University of Hamburg: *Scanning Tunneling Spectroscopy on Semiconductor Hybrid Systems.*

30.10.01: M. Morgenstern, J. Klijn, Chr. Meyer, D. Haude, and R. Wiesendanger, AVS, 48th International Symposium of the American Vacuum Society, San Francisco, USA: *Scanning Tunneling Spectroscopy on Adsorbate Induced Two Dimensional Electron Systems on InAs(110).*

31.10.01: U.D. Schwarz, H. Hölscher, W. Allers, S. Langkat, B. Gotsmann, H. Fuchs, and R. Wiesendanger, AVS, 48th International Symposium of the American Vacuum Society, San Francisco, USA: *Progress in Dynamic Force Microscopy: From High-Resolution Imaging of Insulators to the Measurement of Dissipative Interaction Forces.*

01.11.01: M. Morgenstern, D. Haude, I. Meinel, and R. Wiesendanger, AVS, 48th International Symposium of the American Vacuum Society, San Francisco, USA: *Two Dimensional Electronic Properties of a Disordered Three Dimensional Conductor in the Extreme Quantum Limit.*

01.11.01: M. Morgenstern, Chr. Meyer, J. Klijn, and R. Wiesendanger, AVS, 48th International Symposium of the American Vacuum Society, San Francisco, USA: *Probing a One Dimensional Conductor Below a Charged Step Edge.*

05.11.01: M. Morgenstern, Seminar an der University of California, Berkeley, USA: *Probing the Local Density of States of Dilute Electron Systems in Different Dimensions.*

05.11.01: M. Bode, O. Pietzsch, A. Kubetzka, and R. Wiesendanger, Arizona State University, Tempe, USA: *Imaging magnetic structures by spin-polarized STM.*

07.11.01: M. Bode, O. Pietzsch, A. Kubetzka, and R. Wiesendanger, Colloquia Series at the Georgia Institute of Technologie, Atlanta, USA: *Imaging Magnetic Nanostructures by Spin-Polarized STM.*

09.11.01: M. Morgenstern, Seminar at the University of California, Santa Barbara, USA: *Probing the Local Density of States of Dilute Electron Systems in Different Dimensions.*

14.11.01: M. Liebmann, A. Schwarz, U.H. Pi, D.W. Kim, T.W. Noh, Z.G. Khim, and R. Wiesendanger, Conference on Magnetism and Magnetic Materials, Seattle, USA: *H-dependent domain structure of* $La_{0.7}Sr_{0.3}MnO_3$ *epitaxial thin films studied by low-temperature MFM.*

17.11.01: R. Wiesendanger, Seminar at the University of Tokyo, Japan: *Spin-resolved spectro-microscopy at the atomic level.*

30.11.01: R. Wiesendanger, Seminar at the Technical University of Hanover, Germany: *Nano-scale studies of quantum phenomena by scanning probe spectroscopy.*

04.12.01: M. Morgenstern, Seminar at the University of Leoben, Austria: *Probing the Local Density of States of Dilute Electron Systems in Different Dimensions.*

05.12.01: M. Morgenstern, Seminar at the University of Linz, Austria: *Probing the Local Density of States of Dilute Electron Systems in Different Dimensions.*

08.12.01: J. Bansmann, K.H. Meiwes-Broer, M. Getzlaff, and J. Braun, XRMS 2001, Halle, Germany: *Angle resolved ultraviolet photoelectron spectroscopy at thin cobalt films on W(110): experimental results and analysis of the electronic structure.*

12.12.01: R. Wiesendanger, Seminar TU Delft, The Netherlands: *Novel insight into nano-scale magnetism by spin-polarized STM.*

7.2.2 Posters

04.01.99: M. Bode, M. Getzlaff, R. Pascal, and R. Wiesendanger, 211. WE-Heraeus Seminar on Nanomagnetic Structures, Bad Honnef, Germany: *Electronic properties of rare-earth metal (0001) surfaces and their relevance for the development of spin-polarized scanning tunneling microscopy.*

05.01.99: X. Nie, S. Heinze, M. Weinert, and S. Blügel, 211. WE-Heraeus Seminar (Magnetic Nanostructures) Physikzentrum Bad Honnef, Germany: *Magnetic surfaces under static external electric fields.*

05.01.99: M. Getzlaff, R. Pascal, H. Tödter, M. Bode, and R. Wiesendanger, Workshop "Nanomagnetic Structures"(1999), Bad Honnef, Germany: *STM study of* $GdFe_2$ *alloy formation.*

20.01.99: M. Morgenstern, M. Getzlaff, D. Haude, R. L. Johnson, and R. Wiesendanger, Hamburg, Germany (User-Treffen des Hamburger Synchrotronstrahlungslabors HASYLAB): *Coverage Dependence of Fe-induced Fermi Level Pinning in the Conduction Band of InAs(110).*

22.03.99: D. Haude, M. Morgenstern, Chr. Wittneven, R. Dombrowski, M. Getzlaff, and R. Wiesendanger, Frühjahrstagung der Deutschen Physikalischen Gesellschaft, Münster, Germany: *Untersuchung des Fe induzierten zweidimensionalen Elektronengases auf InAs(110) mittels STM und UPS.*

25.03.99: H. Hölscher, A. Schwarz, U. D. Schwarz, W. Allers, and R. Wiesendanger, Frühjahrstagung der Deutschen Physikalischen Gesellschaft, Münster, Germany: *Analyse der Frequenzverschiebung in der dynamischen Rasterkraftmikroskopie.*

25.03.99: U. D. Schwarz, H. Hölscher, and R. Wiesendanger, Frühjahrstagung der Deutschen Physikalischen Gesellschaft, Münster, Germany: *Analyse des Kontrastmechanismus in der dynamischen Rasterkraftmikroskopie.*

25.03.99: O. Pietzsch, A. Kubetzka, M. Bode, and R. Wiesendanger, Frühjahrstagung der Deutschen Physikalischen Gesellschaft, Münster, Germany: *Neues UHV-Tieftemperatur-STM mit Magnetkryostat.*

19.07.99: M. Getzlaff, A. Pundt, M. Bode, R. Kirchheim, and R. Wiesendanger, 10th International Conference on Scanning Tunneling Microscopy/Spectroscopy and Related Techniques, Seoul, South Korea: *Imaging of hydrogen-induced plastic deformation of Gadolinium.*

19.07.99: S. Heinze, S. Blügel, and R. Wiesendanger, 10th International Conference on Scanning Tunneling Microscopy/Spectroscopy and Related Techniques, Seoul, South Korea: *What can be learnt by non-spinpolarized Scanning Tunneling Microscopy about surface magnetism of Cr and Mn on Fe(001)?.*

19.07.99: M. Getzlaff, R. Pascal, Ch. Zarnitz, L. Busse, M. Bode, and R. Wiesendanger, 10th International Conference on Scanning Tunneling Microscopy/Spectroscopy and Related Techniques, Seoul, South Korea: *Ordered* $GdFe_2$ *- alloy formation: structure and electronic properties.*

20.07.99: A. Schwarz, W. Allers, U. D. Schwarz, and R. Wiesendanger, 10th International Conference on Scanning Tunneling Microscopy/Spectroscopy and Related Techniques, Seoul, South Korea: *Point defects on cleaved n-InAs(110)-(1x1) investigated with dynamic scanning force microscopy un ultrahigh vacuum and at low temperatures.*

20.07.99: A. Pundt, M. Getzlaff, M. Bode, R. Wiesendanger, and R. Kirchheim, Gordon Research Conference "Metal-hydrogen systems" , Henniker, USA: *Surface modifications due to hydrogen induced plastic deformation of Gd films.*

21.07.99: W. Allers, A. Schwarz, U. D. Schwarz, and R. Wiesendanger, 10th International Conference on Scanning Tunneling Microscopy/Spectroscopy and Related Techniques, Seoul, South Korea: *Dynamic scanning force microscopy at low temperatures on van der Waals surfaces: graphite (0001) and xenon (111).*

21.07.99: A. Born, J. Isenbart und R. Wiesendanger, 10th International Conference on Scanning Tunneling Microscopy/Spectroscopy and Related Techniques, Seoul, South Korea: *Scanning Capacitance Microscopy and Spectroscopy on Semiconductor Devices.*

26.07.99: M. Getzlaff, R. Pascal, Ch. Zarnitz, L. Busse, M. Bode, and R. Wiesendanger, ICSOS-6 , Vancouver, Canada: *Preparation of high-qualtiy* $GdFe_2$ *alloys.*

26.07.99: M. Getzlaff, A. Pundt, M. Bode, R. Kirchheim, and R. Wiesendanger, ICSOS-6, Vancouver, Canada: *Hydrogen-induced plastic deformation of Gd thin films.*

01.09.99: W. Allers, H. Hölscher, U. D. Schwarz, A. Schwarz, and R. Wiesendanger, Second International Workshop on Non-Contact Atomic Force Microscopy, Pontresia, Switzerland: *Analysing the tip-sample interaction in dynamic mode scanning force microscopy.*

01.09.99: A. Schwarz, W. Allers, U. D. Schwarz, and R. Wiesendanger, Second International Workshop on Noncontact Atomic Force Microscopy, Pontresina, Switzerland: *Screened Coulomb potentials of doping atoms in InAs detected by scanning force microscopy in the dynamic mode.*

21.09.99: Ch. Zarnitz, L. Busse, T. Liu, M. Bode, M. Getzlaff, and R. Wiesendanger, European Conference of Surface Science , Vienna, Austria: *STM investigation of structural and electronic properties of Fe on Gd(0001) and Gd on Fe(110).*

22.09.99: M. Getzlaff, M. Bode, and R. Wiesendanger, European Conference of Surface Science, Vienna, Austria: *Magnetic domain imaging by spin-polarized vacuum tunneling.*

23.09.99: J. Bansmann, M. Getzlaff, M. Fluchtmann, and J. Braun, European Conference of Surface Science, Vienna, Austria: *Epitaxial cobalt films on W(110) - an experimental and theoretical photoemission study with polarized synchrotron radiation.*

23.09.99: M. Getzlaff, Ch. Zarnitz, A. Pundt, M. Bode, R. Kirchheim, and R. Wiesendanger, European Conference of Surface Science, Vienna, Austria: *Plastic deformation of rare earth metal thin films during hydrogen absorption.*

23.09.99: M. Morgenstern, M. Getzlaff, D. Haude, R. L. Johnson, and R. Wiesendanger, European Conference of Surface Science, Vienna, Austria: *ARUPS-investigation of the Fe induced Fermi-level shift and the two-dimensional electron gas at the InAs(110) surface.*

18.11.99: S. Heinze, T. Asada, and S. Blügel, 44th Annual Conference on Magnetism and Magnetic Materials, San Jose, California, USA: *Theoretical analysis of STM and STS on magnetic thin films.*

30.11.99: A. Pundt, M. Getzlaff, M. Bode, R. Wiesendanger, and R. Kirchheim, Symposium Thin films Stresses and Mechanical Properties VIII , Boston, USA: *Surface modifications due to hydrogen induced plastic deformation.*

05.01.00: M.Bode, O.Pietzsch, A.Kubetzka, and R.Wiesendanger, 228. WE-Heraeus Seminar on Metal-Nonmetal Structures for Magnetoelectronics, Bad Honnef, Germany: *Real-space observation of dipolar antiferromagnetism in magnetic nanowires by spin-polarized scanning tunneling spectroscopy.*

05.01.00: S. Heinze, D. Wortmann, G. Bihlmayer, and S. Blügel, 228.WE-Heraeus Seminar (Metal-Nonmetal Structures for Magnetoelectronics), Physikzentrum Bad Honnef, Germany: *Ab Initio Calculations of Tunneling through MgO Barriers on Fe(001).*

14.02.00: M.Bode, O.Pietzsch, A.Kubetzka, and R.Wiesendanger, 3rd Gordon Research Conference on Magnetic Nanostructures, Ventura, CA/USA: *Real-space observation of dipolar antiferromagnetism in magnetic nanowires by spin-polarized scanning tunneling microscopy.*

23.02.00: M. Morgenstern, 11. Int. Winterschule Mauterndorf, Germany: Low Dimensional Systems: Fundamentals and Applications: *A nanoscale view to Landau oscillations and spin splitting of a quantum dot.*

15.03.00: T. Richter, J. H. Müller, U. D. Schwarz, and R. Wiesendanger, Digital Instruments-Veeco User Meeting, Mainz, Germany: *Untersuchung des Quellverhaltens menschlicher Hautzellen in verschiedenen Medien mittels Rasterkraftmikroskopie.*

15.03.00: A. Wehner, V. Hagen, A. Born, and R. Wiesendanger, D.I.-Veeco User Meeting, Mainz, Germany: *IC-Charakterisierung mittels Rastersondenmethoden.*

15.03.00: D. Haude, I. Meinel, M. Morgenstern, R. Wiesendanger, 18th General Conference of the Condensed Matter Division, European Physical Society, Montreux, Switzerland: *Magnetic field induced localization imaged with scanning tunneling microscopy.*

16.03.00 O. Pietzsch, A. Kubetzka, M. Bode, and R. Wiesendanger, 18th General Conference of the Condensed Matter Division, European Physical Society, Montreux, Switzerland: *Direct Visualization of Dipolar Antiferromagneticically coupled Nanowires by Spin Polarized Scanning Tunneling Spectroscopy.*

27.03.00: W. Allers, H. Hölscher, A. Schwarz, U. D. Schwarz, and R. Wiesendanger, Frühjahrstagung der Deutschen Physikalischen Gesellschaft, Regensburg, Germany: *Analyse der Spitze-Probe-Wechselwirkung im dynamischen Modus der Rasterkraftmikroskopie.*

27.03.00: S. Langkat, W. Allers, U. D. Schwarz, and R. Wiesendanger, Frühjahrstagung der Deutschen Physikalischen Gesellschaft, Regensburg, Germany: *Tieftemperatur-Rasterkraftmikroskop mit 3D-Probenpositionierung und atomarer Auflösung.*

27.03.00: J. H. Müller, U. D. Schwarz, and R. Wiesendanger; Frühjahrstagung der Deutschen Physikalischen Gesellschaft, Regensburg, Germany: *Kryo-Rasterkraftmikroskopie im Nichtkontaktbetrieb zur Charakterisierung biologischer Proben.*

27.03.00: T. Richter, J. H. Müller, U. D. Schwarz, and R. Wiesendanger, Frühjahrstagung der Deutschen Physikalischen Gesellschaft, Regensburg, Germany: *Untersuchung des Quellverhaltens menschlicher Hautzellen in verschiedenen Medien mittels Rasterkraftmikroskopie.*

27.03.00: A. Wachowiak, J. Wiebe, D. Haude, M. Morgenstern, and R. Wiesendanger, Frühjahrstagung des Arbeitskreises Festkörperphysik der Deutschen Physikalischen Gesellschaft, Regensburg, Germany: *Aufbau einer (300 mK / 14 T)-Rastertunnelmikroskopie-Anlage.*

27.03.00: Th. Maltezopoulos, M. Morgenstern, S. Haubold, and R. Wiesendanger, Frühjahrstagung der Deutschen Physikalischen Gesellschaft, Regensburg, Germany: *Deposition von InAs-Clustern auf HOPG.*

30.03.00: Chr. Meyer, J. Wiebe, M. Morgenstern, and R. Wiesendanger, Frühjahrstagung des Arbeitskreises Festkörperphysik der Deutschen Physikalischen Gesellschaft, Regensburg, Germany: *Das Wachstum von Niob auf InAs(110).*

14.06.00: M. Morgenstern, D. Haude, V. Gudmundsson, R. Dombrowski, Chr. Wittneven, Chr. Steinebach, and R. Wiesendanger, WE-Hereaus Workshop "Interacting Electrons in Nanostructures", Bad Honnef, Germany: *A nanoscale view to Landau oscillations and spin splitting of a quantum dot.*

21.06.00: J. Klijn, D. Haude, M. Getzlaff, Chr. Meyer, R.L. Johnson, M. Morgenstern, and R. Wiesendanger, Second International Conference on Scanning Probe Spectroscopy, Hamburg, Germany: *Scanning tunneling spectroscopy of the Fe-induced two dimensional electron gas on InAs(110).*

03.07.00: M. Morgenstern, M. Getzlaff, D. Haude, R. L. Johnson, and R. Wiesendanger, Symposium on Spin Electronics, Halle, Germany: *The Fe induced two dimensional electron gas at the surface of InAs(110).*

06.07.00: M. Morgenstern, D. Haude, I. Meinel, and R. Wiesendanger, Workshop "Quantum Hall Effect", Schloß Ringberg, Germany: *Magnetic field induced localization in a semiconductor 3DEG imaged with scanning tunneling microscopy.*

17.07.00: H. Hölscher, W. Allers, A. Schwarz, U. D. Schwarz, and R. Wiesendanger, Third International Workshop on Non-Contact Atomic Force Microscopy, Hamburg, Germany: *Interpretation of "true atomic" resolution images in non-contact atomic force microscopy.*

17.07.00: J. H. Müller, U. D. Schwarz, R. Wepf, and R. Wiesendanger, Third International Workshop on Non-Contact Atomic Force Microscopy, Hamburg, Germany: *A cryogenic scanning force microscope for the imaging of frozen biological samples in non-contact mode.*

17.07.00: T. Richter, J. H. Müller, U. D. Schwarz, and R. Wiesendanger, Third International Workshop on Non-Contact Atomic Force Microscopy, Hamburg, Germany: *Investigation of the swelling of human skin cells in liquid media by tapping mode scanning force microscopy.*

17.07.00: M. Kleiber, M. Bode, R. Ravlic, and R. Wiesendanger, 3rd International Conference on Non-Contact Atomic Force Microscopy, Hamburg, Germany: *Ultrathin Fe-Films on Cr(001) investigated by MFM under UHV Conditions.*

21.07.00: H. Hölscher, W. Allers, A. Schwarz, U. D. Schwarz, and R. Wiesendanger, Second International Conference on Scanning Probe Spectroscopy, Hamburg, Germany: *Determination and analysis of tip-sample interaction forces by dynamic force spectroscopy.*

21.07.00: O. Pietzsch, A. Kubetzka, M. Bode, and R. Wiesendanger, 2nd International Conference on Scanning Probe Spectroscopy, and 30th IUVSTA Workshop, Hamburg, Germany: *Direct Visualization of Dipolar Antiferromagneticically coupled Nanowires by Spin Polarized Scanning Tunneling Spectroscopy.*

21.07.00: M. Kleiber, R. Ravlic, M. Bode, and R. Wiesendanger, 2nd International Conference on Scanning Probe Spectroscopy, and 30th IUVSTA Workshop, Hamburg, Germany: *A STS Study of the Cr(001) Surface.*

21.07.00: S. Heinze, M. Bode, A. Kubetzka, D. Wortmann, Ph. Kurz, O. Pietzsch, X. Nie, S. Blügel, and R. Wiesendanger, 2nd International Conference on Scanning Probe Spectroscopy, Hamburg, Germany: *Real Space Imaging of Surface Antiferromagnetism on the Atomic Scale.*

21.07.00: M. Getzlaff, Ch. Zarnitz, L. Busse, and R. Wiesendanger, 2nd International Conference on Scanning Probe Spectroscopy , Hamburg, Germany: *Chemical imaging of Gd on Fe(110) and Fe on Gd(0001) nanostructures.*

21.07.00: J. Klijn, D. Haude, M. Morgenstern, and R. Wiesendanger, 2nd International Conference on Scanning Probe Spectroscopy, and 30th IUVSTA Workshop, Hamburg, Germany: *Scanning tunneling spectrocopy of the Fe-induced two-dimensional electron gas on InAs(110).*

21.07.00: A. Kubetzka, O. Pietzsch, M. Bode, and R. Wiesendanger, 2nd International Conference on Scanning Probe Spectroscopy, and 30th IUVSTA Workshop, Hamburg, Germany: *Correlation of structural and magnetic properties of ultra-thin Fe-films on W(110) by spin-polarized STM/STS.*

21.07.00: A. Kelch, 2nd International Conference on Scanning Probe Spectroscopy, and 30th IUVSTA Workshop, Hamburg, Germany: *Thin cross-sections of hairs investigated by scanning near-field optical microscopy in fluorescence and transmission mode.*

06.09.00: O. Pietzsch, A. Kubetzka, M. Bode, M. Getzlaff, and R. Wiesendanger, ECOSS-19 , Madrid, Spain: *Ferromagnetic nanowires and nanodots: imaging of magnetic domains by spin polarized scanning tunneling spectroscopy.*

07.09.00: M. Getzlaff, M. Morgenstern, Ch. Meyer, J. Klijn, R. Brochier, R.L. Johnson and R. Wiesendanger, ECOSS-19 , Madrid, Spain: *Dispersion behavior of a two-dimensional electron gas induced by Nb on InAs(110).*

07.09.00: M. Getzlaff, R. Pascal, Ch. Zarnitz, and R. Wiesendanger, ECOSS-19 , Madrid, Spain: *Thin film growth of GdFe2 intermetallics.*

07.09.00: M. Getzlaff and R. Wiesendanger, ECOSS-19 , Madrid, Spain: *Magnetic properties of Pd overlayers on Fe(110).*

26.01.01: J. Klijn, Chr. Meyer, M. Getzlaff, M. Morgenstern, R. Wiesendanger, R. Brochier, L. Plucinski, R.L. Johnson, R. Adelung, L. Kipp, and M. Skibowski, Hasylab User‘s Meeting "Research with Synchotron Radiation", Hamburg, Germany: *Photoelectron spectroscopy and scanning tunneling spectroscopy of adsorbate induced two-dimensional electron systems.*

26.03.01: Chr. Meyer, J. Klijn, L. Sacharow, M. Morgenstern, and R. Wiesendanger, Frühjahrstagung der Deutschen Physikalischen Gesellschaft, Hamburg, Germany: *Die Atomare Auflösung auf InAs(110).*

27.03.01: A. Kubetzka, O. Pietzsch, M. Bode, and R. Wiesendanger, Frühjahrstagung der Deutschen Physikalischen Gesellschaft, Hamburg, Germany: *Korrelation struktureller und magnetischer Eigenschaften ultradünner Fe-Filme auf W(110) mittels SP-STM/STS.*

28.03.01: M. Liebmann, A. Schwarz, and R. Wiesendanger, Frühjahrstagung der Deutschen Physikalischen Gesellschaft, Hamburg, Germany: *UHV-Tieftemperatur-Magnetkraftmikroskop mit 5T-Magnet und xy-Verschiebetisch: Aufbau und Test.*

28.03.01: L. Tröger, W. Allers, and R. Wiesendanger, Frühjahrstagung der Deutschen Physikalischen Gesellschaft, Hamburg, Germany: *Aufbau eines Tieftemperatur-Rasterkraftmikroskops.*

28.03.01: Th. Maltezopoulos, M. Morgenstern, A. Rogach, S. Haubold, M. Tews, and R. Wiesendanger, Frühjahrstagung der Deutschen Physikalischen Gesellschaft, Hamburg, Germany: *Rastertunnelmikroskopie an Halbleiter-Clustern.*

25.06.01: R. Ravlic, M. Kleiber, M. Bode, and R. Wiesendanger, Symposium on Magnetic Multilayers, MML ‘01, Aachen, Germany: *Properties of Fe/Cr(001) Studied by MFM and SP-STM.*

27.06.01: M. Getzlaff and R. Wiesendanger, Symposium on Magnetic Multilayers, MML '01, Aachen, Germany: *Magnetic dichroism study on interfacial magnetism.*

16.07.01: A. Schwarz, M. Liebmann, U.H. Pi, D.W. Kim, T.W. Noh, Z.G. Khim, and R. Wiesendanger, 11th International Conference on Scanning Tunneling Microscopy/Spectroscopy and Related Techniques STM '01, Vancouver, Canada: *Investigation of perovskite manganites with a 5T low temperature force microscope in UHV.*

16.07.01: A. Wachowiak, J. Wiebe, D. Haude, M. Morgenstern, and R. Wiesendanger, 11th International Conference on Scanning Tunneling Microscopy/Spectroscopy and Related Techniques STM '01, Vancouver, Canada: *A Scanning Tunneling Microscope for Ultra High Vacuum Investigations at 300mk.*

16.07.01: A. Kubetzka, O. Pietzsch, M. Bode, and R. Wiesendanger, 11th International Conference on Scanning Tunneling Microscopy/Spectroscopy and Related Techniques STM '01, Vancouver, Canada: *Magnetism of Nanoscale Islands investigated by SP-STM/STS.*

17.07.01: S. Langkat, W. Allers, and R. Wiesendanger, 11th International Conference on Scanning Tunneling Microscopy/Spectroscopy and Related Techniques STM '01, Vancouver, Canada: *Non-contact Scanning Force Microscopy on Transition Metal Oxides.*

18.07.01: M. Morgenstern, M. Getzlaff, J. Wiebe, D. Haude, J. Klijn, Chr. Meyer, A. Wachowiak, R. Wiesendanger, R. Brochier, L. Plucinks, R. L. Johnson, R. Adelung, L. Kipp, and M. Skibowski, 11th International Conference on Scanning Tunneling Microscopy/Spectroscopy and Related Techniques STM '01, Vancouver, Canada: *The near-surface two-dimensional electron system on InAs(110) investigated by scanning tunneling spectroscopy and photoelectron spectroscopy.*

25.07.01: M. Getzlaff, M. Morgenstern, J. Klijn, Chr. Meyer, A. Wachowiak, J. Wiebe, L. Plucinks, R.L. Johnson, R. Adelung, K. Roßnagel, L. Kipp, M. Skibowski, and R. Wiesendanger, 13th International Conference on Vacuum Ultraviolet Radiation Physics VUV–XIII, Triest, Italy: *Photoemission on two-dimensional electron system.*

30.07.01: M. Morgenstern, D. Haude, and R. Wiesendanger, 14th International Conference on the Electronic Properties of Two-Dimensional Systems, Prague, Czech Republic: *Two-dimensional properties of a three-dimensional electron system in the extreme quantum limit.*

31.07.01: J. Klijn, Ch. Meyer, D. Haude, M. Morgenstern, M. Getzlaff, R. Adelung, L. Kipp, M. Skibowski, and R. Wiesendanger, 14th International Conference on the Electronic Properties of Two-Dimensional Systems, Prague, Czech Republic: *Scanning tunneling spectroscopy on adsorbate induced two-dimensional electron systems on InAs(110).*

11.09.01: M. Liebmann, A. Schwarz, U. Kaiser, and R. Wiesendanger, WE-Heraeus-Ferienkurs, Dresden (Germany): *Low-temperature magnetic force microscopy on manganese perovskites.*

22.09.01: M. Morgenstern, D. Haude, Chr. Meyer, R. Wiesendanger, 3. Symposium Schwerpunkt Quanten-Hall-Effekt, Gedern, Germany: *Two-Dimensional Properties of a three dimensional electron system in the extreme quantum limit.*

Chapter 8

Talks Given by Guests

01.02.99: Prof. Dr. M. Johnson (Washington, USA): *Hybrid Ferromagnet-Semiconductor Magnetoelectronic Devices.*

01.02.99: Prof. Dr. P. Bruno (MPI Halle, Germany): *Magnetic Scanning Tunneling Microscopy: Theory.*

01.02.99: Prof. Dr. G. Bayreuther (Regensburg, Germany): *Spin-Polarized Electrons in Metal-Semiconductor Heterostructures.*

02.02.99: Prof. Dr. G. Güntherodt (Aachen, Germany): *Magnetoresistive memory cells: spin-polarized tunneling and exchange bias.*

02.02.99: Dr. R. Mattheis (Jena, Germany): *XMR effects in spin electronics.*

02.02.99: Prof. Dr. J. Chapman (Glasgow, Great Britain): *Magnetization reversal process in thin films and multilayer magnetic elements.*

04.02.99: Dipl.-Phys. Ph. Kurz (FZ Jülich): *Dichtefunktionalrechnungen zur Bandstruktur von Gd.*

10.02.99: Dipl.-Phys. J. Hartwich (Universität Bielefeld): *Herstellung und Untersuchung lateraler Nanostrukturen in Resistschichten und Multischichtsystemen mittels Rastersondenmethoden.*

17.03.99: Dr. M. Löhndorf (NIST Boulder, USA): *Field Mapping with the Magnetic Resonance Force Microscope.*

26.04.99: Dr. A. Pundt (Universität Göttingen): *Wasserstoffabsorption in dünnen Metallschichten und -clustern.*

27.04.99: Prof. Dr. Y. Manassen (Ben Gurion University, Israel): *Novel applications of SPM: nanomagnetism, disordered surfaces and nm-sized transistors.*

03.05.99: Dr. M. Scherge (TU Ilmenau): *Tribologie im Bereich zwischen Makro und Nano.*

17.05.99: Dipl.-Phys. Ch. Sommerhalter (HMI Berlin): *Hochempfindliche quantitative Kelvinsondenmikroskopie mit einem UHV-NC-AFM.*

31.05.99: Dr. W. Swiech (University of Illinois at Urbana, USA): *Low-energy electron microscopy investigation of refractory bcc metal (110) thin films grown on sapphire substrates.*

14.06.99: Dr. W. Wulfhekel (MPI für Mikrostrukturphysik Halle): *Ein einfacher Ansatz zum spinpolarisierten STM.*

12.07.99: Prof. Dr. B. Bhushan (Ohio State University, USA): *Micro-/Nanotribology and its Applications.*

29.09.99: Dr. H. P. Oepen (MPI Halle): *Magnetische Nanostrukturen und ultradünne Ferromagnete.*

29.09.99: Dr. W. Lutzke (MPI Halle): *Magnetische Mikrostrukturen: Experimente und Simulationen.*

29.09.99: Dr. E. Vedmedenko (MPI Halle): *Magnetische Ordnung in ultradünnen Filmen: Monte-Carlo-Untersuchungen.*

29.09.99: Dr. S. Förster (MPI Teltow): *Magnetische Cluster in Polymeren.*

29.09.99: Dr. W. Wurth (TU München): *Röntgenabsorptionsspektroskopie an deponierten magnetischen Clustern.*

29.09.99: Prof. Dr. F. U. Hillebrecht (Universität Düsseldorf): *Photoelektronenspektroskopie mit Synchrotronstrahlung: eine leistungsfähige Methode zur Untersuchung magnetischer Nanostrukturen.*

20.10.99: Dipl.-Phys. D. Wortmann (FZ Jülich): *Theorie der Rastertunnelmikroskopie von metallischen Oberflächenlegierungen.*

15.11.99: Dr. H. Hoevel (Universität Dormund): *Geometrie und elektronische Response von Edelgas-Monolagen und Nanostrukturen.*

22.11.99: Dr. M. Wenderoth (Universität Göttingen): *Rastertunnelmikroskopie an III-V-Verbindungshalbleitern.*

29.11.99: Dr. A. Kühnle (University of Aarhus, Danmark): *Manipulation von Diiodbenzol mit dem STM - Experiment und Simulation.*

07.12.99: Dr. A. Schreyer (Universität Bochum): *Frustrationseffekte in dünnen Cr-Schichten.*

17.01.00: Dr. M. Hansmann (Universität Heidelberg): *Rastertunnelmikroskopie an Schichtstruktur-Halbleitern.*

21.01.00: Dr. Ph. Avouris (IBM, Yorktown Heights, USA): *Carbon Nanotubes: Electronic Properties and Devices.*

21.01.00: Prof. Dr. R. Taylor (Computer Science Dept., University of North Carolina, USA): *The Nanomanipulator: Computer Scientists and Physicists Building Tools for Science and Education.*

21.01.00: Prof. Dr. K. v. Klitzing (MPI for Solid State Research , Stuttgart, Germany): *Semiconductor Nanostructures.*

21.01.00: Prof. Dr. P. Fromherz (MPI for Biochemistry, Martinsried/Munich, Germany): *Nanometers and Gigaohms in Membrane-Semiconductor Contacts.*

21.01.00: Prof. Dr. D. Fitzmaurice (Chemistry Dept., University of Dublin, Ireland): *Using Biology to Programme the Assembly of Nanostructured Materials.*

22.01.00: Dr. D. Eigler (IBM, San Jos, USA): *Quantum Mirages: :Electronic Projection of Phantom Atoms.*

22.01.00: Prof. Dr. H. Craighead (Appl. & Eng. Physics, Cornell University, USA): *Nanostructures for Biological Studies.*

22.01.00: Prof. Dr. P. Matsudaira (White Institute, MIT, USA): *The Present and Future of BioMEMS Technologies.*

22.01.00: Prof. Dr. K. Conradsen (Dept. of Mathematical Modelling, Lyngby Denmark): *Modern Techniques in Image Analysis Applicable in Nanotechnology.*

22.01.00: Dr. R. Frank (German National Research Centre, Braunschweig, Germany): *Multiplexed Biochemical Assays in Array Formats.*

22.01.00: Prof. Dr. T. Yanagida (Osaka University, Medical School, Japan): *Single Molecule Techniques in Life Sciences.*

24.01.00: Dr. Bäumle (Universität GH Essen): *Ein-, zwei- und drei-dimensionale Anordnungen von Metallnanopartikeln.*

17.02.00: Dipl.-Phys. M. Tews (Michigan Technical University, USA): *Berechnung relativistischer Kontinuumswellenfunktionen in N-Elektronen-Atomen.*

18.02.00: Dipl.-Phys. T. Miokovic (TU Karlsruhe): *Magnetisierung eines Ce-Systems mit niedrigster Ladungsträgerkonzentration.*

10.04.00: Dr. M. Ashino (JRCAT-ATP, Tsukuba, Japan): *Preparation and observation of* TiO_2*(110) surface for molecular imaging of DNA using non-contact AFM.*

17.04.00: Prof. Dr. H. J. Elmers (Universität Mainz): *Magnetische Nanostrukturen.*

08.05.00: Dr. J. F. Pascual (FHI Berlin, Germany): *Vibrational excitations of single molecular adsorbates with a low temperature STM.*

11.05.00: Prof. Dr. Wilson Ho (Cornell University, USA): *Single Molecule Vibrational Spectroscopy and Chemistry with the STM.*

15.05.00: Dr. A. Shluger (University College London, Great Britain): *Theory of Non-Contact Atomic Force Microscopy.*

22.06.00: Prof. Dr. G. E. W. Bauer (Delft University of Technology, The Netherlands): *Physics of spintronics.*

22.06.00: Dr. S. Blügel (IFF, Forschungszentrum Jülich, Germany): *Nanomagnetism meets magnetoelectronics.*

22.06.00: Prof. Dr. J. M: MacLaren (Tulane University, New Orleans, Louisiana, USA): *Theory of spin dependent tunneling.*

27.06.00: Prof. Dr. U. Gradmann (MPI Halle): *Der Magnetismus von Fe auf W(110).*

29.06.00: Dr. T. Hesjedal (Stanford University): *Akustische Rastersondenmikroskopie.*

27.07.00: Dipl. Chem. K. v. Bergmann (Universität Bonn): *Rastertunnelmikroskopische Untersuchung von Manganclustern auf einem ultradünnen Aluminiumoxidfilm auf Ni3Al(111).*

27.11.00: Dipl.- Phys. U. H. Pi (Seoul National University, Korea): *Percolative transport of LCMO/LAO films.*

18.12.00: Dr. Teichert (Uni Leoben, Austria): *Self-organized SiGe nanostructures and their use as templates for magnetic thin films.*

20.12.00: Dr. M. Dreyer (University of Maryland, USA): *Magnetische Untersuchungen an dünnen strukturierten Filmen.*

15.01.01: Prof. Dr. M. Farle (TU Braunschweig): *Der Spin-Reorientierungs-Phasenübergang in magnetischen Monolagen.*

25.01.01: Dr. I. Gebeshuber (TU Wien, Austria): *UHV-AFM/STM studies of ion-induced nano-defect formation.*

29.01.01: Dr. R. A. Römer (TU Chemnitz, Germany): *Wavefunction statistics in the Anderson model of localization.*

05.02.01: Dr. M. Müser (Universität Mainz): *Atomistische Betrachtungen der Reibung zweier Festkörper und was wir hierzu von Computersimulationen neues lernen können.*

12.02.01: Prof. Dr. C. Laubschat (TU Dresden): *Elektronische Struktur geordneter Dünnschichten von Seltenerd- und Uranverbindungen.*

22.02.01: L. Berbil-Bautista (University of Madrid, Spain): *Role of the Metal/Semiconductor Interface in Quantum Size Effects.*

29.05.01: Dr. R. Roehlsberger (Universität Rostock): *Spinstruktur von magnetischen Nanostrukturen mittels kernresonanter Röntgenstreuung.*

01.06.01: Prof. Dr. W. D. Doyle (University of Alabama, USA): *Future Storage Technology.*

11.06.01: Dr. G. Hoffmann (Universität Kiel): *RTM induzierte Lichtemission von metallischen Quantum Wells.*

02.07.01: Dr. S. Lemay (University of Delft, The Netherlands): *Two-dimensional imaging of electronic wavefunctions in carbon nanotubes: an illustration of Bloch's theorem.*

20.07.01: Dr. Hiroshi Yamaguchi (NTT, Japan): *InAs/GaAs(111)A heterostructures. - from LT-STM study to the application for electromechanical devices -.*

31.10.01: Prof. Dr. R.M. Feenstra (University of Pittsburgh, USA): *Semiconductor Heterostructures studied by Scanning Tunneling Microscopy.*

26.11.01: Prof. Dr. A.L. Vázquez de Parga (University Autonoma de Madrid, Spain): *Detecting electronic states at stacking faults in magnetic thin films by tunneling spectroscopy.*

Chapter 9

Lectures and Courses at the University of Hamburg

Einführung in die Struktur der Materie (Kursvorlesung)

Festkörperphysik II: Elektronen in Festkörpern

100 Jahre Quantentheorie - neue Anwendungen im Nanokosmos

Nanotechnologie - die industrielle Revolution des 21. Jahrhunderts

Einführung in die Rastersensormikroskopie

Anwendungen der Rastersensormikroskopie

Elektronenspektroskopie

Ringvorlesung "Physik der Mikro- und Nanostrukturen"

Seminar über Nahfeldgrenzflächenphysik und Nanotechnologie

Seminar über aktuelle Probleme der Rastersensorphysik

Proseminar über Mikroskopische Methoden der Oberflächenphysik

Proseminar über Neue Materialien

Übungen zur Einführung in die Struktur der Materie

Übungen zur Elektronik I und II

Übungen zur Einführung in die Rastersensormikroskopie

Fortgeschrittenenpraktikum

TU - Praktikum

UHV - Blockpraktikum

Laborpraktikum

Diplompraktikum

Chapter 10

Contributions to International Organizations and Journals

Organizations

- Chair of the Nano-Science and Technology Division of the International Union for Vacuum Science, Technique and Applications (IUVSTA)
- Chair of the Nano-Science and Technology Division of the German Vacuum Society
- Chair of the German Center of Competence in Nano-Scale Analysis (since 2000)

Conferences

- Co-Organizer of the 5th Hamburg Symposium "Physics of Micro- and Nanostructures (Hamburg 1999)
- Member of the Program Committee of the 10th International Scanning Tunneling Microscopy-Conference "STM‘99" (Seoul, Korea 1999)
- Member of the Steering Committee of the "2nd International Workshop on Non-contact Atomic Force Microscopy" (Pontresina, Switzerland 1999)
- Organizer of the Hamburg Workshop "Magnetic Nanostructures: Physical Principles and Applications" (Hamburg, 1999)
- Member of the International Advisory Committee of the "3rd International Symposium on Surface Science for Micro- and Nano-Device Fabrication", ISSS-3 (Tokyo, Japan 1999)
- Organizer of the 1st International Hamburg Symposium "Interdisciplinary Nanosciences" (Hamburg, 2000)

- Chairman of the "3rd International Conference on Noncontact Atomic Force Microscopy" NC-AFM 2000 (Hamburg, 2000)
- Co-Chairman of the 2nd International Conference on Scanning Probe Spectroscopy "SPS2000" (Hamburg, 2000)
- Co-Chairman of the SPM-Symposium within the IUMRS-ICA'2000 - Conference (Hong Kong, 2000)
- Member of the International Program and Advisory Committee of the "4th International School on the Applications of Surface Science Techniques", ISASST-4 (Erice, Italy 2000)
- Member of the International Program Committee of the "4th International Conference on the Development and Technological Application of Scanning Probe Methods" SXM4 (Münster, 2000)
- Member of the International Program Committee of the "6th International Conference on Nanometer-Scale Science and Technology" NANO-6 (Boston, USA 2000)
- Member of the Program Committee of the Japanese-German Nanotechnology-Symposium 2000 (Berlin, 2000)
- Member of the Program Committee of the "26th International Symposium for Testing and Failure Analysis ISTFA 2000" (Bellevue, Washington, USA 2000)
- Member of the European Program and Advisory Committee of the "4th International Conference on Metallic Multilayers", MML'01 (Aachen, 2001)
- Member of the Steering Committee of the "11th International Conference on Scanning Tunneling Microscopy STM'01" (Vancouver, Canada 2001)
- Member of the Steering Committee of the "4th International Conference on Noncontact Atomic Force Microscopy" (Kyoto, Japan 2001)
- Co-organizer of the "3rd Workshop on Quantum Hall Systems" (Gedern, Germany 2001)
- Organizer of the 2nd Hamburg Symposium "Interdisciplinary Nanosciences" (Hamburg, 2001)
- Chair of the Nanometer Structures Division Program Committee of the "15th International Vacuum Congress" IVC-15 (San Francisco, USA 2001)

Journals

- Co-Editor of Applied Physics A (Topic: Nanostructure Physics and Technology, until 2000)
- Co-Editor of the Springer Series in Nano-Science and Technology

Chapter 11

How to reach us

... by mail	write to University of Hamburg, Microstructure Advanced Research Center and Institute of Applied Physics, Jungiusstraße 11, D-20355 Hamburg, Germany.
... by phone	call (++49) 40 42838 5244.
... by fax	send to (++49) 40 42838 6188.
... by e-mail	send to `wiesendanger@physnet.uni-hamburg.de`
... within the WWW	`www.nanoscience.de`
... personally